COMPUTATIONAL ANALYSIS OF STRAIGHT AND MANEUVERING BAT FLIGHT AERODYNAMICS

Peter Windes

Dissertation submitted to the faculty of Virginia Polytechnic Institute and State University in partial fulfillment of the requirements for the degree of

Doctor of Philosophy
in
Mechanical Engineering

Danesh K. Tafti – Chair
Andrew J. Kurdila
Rolf Müller
Mark R. Paul
John J. Socha

May 8, 2020
Blacksburg, Virginia

Keywords: Bat flight, Computational Fluid Dynamics, Bat kinematics, Bat aerodynamics, Maneuvering flight, Immersed Boundary Method

Computational Analysis of Straight and Maneuvering Bat Flight Aerodynamics

Peter Windes

Abstract

Bats have many impressive flight characteristics such as the ability to rapidly change direction, carry substantial loads, and maintain good flight efficiency. For several years, researchers have been working towards an understanding of the specific aerodynamic phenomena which relate the unique wing structure of bats to their flight abilities. Computational fluid dynamics, a powerful tool used extensively across aerospace research, has led to substantial progress in the understanding of insect flight. However, due to technical challenges, numerical simulation has seen limited use in bat flight research. For this research, I develop, validate, and apply computational modeling techniques to three modes of bat flight: straight flight, sweeping turn, and U-turn maneuver. 3D kinematic data collection was achieved using a 28 camera multi-perspective optical motion capture system. The calibration of the cameras was conducted using a multi-camera self-calibration method. Point correspondences between cameras and frames was achieved using a human-supervised software package developed for this project.

After the collection of kinematic data, aerodynamic flow simulations were run using the incompressible Navier-Stokes solver, GenIDLEST. The immersed boundary method (IBM) was used to impose moving boundary conditions representing the wing kinematics. Validation of the computational model was preformed through a grid independence study as well as careful evaluation of other relevant simulation parameters. Verification of the model was performed by comparing simulated aerodynamic loads to the expected loads based on the observed flight trajectories. Additionally, it was established that a sufficient resolution of the wing kinematics was achieved, by calculating the sensitivity of the simulation results to the number of kinematic markers used during motion capture.

For this study, three particular flights are analyzed—a straight and level flight, a sweeping turn, and a sharp 180 degree turn. During straight flight, typical flight velocities observed in the flight tunnel were 2-3 m/s resulting in a Reynolds number of about 12,000. Lift generation occurred almost exclusively during the downstroke, and peaks mid-downstroke. At the beginning of each downstroke, the effective angle of attack of the wings transitions from negative to positive and a leading edge vortex (LEV) quickly forms. LEVs are known to augment lift generation in flapping flight and allow lift to remain high at large angles of attack. During the end of each

downstroke, the LEVs break up and lift drops substantially. As the wingbeat cycle transitions from downstroke to upstroke, the wings rotate such that the wing chordline is vertical as the wing moves upward. This wing rotation is critical for mitigating negative lift during the upstroke.

Many of the basic flight mechanisms used for straight flight—i.e. LEV formation, wing rotation during upstrokes—were also observed during the sweeping turn. In addition, asymmetries in the wing kinematics and consequently the aerodynamics were observed. Early in the turn, the bank angle was low and elevated levels of thrust were generated by the outer wing during both the upstroke and downstroke causing a yaw moment. As the bat moved towards the middle of the turn, the bank angle increased to 20-25 degrees. Although the bank angle remained nominally constant during the middle and later portion of the turn, there was variation within each wingbeat cycle. Specifically, the bank angle dropped during each upstroke and subsequently was recovered during each downstroke as a consequence of elevated lift on the outer wing. Banking served to redirect the net force vector laterally causing a radial, centripetal force. Considering the mass of the bat, the nominal flight velocity, and the radius of curvature, the magnitude of the radial force fully explained the expected centripetal acceleration during the middle and later portion of the turn. Over the entire turn, yaw was found to be important in initiating the turn while banking was more important during the middle part of the turn. Over the course of 5 wingbeat cycles, the change in bearing angle (direction of flight) was about 45 degrees.

Analysis of the U-turn flight showed many of the same characteristics as were observed during the sweeping turn, as well as a few key differences. The bat's ability to rotate its body rapidly appears to be more limited than its ability to change its trajectory. For this reason, the yaw rotation began about one to two cycles before the rapid bearing angle change and was stretched out over several wingbeat cycles. At the apex of the U-turn, the bat combined a high roll angle with a low flight velocity magnitude to very rapidly redirect its bearing direction and negotiate a low radius of curvature flight trajectory. Increases in roll angle occurred almost exclusively during the downstrokes, while both the upstroke and downstroke were active in generating yaw. Elevated thrust on the left outer wing during the end of the upstroke was observed throughout the flight, and elevated drag on the right inside wing did not appear to have an impact on the turn.

We hope that this project motivates and facilitates further computational analysis into bat flight aerodynamics. Additionally, the data and findings will be useful for applications such as the design of bioinspired MAVs or flexible membrane energy harvesting technology.

Computational Analysis of Straight and Maneuvering Bat Flight Aerodynamics

Peter Windes

General Audience Abstract

Bats have many impressive flight characteristics such as the ability to rapidly change direction, carry substantial loads, and maintain good flight efficiency. A better understanding of the physics of how bats fly can help scientists and engineers build more maneuverable, quieter, and more efficient bioinspired micro air vehicles (known colloquially as “drones”). A bioinspired engineering approach leverages the incredible capabilities of animals observed in nature, but requires detailed knowledge of the animal’s biomechanics. Computational fluid dynamics (CFD), a powerful tool used extensively across aerospace research, has led to substantial progress in the understanding of animal flight broadly. However, due to technical challenges, computer simulation has seen limited use in bat flight research. For this research, I develop, validate, and apply computer modeling techniques to the investigation of bat flight aerodynamics. Three particular modes of flight were analyzed—a straight and level flight, a sweeping turn, and a sharp 180-degree turn. During straight flight, typical flight velocities observed in the flight tunnel were 2-3 m/s. Lift generation, the force keeping the bat aloft, occurred almost exclusively during the downstroke, and peaks mid-downstroke. As the wing flap transitions from downstroke to upstroke, the wings rotate such that the wing is vertical as it moves upward. This wing rotation is critical for maximizing lift force during flight. During the sweeping turn, asymmetries in the wing kinematics and consequently the aerodynamics were observed. Early in the turn, the bat’s bank angle was low and elevated levels of thrust were generated by the outer wing during both the upstroke and downstroke causing rotation of the bat. As the bat moved towards the middle of the turn, the bank angle increased to 20-25 degrees. Banking served to redirect the net force vector laterally causing a turning force. Over the course of five wingbeat cycles, the change in direction of flight was about 45 degrees. Analysis of the U-turn flight showed many of the same characteristics as were observed during the sweeping turn, as well as a few key differences. At the apex of the U-turn, the bat combined a high roll angle with a low flight velocity magnitude to very rapidly redirect its flight direction. It is intended that this project motivates and facilitates further computer simulations studying bat flight aerodynamics. Additionally, the data and findings will be useful for applications such as the design of bioinspired vehicles or flexible membrane energy harvesting technology.

Acknowledgements

I would like to express my sincere gratitude for my advisor Dr. Danesh Tafti for all his insight and support while working on this project. Over the past several years I have learned a tremendous amount from him, and thoroughly enjoyed all the interesting conversations and discussions about bat flight and CFD. I would also like to thank my committee members—Dr. Andrew J. Kurdila, Dr. Rolf Müller, Dr. Mark R. Paul, and Dr. John J. Socha—for their help and insight along the way.

The support and collaboration from all the past and present members of the HPCFD lab is greatly appreciated. The feedback on my work during weekly lab meetings was invaluable. I would also like to thank my project collaborators Xiaozhou Fan, Dr. Susheel Sekhar, Aevelina Rahman, Dr. Matt Bender, and Yang Xu.

I would like to thank Dr. Nagendra Krishnamurthy and Dr. Long He for their help and insight on the immersed boundary method; Dr. Matt Bender and Xang Yu for pioneering the experimental setup and helping with computer vision insight throughout the project; Dr. Susheel Sekhar and Xiazhou Fan for all the valuable brainstorming and collaboration; Dr. Keyur Joshi for his help learning Fortran and MPI in the early days of the project; Dr. Andrew J. Kurdila for helpful discussions about scattered data approximation; and all my undergraduate collaborators Josh Lesser, Yuxian Ye, Mengfan Wang, Junyang Xu, Han Xu, and Xuchen Gu.

I would also like to thank the Department of Mechanical Engineering at Virginia Tech for giving me the opportunity to study at Virginia Tech over the past several years. I would like to acknowledge Advanced Research Computing at Virginia Tech for providing the computational resources and technical support which made this work possible.

I would lastly like to sincerely thank my friends and family for supporting and encouraging me during my studies at Virginia Tech. Particularly, I would like to thank my parents, Lois and Larry Windes, for their continuous and unwavering support and belief in me.

Table of Contents

1. Introduction

Background[1]

Recently, there has been growing interest in understanding and optimizing low Reynolds number flight in the regime, Re ≈ (10^2) to $\mathcal{O}(10^5)$. For example, micro air vehicles (MAVs) have been proposed as sensing and monitoring platforms for agriculture, security, and other applications (Shyy et al., 2010). However, the aerodynamics of small flight vehicles is fundamentally different from large aircraft which operate in the high Reynolds number regime, Re ≈ (10^6) to $\mathcal{O}(10^9)$. Looking to nature, biological flapping fliers such as insects, birds, and bats can lend insight towards the design of MAVs (Lentink et al., 2010; Shyy et al., 1999).

One hallmark of flapping flight is that it remains effective at low Reynolds numbers, where the efficiency of fixed wing systems begin to decline. Flow separation over an airfoil at high angles of attack leads to the stall condition, resulting in a large drop in the lift to drag ratio (Shyy et al., 1999). In contrast, flapping flight allows for much more versatility in controlling the behavior of vortices in the flow (Chin and Lentink, 2016a; Ho et al., 2003; Shyy et al., 2010). This translates to improved flight performance over a range of Reynolds numbers.

Biological organisms have emerged as natural models for engineered flapping flight vehicles (Shyy et al., 2010). Despite progress, a comprehensive understanding of animal flight biomechanics remains incomplete (Chin and Lentink, 2016b). Early research into animal flight applied quasi-steady models borrowed from fixed-wing theory. However, it was quickly recognized that unsteady aerodynamic effects caused by wing flapping must be considered to obtain a clear understanding of animal flight (Ellington, 1984; Maxworthy, 1981).

Of the three taxa capable of sustaining active flight—insects, bats, and, birds—the former two exhibit strongest dependence on unsteady aerodynamic effects. Researchers initially showed that the leading edge vortex (LEV) enhances lift by delaying stall during insect flight (Ellington et al., 1996), and subsequently discovered several additional unsteady mechanisms (Dickinson,

[1] Section of this chapter are adapted variously from two of the author's prior manuscripts: Windes, P., Fan, X., Bender, M., Tafti, D. K., & Müller, R. (2018). A computational investigation of lift generation and power expenditure of Pratt's Roundleaf bat (*Hipposideros pratti*) in forward flight. *PLOS ONE*; and Windes, P., Tafti, D. K., & Müller, R. (2019). Determination of spatial fidelity required to accurately mimic the flight dynamics of a bat. *Bioinspiration & Biomimetics*.

1999). While a substantial amount of progress has been made towards the understanding of insect flight (Sane, 2003; Shyy et al., 2010; Wang, 2005), bat flight has received comparatively less attention (Chin and Lentink, 2016b).

Survey of Literature

The complex morphology of a bat wing makes the investigation of bat flight technically challenging. In contrast to insect wings or bird wings, bat wings have a flexible actively controlled membrane, and an articulated skeletal structure (Swatz et al., 2005). The study of bat flight over the last several decades has evolved through several phases, each limited by the technology available to researchers at the time. During early research, it was hypothesized that bats were particularly adept at rapid maneuvers and load-carrying due to their high wing surface area to weight ratio, articulated skeletal structure, and flexible wing membrane (Aldridge, 1987; Hartman, 1963). In 1987, Norberg and Rayner conducted an extensive study qualitatively correlating aspects of bat morphology to various flight capabilities—namely, speed, maneuverability, agility, efficiency, and load carrying ability (Norberg and Rayner, 1987).

Since Norberg and Rayner's study, researchers have been attempting to quantitatively link the unique physiology of bats to their impressive flight capabilities with detailed aerodynamic explanations, yet much progress remains. In 1975, Norberg used Kodak 16 mm high-speed film to record lateral, ventral, and frontal 2D projections of a Long-eared bat (*Plecotus auritus*) in straight flight. The projected location of 13 discrete points—3rd to 5th digits, wrist, elbow, ankle, and tail—were measured every 1/100 seconds during the 2.35 m/s flight. Several years later, a significant breakthrough was made by Rayner and Aldridge in 1985, when they incorporated multiple cameras to directly measure wing motion during flight using 3D reconstruction (Rayner and Aldridge, 1985). In their paper, they provided a framework for capturing wing kinematic data including filming, 3D reconstruction, data smoothing, and interpolating data voids. However, during their study only a single 3D point representing the trajectory of the body of the bat was tracked.

The advent of low cost, high quality digital cameras and more powerful computing has aided researchers in obtaining better 3D kinematic data from bat flight. A variety of techniques for measuring 2D and 3D kinematics of biological systems were outlined by Hedrick in 2008 (Hedrick, 2008), and have been applied to bat flight by Tian, Riskin, Hubel, Wolf, Muijres, von Busse, Johansson, Henningsson and others (Hubel et al., 2010a; Hubel et al., 2012; Muijres et al.,

2011; Muijres et al., 2012; Riskin et al., 2012; Tian et al., 2006; von Busse et al., 2014; Von Busse et al., 2012; Wolf et al., 2010). The temporal resolution (measurements per second) and spatial resolution (points measured per frame) of wing kinematic measurements have varied widely from just a single point tracking the center of mass, to over a hundred points measuring detailed membrane deformation.

In addition to studying wing kinematics, aerodynamic analysis must be conducted to construct a clear understanding of bat flight. Between 2005 and 2010 researchers began to employ particle image velocimetry (PIV) to measure air flow in the wake of flying bats (Hedenstrom et al., 2007; Hedenström et al., 2009; Hedenström et al., 2010; Hubel et al., 2010b; Johansson et al., 2008; Johansson et al., 2010; Muijres et al., 2008). Estimates of lift and power output were made from measurements of the circulation and kinetic energy in the wakes (Hedenstrom and Johansson, 2015; Spedding and Hedenström, 2010). This was a significant improvement over previous steady-state models, and allowed for the investigation of unsteady flow phenomena. In 2008, Muijres *et al.*, used PIV to show that the LEV was present and significant in lift prodection during bat flight (Muijres et al., 2008). Power expenditure and flight efficiency of bats have been explored by several researchers (Hedenström et al., 2009; Muijres et al., 2011; Muijres et al., 2012; von Busse et al., 2013; von Busse et al., 2014). Additionally, load-carrying ability (MacAyeal et al., 2011) and maneuvering flight (Aldridge, 1987; Henningsson et al., 2018; Iriarte-Diaz and Swartz, 2008; Rayner and Aldridge, 1985) have received some attention, but an understanding of the relevant aerodynamic mechanisms remains to be discovered.

Recent research has raised questions regarding the accuracy of wake based methods by suggesting that some of the underlying assumptions may not hold (Dabiri, 2005; Gutierrez et al., 2016). The frozen turbulence hypothesis—a prerequisite for application of the Kutta-Joukowski theorem, vortex ring model, and the actuator disk model—posits that vortices remain intact as they advect downstream into the wake, which is rarely the case in animal flight [31]. In their 2015 review on bat flight, Hedenström *et al.* noted that numerical simulation, when they become computationally feasible, have the potential to advance the state of the art and augment existing bat flight research (Hedenstrom and Johansson, 2015).

Numerical simulations are a powerful tool to analyze complex unsteady fluid flows, such as the flow of air around animal wings. In 1996, Smith *et al.* applied the unsteady panel method to the study of hawkmoth flight (Smith et al., 1996), and shortly after, Liu *et al.* used a full Navier-

Stokes solver to further investigate the same (Liu et al., 1998). Since then, the use of computational tools has greatly enhanced our understanding of insect flight aerodynamics by providing researchers exceptional spatial and temporal resolution of air pressure and velocity fields in proximity to the wing. Numerous computational studies have been conducted on the flight of cicadas (Wan et al., 2014), dragonflies (Koehler et al., 2012; Li and Dong, 2017; Vargas et al., 2008), hummingbirds (Ren et al., 2016; Song et al., 2014), and other insects (Liu, 2009; Shyy et al., 2010). One feature all these animals have in common is their relatively stiff wings in comparison to bats. Fewer degrees of freedom greatly simplifies both data collection as well as the flow simulations.

Despite being a well established method to investigate flapping flight, aerodynamic simulations were not applied to bat flight until Viswanath *et al.* simulated the left wing of a fruit bat in climbing flight (Viswanath et al., 2014). In 2015, Wang *et al*. published a computational study of bat flight, however a mismatch in species between the morphological model and the kinematic model raise questions about its accuracy (Wang et al., 2015). Additionally, the kinematic data set contained only skeletal motion data. That is, the membrane surface location was inferred from the skeleton pose. In 2018, Windes *et al.* conducted a numerical simulation of a Pratt's roundleaf bat (*Hipposideros pratti)* in straight flight using kinematic data consisting of 108 discrete marker points distributed over both wings, including approximately 40 marker points measuring the deformation of the wing membrane (Windes et al., 2018).

Overview of Following Chapters

In order to achieve the goals of this research project—investigate bat flight aerodynamics using computational simulations—we had to collect high quality kinematic data, develop and validate a computational framework, and analyze the results.

Chapter 2 describes wing kinematic data collection using a 3D motion capture system. The basic method was originally developed by Matt Bender and collaborators from 2014 to 2016. During the summer of 2017, I along with collaborators made several key changes to improve the data quality and reliability of the system. The particular setup and methods outlined in Chapter 2 relates to the data collection conducted during the summer of 2017. The majority of the Chapter is adapted from the manuscript "Quantifying the relationship between wing shape and aerodynamic performance of flying bats" (Windes, Tafti, & Mueller, 2019) which is currently under review.

Chapter 3 describes the development and validation of the computational model. Initial work on the computational model was conducted using a kinematic data set of a straight and level flight collected during the summer of 2016 by collaborators. The majority of the chapter is adapted from “A computational investigation of lift generation and power expenditure of Pratt's Roundleaf bat (*Hipposideros pratti*) in forward flight” which was published in *PLOS ONE* in 2018.

Chapters 4 and 5 provides results and analysis from the study of two flight maneuvers—a sweeping turn and a 180 degree U-turn. Additionally, results from a straight flight are included for comparison. The data collection and computational framework used are similar to that which was used to analyze the straight fluight described in chapter 3. However, the analysis framework was significantly extended and generalized to handle a rotating flight reference frame. Metrics which were not particularly relevant to straight flight such as body orientation (roll, pitch, and yaw), and aerodynamic force moment were calculated and reported for the flight maneuvers.

References

Aldridge, H. D. (1987). Turning flight of bats. *J. Exp. Biol.* **128**, 419–425.

Carr, J. C., Beatson, R. K., Evans, T. R., Mitchell, T. J., Cherrie, J. B., McCallum, B. C. and Fright, W. R. (2005). Reconstruction and representation of 3D objects with radial basis functions. *Proc. 28th Annu. Conf. Comput. Graph. Interact. Tech.* 67–76.

Cheney, J. A., Konow, N., Middleton, K. M., Breuer, K. S., Roberts, T. J., Giblin, E. L. and Swartz, S. M. (2014). Membrane muscle function in the compliant wings of bats. *Bioinspir. Biomim.* **9**, 025007.

Chin, D. D. and Lentink, D. (2016a). Flapping wing aerodynamics: from insects to vertebrates. *J. Exp. Biol.* **219**, 920–932.

Chin, D. D. and Lentink, D. (2016b). Flapping wing aerodynamics: from insects to vertebrates. *J. Exp. Biol.*

Dabiri, J. O. (2005). On the estimation of swimming and flying forces from wake measurements. *J. Exp. Biol.* **208**, 3519–3532.

Dickinson, M. H. (1999). Wing Rotation and the Aerodynamic Basis of Insect Flight. *Science (80-.).* **284**, 1954–1960.

Ellington, C. P. (1984). The Aerodynamics of Hovering Insect Flight. I. The Quasi-Steady Analysis. *Philos. Trans. R. Soc. B Biol. Sci.* **305**, 1–15.

Ellington, C. (1991). Limitations on animal flight performance. *J. Exp. Biol.* **91**, 71–91.

Ellington, C. P., van den Berg, C., Willmott, A. P. and Thomas, A. L. R. (1996). Leading-edge vortices in insect flight. *Nature* **384**, 626–630.

Germano, M., Piomelli, U., Moin, P. and Cabot, W. H. (1991). A dynamic subgrid-scale eddy viscosity model. *Phys. Fluids A Fluid Dyn.* **3**, 1760–1765.

Gutierrez, E., Quinn, D. B., Chin, D. D. and Lentink, D. (2016). Lift calculations based on accepted wake models for animal flight are inconsistent and sensitive to vortex dynamics. *Bioinspir. Biomim.* **12**, 016004.

Hartman, F. a (1963). Some Flight Mechanisms of Bats. *Ohio J. Sci.* **63**, 59–65.

Hedenstrom, A. and Johansson, L. C. (2015). Bat flight: aerodynamics, kinematics and flight morphology. *J. Exp. Biol.* **218**, 653–663.

Hedenstrom, A., Johansson, L. C., Wolf, M., von Busse, R., Winter, Y. and Spedding, G. R. (2007). Bat Flight Generates Complex Aerodynamic Tracks. *Science (80-.).* **316**, 894–897.

Hedenström, A., Johansson, L. C. and Spedding, G. R. (2009). Bird or bat: comparing airframe design and flight performance. *Bioinspir. Biomim.* **4**, 015001.

Hedenström, A., Muijres, F. T., Von Busse, R., Johansson, L. C., Winter, Y. and Spedding, G. R. (2010). High-speed stereo DPIV measurement of wakes of two bat species flying freely in a wind tunnel. In *Animal Locomotion*, pp. 361–370.

Hedrick, T. L. (2008). Software techniques for two- and three-dimensional kinematic measurements of biological and biomimetic systems. *Bioinspir. Biomim.* **3**,.

Henningsson, P., Jakobsen, L. and Hedenström, A. (2018). Aerodynamics of manoeuvring flight in brown long-eared bats (Plecotus auritus). *J. R. Soc. Interface* **15**,.

Ho, S., Nassef, H., Pornsinsirirak, N., Tai, Y. C. and Ho, C. M. (2003). Unsteady aerodynamics and flow control for flapping wing flyers. *Prog. Aerosp. Sci.* **39**, 635–681.

Hubel, T. Y., Riskin, D. K., Swartz, S. M. and Breuer, K. S. (2010a). Wake structure and wing kinematics: the flight of the lesser dog-faced fruit bat, Cynopterus brachyotis. *J. Exp. Biol.* **213**, 3427–3440.

Hubel, T. Y., Hristov, N. I., Swartz, S. M. and Breuer, K. S. (2010b). Time-resolved wake structure and kinematics of bat flight. *Anim. Locomot.* 371–381.

Hubel, T. Y., Riskin, D. K., Swartz, S. M. and Breuer, K. S. (2010c). Wake structure and wing kinematics: the flight of the lesser dog-faced fruit bat, Cynopterus brachyotis. *J. Exp. Biol.* **213**, 3427–3440.

Hubel, T. Y., Hristov, N. I., Swartz, S. M. and Breuer, K. S. (2012). Changes in kinematics and aerodynamics over a range of speeds in Tadarida brasiliensis, the Brazilian free-tailed bat. *J. R. Soc. Interface* **9**, 1120–1130.

Hubel, T. Y., Hristov, N. I., Swartz, S. M. and Breuer, K. S. (2016). Wake structure and kinematics in two insectivorous bats. *Philos. Trans. R. Soc. B Biol. Sci.* **371**, 20150385.

Iriarte-Diaz, J. and Swartz, S. M. (2008). Kinematics of slow turn maneuvering in the fruit bat Cynopterus brachyotis. *J. Exp. Biol.*

Johansson, L. C., Wolf, M., von Busse, R., Winter, Y., Spedding, G. R. and Hedenström, A. (2008). The near and far wake of Pallas' long tongued bat (*Glossophaga soricina*). *J. Exp. Biol.* **211**, 2909–18.

Johansson, L. C., Wolf, M. and Hedenström, A. (2010). A quantitative comparison of bird and bat wakes. *J. R. Soc. Interface* **7**, 61–66.

Koehler, C., Liang, Z., Gaston, Z., Wan, H. and Dong, H. (2012). 3D reconstruction and analysis of wing deformation in free-flying dragonflies. *J. Exp. Biol.* **215**, 3018–3027.

Lentink, D., Jongerius, S. R. and Bradshaw, N. L. (2010). The scalable design of flapping micro-air vehicles inspired by insect flight. In *Flying Insects and Robots*, pp. 185–205.

Li, C. and Dong, H. (2017). Wing kinematics measurement and aerodynamics of a dragonfly in turning flight. *Bioinspir. Biomim.* **12**, 026001.

Liu, H. (2009). Integrated modeling of insect flight: From morphology, kinematics to aerodynamics. *J. Comput. Phys.* **228**, 439–459.

Liu, Ellington, Kawachi and c (1998). A computational fluid dynamic study of hawkmoth hovering. *J. Exp. Biol.*

MacAyeal, L. C., Riskin, D. K., Swartz, S. M. and Breuer, K. S. (2011). Climbing flight performance and load carrying in lesser dog-faced fruit bats (*Cynopterus brachyotis*). *J. Exp. Biol.* **214**, 786–793.

Maxworthy, T. (1981). The Fluid Dynamics of Insect Flight. *Annu. Rev. Fluid Mech.*

Muijres, F. T., Johansson, L. C., Barfield, R., Wolf, M., Spedding, G. R. and Hedenstrom, A. (2008). Leading-Edge Vortex Improves Lift in Slow-Flying Bats. *Science (80-.).* **319**, 1250–1253.

Muijres, F. T., Johansson, L. C., Winter, Y., Hedenström, A., Muijres, F. T., Johansson, L. C. and Winter, Y. (2011). Comparative aerodynamic performance of flapping flight in two bat species using time-resolved wake visualization Comparative aerodynamic performance of flapping flight in two bat species using time-resolved wake visualization. *J. R. Soc. Interfac Interfac*.

Muijres, F. T., Johansson, L. C., Bowlin, M. S., Winter, Y. and Hedenström, A. (2012). Comparing aerodynamic efficiency in birds and bats suggests better flight performance in birds. *PLoS One* **7**,.

Nagendra, K., Tafti, D. K. and Viswanath, K. (2014). A new approach for conjugate heat transfer problems using immersed boundary method for curvilinear grid based solvers. *J. Comput. Phys.* **267**, 225–246.

Najjar, F. M. and Tafti, D. K. (1996). Study of discrete test filters and finite difference approximations for the dynamic subgrid-scale stress model. *Phys. Fluids* **8**, 1076–1088.

Norberg, U. M. and Rayner, J. M. V. (1987). Ecological Morphology and Flight in Bats

(Mammalia; Chiroptera): Wing Adaptations, Flight Performance, Foraging Strategy and Echolocation. *Philos. Trans. R. Soc. B Biol. Sci.* **316**, 335–427.

Pennycuick, C. (1989). *Bird Flight Perfomance*. Oxford University Press.

Rayner, J. M. V (1978). A new approach to animal flight mechanics. *J. Exp. Biol.* **80**, 17–54.

Rayner, J. M. V and Aldridge, H. D. (1985). Three-dimensional reconstruction of animal flight paths and the turning flight of microchiropteran bats. *J. Exp. Biol.* **118**, 247–265.

Rayner, J. M. V., Viscardi, P. W., WARD, S. and Speakman, J. R. (1999). Aerodynamics and energetics of intermittent flight in birds. *Am. Zool.* **39**, 4A–5A.

Ren, Y., Dong, H., Deng, X. and Tobalske, B. (2016). Turning on a dime: Asymmetric vortex formation in hummingbird maneuvering flight. *Phys. Rev. Fluids* **1**, 050511.

Riskin, D. K., Willis, D. J., Iriarte-D??az, J., Hedrick, T. L., Kostandov, M., Chen, J., Laidlaw, D. H., Breuer, K. S. and Swartz, S. M. (2008). Quantifying the complexity of bat wing kinematics. *J. Theor. Biol.* **254**, 604–615.

Riskin, D. K., Bergou, A., Breuer, K. S. and Swartz, S. M. (2012). Upstroke wing flexion and the inertial cost of bat flight. *Proc. R. Soc. B Biol. Sci.* **279**, 2945–2950.

Sane, S. P. (2003). The aerodynamics of insect flight. *J. Exp. Biol.*

Shyy, W., Berg, M. and Ljungqvist, D. (1999). Flapping and flexible wings for biological and micro air vehicles. *Prog. Aerosp. Sci.* **35**, 455–505.

Shyy, W., Aono, H., Chimakurthi, S. K., Trizila, P., Kang, C. K., Cesnik, C. E. S. and Liu, H. (2010). Recent progress in flapping wing aerodynamics and aeroelasticity. *Prog. Aerosp. Sci.* **46**, 284–327.

Smith, M. J. C., Wilkin, P. J. and Williams, M. H. (1996). The Advantages of an Unsteady Panel Method in Modelling the Aerodynamic Forces on Rigid Flapping Wings. *J. Exp. Biol.*

Song, M. H. and Godøy, R. I. (2016). How fast is your body motion? Determining a sufficient frame rate for an optical motion tracking system using passive markers. *PLoS One*.

Song, J., Luo, H. and Hedrick, T. L. (2014). Three-dimensional flow and lift characteristics of a hovering ruby-throated hummingbird. *J. R. Soc. Interface* **11**, 20140541–20140541.

Spedding, G. R. and Hedenström, A. (2010). PIV-based investigations of animal flight. In *Animal Locomotion*, pp. 187–201.

Svoboda, T., Martinec, D. and Pajdla, T. (2005). A convenient multicamera self-calibration for virtual environments. *PRESENCE teleoperators virtual Environ.* **14**, 407–422.

Swatz, S. M., Bishop, K. L. and Ismael-Aguirre, M. F. (2005). Dynamic complexity of wing form in bats: implications for flight performance. In *Functional and evolutionary ecology of bats*, pp. 110–130.

Tafti, D. K. (2001). GenIDLEST: A scalable parallel computational tool for simulating complex turbulent flows. In *ASME-PUBLICATIONS-FED*, pp. 347–356.

Tafti, D. K. (2011). Time-accurate techniques for turbulent heat transfer analysis in complex geometries. In *Computational Fluid Dynamics and Heat Transfer* (ed. Amano, R.) and Sunden, B.), pp. 217–264. Southampton, UK: WIT Press.

Thomas, S. P. and Suthers, R. A. (1972). The physiology and energetics of bat flight. *J. Exp. Biol.* **57**, 317–335.

Tian, X., Iriarte-Diaz, J., Middleton, K., Galvao, R., Israeli, E., Roemer, A., Sullivan, A., Song, A., Swartz, S. and Breuer, K. (2006). Direct measurements of the kinematics and dynamics of bat flight. *Bioinspir. Biomim.* **1**, S10–S18.

Turk, G., Dinh, H. Q., O'Brien, J. F. and Yngve, G. (2001). Implicit surfaces that interpolate. In *Proceedings - International Conference on Shape Modeling and Applications, SMI 2001*, .

Vargas, A., Mittal, R. and Dong, H. (2008). A computational study of the aerodynamic performance of a dragonfly wing section in gliding flight. *Bioinspir. Biomim.* **3**, 026004.

Viswanath, K., Nagendra, K., Cotter, J., Frauenthal, M. and Tafti, D. K. (2014). Straight-line climbing flight aerodynamics of a fruit bat. *Phys. Fluids* **26**,.

von Busse, R., Swartz, S. M. and Voigt, C. C. (2013). Flight metabolism in relation to speed in Chiroptera: testing the U-shape paradigm in the short-tailed fruit bat Carollia perspicillata. *J. Exp. Biol.*

von Busse, R., Waldman, R. M., Swartz, S. M., Voigt, C. C. and Breuer, K. S. (2014). The aerodynamic cost of flight in the short-tailed fruit bat (*Carollia perspicillata*): comparing theory with measurement. *J. R. Soc. Interface* **11**, 20140147.

Von Busse, R., Hedenstrom, A., Winter, Y. and Johansson, L. C. (2012). Kinematics and wing shape across flight speed in the bat, Leptonycteris yerbabuenae. *Biol. Open* **1**, 1226–1238.

Wan, H., Dong, H. and Gai, K. (2014). Computational investigation of cicada aerodynamics in forward flight. *J. R. Soc. Interface* **12**, 20141116–20141116.

Wang, Z. J. (2005). Dissecting insect flight. *Annu. Rev. Fluid Mech.* **37**, 183–210.

Wang, S., Zhang, X., He, G. and Liu, T. (2015). Lift enhancement by bats' dynamically changing wingspan. *J. R. Soc. Interface*.

Windes, P., Fan, X., Bender, M., Tafti, D. K. and Müller, R. (2018). A computational investigation of lift generation and power expenditure of Pratt's roundleaf bat (<i>Hipposideros pratti<\i>) in forward flight. *PLoS One* **13**, e0207613.

Withers, B. Y. P. C. and Timko, P. L. (1977). The significance of ground effect to the aerodynamic cost of flight and energetics of the black skimmer (Rhyncops Nigra). *J. Exp. Biol.* **70**, 13–26.

Wolf, M., Johansson, L. C., von Busse, R., Winter, Y. and Hedenstrom, A. (2010). Kinematics of flight and the relationship to the vortex wake of a Pallas' long tongued bat (*Glossophaga soricina*). *J. Exp. Biol.* **213**, 2142–2153.

2. Kinematic Data Collection

Reprint of, "Determination of spatial fidelity required to accurately mimic the flight dynamics of a bat."

The following chapter is a reprint of a paper published in *Bioinspiriation & Biomimetics* (accepted August 2019). The goal of the paper was to characterized the impact of small perturbations of the wing kinematics on the aerodynamics. In the larger context of the project, it was important to know how sensitive the aerodynamics are to the kinematic data. Since 3D motion capture measures the shape and position of the bat's wings as a discrete constellation of points, it is useful to quantitatively know how many points are needed in order to get accurate aerodynamic results from numerical simulations. We both wanted to verify that we had enough points to represent the wings and also determine if subsequent studies could use fewer points and still get good results. Kinematic datasets containing constellations of 10, 22, 35, 68, 120, and 238 points were compared. The paper also goes into some detail about the experimental setup for collecting the kinematic data as well as the data processing procedure.

Bioinspiration & Biomimetics

PAPER

Determination of spatial fidelity required to accurately mimic the flight dynamics of a bat

Bioinspiration & Biomimetics

PAPER

Determination of spatial fidelity required to accurately mimic the flight dynamics of a bat

Peter Windes[1], Danesh K Tafti[1,3] and Rolf Müller[1,2]

[1] Department of Mechanical Engineering, Virginia Tech, Blacksburg, VA, United States of America
[2] Shandong University Virginia Tech International Laboratory, Jinan, People's Republic of China
[3] Author to whom any correspondence should be addressed.

E-mail: dtafti@exchange.vt.edu

RECEIVED
13 May 2019

REVISED
4 August 2019

ACCEPTED FOR PUBLICATION
23 August 2019

PUBLISHED
24 September 2019

Keywords: bat flight, unsteady aerodynamics, motion capture, computational fluid dynamics, flapping flight, animal flight

Supplementary material for this article is available online

Abstract

Bats possess unique flight capabilities enabled by their wing morphology. While the articulated bone structure and flexible membrane constituting the wing are known to play a critical role in aerodynamic performance, the relationship has never been robustly quantified. Characterization of the sensitivity between precise wing contour and aerodynamic performance is important when designing a biomimetic flight vehicle based on experimentally measured wing kinematics. 3D optical motion capture, a standard method for obtaining wing kinematic measurements, discretely samples the smooth surface of a bat wing during flight. If the constellation of tracked 3D points is too sparse, a loss of critical information occurs. Here, we have explored the relationship between the density of wing surface points and several aerodynamic metrics, specifically, wing surface area variation, aerodynamic loads, and power expenditure. Loads and power were calculated using an incompressible Navier–Stokes solver. Of the metrics examined, aerodynamic power was found to be most sensitive to the spatial fidelity of the wing—the normalized root mean squared difference (NRMSD) between the 10- and 238-point cases was 35%. Load calculations varied slightly less with a peak NRMSD of 24% between the highest and lowest fidelity cases. Lastly, the wing surface area was least sensitive to the spatial fidelity of the wing kinematics, with a maximum NRMSD surface area of 8%. Close similarity in aerodynamic behavior was observed when using either a 120- and 238-point surface representation, establishing a bound to the sensitivity between wing shape and aerodynamics. The results from the 10- and 22-point configurations demonstrate that sparse representation of a wing surface can lead to a loss of information. The characterization of kinematic complexity of the wings both informs how many degrees of freedom are important to measure and also informs how many degrees of freedom are required to robotically reproduce the flapping flight.

1. Introduction

As the interest in small-scale flight has risen in recent years, biological organisms have emerged as natural models for engineered flight vehicles (Shyy *et al* 2010). Despite progress, a comprehensive understanding of animal flight biomechanics remains incomplete (Chin and Lentink 2016). Early research into animal flight applied quasi-steady models borrowed from fixed-wing theory. However, it was quickly recognized that unsteady aerodynamic effects caused by wing flapping must be considered to obtain a clear understanding of animal flight (Maxworthy 1981, Ellington 1984).

Of the three taxa capable of sustaining active flight—insects, bats, and, birds—the former two exhibit strongest dependence on unsteady aerodynamic effects. Researchers initially showed that the leading edge vortex (LEV) enhances lift by delaying stall during insect flight (Ellington *et al* 1996), and subsequently discovered several additional unsteady mechanisms (Dickinson 1999). While a substantial amount of progress has been made towards the understanding of insect flight (Sane 2003, Wang 2005, Shyy *et al* 2010), bat flight has received comparatively less attention (Chin and Lentink 2016).

The complex morphology of a bat wing makes the investigation of bat flight technically challenging.

In contrast to insect wings or bird wings, bat wings have a flexible actively controlled membrane, and an articulated skeletal structure (Swatz *et al* 2005). During early research, it was hypothesized that bats were particularly adept at rapid maneuvers and load-carrying due to their high wing surface area to weight ratio, articulated skeletal structure, and flexible wing membrane (Hartman 1963, Aldridge 1987). In 1987, Norberg and Rayner conducted an extensive study qualitatively correlating aspects of bat morphology to various flight capabilities—namely, speed, maneuverability, agility, efficiency, and load carrying ability (Norberg and Rayner 1987).

Since Norberg and Rayner's study, researchers have been attempting to quantitatively link the unique physiology of bats to their impressive flight capabilities with detailed aerodynamic explanations, yet much progress remains. In 2008, Muijres *et al*, used particle image velocimetry (PIV) to show that the LEV was present and significant in lift production during bat flight (Muijres *et al* 2008). Power expenditure and flight efficiency of bats have been explored by several researchers (Hedenström *et al* 2009, Muijres *et al* 2011, 2012, von Busse *et al* 2013, 2014). Additionally, load-carrying ability (MacAyeal *et al* 2011) and maneuvering flight (Rayner and Aldridge 1985, Aldridge 1987, Iriarte-Diaz and Swartz 2008, Henningsson *et al* 2018) have received some attention, but an understanding of the relevant aerodynamic mechanisms remains to be discovered.

A particularly underdeveloped aspect of bat flight research, is the area of aerodynamic modeling (Hedenstrom and Johansson 2015). Numerical simulations are a powerful tool to analyze complex unsteady fluid flows, such as the flow of air around animal wings. In 1996, Smith *et al* applied the unsteady panel method to the study of hawkmoth flight (Smith *et al* 1996), and shortly after, Liu *et al* used a full Navier–Stokes solver to further investigate the same (Liu *et al* 1998). Since then, the use of computational tools has greatly enhanced our understanding of insect flight aerodynamics by providing researchers exceptional spatial and temporal resolution of air pressure and velocity fields in proximity to the wing. Numerous computational studies have been conducted on the flight of cicadas (Wan *et al* 2014), dragonflies (Vargas *et al* 2008, Koehler *et al* 2012, Li and Dong 2017), hummingbirds (Song *et al* 2014, Ren *et al* 2016), and other insects (Liu 2009, Shyy *et al* 2010).

Despite being a well-established method to investigate flapping flight, aerodynamic simulations were not applied to bat flight until Viswanath *et al* simulated the left wing of a fruit bat in climbing flight (Viswanath *et al* 2014). In 2015, Wang *et al* published a computational study of bat flight; however, a mismatch in species between the morphological model and the kinematic model raise questions about its accuracy (Wang *et al* 2015). Additionally, the kinematic data set contained only skeletal motion data. That is, the membrane surface location was inferred from the skeleton pose. In 2018, Windes *et al* conducted a numerical simulation of a Pratt's roundleaf bat (*Hipposideros pratti*) in straight flight using kinematic data consisting of 108 discrete marker points distributed over both wings, including approximately 40 marker points measuring the deformation of the wing membrane (Windes *et al* 2018).

Detailed wing kinematic data, representing time-varying boundary conditions in the surrounding air flow, is a strict prerequisite to conducting physically relevant aerodynamic simulations. However, the stretching, twisting, and folding of bat wings during flight make the measurement of kinematics challenging (Bergou *et al* 2011). In 1975, Norberg used Kodak 16 mm high-speed film to record lateral, ventral, and frontal 2D projections of a Long-eared bat (*Plecotus auritus*) in straight flight. The projected location of 13 discrete points—3rd to 5th digits, wrist, elbow, ankle, and tail—were measured every 1/100 s during the 2.35 m s^{-1} flight. Several years later, a significant breakthrough was made by Rayner and Aldridge in 1985, when they incorporated multiple cameras to directly measure wing motion during flight using 3D reconstruction (Rayner and Aldridge 1985). In their paper, they provided a framework for capturing wing kinematic data including filming, 3D reconstruction, data smoothing, and interpolating data voids. However, during their study only a single 3D point representing the trajectory of the body of the bat was tracked.

The advent of low cost, high quality digital cameras and more powerful computing has aided researchers in obtaining better 3D kinematic data from bat flight. A variety of techniques for measuring 2D and 3D kinematics of biological systems were outlined by Hedrick (2008), and have been applied to bat flight by several researchers (Tian *et al* 2006, Hubel *et al* 2010, 2012, Wolf *et al* 2010, Muijres *et al* 2011, 2012, Riskin *et al* 2012, Von Busse *et al* 2012, von Busse *et al* 2014). The temporal resolution (measurements per second) and spatial resolution (points measured per frame) of wing kinematic measurements have varied widely from just a single point tracking the center of mass, to over a hundred points measuring detailed membrane deformation.

Ideally, the spatial resolution captured during the kinematic measurements should correspond to the degrees of freedom of the wing. Risken *et al*, measured 17 kinematic markers on the left wing of a lesser short-nosed fruit bat (*Cynopterus brachyotis)* flying in a wind tunnel in order to quantify the number of degrees of freedom of a bat wing (Riskin *et al* 2008). They tracked the shoulder, elbow, wrist, and three points each of the 3rd to 5th digits. Using POD analysis, it was determined that increasing the marker density on the wing increased the dimensional complexity of the kinematics, but had diminishing returns. While insightful, the study had two key limitations. First, only skeleton points were used in the analysis so membrane deformation was not captured. Researchers have surmised that bats derive their agility and flight efficiency

from their compliant wing membrane. It has even been proposed that active control of membrane tension through plagiopatagiales propii muscles augments flight performance (Cheney *et al* 2014). However, if no measurements of the membrane are taken during kinematic data collection, aerodynamic phenomena relating to membrane behavior cannot be investigated. Second, Risken *et al*, did not include aerodynamic analysis. This is impactful because of the non-linear relationship between kinematics and aerodynamics. By only evaluating kinematics, certain aspects of wing motion may be deemed insignificant if they constitute a small percent of dimensional complexity. Yet small motions can have a disproportionately large effect on lift or thrust during flight by affecting critical vortex dynamics.

Since the number of degrees of freedom of a flexible membrane cannot be analytically calculated, an alternate method is desired for determining adequate surface resolution when representing a bat wing. During flight, a wing membrane represents a smooth surface, continuously changing position and shape over time. However, measurement of a bat's wing position by 3D motion capture is discrete. Discrete to continuous conversion (i.e. regression) can be performed during post-processing only if the underlying data set has sufficient spatial-temporal resolution. The difference between a bat's actual smooth wing surface and the discrete representation of that same wing can be considered a spatial discretization error. If the sensitivity of aerodynamic properties to the precise shape of a bat wing can be robustly established, then an acceptable level of spatial resolution can be estimated in order to mimic the flight. This analysis has application for both optimizing experimental measurements of flapping flight, as well as the design of biomimetic bat-like flying vehicles. Specifically, identifying the kinematic complexity of the wings both informs how many degrees of freedom are important to measure, and also informs how many degrees of freedom are required in order to robotically reproduce the flapping flight.

In the present study, we captured highly resolved wing surface kinematic data as a baseline to quantify the discretization error of sparser kinematic datasets. Then, controlled levels of discretization error were introduced by considering subsets of the original kinematic data. Analysis using numerical flow simulations was conducted, allowing us to evaluate the impact of the kinematic differences on aerodynamic properties—specifically, lift, thrust, lateral force, power expenditure during flight.

2. Materials and methods

In order to quantify the impact of wing kinematic measurement resolution on aerodynamic analysis, three experimental phases were conducted. First, a great roundleaf bat (*Hipposideros armiger)* was video recorded flying through a canvas flight tunnel with a large camera array. Second, stereo triangulation was used to digitally reconstruct 3D points on the wing surface over the course of the flight from the collected video. Lastly, aerodynamics simulations were conducted using several subsets of the kinematic data—each with varying surface point density. The three experimental phases are described in detail below.

2.1. Multiple view flight video capture

A rectangular canvas fight tunnel was outfitted with 28 video cameras (Hero4 Black, GoPro, San Mateo, California) in order to conduct high resolution motion capture of a flying bat. The tunnel was approximately 1.2 m × 1.2 m in cross section, and 4 m long. The cameras were arranged radially inside the tunnel in four rings of seven, with each camera pointing towards the center-line of the tunnel as can be seen in figure 1. In the present setup, the bat traverses a relatively large distance through the tunnel necessitating a large motion capture volume achieved by distributing cameras down the length of the tunnel. Notably, wind tunnel setups do not require such a large capture volume; however, are limited to studying mostly straight flights or small, subtle turns.

Several plumb bobs were placed in the tunnel to establish the exact direction of gravity for use during data analysis. The ground coordinate system was defined such that the bat was flying roughly along the x-axis—down the length of the tunnel—and the $-z$ direction was positioned in the direction of gravity as shown in figure 1.

The video recording was conducted at 120 frames per second (fps) and in 1920 × 1080 resolution. Synchronization of the camera array was critical to the camera calibration process, and stereoscopic reconstruction of the bat wing. This is because 3D reconstruction requires the observation of a single point in space by two or more cameras. If the cameras are not capturing a moving point at the same instant in time, they are effectively observing two different points. In order to ensure synchronization of the camera footage, a trigger signal was distributed from a central controller to each camera using an Ethernet network. A custom Arduino chip (model, Orangkucing Lab, Tokyo, Japan) was connected to each GoPro, and received a trigger signal that initiated simultaneous recording. Prior to the flight experiment, temporal synchronicity of the system was verified to within ±20 ms. This test was conducted by pulsing a strobe light in a dark room with all cameras recording, and using inference from the rolling shutters to calculate a bound for any temporal discrepancy between the 28 cameras.

The relatively high frame rate of 120 fps necessitated bright direct lighting on the subject. For comparison, cinematic features are typically shot at 30 fps. When recording at a high frame rate, the camera shutter is open for a shorter duration letting less light hit the sensor. Inadequate lighting would result in motion blur of the bat wings. In order to

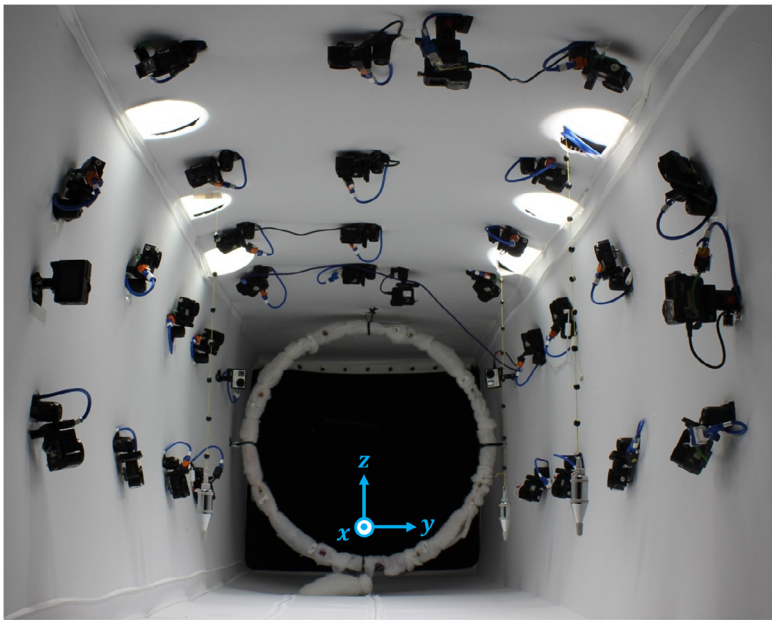

Figure 1. Flight tunnel configured for 3D motion capture of bat wings. An array of 28 cameras allowed for redundancy as well as mitigated occlusions of the wing landmarks. Six lights in the ceiling illuminated the subject during recorded to avoid motion blur. Gravity plumb lines establish an accurate gravity vector during post processing.

mitigate this effect, six lights were placed in the top corners of the flight tunnel as shown in figure 1. Since too much back-light would render unusable footage, no cameras were positioned on the bottom of the tunnel pointing upward. In order to minimize self-occlusions of the wings, the lowest two cameras on either side of the tunnel were slightly pointed upward by about 5–10°, just low enough to avoid shooting directly into the lights. When a subject flew at the approximate vertical level of the lowest cameras the underside of the wing could be observed.

The bats selected for study were great roundleaf bats (*H. armiger*) that had been previously obtained from caves in southeast China. This species has a typical weight of 55–65 g, and a typical wingspan of 45–50 cm. *H. armiger* hunts insect prey by slow hawking and perch hunting, often in dense vegetation. These hunting strategies require flight agility to succeed. During the present study, several *H. armiger* individuals were trained to fly through the tunnel and land on a cork perch on the opposite side where they were rewarded with a mealworm. In between experiments, the bats were housed in a large climate controlled aviary in which they had ample space to fly around and exercise. The humidity and temperature in the enclosure were closely monitored, and mealworms were fed to each bat daily. A basin of water was provided allowing the bats to drink on the wing. Personal protective equipment was worn by all researchers directly in contact with the bats during care or experimentation. Ethical animal care and handling procedures were followed with oversight from Virginia Tech's Institutional Animal Care and Use Committee (IACUC) under protocol number 15-067.

In order to aid software tracking of the wings during flight, small white non-toxic landmarks were placed on the bat wings. Each landmark was approximately 3 mm in diameter, and was negligible in weight.

In total, 238 markers were applied to the dorsal and ventral sides of the bat as shown in figure 2. Markers were distributed along the bones and edges of each wing at approximately 1 cm intervals, and placed on the internal sections of membrane as evenly as possible. Of the 238 points, 115 were placed on the right and left wings, while 8 were placed on the tail. Approximately 35 percent of the markers were placed on the skeleton, while the remaining 65 percent were placed on the membrane.

During video data collection, several flights were recorded. Typical flight velocities were observed to range from 1–3 m s^{-1}. A representative section of video containing 2.5 flap cycles was selected for detailed analysis (supplementary material, Movie 1 (stacks.iop.org/BB/14/066011/mmedia)). This section of flight consisted of slight deceleration, moderate gain of altitude, and a gentle left turn. The individual recorded was an adult male *H. armiger* weighing 54.5 g, with an approximate outstretched wingspan of 48 cm. More detailed quantitative analysis of the kinematics are presented in the results section.

2.2. 3D wing reconstruction

While techniques and algorithms for motion tracking humans, quadrupedal mammals, and even insect wings are widely known, accurate automated tracking of bat wings during flight remains a challenge. Establishing point correspondence between common points in different cameras at different frames is often done manually or mostly manually for bats. Tracking wing tips, wrist points, elbow points, and digits is relatively straight forward; however, accurately capturing the

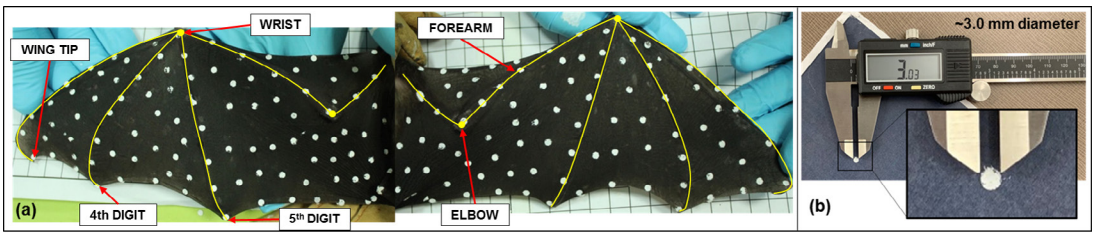

Figure 2. (a) Dorsal view of the right and left wings. Small white marker points were place on the wing surface for motion capture tracking. (b) The markers were made from medical tape, and were 3.0 mm in diameter.

non-linear, anisotropic deformations of the wing membrane is non-trivial. This is one of the primary reasons that kinematic data from past studies on bat flight has mostly neglected measuring membrane points. If too few camera perspectives are used, wing self-occlusions will prohibit 3D reconstruction of a given section of the wing membrane. For this reason, many 120 fps cameras were used in the present study in contrast to using a small number of ~1000 fps cameras as has been common practice in other research.

This trade off allowed us to achieve the measurement of many points on the surface of the bat wing, without suffering self-occlusion. While the chosen frame rate of 120 fps was deemed sufficient to resolve the wing motion temporally, it led to challenges in automatically tracking marker points. As past research has found, automatically tracking points over large intra-frame displacements becomes infeasible (Song and Godøy 2016). In order to overcome this challenge, we developed model-based software solutions in which a supervised pseudo-automatic tracker was employed. Human supervision was found to drastically improve the data quality and reliability of the tracker, yet the pace of data processing was much faster than using manual methods.

Model-based tracking methods, which are often used for insect motion capture, incorporate *a priori* knowledge of the physical structure of the subject to constrain the possible locations to which a feature will move in the following frame. These techniques can only be loosely applied to a bat, because of the unpredictable wing deformations which occur during flight. In the present study, a 2D manifold was fit to known data points using the summation of radial basis functions (Turk *et al* 2001, Carr *et al* 2005). Using this approach, points which were easier to track, such as the wing tips, elbows, and wrists, were used to inform the location of subsequent membrane points.

3D reconstruction of data during motion tracking require calibration of the camera array. Camera calibration is defined as the determination of the location, orientation, and lens distortion of each camera in the array. 'Extrinsic' calibration parameters define the location and orientation of a camera. 'Intrinsic' calibration parameters define the lens distortion of a camera. Given the intrinsic and extrinsic calibration parameters from two cameras, a scene point common to images from both cameras may be triangulated. That is, a vector location can be solved for relative to the camera locations.

Many calibration techniques use pairwise calibration. That is, two cameras are calibrated relative to each other. A common method for pairwise calibration is to use a checkerboard of known size. For a small number of cameras, this technique has several advantages such as being able to explicitly solve for the calibration parameters.

However, multi-camera calibration is more suitable for a large camera array. The advantage of multi-camera calibration is that any camera pair derived from the entire array is calibrated together. For an array of 32 cameras, 496 pairwise calibrations would need to be done to achieve the same results.

The Svoboda Multi-Camera Self-Calibration method was used to generate the calibration parameters (Svoboda *et al* 2005). For this calibration method, a 'laser candle' is made from a standard laser pointer modified by putting a translucent object in the path of the laser in order to create a small point source of light. Next several minutes of video are recorded while the laser candle is swept through the entire capture volume of the flight tunnel with all the other lights turned off. During the video recording, all cameras must be synchronized and recording. Each frame of video consists of a dark scene with a singular laser point representing a common 3D point for all cameras. The resulting videos are post-processed and the 2D pixel coordinates of the light dot are extracted for each video frame of each camera. Then an estimated camera matrix for each camera is iteratively refined until a satisfactory calibration is obtained. A successful calibration returns the camera matrix containing the combined intrinsic and extrinsic calibration parameters for each camera as well as mean and standard deviation calibration error in pixel units. Several complications may lead to divergence of the calibration solver. In the event that no adjustment of calibration parameters leads to a successful calibration, one or more cameras may be excluded from the calibration process. Often an acceptable subset of the array may be then successfully calibrated, for example 25 out of 28 cameras could still lead to quality 3D reconstructions.

2.3. Estimation of 3D reconstruction uncertainty

The multi-camera calibration process provides 2D reprojection error estimates for each camera (Svoboda

et al 2005). However, the propagation of error from 2D pixel space to the 3D reconstructed scene is complicated and based on the relative position of the cameras and the target (Hedrick 2008). That is, the relationship changes based on the location of the bat and which cameras are being used to measure it at that instant. As an alternative, the reliability of the kinematic measurements was quantified for the present study using two approaches. First, global mean 3D uncertainty was estimated, and then forearm measurements were used to further establish measurement accuracy.

Any point on the bat at any instant in time can be measured by two cameras. This coordinate is considered a single discrete 3D observation of that physical point. Using three or more cameras, multiple pairwise reconstructions can be done to get many observations of the same 3D point. A normal distribution was fit to the 3D point cloud in the direction of greatest variance (determined by principle component analysis), and a 95 percent confidence interval was calculated. This was repeated for each point at each frame. The mean confidence interval was ± 2.56 mm, signifying that the average 3D reconstructed point had a 95 percent chance of being less than 2.56 mm from the measured 3D mean. Furthermore, 50 percent of points had an interval of less than 1.96 mm, and 90 percent of the points had an interval of less than ± 4.79 mm.

Additionally, the length of the right and left forearm was used to further validate the reconstruction process. Using the 3D reconstructed data from 34 frames, the right and left forearms were measured to be 88.686 ± 0.428 mm and 88.666 ± 0.429 mm, respectively. These lengths were used as a baseline to compute the accuracy of measurement at an arbitrary frame. From the error distribution, there was found to be a 95 percent chance that the length of the right forearm would be correctly predicted within ± 2.406 mm, and the left within ± 2.412 mm. Thus, both methods of uncertainty estimation bound the 3D point measurement error to be on the order of the diameter of the white wing markers, 3 mm.

2.4. Numerical methods for evaluating aerodynamics

The full kinematic data set containing 238 discrete 3D points was partitioned into six subsets of increasing surface resolution as shown in figure 3. The partition was carefully conducted in order to maintain the following properties.

- Approximately even spacing of points along bones and wing edges, regardless of the overall point density.
- Similar ratio of points allocated to the bones, edges, wing membrane, and tail across all six configurations.
- Within each configuration, approximately even spacing of membrane points in different regions of the wings was maintained.

A refinement factor, RF, is defined based on how many times the edge length of a minimal surface representation is halved in order to achieve a given mesh.

$$RF = \log_2\left(\sqrt{N_{surf,pts}} - 1\right).$$

A wing surface mesh minimally represented by a rectangle with four nodes, has a corresponding $RF = 0$, as the mesh is unrefined. A surface mesh with nine nodes has each edge length halved once, on average, relative to the four node mesh—thus, $RF = 1$.

A numerical simulation was run for each of the resulting kinematic data subsets using the GenIDLEST incompressible flow solver (Tafti 2001) with the immersed boundary method (Nagendra *et al* 2014). More details of the numerical implementation as well as a grid independence validation can be found in Windes *et al* (2018).

For the present study, an 82 million fluid cell Cartesian structured grid was generated with a grid spacing in proximity to the wing of 50 cells per mean wing chord length. The standard mean wing chord, defined as the maximum planform area of the wing divided by the span, was 8.1 cm as calculated from the 238-point kinematic data. The grid spacing was varied in order to be finest in the region containing the bat wings and coarsening towards the boundaries. The simulation was conducted using a constant velocity moving reference frame which followed the location of the bat in order to minimize the volume in which the finest grid cell refinement was required. Completion of each of the six simulations required approximately 100 h of compute time on 168 processing cores (Intel Xeon E5-2680 v3, 'Haswell').

Time-varying surface integrated force and power quantities can be calculated to obtain the net aerodynamic performance of a flying bat. The simulation output provided flow velocity and pressure data in the entire simulation domain over the duration of the 2.5 flap cycles. Pressure and shear data in direct proximity to the wing was used to calculate the instantaneous local force on a discretized element of the immersed surface representing the wings. For N discrete wing surface elements, the net aerodynamic forces at each instant in time was calculated by,

$$\vec{F}_{net} = \sum_{i=1}^{N} \vec{F}_i = \sum_{i=1}^{N} (\vec{\tau}_i - p_i\vec{n}_i)A_i$$

where $\vec{F}$ is force, $\vec{\tau}$ is shear, p is pressure, $\vec{n}$ is the surface unit normal, and A is the surface area of the ith element. Similarly, the time-varying net aerodynamic power expenditure was calculated by,

$$P_{net} = \frac{dW}{dt} = \sum_{i=1}^{N} \vec{F}_i \cdot \vec{v}_i$$

where W is the work done by the wing, and $\vec{v}$ is the instantaneous velocity of the ith wing surface element. Positive values of power represent the rate of work done by the wing membrane on the fluid. Conversely,

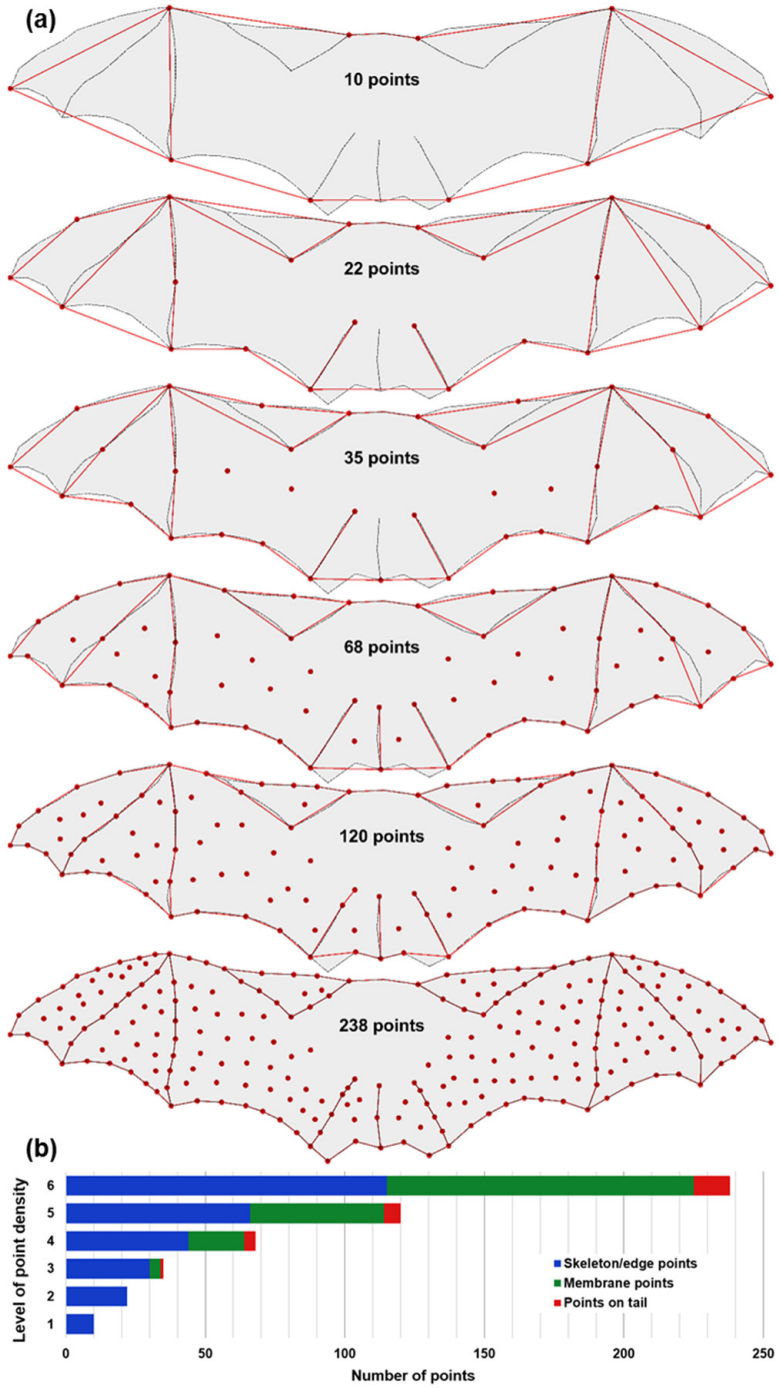

Figure 3. (a) Partition of the 238 point data set into six test cases of varying surface resolution. The 10 and 22 point cases contain skeleton and edge points only, while the remaining four cases have skeleton and membrane points. (b) The distribution between skeleton, membrane, and tail points can be seen in the bat plot.

negative power values represent the rate of work done by the fluid on the membrane.

3. Results

3.1. Flight characterization

The segment of flight selected for analysis consisted of 34 video frames or 275 ms of flight. During this window of time, the bat completed two full upstrokes and two full downstrokes. Since the bat was freely flying in the motion capture tunnel, no *a priori* trajectory could be imposed on it. This setup has advantages and disadvantages compared to wind tunnel studies—specifically, the flight trajectory is less regular and predictable, but is more natural and representative of realistic flying patterns. Nominally, the flight in the present study can be classified as climbing with some slight turning. An animation of the 3D reconstructed points can be seen in Movie 2 for the case containing the full 238-point kinematics. Delaunay triangulation was used to generate the connectivity between the marker points, thereby forming a continuous surface.

In order to more robustly quantify the mode of flight, some basic descriptive parameters were

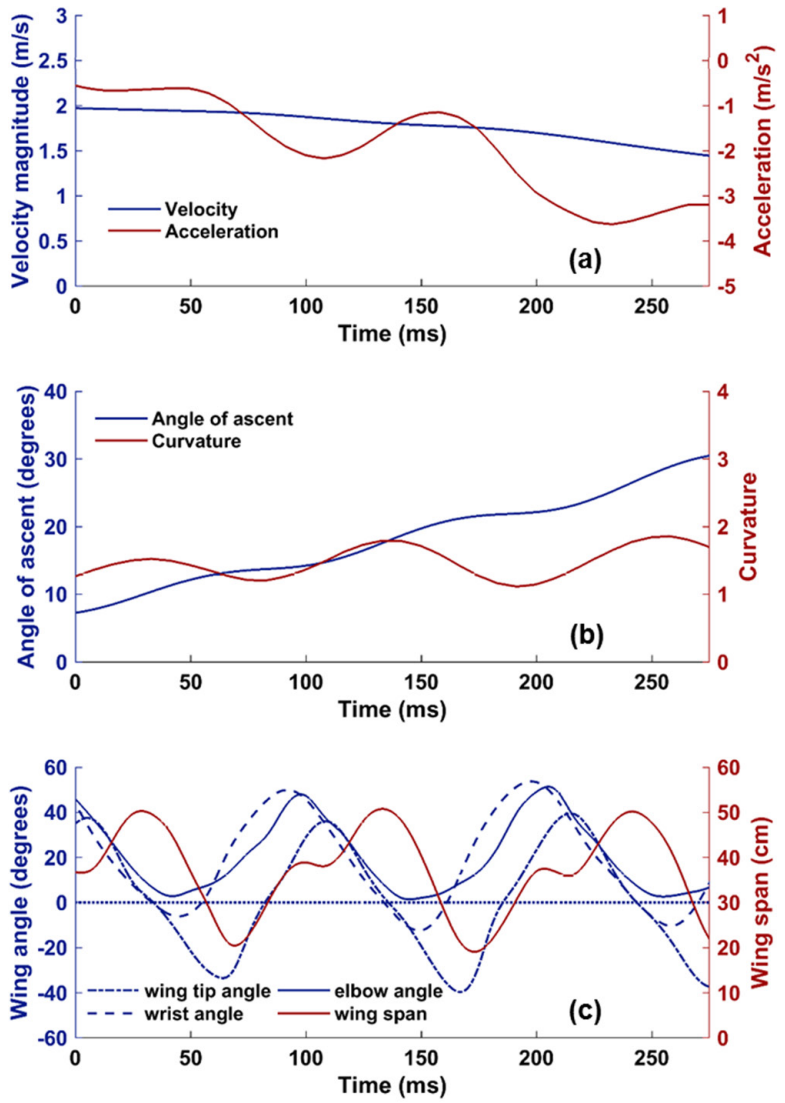

Figure 4. (a) Magnitude of flight velocity in forward direction (blue), along with body acceleration (red). (b) Angle of ascent relative to the horizontal (blue), and turning curvature (red). (c) Wing flap angle relative to the horizontal measured based the wing tip, wrist, and elbow locations (blue). In addition, the instantaneous wing span as defined as the distance between the right and left wing tips is shown (red).

calculated from the trajectory of the bat's body and wing tips—specifically, flight velocity, acceleration, angle of ascent/decent, curvature of flight path, flap angle, and wing span. These parameters represent a high-level summary of the flight, and consider the wings, body, head, and tail as an aggregate system. Notably, the values are the same for all six test cases since the data was derived from the body and wing tip trajectories which are contained in all six subsets of the marker point partition.

The flight velocity magnitude ranged from 2.0 to 1.6 m s^{-1}, with a mean of 1.73 m s^{-1} as shown in figure 4. Our prior research has shown that the similar sized *H. pratti*, a closely related species to the *H. armiger*, typically flies between 1.5 and 3.0 m s^{-1} when navigating in confined spaces such as the experimental flight tunnel (Windes *et al* 2018). As seen in the acceleration curve of figure 4, mild deceleration was present across the duration of the flight. Thus, in the subsequent aerodynamic analysis we anticipated observing a higher magnitude of drag compared to thrust.

The angle of ascent was calculated by taking the angle between the instantaneous flight direction vector, and a horizontal plane. The bat can be seen steadily ascending throughout the flight. Over the course of the 2.5 flaps, the bat climbs beginning at an angle of 8°, increasing to a final value of 28°. The curvature of turn was calculated by projecting the trajectory of the bat onto the horizontal *x*-*y* plane, and is show for the present flight in figure 4. Curvature, κ, is equal to the inverse of the radius of curvature and calculated by the following equation,

$$\kappa = \frac{x'y'' - y'x''}{(x'2 + y'2)^{\frac{3}{2}}}$$

$$\left(\text{where}, x' = \frac{dx}{dt} \text{ and } x'' = \frac{d^2x}{dt^2}\right)$$

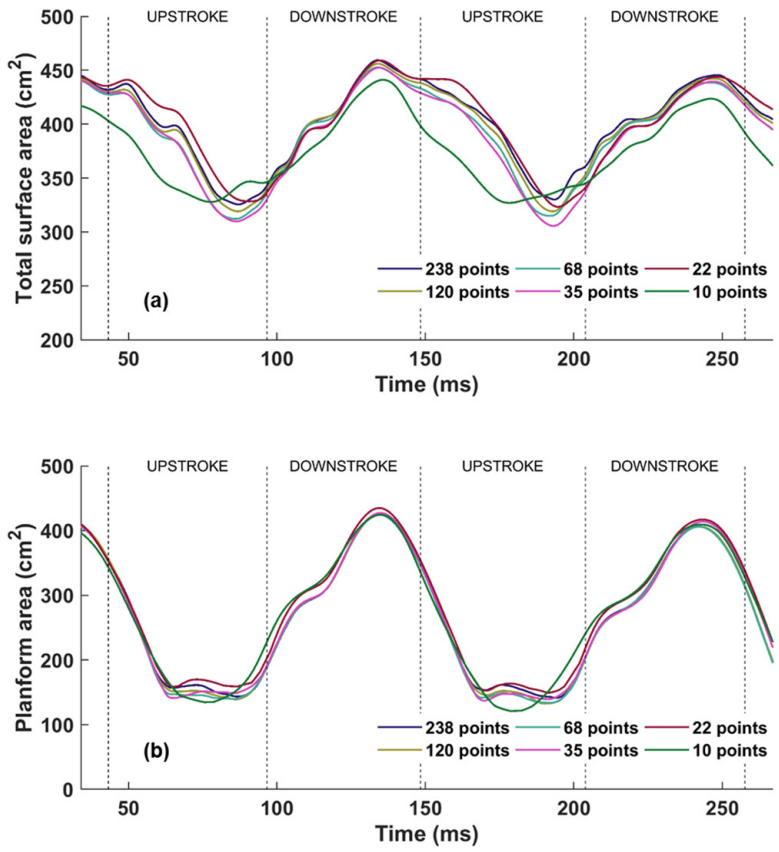

Figure 5. (a) Temporal variation of the total wing surface area for six cases. (b) Temporal variation of the planform area for the six cases.

where x and y are the coordinates of the trajectory of the body. When a bat is flying straight, the radius of curvature is undefined, but the curvature is zero, thus it is often preferable to report curvature. For the present flight trajectory, curvature fluctuated between 1 and 2 m^{-1} corresponding to a turning radius between 0.5 to 1 m.

Figure 4(c) shows the flap angle defined based on the location of three different reference points on the wing—the wing tip, the wrist, and the elbow. Since the wing is flexible, these three point can move independently of each other—that is, the wing does not rotate uniformly as a rigid body. The angle is calculated by taking the instantaneous angle between a vector pointing from the body to the reference point—i.e. the wing tip—and the horizontal. For all three methods, the flap angle was calculated each for the right and left wing and averaged. The time variation of flap angle can be used to estimate a flap frequency. The variation of the flap angle for the wrist and elbow are closely related, while the angle calculated from the wing tip is phase shifted. For the present flight, the wingbeat frequency varied from 9.3 to 10.1 Hz. These values fall within a typical range for bats of comparable size. Large bats such as *H. armiger*, as a general rule, tend to fly with lower flap frequencies than their smaller counterparts.

3.2. Wing surface area analysis

An important aspect of fight performance for a bat is the flexibility of the wing membrane. Bat wings, in contrast to insect wings and bird wings, elastically stretch and contract during the wingbeat cycle. The temporal variation of the wing surface area and planform area are shown in figure 5 for all six cases. The planform area is defined as the projected area of the wing in the x-y plane (based on the coordinate system in figure 1) as if a viewer were observing the wings from the top of the bat. During the midpoint of the down stroke, both the total surface area and the planform area are maximum. The wing camber, or curvature of the wing surface, is only reflected in the total surface area. Notably, the variation between cases is much higher for the total surface area as compared to the planform area. The wing surface area of the 10-point case differs significantly with the other five cases. Since the 10-point wing has fewer degrees of freedom, the variation between the maximum and minimum wing surface area is less than the other cases. Additionally, this case does not capture the wing camber during the downstroke as can be seen in the lower maximum surface area relative to the other five cases. The remaining five cases are more clustered, but not totally convergent. In fact there is some small but noticeable difference between the total surface area of the 120- and 238-point cases. Generally, the trend is that a higher number of surface points corresponds to a marginally higher mean surface area. The variation in planform area is nearly identical between all six cases.

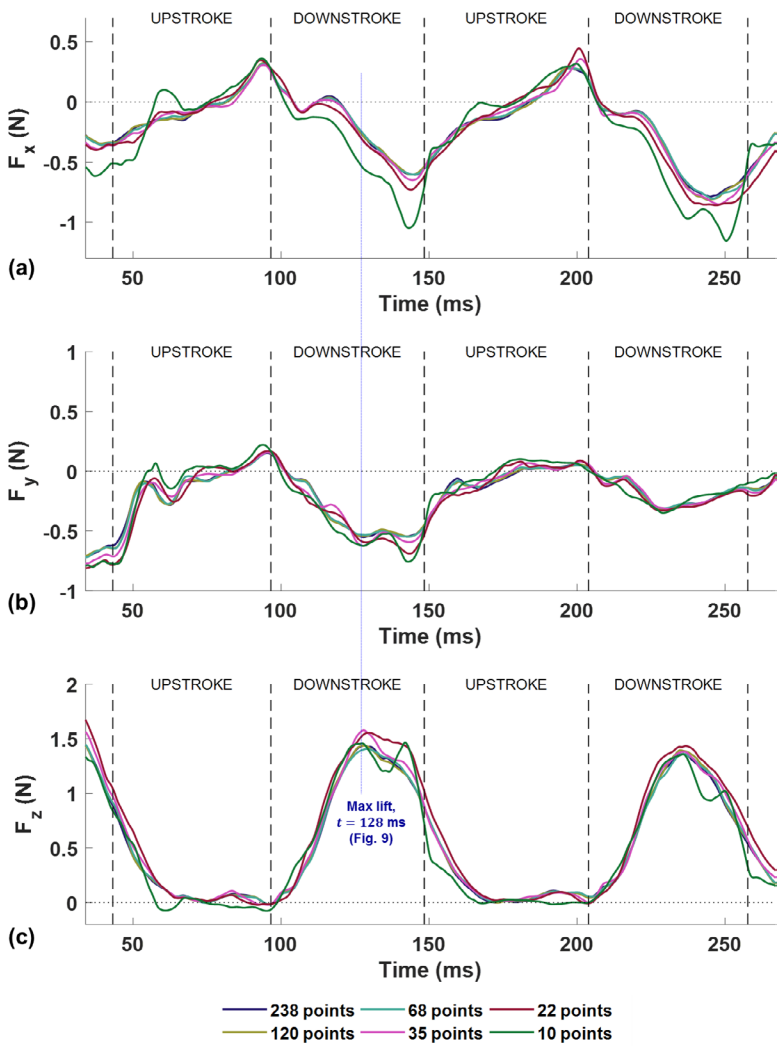

Figure 6. Temporal variation of each component of aerodynamic load: *Fx*, *Fy*, and *Fz*.

3.3. Aerodynamic force and power analysis

A critical metric for evaluating aerodynamic performance is the total integrated fluid force over the wings. The three components of total force for each of the six cases are shown in figure 6. The *x*-direction is aligned with the direction of fight, while the *z*-direction points upward—thus, gravity acts in the negative *z*-direction. The *y*-direction points towards the bat's left wing according to a right handed coordinate system.

The *x*-component of the force represents the net difference between the thrust and drag force. In this flight, the *x*-component of force is predominately negative reflecting a larger drag force compared to the thrust force. This observation is in agreement with the center of mass deceleration shown in figure 4(a). The 10-point case substantially under predicts the thrust force, resulting in a lower net *x*-direction force compared to the other five cases. The 22-point case marginally under predicts the thrust and the end of the down stroke, but to a much smaller degree than the 10-point cases. The *y*-component of force represents the lateral or turning force, with a positive value initiating a left turn, and a negative value initiating a right turn. Figure 6(b) indicates that any systematic difference in *y*-force between the six cases is quite small. The *z*-component of the aerodynamic force opposed the weight of the bat. The magnitude of the *z*-direction force is substantially larger than the other two components, since that is the component providing lift for the bat to stay aloft. The maximum difference between the six cases can be observed during the middle of the down stoke. During that time, the 10-, 22-, and 35-point cases all show moderate deviation; however, no systematic trend is immediately apparent. During the upstroke, the 10-point cases shows some deviation from the others, but the remaining five cases agree well.

For a straight flight, the mean lift force calculated should be equal to the weight of the bat. Comparison between the lift force and the weight of the animal is a good method to evaluate the accuracy of the calculated forces (Gutierrez *et al* 2016). In the present work the bat is ascending, so the comparison is not perfect. However, it does provided an approximate estimate of accuracy. For the 238-point case, the lift to weight ratio is calculated to be 1.04. Compared to other force estimation methods, this is a reasonable value—experimentally calculated forces using PIV-based methods are subject to a number of assumptions. Based on

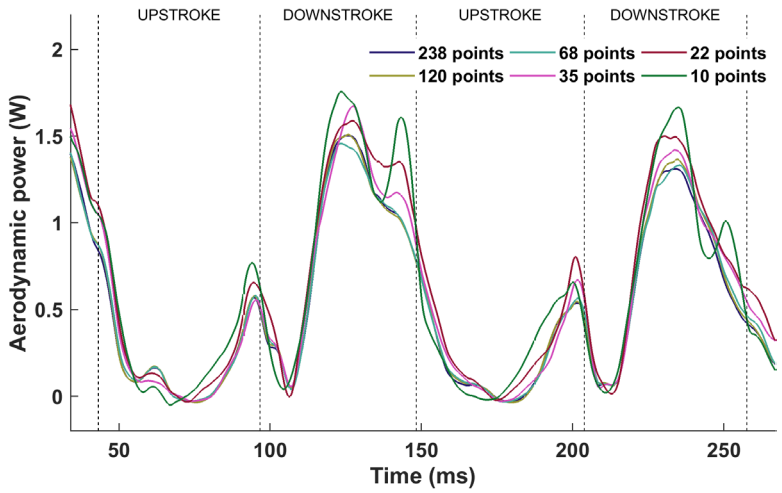

Figure 7. Temporal variation of aerodynamic power output by the wings during flight.

meta-analysis conducted by Gutierrez *et al* as well as examination of the underlying studies, we estimate that PIV-based wake methods typically capture the true aerodynamic forces ±15%–20% when compared to the weight of the animal (Gutierrez *et al* 2016, Henningsson *et al* 2018). A more detailed investigation of the accuracy of our computational method can be found in our prior work in which a grid independence assessment and mass dynamics analysis is conducted (Windes *et al* 2018). Further, we assume that any discrepancy which may exist between our calculated aerodynamic forces and the actual forces in the present work would be relatively uniform between the six different cases—thus, our conclusions would not be compromised.

The flight efficiency of the bat can be reflected in the aerodynamic power expended during flight, which is plotted in figure 7 for the six cases. The bat expends maximum power during the down stroke in order to provide lift and thrust, as reflected in the peaks in power observed in figure 7(d). Noticeable variation is observed between the 10-, 22-, 35-, and 68-point cases. However, the 120- and 238-point cases appear nearly identical. The trend between power expenditure decreasing with increasing surface point resolution may be explained by stretching of the wing not being as precisely captured in the lower resolution cases. This suggest that membrane flexibility, whether active or passively controlled, aids in flight efficiency. However, additional study is warranted to make definitive claims. When the force and power trends are compared to each other, it can be seen that there is more difference between the six cases in the power data relative to the force data. This is important as it indicates that even if forces are correctly predicted, the accuracy of aerodynamic power is not guaranteed to be correct for the given data.

Figures 5–7 visually show the temporal trends of the surface area, forces, and power; however, it is difficult to precisely identify the degree to which the trends deviate from each other. In order to robustly quantify the differences, the normalized root mean squared difference (NRMSD) between each case and the highest fidelity, 238 point case, was calculated for area, force, and power using the following equations.

$$NRMSD_{area} = \frac{\sqrt{\overline{\left(S_{N\ points} - S_{238}\right)^2}}}{\overline{S_{238}}}$$

$$NRMSD_{force} = \frac{\sqrt{\overline{\left(\left|\vec{F}\right|_{N\ points} - \left|\vec{F}\right|_{238}\right)^2}}}{\overline{\left|\vec{F}\right|_{238}}}, \quad \left|\vec{F}\right| = \sqrt{F_x^2 + F_y^2 + F_z^2}$$

$$NRMSD_{power} = \frac{\sqrt{\overline{\left(P_{N\ points} - P_{238}\right)^2}}}{\overline{P_{238}}}.$$

The 238-point cases has the highest spatial fidelity, thus it is used as the baseline for comparison. Normalizing the root mean squared difference by the mean gives a non-dimensional factor, or percentage to gauge the accuracy of each of the three metrics investigated. Figure 8 shows the results of the NRMSD calculations. In agreement with earlier observations from figure 7, aerodynamic power is the most sensitive to spatial fidelity. The calculated loads are slightly less sensitive than power, but follow a similar trend.

The temporal differences in surface area are quite marginal even when comparing the highest and lowest fidelity cases. Additionally, the trend of NRMSD surface area in not monotonic. Specifically, the 22-point case is closer to the 238-point case than the 35- and 68-point cases. This is a result of the way the trailing edge of the bat wing is discretized as show in figure 3. The planform area of the wing in the 22-point case is over predicted, causing the total surface area to also be larger. While this effectively leads to a better prediction of the total surface area, the actual precise curvature of the wing during the flight is not well captured. Thus, the force and power are substantially different relative to the 238-point case. Notably, the wing surface area is strictly a function of the wing kinematics, while both the forces and power are derived from the numerical simulations of the aerodynamics. As such, the results shown in figure 8 reflect a non-linear interaction between the kinematics and the aerodynamics.

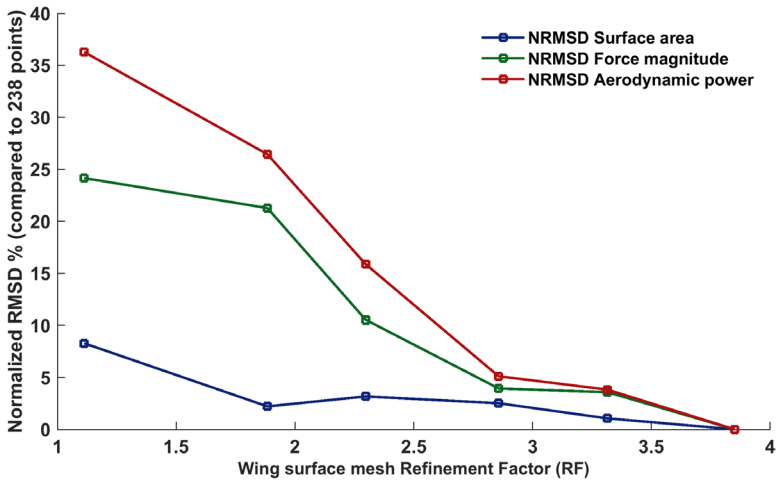

Figure 8. Comparison of the six cases by root mean squared difference, normalized as a percentage of the mean of the highest fidelity case. Percent differences are shown for total wing surface area (blue), aerodynamic force magnitude (green), and aerodynamic power (red). For N surface mesh points, $RF = \log_2\left(\sqrt{N} - 1\right)$.

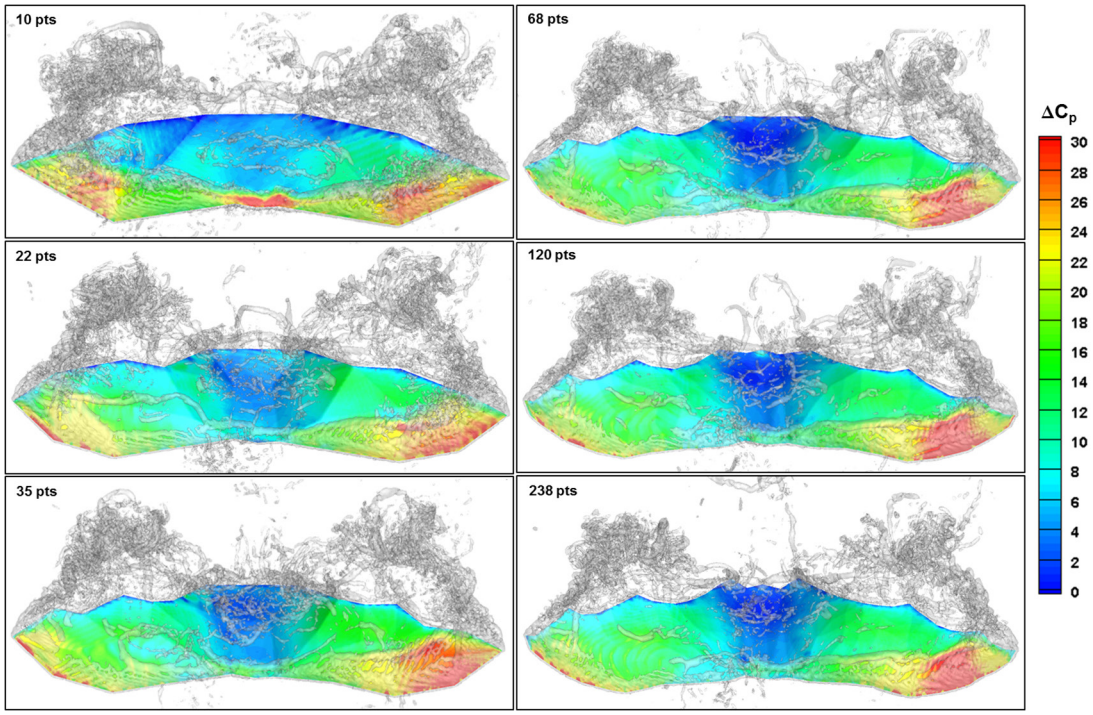

Figure 9. Isosurface of coherent vorticity along with surface contours of pressure coefficient difference above and below wing at the instant during the downstroke at which lift production was maximum ($t = 128$ ms). The LEV can be observed in all cases, yet differs in shape and strength.

The underlying aerodynamic phenomena which cause differences between the six cases can be further investigated by examination of the instantaneous flow field of air around the wings. Coherent vorticity and pressure differential at the time of maximum lift are shown in figure 9 at the time instant, $t = 128$ ms—the time at which the figure 9 is plotted is also indicated on figure 6. The pressure differential is defined as the pressure coefficient below the wing (generally high pressure) minus the pressure coefficient above the wing (generally low pressure). A positive pressure differential will be generated at non-zero angles of attack leading to lift and thrust forces.

An unsteady force enhancement mechanism widely observed in flapping flight is the LEV. The LEV, previously observed in many past studies on bat flight, can be observed as a coherent vortex located at the leading edge as seen in all cases in figure 9. Significant differences between both the LEV shape and the pressure difference exist when comparing the 10-point case to the other five. The differences in the surface distribution of pressure between the 10-point case and the other cases manifests predominately in the x-direction force as can be seen in figure 6. Large tip vortices (TiV) are prominent in all six cases, and show relative similarity between cases. This suggests relatively lesser

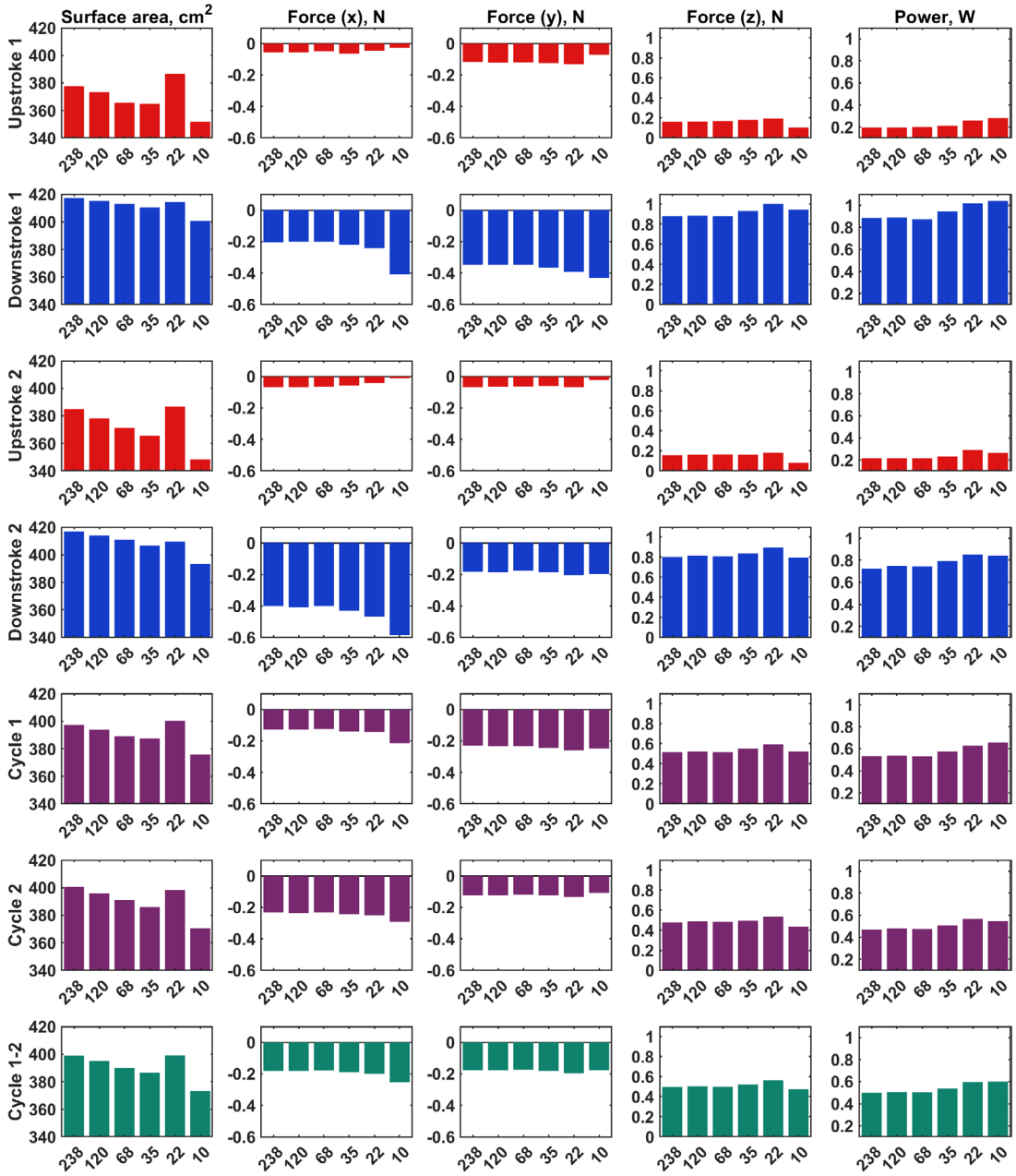

Figure 10. Comparison of mean values. Columns correspond to different parameters—surface area, three force components, and power. The rows correspond to different intervals of time averaging—rows 1–4 show half-stroke averages, rows 5–6 show cycle averages, while row 7 shows flight averaged values.

aerodynamic importance of the TiV compared to the LEV. The close similarity of pressure distribution and vorticity between the 238- and 120-point cases confirms the trends observed in figures 6 and 7. The larger LEV on the left wing of the 22- and 35-point cases is reflected in an apparent over prediction of lift at that instant. However, figure 6 indicates that the over prediction of the force is a short duration phenomenon. The differences in wing camber between the 22-, 35-, 68-, 120-, and 238-point cases does not appear to lead to a significant difference in the pressure distribution on the surface of the wing at the instant of maximum lift. A transient view of the surface pressure differential and coherent vorticity for the 238-point case can be found in the supplementary material, Movie 3.

The surface area, force, and power results for each of the six cases were time-averaged over each half stroke, full stroke, and flight as summarized in figure 10. The first column of the plot corresponds to total surface area, columns two to four forces, and column five corresponds to power. Rows one to four are half-cycle averaged results, rows five and six are cycle average results, and row seven is flight averaged. Each individual subplot shows the comparison between the six test cases. This figure allows for a high level summary of the detailed temporal data from figures 5–7.

For the highest spatial fidelity case, 238-points, the surface area is approximately 380 cm^2 during the up stroke and 420 cm^2 during the down stroke. With the exception of the 22-point case, the wing surface

area decreases with decreasing spatial resolution. This reflects expectations based on how the surface area of an arbitrary curved surface such as a hemisphere behaves when discretized. The 22-point cases is an outlier due to the way the perimeter of the planform of the wing gets discretized. To extend the analogy, suppose the hemisphere is represented with fewer points, but the diameter is increased counteracting the reduced surface area. All three force components are significantly larger during the down stoke. Between the six cases, the forces follow mostly, but not strictly monotonic trends. The lower spatial fidelity cases all reflect higher aerodynamic power requirements. This trend holds throughout the upstroke, downstoke, and cycle averages.

Comparison between the first and second cycle means (rows five and six of figure 10) provides insight on how consistent the trends between the six cases are. The trends appear to be consistent despite changes in magnitude between cases. For example, the magnitude of F_x is significantly larger in cycle 1 compared to cycle 2; however, the trend of higher F_x with increasing number of points is consistent between the two cycles. Similarly, the power expenditure is nominally larger in cycle 1 compared to cycle 2, yet the trend remains that more points corresponds to lower power expenditure.

4. Discussion

Many researchers have postulated that bats owe their unique combination of flight capabilities—agility, efficiency, and load-carrying—to their unique wing structure and membrane properties. Indeed, bat wings are considerably more articulated and flexible compared to insects or birds. In order to construct biomimetic designs based on a bat's measured wing kinematics, a sufficiently resolved representation of the wing surface is needed.

Wing kinematics represent time-varying boundary conditions directly driving the aerodynamic phenomena responsible for sustained flight. While researchers often isolate bat wing kinematics and flight aerodynamics for convenience, they are a two-way coupled system. That is, the wing kinematics fully dictate a singular flow solution in a deterministic manner. Regardless of whether the flow field around a bat wing is measure experimentally through PIV or simulated with numerical methods, the aerodynamics should be analyzed in conjunction with the kinematics. Many recent studies have recognized this and coupled kinematic and PIV analysis.

Additionally, it is desirable for the kinematics data to contain sufficient information to explain any aerodynamic phenomena under examination. For example, a kinematic data set containing a single body point will provide information about the velocity, acceleration, and trajectory of the fight, but lacks information about unsteady effects such as the flapping frequency and flapping amplitude. Using such a limited dataset constrains what insights can be drawn from the data. The addition of two points, one on each wing tip, will provide additional insight on unsteady effects. However, three kinematic points provide no information about the wing aspect ratio, area, or angle of attack. The addition of several points distributed over the skeleton adds information about the surface area and angle of attack, but lacks information about the membrane deformation and wing camber.

In the present study, we take a wide net approach to studying bat flight. Instead of making *a priori* assumptions that certain kinematic features are unimportant, we attempt to finely resolve all aspects of the kinematics and then work backwards to determine a reasonable level of simplification. For this approach to be successful, a data set containing an unprecedented level of spatial resolution was required, which is non-trivial. Manual digitization of kinematic data has been standard in bat flight research owing to the complex motion of the wings. Standard automatic motion tracking software has proven unable to handle the frequent self-occlusions and erratic movements common in bat flight. In fact, the substantial computer vision literature on human motion tracking is of little help.

Three important choices were made during the kinematic data collection stage. First, a static flight tunnel was used instead of a wind tunnel. This was to allow the bat to fly freely in any direction for the later study of flight maneuvers such as a U-turn. Second, many cameras were used to mitigate self-occlusions of the wing. In the present data set, interpolation of missing points was limited to 1 per 903 measured 3D points. That is 99.89 percent of the kinematic data points were observed by 2 or more of the 25 cameras. Third, higher spatial resolution was targeted at the expense of temporal resolution. A typical study on bat flight uses 2–4 cameras recording 1–15 points at around 1000 fps. In our view, this is an unnecessary level of temporal resolution to study a bat flapping at 8–10 Hz, but too low of a spatial resolution to capture interesting phenomena relating to wing shape, angle of attack, and membrane deformation.

The spatial fidelity of the wing kinematics that is required for any given study is contingent upon the goals of that study. Thus, no blanket recommendation for number of marker points can be provided which would be applicable to all studies. However, broad recommendations can be made from the results of the present work. The 10-point case performed relatively poorly by all metrics. Forces are routinely over and underestimated by up to 50 percent. The cycle averaged power is overestimated by 15–20 percent. The surface area is the most accurate metric captured, yet is off by 5–10 percent throughout the flap cycle. Analysis using 10 tracked points may provide some general information about the flight, but is not sufficiently detailed to uncover the novel insights needed to progress the state-of-the-art.

A relatively linear improvement was observed between the 22-, 35-, and 68-point cases. When possible, measuring up to 30 or 40 points per wing will provide material improvement to a kinematic dataset, and give researchers access to additional insights. However, in our analysis, measuring 80 or more points per wing (>160 total points) appears to yield diminishing returns. For example, the cycle averaged surface area, force, and power calculated from the 120 points case all fall within 1 percent of the 238-point case.

In summary, the close agreement between the 120 and 238 point cases provides strong evidence that we are capturing all aspects of the wing kinematics which are directly impactful to the aerodynamics. On the lower end of surface resolution, 10 points is shown to be a crude representation at best. The 22- and 35-point cases prove to be decent low order approximations of the kinematics appropriate in some contexts. Minimal differences were observed between data sets containing over 100 points.

We foresee two primary applications of the present work. The design of a MAV based on bat biomechanics, requires the measurement wing kinematics for the robot to mimic. Our results give guidance for how many degrees of freedom should be measured in order to capture the important kinematic information. Additionally, the calculation of aerodynamic forces from the measured wing kinematics, as done in the present work, can be used to tune control algorithms for a bat mimetic flying robot. Second, the present work provides insight into the sensitivity or lack thereof of aerodynamic performance to the precise contour of a compliant wing. This may be insightful for selecting material properties of a synthetic membrane, and for designing the number of degrees of freedom a bat mimetic actuation system would require.

In the future, we anticipate growing interest in using numerical simulations and biomimetic robots to study bat flight aerodynamics, especially in the areas of agility and maneuver. While these techniques provide great flexibility to researchers many pitfalls exist. Specifically, computational or robotic bat models driven by sparse kinematic measurements contain high surface discretization error, and may lead to erroneous conclusions about the mechanisms underpinning bat flight.

Acknowledgments

The authors would like to thank all our collaborators for valuable insight and discussions—Matt Bender, Yang Xu, and Dr Lynn Abbott for computer vision insight; Dr Susheel Sekhar and Xiaozhou Fan for brainstorming; Yuxian Ye, Mengfan Wang, Junyang Xu, Han Xu, and Xuchen Gu for help with data collection; Josh Lesser for help with video processing; Dr Andrew Kurdila for guidance on scattered data approximation. Additionally, the authors acknowledge Advanced Research Computing at Virginia Tech for providing computational resources critical to the success of the research (URL: http://www.arc.vt.edu).

Competing interests

The authors declare no competing or financial interests.

Funding

This research received financial support from NSF CBET Grant No. 1510797, NSF IRES Grant No. 1658620, support from VT ICTAS/BIST Center, National Natural Science Foundation of China (Grant Nos. 11374192 & 11574183), and Chinese Ministry of Education Tese Grant for international faculty exchange

ORCID iDs

Peter Windes https://orcid.org/0000-0002-6059-5128
Danesh K Tafti https://orcid.org/0000-0002-9511-3301
Rolf Müller https://orcid.org/0000-0001-8358-4053

References

Aldridge H D 1987 Turning flight of bats *J. Exp. Biol.* **128** 419–25
Bergou A J, Swartz S, Breuer K and Taubin G 2011 3D reconstruction of bat flight kinematics from sparse multiple views *Proc. of the IEEE Int. Conf. on Computer Vision* pp 1618–25
Carr J C, Beatson R K, Evans T R, Mitchell T J, Cherrie J B, McCallum B C and Fright W R 2005 Reconstruction and representation of 3D objects with radial basis functions *Proc. of the 28th Annual Conf. on Computer Graphics and Interactive Techniques* pp 67–76
Cheney J A, Konow N, Middleton K M, Breuer K S, Roberts T J, Giblin E L and Swartz S M 2014 Membrane muscle function in the compliant wings of bats *Bioinspir. Biomim.* **9** 25007
Chin D D and Lentink D 2016 Flapping wing aerodynamics: from insects to vertebrates *J. Exp. Biol.* **219** 920–32
Dickinson M H 1999 Wing rotation and the aerodynamic basis of insect flight *Science* **284** 1954–60
Ellington C P 1984 The aerodynamics of hovering insect flight. I. The quasi-steady analysis *Phil. Trans. R. Soc.* B **305** 1–15
Ellington C P, van den Berg C, Willmott A P and Thomas A L R 1996 Leading-edge vortices in insect flight *Nature* **384** 626–30
Gutierrez E, Quinn D B, Chin D D and Lentink D 2016 Lift calculations based on accepted wake models for animal flight are inconsistent and sensitive to vortex dynamics *Bioinspir. Biomim.* **12** 16004
Hartman F A 1963 Some flight mechanisms of bats *Ohio J. Sci.* **63** 59–65
Hedenstrom A and Johansson L C 2015 Bat flight: aerodynamics, kinematics and flight morphology *J. Exp. Biol.* **218** 653–63
Hedenström A, Johansson L C and Spedding G R 2009 Bird or bat: comparing airframe design and flight performance *Bioinspir. Biomim.* **4** 15001
Hedrick T L 2008 Software techniques for two- and three-dimensional kinematic measurements of biological and biomimetic systems *Bioinspir. Biomim.* **3** 034001
Henningsson P, Jakobsen L and Hedenström A 2018 Aerodynamics of manoeuvring flight in brown long-eared bats (*Plecotus auritus*) *J. R. Soc. Interface* **15** 20180441
Hubel T Y, Hristov N I, Swartz S M and Breuer K S 2012 Changes in kinematics and aerodynamics over a range of speeds in *Tadarida brasiliensis*, the Brazilian free-tailed bat *J. R. Soc. Interface* **9** 1120–30

Hubel T Y, Riskin D K, Swartz S M and Breuer K S 2010 Wake structure and wing kinematics: the flight of the lesser dog-faced fruit bat, *Cynopterus brachyotis J. Exp. Biol.* **213** 3427–40
Iriarte-Diaz J and Swartz S M 2008 Kinematics of slow turn maneuvering in the fruit bat *Cynopterus brachyotis J. Exp. Biol.* **211** 3478–89
Koehler C, Liang Z, Gaston Z, Wan H and Dong H 2012 3D reconstruction and analysis of wing deformation in free-flying dragonflies *J. Exp. Biol.* **215** 3018–27
Li C and Dong H 2017 Wing kinematics measurement and aerodynamics of a dragonfly in turning flight *Bioinspir. Biomim.* **12** 26001
Liu H 2009 Integrated modeling of insect flight: from morphology, kinematics to aerodynamics *J. Comput. Phys.* **228** 439–59
Liu H, Ellington C and Kawachi K 1998 A computational fluid dynamic study of hawkmoth hovering *J. Exp. Biol.* **201** 461–77
MacAyeal L C, Riskin D K, Swartz S M and Breuer K S 2011 Climbing flight performance and load carrying in lesser dog-faced fruit bats (*Cynopterus brachyotis*) *J. Exp. Biol.* **214** 786–93
Maxworthy T 1981 The fluid dynamics of insect flight *Annu. Rev. Fluid Mech.* **13** 329–50
Muijres F T, Johansson L C, Barfield R, Wolf M, Spedding G R and Hedenstrom A 2008 Leading-edge vortex improves lift in slow-flying bats *Science* **319** 1250–3
Muijres F T, Johansson L C, Bowlin M S, Winter Y and Hedenström A 2012 Comparing aerodynamic efficiency in birds and bats suggests better flight performance in birds *PLoS One* **7** e37335
Muijres F T, Johansson L C, Winter Y, Hedenström A, Muijres F T, Johansson L C and Winter Y 2011 Comparative aerodynamic performance of flapping flight in two bat species using time-resolved wake visualization comparative aerodynamic performance of flapping flight in two bat species using time-resolved wake visualization *J. R. Soc. Interface* **8** 1418–28
Nagendra K, Tafti D K and Viswanath K 2014 A new approach for conjugate heat transfer problems using immersed boundary method for curvilinear grid based solvers *J. Comput. Phys.* **267** 225–46
Norberg U M and Rayner J M V 1987 Ecological morphology and flight in bats (Mammalia; Chiroptera): wing adaptations, flight performance, foraging strategy and echolocation *Philos. Trans. R. Soc.* B **316** 335–427
Rayner J M V and Aldridge H D 1985 Three-dimensional reconstruction of animal flight paths and the turning flight of microchiropteran bats *J. Exp. Biol.* **118** 247–65
Ren Y, Dong H, Deng X and Tobalske B 2016 Turning on a dime: asymmetric vortex formation in hummingbird maneuvering flight *Phys. Rev. Fluids* **1** 50511
Riskin D K, Bergou A, Breuer K S and Swartz S M 2012 Upstroke wing flexion and the inertial cost of bat flight *Proc. R. Soc.* B **279** 2945–50
Riskin D K, Willis D J, Iriarte-Díaz J, Hedrick T L, Kostandov M, Chen J, Laidlaw D H, Breuer K S and Swartz S M 2008 Quantifying the complexity of bat wing kinematics *J. Theor. Biol.* **254** 604–15
Sane S P 2003 The aerodynamics of insect flight *J. Exp. Biol.* **206** 4191–208
Shyy W, Aono H, Chimakurthi S K, Trizila P, Kang C K, Cesnik C E S and Liu H 2010 Recent progress in flapping wing aerodynamics and aeroelasticity *Prog. Aerosp. Sci.* **46** 284–327
Smith M J C, Wilkin P J and Williams M H 1996 The advantages of an unsteady panel method in modelling the aerodynamic forces on rigid flapping wings *J. Exp. Biol.* **199** 1073–83
Song J, Luo H and Hedrick T L 2014 Three-dimensional flow and lift characteristics of a hovering ruby-throated hummingbird *J. R. Soc. Interface* **11** 20140541
Song M H and Godøy R I 2016 How fast is your body motion? Determining a sufficient frame rate for an optical motion tracking system using passive markers *PLoS One* **11** e0150993
Svoboda T, Martinec D and Pajdla T 2005 A convenient multicamera self-calibration for virtual environments *Presence Teleoperators Virtual Environ.* **14** 407–22
Swartz S M, Bishop K L and Ismael-Aguirre M F 2005 Dynamic complexity of wing form in bats: implications for flight performance *Functional and Evolutionary Ecology of Bats* ed Z Akbar, G McCracken, and T H Kunz, (Oxford, UK: Oxford University Press) pp 110–30
Tafti D K 2001 GenIDLEST: A scalable parallel computational tool for simulating complex turbulent flows *ASME-Publications-FED* **256** 347–56
Tian X, Iriarte-Diaz J, Middleton K, Galvao R, Israeli E, Roemer A, Sullivan A, Song A, Swartz S and Breuer K 2006 Direct measurements of the kinematics and dynamics of bat flight *Bioinspir. Biomim.* **1** S10–8
Turk G, Dinh H Q, O'Brien J F and Yngve G 2001 Implicit surfaces that interpolate *Proc.—Int. Conf. on Shape Modeling and Applications SMI 2001*
Vargas A, Mittal R and Dong H 2008 A computational study of the aerodynamic performance of a dragonfly wing section in gliding flight *Bioinspir. Biomim.* **3** 26004
Viswanath K, Nagendra K, Cotter J, Frauenthal M and Tafti D K 2014 Straight-line climbing flight aerodynamics of a fruit bat *Phys. Fluids* **26** 604
von Busse R, Hedenstrom A, Winter Y and Johansson L C 2012 Kinematics and wing shape across flight speed in the bat, *Leptonycteris yerbabuenae Biol. Open* **1** 1226–38
von Busse R, Swartz S M and Voigt C C 2013 Flight metabolism in relation to speed in Chiroptera: testing the U-shape paradigm in the short-tailed fruit bat *Carollia perspicillata J. Exp. Biol.* **216** 2073–80
von Busse R, Waldman R M, Swartz S M, Voigt C C and Breuer K S 2014 The aerodynamic cost of flight in the short-tailed fruit bat (*Carollia perspicillata*): comparing theory with measurement *J. R. Soc. Interface* **11** 20140147
Wan H, Dong H and Gai K 2014 Computational investigation of cicada aerodynamics in forward flight *J. R. Soc. Interface* **12** 20141116
Wang S, Zhang X, He G and Liu T 2015 Lift enhancement by bats' dynamically changing wingspan *J. R. Soc. Interface*
Wang Z J 2005 Dissecting insect flight *Annu. Rev. Fluid Mech.* **37** 183–210
Windes P, Fan X, Bender M, Tafti D K and Müller R 2018 A computational investigation of lift generation and power expenditure of Pratt's roundleaf bat (*Hipposideros pratti*) in forward flight *PLoS One* **13** e0207613
Wolf M, Johansson L C, von Busse R, Winter Y and Hedenstrom A 2010 Kinematics of flight and the relationship to the vortex wake of a Pallas' long tongued bat (*Glossophaga soricina*) *J. Exp. Biol.* **213** 2142–53

3. Analysis of a Pratt's Roundleaf Bat in Straight Flight

Reprint of, "A computational investigation of lift generation and power expenditure of Pratt's roundleaf bat (Hipposideros pratti) in forward flight"

The following chapter is a reprint of a paper published in *PLOS ONE* (accepted November 2018). This paper describes how wing kinematic data from 3D motion capture can be used to conduct a fluid dynamics simulation for the calculation of aerodynamic parameters such as force on the wings and power expenditure. The study of a straight flight was conducted as validation for the broader computational framework and also in order to investigate mechanisms used by bats during straight flight. As part of the validation of the methods, a detailed grid independence study was conducted. This was important information in the context of the research project since it characterized grid requirements for subsequent simulations of other flights as well. The paper demonstrates a pathway for the broader use of computational methods in the study of bat flight. In particular, we showed the ability to generate aerodynamic data with a high degree of spatial and temporal granularity—this capability to calculate detailed aerodynamic data proves to be useful in the subsequent chapters (4-5) which study maneuvering modes of flight.

PLOS ONE

RESEARCH ARTICLE

A computational investigation of lift generation and power expenditure of Pratt's roundleaf bat (*Hipposideros pratti*) in forward flight

Peter Windes[1], Xiaozhou Fan[1], Matt Bender[1], Danesh K. Tafti[1]*, Rolf Müller[1,2]

1 Department of Mechanical Engineering, Virginia Tech, Blacksburg, Virginia, United States of America,
2 Shandong University Virginia Tech International Laboratory, Jinan, China

* dtafti@exchange.vt.edu

OPEN ACCESS

Citation: Windes P, Fan X, Bender M, Tafti DK, Müller R (2018) A computational investigation of lift generation and power expenditure of Pratt's roundleaf bat (*Hipposideros pratti*) in forward flight. PLoS ONE 13(11): e0207613. https://doi.org/10.1371/journal.pone.0207613

Editor: Roi Gurka, Coastal Carolina University, UNITED STATES

Received: April 16, 2018

Accepted: November 2, 2018

Published: November 28, 2018

Data Availability Statement: All relevant data are within the manuscript and its Supporting Information files.

Funding: The financial support of the NSF CBET Grant No. 1510797, NSF IRES Grant No. 1658620, support from VT ICTAS/BIST Center, National Natural Science Foundation of China (Grant Nos. 11374192 & 11574183), Chinese Ministry of Education Tese Grant for international faculty exchange is gratefully acknowledged.

Abstract

The aerodynamic mechanisms of bat flight have been studied using a numerical approach. Kinematic data acquired using a high resolution motion capture system was employed to simulate the unsteady air flow around a bat's wings. A flapping bat wing contains many degrees of freedom, which make 3D motion tracking challenging. In order to overcome this challenge, an optical motion capture system of 21 cameras was used to reduce wing self-occlusion. Over the course of a meter-long flight, 108 discrete marker points on the bat's wings (Pratt's roundleaf bat, *Hipposideros pratti*) were tracked. The time evolution of the surface of each wing was computationally reconstructed in 3D space. The resulting kinematic model was interfaced with an unsteady incompressible flow solver using the immersed boundary method (IBM) and large eddy simulation (LES). Verification and validation of the flow simulation were conducted to establish accuracy. The aerodynamic forces calculated from the simulation compared well to the forces theoretically needed to sustain the observed flight trajectory. The transient flow field generated by the simulation allowed for the direct calculation of lift, drag, and power output of the bat during flight. The mean lift coefficient was found to be 3.21, and the flap cycle averaged aerodynamic power output was 1.05 W. Throughout the flap cycle, the planform area of the wings varied up to 46% between the largest and smallest values. During the upstroke, wing rotation was found to mitigate negative lift thereby improving overall flight efficiency. The high resolution motion capture and flow simulation framework presented here has the potential to facilitate the understanding of complex bat flight aerodynamics for both straight and maneuvering flight modes.

Introduction

Recently, there has been growing interest in understanding and optimizing low Reynolds number flight in the regime, $Re \sim \mathcal{O}(10^2)$ to $\mathcal{O}(10^5)$. For example, micro air vehicles (MAVs) have been proposed as sensing and monitoring platforms for agriculture, security, and other

Competing interests: The authors have declared that no competing interests exist.

applications [1]. However, the aerodynamics of small flight vehicles is fundamentally different from large aircraft which operate in the high Reynolds number regime, Re ~ (10^6) to (10^9). Looking to nature, biological flapping fliers such as insects, birds, and bats can lend insight towards the design of MAVs [2,3].

One hallmark of flapping flight is that it remains effective at low Reynolds numbers, where the efficiency of fixed wing systems begin to decline. Flow separation over an airfoil at high angles of attack leads to the stall condition, resulting in a large drop in the lift to drag ratio [2]. In contrast, flapping flight allows for much more versatility in controlling the behavior of vortices in the flow [1,4,5]. This translates to improved flight performance over a range of Reynolds numbers.

Bats are unique from other biological fliers due to their highly articulated wing structure, and their ability to actively contour their wing membrane during flight [6–8]. Compared to birds and insects, bats exhibit greater changes in wing surface area during flight, and their wings have more degrees of freedom [9]. These features are evidenced by their ability to weave through dense forests while flying, as well as chase and capture insects [10].

The study of bat flight over the last several decades has evolved through several phases, each limited by the technology available to researchers at the time. Early research focused on morphological measurements derived from specimens, and documenting physiological parameters related to flight performance [6,11–13]. Additionally, video or multiple exposure still images were used to study basic wing kinematics during flight [14–21]. The measured flight kinematics allowed researchers to model aerodynamic forces using a steady-state flow approximation [14].

Between 2005 and 2010, improvement in high-speed digital videography allowed researchers to employ 3D stereoscopic motion capture systems to measure bat wing kinematics in wind tunnels [22,23]. Around the same time, particle image velocimetry (PIV) was employed to measure air flow in the wake of flying bats [9,24–29]. Estimates of lift and power output were made from measurements of the circulation and kinetic energy in the wakes [8,30]. This was a significant improvement over previous steady-state models, and allowed for the investigation of unsteady flow phenomena.

However, recent research has raised questions regarding the accuracy of wake based methods by suggesting that some of the underlying assumptions may not hold [31,32]. The frozen turbulence hypothesis—a prerequisite for application of the Kutta-Joukowski theorem, vortex ring model, and the actuator disk model—posits that vortices remain intact as they advect downstream into the wake, which is rarely the case in animal flight [31]. In their 2015 review on bat flight, Hedenström *et al.* noted that numerical simulation, when they become computationally feasible, have the potential to advance the state of the art and augment existing bat flight research [8].

Numerical analysis is adding a new dimension to the study of unsteady aerodynamic flows. Recently, significant progress has been made towards the simulation of animal flight aerodynamics—for example, dragonflies [33,34], cicadas [35,36], and hummingbirds [37,38]. One feature all these animals have in common is their relatively stiff wings in comparison to bats. Fewer degrees of freedom greatly simplifies both data collection as well as the flow simulations. In contrast, progress towards the simulation of bat flight is lacking in the literature. In 2014, Viswanath *et al.* conducted a first-of-its-kind aerodynamic simulation of the left wing of a fruit bat in climbing flight using the immersed boundary method [39]. The time-varying position of 49 discrete points on the bat wing drove the wing kinematics in the model. In 2015, Wang *et al.* conducted a numerical simulation of bat flight, however the wing kinematics were only defined by 10 discrete points. That is, the wing motion was dictated by the position of the shoulders, legs, and three points per wing. Based on estimates by Riskin *et al.*, the skeleton alone within a bat wing contains over 20 degrees of freedom [23]. When membrane

deformation is included, a minimum of 30–40 discrete points are required to fully capture the complexity of bat wing kinematics.

The goal of the present study is to examine the underlying aerodynamic mechanisms, which make bats effective fliers in the low Reynolds number regime. In the process, we aim to establish and validate a framework for capturing bat flights in 3D, and investigate it using fluid simulations. In order to achieve these goals, we demonstrate two novel advances in the study of bat flight—the use of multiple video cameras for high spatial resolution stereoscopic wing tracking, and the use of numerical flow simulations to allow for detailed examination of unsteady flight aerodynamics. These are some of the first high-resolution studies of bat flight, which give an unprecedented window into the physics of bat flight by direct determination of the time-dependent forces generated at the wing surface unlike experimental studies which attempt to deduce the mean lift forces generated by measurements in the wake.

Motion capture of bat flight

There are several inherent challenges to conducting aerodynamic simulations of bat flight. Unlike insect wings which primarily flex, bat wings are comprised of a highly articulated skeleton which is spanned by an anisotropic, active wing membrane. These significant biological differences allow the bat wing to deform substantially during even the simplest of flight regimes. This has two major implications. First, the wings self-occlude during the flap stroke blocking aspects of the kinematics from observation. This can lead to voids in the final 3D kinematic data set if not properly addressed. Second, no simple parametric model can describe the surface of the bat wing, making the mathematical characterization of the wing shape non-trivial. For these two reasons, other methods which have been recently employed to motion capture wing kinematics of other biological fliers such as parrotlets [40], humming birds [33,41], dragonflies [34], and bees [42] are unsuitable for capturing bat flight.

In order to overcome the aforementioned challenges, a highly redundant camera array was constructed which greatly ameliorated the wing self-occlusion problem. Flight kinematic data was captured in a 1.2 m × 1.2 m cross section flight tunnel fitted with 21 cameras arranged in 3 rings about 40cm apart. The large camera array allowed for an expansive motion capture volume in addition to reducing the number of possible wing occlusions. As demonstrated in the present work, this system is capable of collecting wing kinematic data over an extended flight relative to other existing methods. Furthermore, the motion captured bat flights are not restricted in speed or direction as they are in wind tunnels, allowing for the study of maneuvering flights using the same setup.

Aerodynamic simulation of bat flight

Another challenge is the reconstruction of the bat wing surface from the 3D kinematic data. The interplay between passive and active control of the bat wing membrane is currently not known. Thus, kinematic data collection methods which only track sparse features on the bat wing and reconstruct the surface using *a priori* assumptions about the behavior of the membrane risk mischaracterization of the wing shape. This challenge has been addressed in the present work by increasing the spatial resolution of the wing motion capture relative to other similar studies. Using a high marker density across the bat wings allowed for the direct measurement of all aspects of the wing kinematics—both skeletal joint motion as well as membrane stretching.

The present work uses the immersed boundary method to represent the bat wing in the fluid flow simulation. As other researchers have pointed out, this is an effective strategy for simulating flapping flight as it avoids the need for complex and computationally expensive re-meshing techniques [43]. Many bats, such as the one studied in the present work, fly at a

Reynolds number of order 10^4. This is a challenging intermediate Reynolds number flow to simulate since viscous effects are not negligible, requiring the solution of the full Navier-Stokes equations. Additionally, the wake does not remain strictly laminar. A parallel numerical computation on approximately 200 to 300 CPU cores was required to resolve the flow in one to four days depending on the grid resolution.

Nomenclature

A_R	wing aspect ratio, b^2/S
b	wing span
C_L	lift coefficient
c_m	mean wing chord
f	flapping frequency
F_x, F_y, F_z	streamwise, lateral, and vertical aerodynamic force components
h_a	plunge amplitude
k	reduced frequency
M	mass of bat
Q	wing loading
Re	Reynolds number
S	Wing planform area
St	Strouhal number
U_∞	flight velocity
β	stroke plane angle
φ	stroke angle amplitude
μ	dynamic viscosity of air
ρ	air density

https://doi.org/10.1371/journal.pone.0207613.t001

Methods

Flight data collection

The motion capture system consisted of a large array of action cameras arranged inside a rectangular tunnel, as shown in Fig 1. The approximate dimensions of the tunnel were 1.2m × 1.2m × 4m. The camera model used was the GoPro Hero 3+ Black, with the resolution set to 1280×720 (720p) and the frame rate set to 120 fps. This setup allowed for the capture of up to 4 meters of bat flight. The cameras were arranged on the walls of the rectangular flight tunnel in order to observe the flying bat from various viewing directions and to minimize self-occlusion of the wings.

The cameras were synchronized using a central control unit such that all video frames were captured simultaneously (±0.1 ms) on all 21 cameras. The tunnel was illuminated using six lights mounted in the upper corners to mitigate motion blur while filming at high frame rates. The motion tracking system used in the present work is described in more detail in Bender *et al.*, 2015 [44] and Bender *et al.*, 2016 [45].

In the present study, bat wing kinematic data was obtained from an adult male Pratt"s roundleaf bat (*Hipposideros pratti*), an insectivorous bat indigenous to China and neighboring countries in southeast Asia. The bat was collected from a cave in southern China. Data acquisition was conducted at the Shandong University–Virginia Tech International Laboratory in Jinan, China, with oversight from Virginia Tech's Institutional Animal Care and Use Committee (IACUC) under protocol number 15–067.

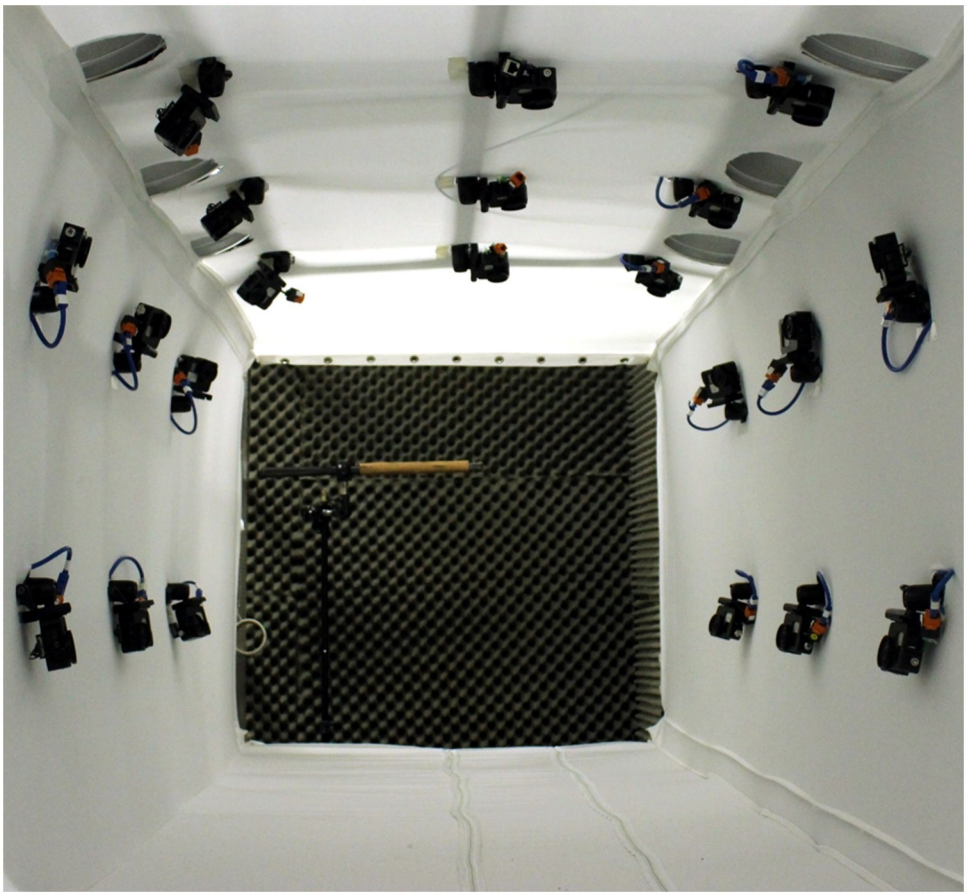

Fig 1. Motion capture system, consisting of 21 GoPro cameras inside a 1.2 x 1.2 meter cross section flight tunnel. The bat was trained to fly through the tunnel and land on the cork perch shown.

https://doi.org/10.1371/journal.pone.0207613.g001

When no experiments were being conducted, the bat was kept in a small group of conspecifics in an indoor flight room (1.3 m wide, 6 m long, and 3 m high). In order to keep the bats active during the daytime experiments, the daytime and nighttime of bats were switched by lighting the bat room at nighttime for 10 hours and darkening the bat room at daytime for 14 hours. The bats were fed a daily diet of mealworms with vitamins and mineral supplements and were provided water *ad libitum*. Measurements of the particular specimen that participated in the experiments are given in Table 1.

Multiple small white "marker points" were placed on each wing as landmarks for tracking, as shown in Fig 2. The spatial resolution of the reconstructed kinematic data was determined by how many markers were used. Using too few points to measure bat flight inadequately captures all the degrees of freedom of the bat wing. In the present work, 108 points were tracked over the course of several wing beat cycles. The final wing kinematic data set consisted of 108 discrete points at 52 instances in time.

The cameras were calibrated using the Svoboda Multi-Camera Self-Calibration toolbox for Matlab [46]. The calibration solves for the position, orientation, and radial distortion of each of the cameras in the array such that the 3D position of any point in the scene can be reconstructed from two camera views. If more than two cameras observe the same point, multiple reconstructions of that point are generated corresponding to each camera pair. The final 3D representation was taken to be the median of the point cluster. Once

Table 1. Measurements of *H. pratti* specimen.

Wing Span, b	Planform Area, S	Mean wing chord, c_m	Aspect Ratio, A_R	Mass, M	Wing Loading, Q
52.0 cm	360 cm^2	7.4 cm	7.5	55 g	12.1 N/m^2

The wing span is measured as the maximum tip-to-tip distance during straight flight. The planform area is the maximum area projected on the x-y plane during straight flight. The mean wing chord is calculated as $c_m = S/b$, the aspect ratio as $A_R = b^2/S$, and the wing loading as $Q = M_g/S$.

https://doi.org/10.1371/journal.pone.0207613.t002

Fig 2. Small white markers were placed on each bat wing to aid 3D reconstruction of the wing kinematics during flight.

https://doi.org/10.1371/journal.pone.0207613.g002

the data was digitized for the entire flight, principal component analysis (PCA) was used to filter out erroneous points in a data cleaning process which is described in Fan *et al.*, 2018 [47]. Finally, a time series of coordinates of each of the marker points on the bat wing was obtained. Fig 3 shows five snapshots from the flight video along with the corresponding 3D reconstruction.

Flight simulation methodology

The aerodynamic simulations were conducted using an in-house incompressible flow solver, GenIDLEST (Generalized Incompressible Direct and Large Eddy Simulation of Turbulence) [48,49]. The flow of air over bat wings is governed by the incompressible Navier-Stokes equations,

$$\frac{\partial \vec{u}}{\partial t} + \vec{u} \cdot \nabla \vec{u} = -\frac{1}{\rho}\nabla p + \nabla^2 \vec{u} \tag{1}$$

$$\nabla \cdot \vec{u} = 0$$

where $\vec{u}$ is the Cartesian velocity vector, p is pressure, t is time, ρ is air density, and ν is kinematic viscosity. In GenIDLEST, solution of the Navier-Stokes equations is achieved using a finite volume framework with a second-order central difference discretization scheme for the convective and viscous terms. The pressure correction method is used with preconditioned BiCGSTAB linear solvers. Message Passing Interface (MPI) is employed for parallelization,

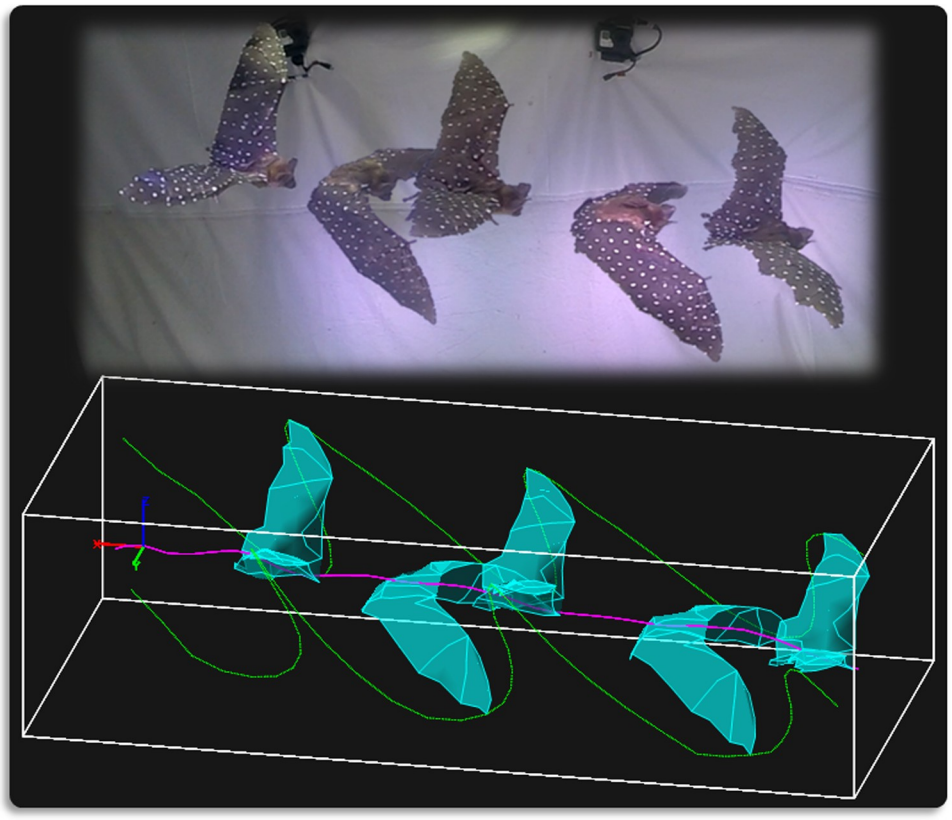

Fig 3. Five snapshots of the bat in flight along with the corresponding 3D reconstructed data. The radial distortion of the camera lens slightly changes the visual perspective of the bat in the video, however that is mathematically accounted for during the camera calibration process. In the digital reconstruction, the magenta trace is the path of the bat body, and the green traces are the path of the wing tips.

https://doi.org/10.1371/journal.pone.0207613.g003

and up to 640 CPU cores were used in the present work. Turbulence modeling was done using Large Eddy Simulation (LES). Specifically, the dynamic Smagorinsky subgrid stress model was used, where the model coefficient is calculated locally at each grid point as the simulation progresses [50,51]. The adaptive nature of the subgrid model is important due to the transitional Reynolds number of the flow (Re = 11,680).

A sharp interface immersed boundary method (IBM) was used to impose the wing surface boundary in the flow (Fig 4). The Navier-Stokes equations were solved on a structured Cartesian background grid, while the bat wing is represented by an unstructured triangular surface grid. Details of the particular implementation and validation of this IBM algorithm can be found in Nagendra *et al*., 2014 [52]. A thin surface approximation was used for the immersed surface, thus the net force on the wing was taken as the vector sum of the force on each side of a given surface element.

Numerical implementation of flapping wings

In order to represent the experimentally generated wing kinematics using the immersed boundary method (IBM), a procedure was developed to interpolate the wing surface spatially and temporally. The 3D reconstructions of the observed wing marker points are referred to in this section as "control points." First, the control point cloud was triangulated using the Delaunay method, resulting in a coarse triangular surface mesh. This surface mesh, however, was

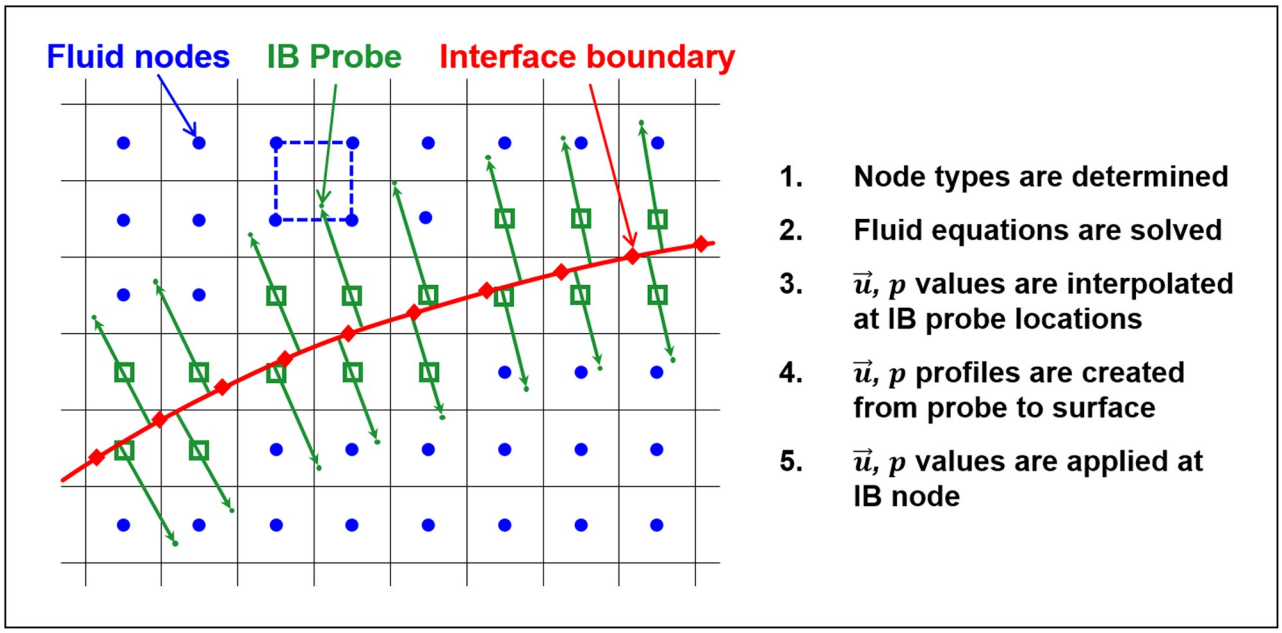

Fig 4. Immersed boundary method setup. A thin interface (red) is embedded into the background fluid grid. The no slip boundary condition is enforced on the interface by applying an appropriate velocity and pressure values to the IB nodes (green) at each time step. The property values at each IB node are determined by creating velocity profiles between the fluid nodes and the no slip surface.

https://doi.org/10.1371/journal.pone.0207613.g004

comprised of elements with edge lengths of approximately 2 cm—too coarse for IBM simulations. Thus, the planar inner region of each control triangle was sub-meshed resulting in a finer mesh with each element edge length on the order of the background fluid mesh edge length. Finally, the wing mesh consisted of 182 control triangles, and 42,839 fine mesh elements depicted in Fig 5. The coarse mesh was used to impart the proper kinematic motion to the immersed surface, while the interpolated fine mesh was used to specify the wing surface location on the background fluid grid.

The location of each fine mesh vertex within a given control triangle can be described as a linear combination of two parameters—α and β—ranging between 0 and 1.

$$\vec{r}_i = \vec{r}_1 + \alpha_i(\vec{r}_2 - \vec{r}_1) + \beta_i(\vec{r}_3 - \vec{r}_1) \tag{2}$$

where $\vec{r}_i$ is the interior point to be interpolated, and $\vec{r}_1$, $\vec{r}_2$, and $\vec{r}_3$ are the three surrounding control point vertices, as shown in Fig 6. The fine mesh is generated based on the initial position and shape of the wings. The alpha and beta values are calculated once from the initial wing state and remain constant as the wing moves, causing the interior points to maintain their relative positions throughout the flapping cycles.

Movement of the immersed surface wing mesh is achieved using piecewise spline equations which describe the continuous evolution of each control point in time. At each time step, the spline equations are evaluated at the given simulation time. Subsequently, all fine mesh points are updated based on their respective stored α and β values as well as the updated control point locations.

Once the wing surface mesh reaches its new location at the next time instance, the centroid of each surface element is located on the computational grid using a search algorithm—that is, the element's i,j,k computational coordinates are determined using its Cartesian x,y,z physical coordinates. This allows for proper data exchange between the fluid and the solid surface to ensure

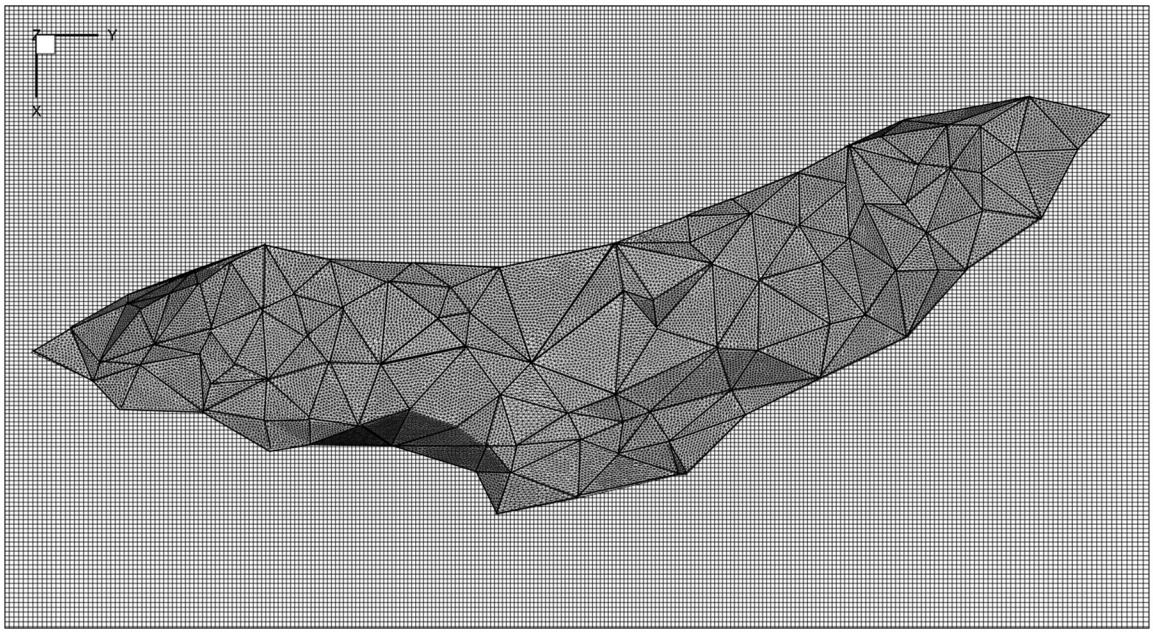

Fig 5. Wing surface mesh viewed from above during the most outstretched point of the downstroke. The coarse and fine wing surface meshes are showed overlaid with the fluid grid in the background. The vertices of the coarse triangular mesh correspond to the white marker points on the bat wings.

https://doi.org/10.1371/journal.pone.0207613.g005

that the presence of the solid surface is manifested in the fluid field. The no-slip boundary condition is applied at the surface using the immersed boundary method. The wing surface velocity is calculated for each element using a second order backward difference scheme. Similarly, the wing acceleration is calculated using the second time derivative of the surface element locations.

Aerodynamic simulation setup

The size of the fluid domain was set $32c_m \times 16c_m \times 16c_m$ along the x-, y-, and z-directions respectively. The dimensions of the cross-section of the domain approximately match the physical size of the flight tunnel. The fluid domain represents a moving reference frame that follows the bat's flight in the x-direction at 2.5 m/s. Thus, 2.5 m/s was subtracted from the absolute x-velocity of the measured wing kinematic data. The displacement of the bat body within the fluid domain during the course of the simulation represented a perturbation relative to the moving reference frame.

The inlet plane and four side-wall faces of the domain were set to a constant velocity boundary condition that was equal to the reference frame velocity of 2.5 m/s. The outlet plane (+x) of the domain was set to a zero gradient boundary condition, allowing air to flow out of the domain. The bat was initially located at the origin, and the domain extends 8 chord lengths upstream of the bat and 24 chord lengths downstream of the bat as shown in Fig 7. During the course of the simulation, no fluid disturbances were observed to propagate through either the inlet or outlet boundary planes. Thus, the $32c_m$ length of the domain in the streamwise direction was deemed sufficient to prevent unphysical interference by the boundary.

The fluid domain was discretized using a non-uniform, orthogonal, Cartesian mesh for optimal computational performance. The grid contained 88.1 million fluid cells and the refined region had an average grid spacing of, $\Delta_{fluid} = 0.020$ chord lengths. Thus, on average there were 50 fluid cells per chord length.

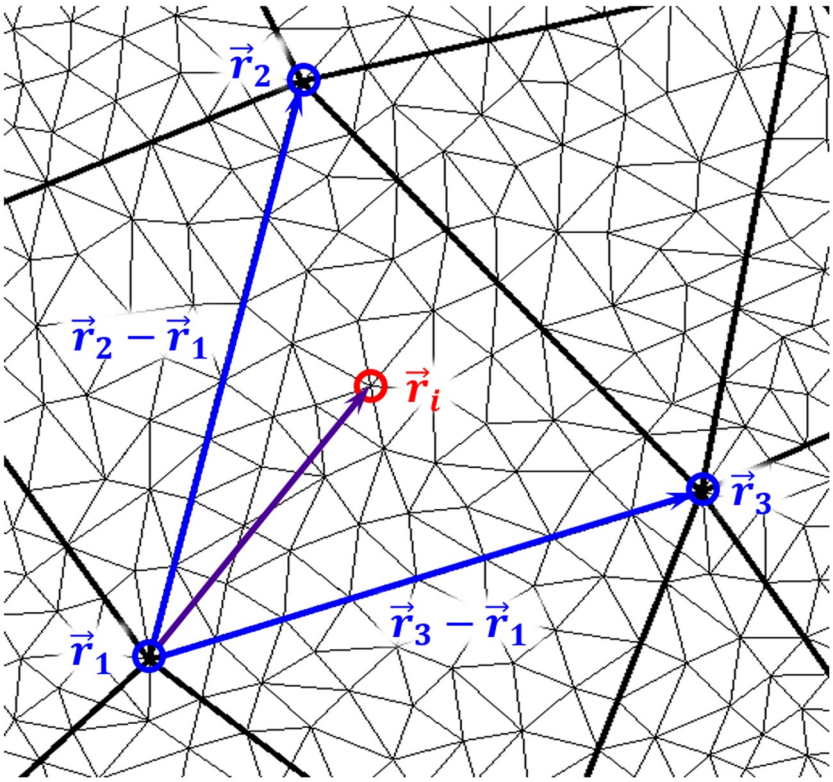

Fig 6. A given control triangle consists of three control points, and several interior points. The area inside the triangle is parameterized into a 2D surface, where every location is described by a unique pair of α and β values. As the wing flaps, the triangles deform and the locations of the interiors points are updated accordingly.

https://doi.org/10.1371/journal.pone.0207613.g006

The mesh for the immersed boundary method was an unstructured triangular surface mesh which contained 21,354 vertices, and 54,238 triangular elements. The initial average edge length was $\Delta_{surface} = 0.022$. As the wing flaps, the area changes and the relative position of the vertices is maintained using the movement algorithm described in Section 2.3.

Grid independence verification

In order to validate the computational grid used in the present work, a grid independence study was conducted. Five grid resolutions were compared to determine a sufficient level of refinement. The number of fluid cells along the wing chord was used to define the grid levels. The five grids used, ranging from 12 million to 210 million fluid cells, are outlined in Table 2.

The fluid grid was refined in the region in which the wing surface passes, and coarsened near the edges of the domain as show in Fig 8. In doing so, the entire swept volume of the wings falls within the refined region, properly resolving the unsteady flow.

Simulations of the bat flight were run on each of the five grids. The difference in cycle averaged force magnitude between each case and the finest grid is shown in Table 2. There is a noticeable difference in force of 5.9% between the 20 and 100 cells per chord grids. However, the difference drops to 1.6% when comparing the forces from the 50 and 100 cells per chord grids which indicates close agreement between the grids. Given the uncertainties in the camera calibration and stereo triangulation, the small differences between the two finest grids can be considered negligible.

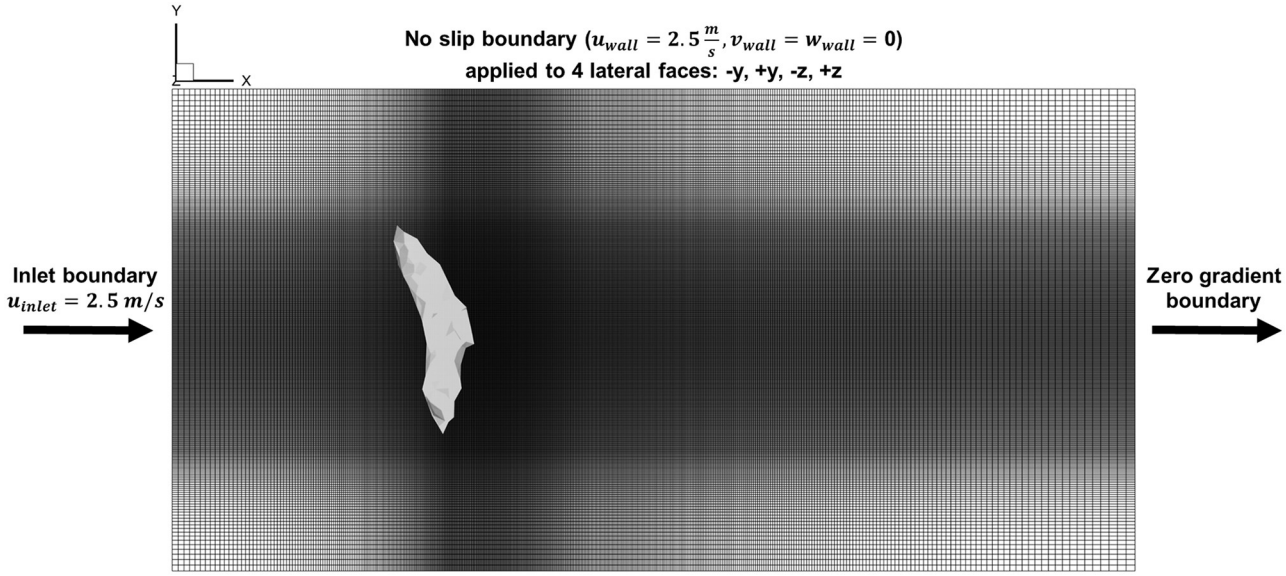

Fig 7. The full fluid grid viewed from above shows the refined region in the vicinity of the bat. The y- and z-faces of the domain reflect the physical size of the experimental flight tunnel, while the x-faces were positioned sufficiently far from the bat to avoid interference from the boundary.

https://doi.org/10.1371/journal.pone.0207613.g007

In order to further ensure grid convergence, the transient surface integrated fluid forces on the wings were compared for the 20, 50, and 100 cells per wing chord cases as shown in Fig 9. The y-dir force is close between all three grids. The x-dir force is close aside from the point of maximum thrust (-x force) between 120 ms to 160 ms. Within this time frame, the 20 cells/chord grid slightly under predicts thrust, however the 50 and 100 cells/chord grids compare closely. The z-dir force compares closely on the upstroke (180 ms to 250 ms), but differences can be observed on the downstroke around the time of peak lift production (120 ms to 180 ms). The 20 cells/chord grid consistently under predicts lift force through most of the downstroke. The 50 and 100 cells/chord grids compare well with only a few small differences, which do not materially impact the results.

Results

Kinematic analysis

In the present study, a 1 m long flight segment was chosen for analysis. The trajectory was mostly straight and level, however the bat was slightly descending at a 5˚ angle and accelerating from 2.2 m/s to 2.7 m/s. This flight spanned 50 frames of video with a total duration of 0.42 s corresponding to about 3 flap cycles. Several snapshots from the flight are shown in Fig 10.

Table 2. Several different grids ranging from 20 fluid cell lengths per wing chord length to 100 were compared to ensure grid independence. The CPU architecture used was Intel Xeon E5-2670 (Sandy Bridge).

Cells per wing chord	Δfluid grid	Total Fluid Cells	CPU-hours	% difference |F| compared to finest
20	0.0500	11.8 million	1,350	5.9%
30	0.0333	31.5 million	2,470	3.1%
40	0.0250	62.9 million	7,130	1.9%
50	0.0200	88.1 million	7,200	1.6%
100	0.0100	209.7 million	34,330	-

https://doi.org/10.1371/journal.pone.0207613.t003

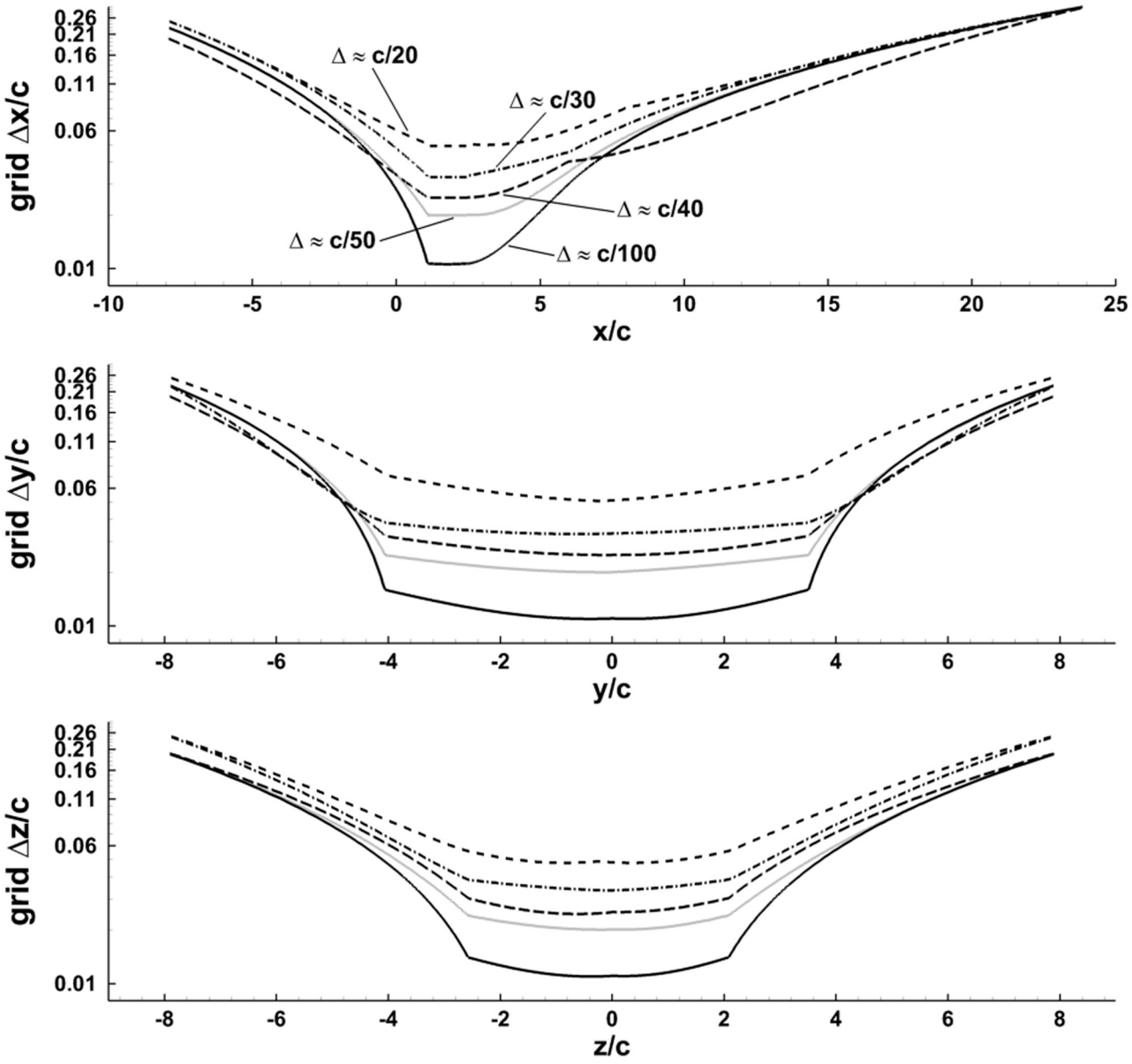

Fig 8. The grid spacing distribution for the five grids described in Table 2.

https://doi.org/10.1371/journal.pone.0207613.g008

The bat had a wingspan of 52.0 cm, and an average wing chord of 7.4 cm. Thus the Reynolds number based on the mean wing chord was, Re = 11,680, and is defined as,

$$Re = \frac{\rho \ U_\infty \ c_m}{\mu} \tag{3}$$

where ρ is the air density, U_∞ is the average flight velocity, c_m is the chord length, and μ is the air viscosity. The flow is dominated by inertia, however the Reynolds number is low enough that viscous effects cannot be neglected. The Strouhal number of the flight was, $St = 0.61$,

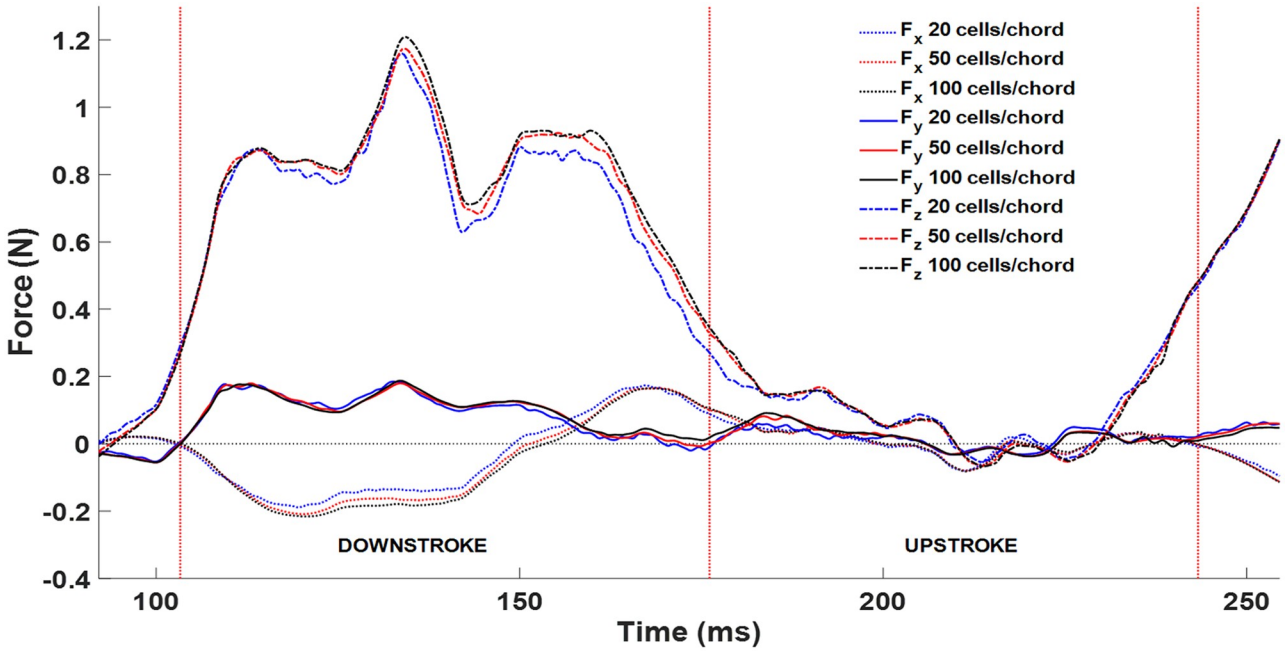

Fig 9. Comparison of the unsteady fluid force components for a complete flap cycle. Some discrepancy can be observed between the coarsest (blue) and finest (black) grids, however the two finest grids—50 and 100 cells per chord—show close agreement throughout the flap cycle for all three force components.

https://doi.org/10.1371/journal.pone.0207613.g009

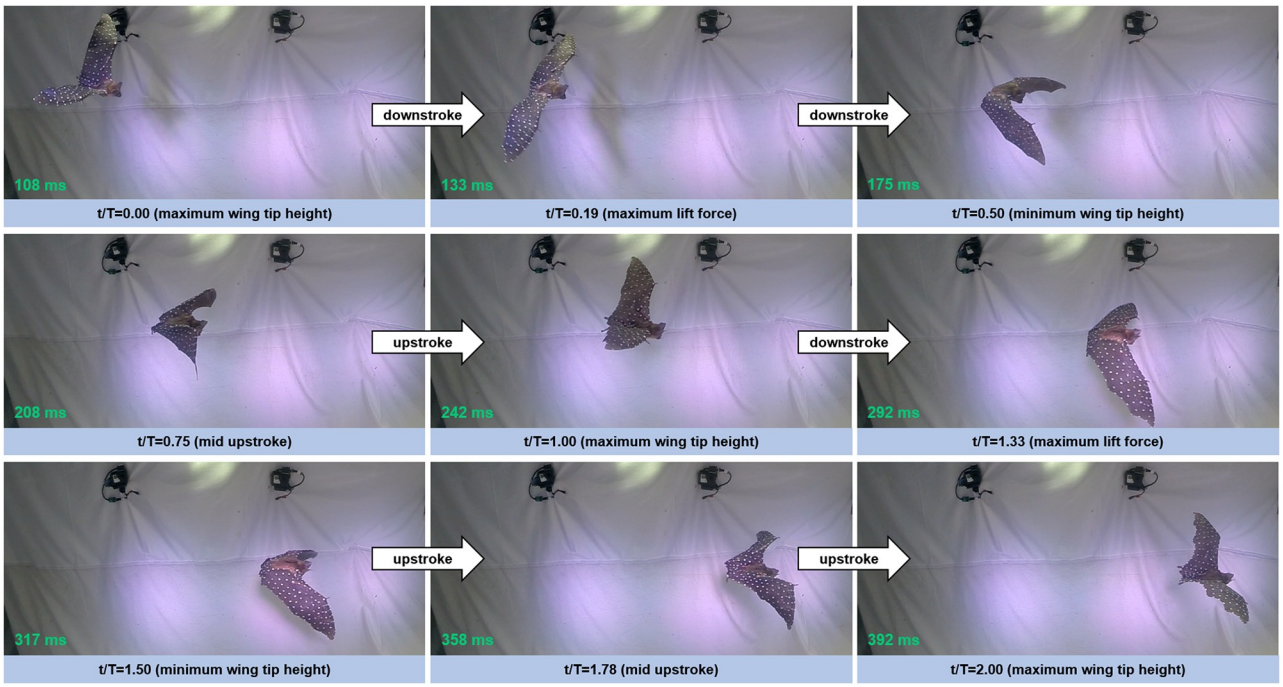

Fig 10. Nine frames sampled from two complete flap cycles are shown. t/T is the normalized time starting from the downstroke, and normalized by the flap period of 138 ms.

https://doi.org/10.1371/journal.pone.0207613.g010

Table 3. Flight parameters from a 1 meter long straight flight by an *H. pratti*.

Average Velocity, U_∞	Flap Frequency, f	Stroke or Plunge Amplitude, h_a	Stroke Plane Angle, β
2.57 m/s	7.25 Hz	±10.9 cm	54.1°

https://doi.org/10.1371/journal.pone.0207613.t004

defined as,

$$St = \frac{2\ f\ h_a}{U_\infty} \tag{4}$$

where f is the flapping frequency, 7.25 Hz, h_a is the stroke or plunge amplitude, 10.9 cm, and U_∞ is the average flight velocity, 2.57 m/s. All the flight parameters are summarized in Table 3.

The plunge amplitude is defined by half the maximum minus minimum wing tip z-positions. This value varies between the left and right wing, and between flaps so the mean was taken. The stroke plane angle is defined by the angle of the stroke plane with respect to horizontal, and describes the balance between lift and thrust. Hovering flight requires low stroke plane angles which correspond to nearly horizontal stroke planes. Conversely, accelerating flight requires a high stroke plane angle to achieve greater thrust. The value of 54.1 degrees for the present straight and level flight is typical of bats in this flight regime [53].

Variations in wing surface area during flight is another aspect of the wing kinematics which can only be studied using a sufficiently spatial resolution of the wings. Fig 11 shows the time evolution of the total wing surface area along with a breakdown between different regions of the bat. The mean total surface was 398 cm^2, and the variation was +17% and -35% for the minimum and maximum, respectively. The minimum total surface area was observed during

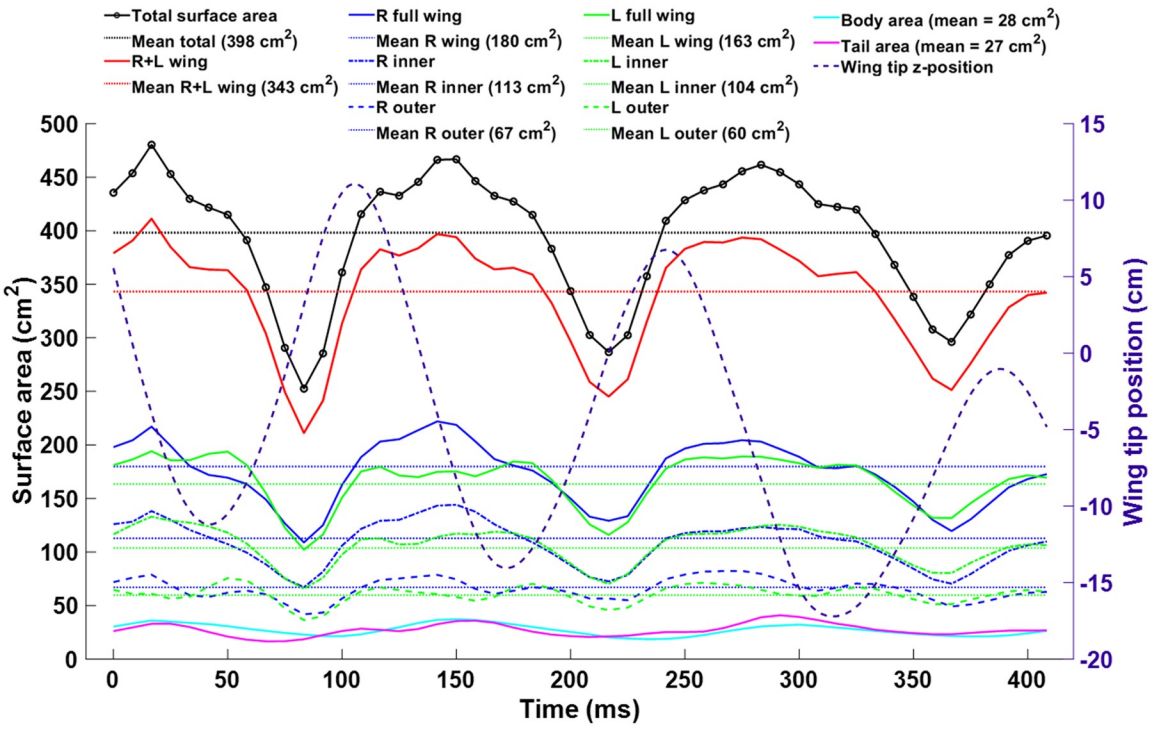

Fig 11. The total surface area variation of the bat wings, tail, and body is shown over the course of the flight (solid black). For context, the wing tip positions are shown (dotted black) to indicate the upstroke and downstroke.

https://doi.org/10.1371/journal.pone.0207613.g011

the latter third of the upstroke, while the maximum was observed near the middle of each downstroke. The wing area begins to increase during the second half of the upstroke. This is possibly due to either active muscular control of the wing, higher air pressure under the wing as it rotates at the top of the upstroke thereby catching the flow, or a combination of both factors.

The trend observed in the wing surface area change is consistent for the left and right wing, as well as the inner and outer portions of each wing. Thus, no section of the wing was observed to experience vastly different percent change in area compared to the wing as a whole.

Validation using lumped mass dynamics

In order to verify the flight simulation, the fluid forces exerted on the bat were examined in relation to the observed flight trajectory. The transient force output from the flow simulation was used to predict the flight trajectory of an equivalent point mass. The bat's body mass of 55g was approximated as being concentrated between the shoulder points at the same location that the net force was applied. This allowed for a comparison that would highlight the accuracy of the numerical solution.

The transient force curve (Fig 9) was calculated by integrating the pressure and shear force over the surface of the wing at each time step. As expected, the dominate force component was lift countering the weight of the bat. For a perfectly straight and level flight, the streamwise and lateral components should be zero. Absent acceleration, the thrust and drag should exactly balance for a net zero x-force. For the present flight, the net x and y forces were indeed near zero as seen in Fig 9.

The lift, thrust, drag, lateral, and weight forces were applied to the bat. The expected acceleration of the bat due to the fluid forces at each time step was calculated by dividing the net fluid force by the mass of the bat.

$$\vec{F}(t) = m\frac{d^2\vec{x}(t)}{dt^2} \tag{5}$$

$$\vec{x}(t) = \int_{t_0}^{t}\int_{t_0}^{t}\frac{\vec{F}(t)}{m}dt\ dt \tag{6}$$

A Runge-Kutta numerical integration was performed on Eq (6) to predict the flight trajectory based on the transient lift and propulsion curves generated by the flow simulation. The trajectory, $\vec{x}(t)$, predicted from the fluid forces was then compared to the observed flight trajectory of the bat as shown in Fig 12.

The dynamics analysis approximates the mass of the bat to be a single rigid body, and ignores the wing inertia. For the assumptions made, the predicted trajectory is remarkably close to the observed flight path of the bat. The one notable discrepancy is an under prediction of the thrust force. Minimal acceleration is predicted, yet the bat accelerated from 2.2 to 2.7 m/s. The grid independence study indicated good convergence of the numerical simulation, thus the slight under-prediction of the x-location is more likely due to small errors in the wing kinematic data. On the other hand, the predicted y- and z- trajectories are very close to the observed values. Overall the dynamics analysis indicates that the forces calculated by the flow simulation are close to the actual fluid forces generated by the bat.

Force analysis

During flight, forces are manifested as a pressure differential across the wings. At the Reynolds number, Re ~ $O(10^4)$, shear stress at the wing is relatively minor compared to the pressure

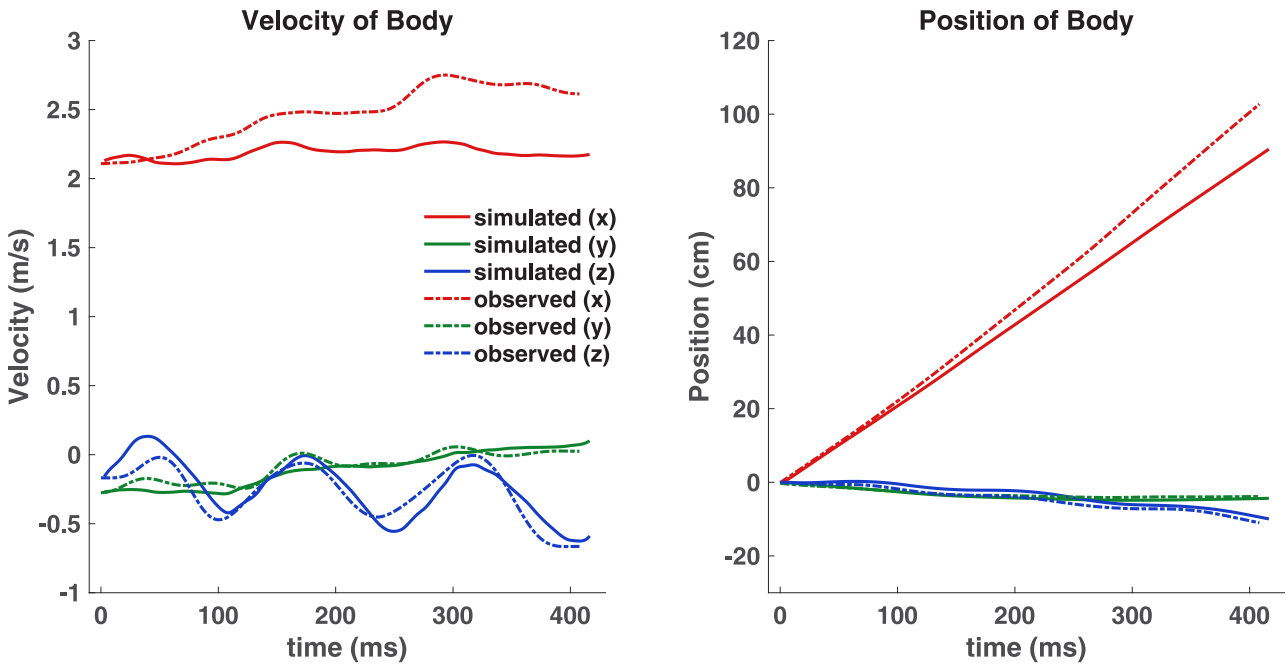

Fig 12. Left: Comparison of the simulated and observed velocity in x, y, and z. Right: The simulated flight trajectory is compared to the observed flight trajectory. The vertical and lateral predictions are very close, however the streamwise position is under predicted by 15 cm.

https://doi.org/10.1371/journal.pone.0207613.g012

force, however both are included in the present analysis. The total aerodynamic force on the wings at each time instant is the surface integral,

$$\vec{F} = \int_S (\vec{\tau} - p\hat{n})\ dS \tag{7}$$

where p is fluid pressure, $\hat{n}$ is the wing surface normal, and $\vec{\tau}$ is the viscous stress tensor. The resulting force curve is shown in Fig 13.

The cycle averaged force values are $\vec{F}_x = 0.005\ N$, $\vec{F}_y = -0.050\ N$, and $\vec{F}_z = 0.525\ N$. Due to the low accelerations experienced during a mostly straight and level flight, the streamwise and lateral forces are expectedly near zero. The much larger z-component represents the lift necessary for flight. The lift can be normalized by standard methods to obtain the lift coefficient,

$$C_L = \frac{F_z}{\frac{1}{2}\rho {U_\infty}^2 S} \tag{8}$$

where F_z is the dimensional vertical force, ρ is the air density, U_∞ is the freestream velocity, and S is the maximum observed planform area of the wing during the flap cycle. The resulting values are plotted over two flap cycles in Fig 14.

The mean value of the lift coefficient was calculated to be 3.21. For fixed wing aircraft, the lift coefficient is only a function of airfoil shape and angle of attack. For this reason, it provides a convenient method to calculate lift at a given angle of attack, or calculate the proper angle of attack given a velocity. However, for bat flight, the wing shape, wing area, angle of attack, and instantaneous velocity vary continuously throughout the stroke. Others have noted the limitations of quasi-steady theory in the study of bat flight as well [8].

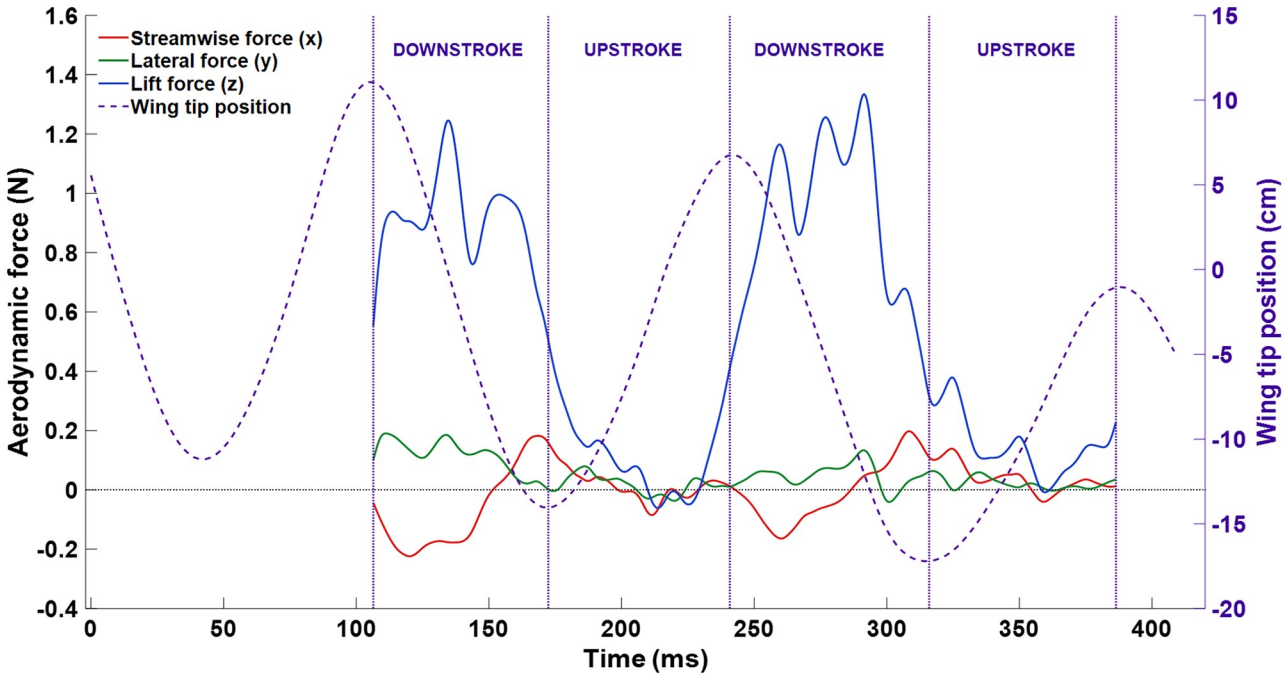

Fig 13. The time variation of aerodynamic force is shown along with the wing tip position for context. The peak lift force was around 1.2 N, and the cycle averaged mean was 0.525 N. The streamwise and lateral forces were both close to zero since the flight was approximately straight and level.

https://doi.org/10.1371/journal.pone.0207613.g013

To understand the aerodynamic phenomena in flapping flight the unsteady flow features in relation to force production are examined. This has been the focus of recent research reviewed by Shyy et al. in 2010 [1]. Coherent vorticity is shown via Δ-criterion isosurfaces in Fig 15. Four instances in time are shown along with the corresponding flight velocity, planform area, instantaneous span, aerodynamic force, and aerodynamic power.

In Fig 15, snapshot (a) corresponds to the top of the upstroke or also the beginning of the downstroke. The lift force at (a) is about 0.45 N, or 35% of maximum lift, despite the wing having no downward velocity. Wing rotation towards the end of the upstroke as the wing readies itself for the downstroke results in a leading edge vortex (LEV) to begin to form. The aerodynamic power at time (a), as shown in Fig 15, is quite low at about 0.3 W, which is less than 10% of the maximum power expenditure. This is due to relatively low instantaneous wing flap velocity at the top of the upstroke. The planform area at time (a) has already increased to a near maximum indicating that either the freestream flow is impacting the underside of the wing stretching the membrane, or that the bat is actively stretching its wing with muscular activation. At time (a), the tip vortex (TiV) shedding is observed to be minimal. Between snapshots (a) and (b), the downward velocity of the wings accelerates rapidly. The majority of lift generation is in a 34 ms time interval from 258 ms to 292 ms which is highlighted in detail in Fig 16.

Fig 16 shows the coefficient of pressure on the bottom and top surfaces of the wing. In addition, the pressure difference—defined as the pressure under the wing minus the pressure on the top of the wing—is shown along with iso-surfaces of coherent vorticity. During both downstrokes, a notable pattern of three local maxima in the lift force can be observed (110–160 ms and 260–290 ms). Since this pattern emerges in different flap cycles, it is more likely a feature of the aerodynamics rather than random fluctuations in force. In order to explore the phenomenon in more detail, each of the five time instances shown in Fig 16 correspond to a local maxima or local minima in the force curve.

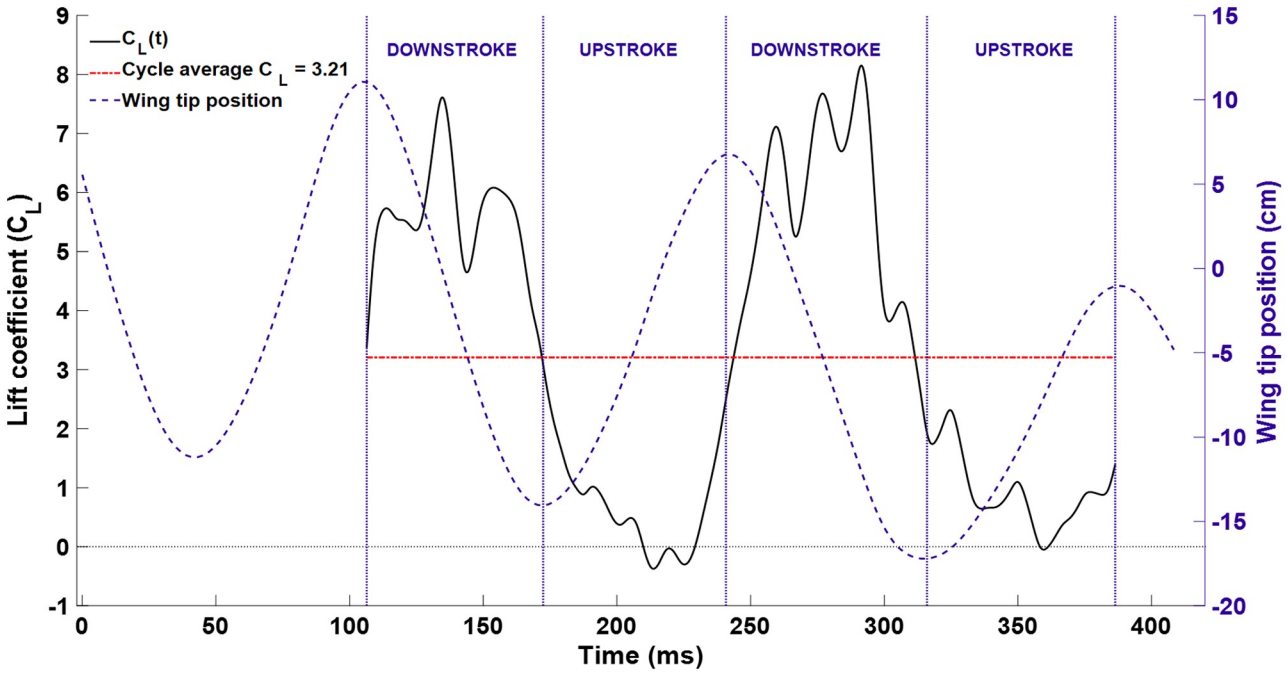

Fig 14. The lift coefficient is plotted along with the wing tip location for context. The mean value was C_L = 3.21.

https://doi.org/10.1371/journal.pone.0207613.g014

The first local maximum depicted in Fig 16, t = 258 ms, shows a coherent low pressure band on the leading edge of the wing. Moving along the chord from the leading to trailing edge, there is a distinct location, about a third of the way down the wing chord, at which the pressure rises, representing the bound of the influence of the LEV. At this instant in time, the stagnation pressure under the wing is maximum causing the large lift force—approximately 81% of the absolute maximum lift. The first local minimum in lift, t = 267 ms (Fig 16), shows the LEV convecting down the wing and breaking up slightly. Comparing to t = 258 ms, the low pressure band on the leading edge is not as complete. The stagnation pressure is also not as high at t = 267 ms compared to the previous local maximum at t = 258 ms. As such, the lift force is only 62% of the absolute maximum. At the second local maximum of lift (t = 275 ms in Fig 16), the low pressure region on the top of the wing grows in area as the LEV continues to convect along the wing. This in combination with the stagnation pressure rising slightly from t = 267 ms to t = 275 ms, causes the lift to rise to 90% of the absolute maximum. At t = 286 ms, the LEV becomes somewhat less coherent on the top surface and the low pressure region decreases in strength causing another local minimum if lift at 79% of the peak lift value.

Finally, the fifth and last instant shown in Fig 16, t = 292 ms, corresponds to the absolute maximum of lift which is also snapshot (b) from Fig 15. At this instant, a strong LEV can be seen which helps keep the flow remain attached despite a relatively high angle of attack. The LEV also maintains a strong low pressure region on the top of the wing directly contributing to lift. Flow stagnation under the wing creates an elevated pressure, which is especially pronounced towards the outer region of each wing. Additionally, prominent TiVs are shed which has also been observed in PIV experiments of bat flight [22,24,25,29,54–57]. In contrast to fix wing high Reynolds number flight, in which TiVs are known to be detrimental, flapping fliers can use TiVs to augment lift and thrust due to interactions with the leading and trailing edge vortices [1]. The point of peak lift force also is the point of maximum power expenditure at about 3.6 watts. The vertical velocity component at this time is also rising. The cyclical nature

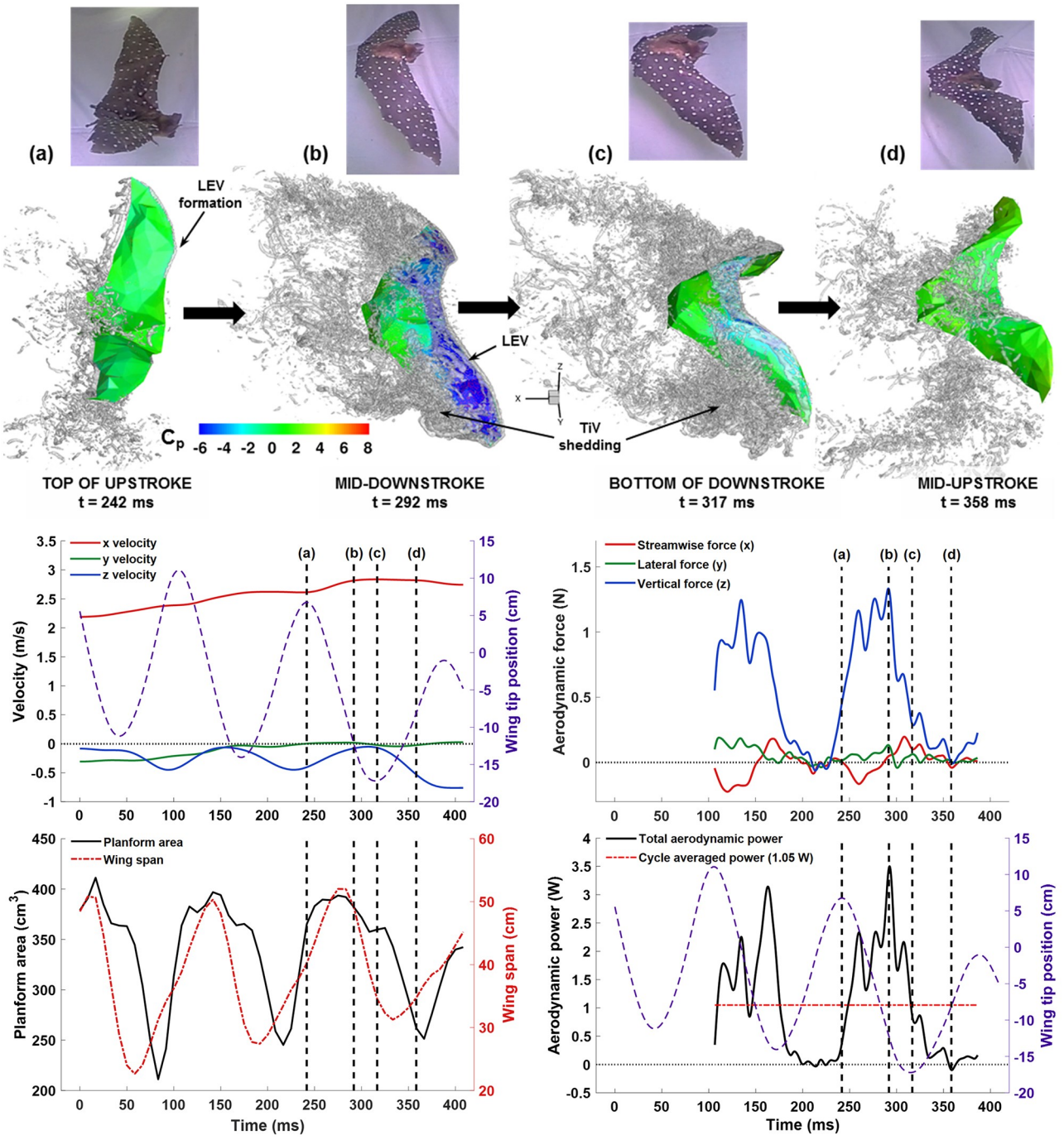

Fig 15. Top: Coherent vorticity (iso-surfaces of Δ-criterion) is shown along with the wing surface pressure at four snapshots throughout the flap cycle. Bottom: Flight velocity, planform area, wing span, aerodynamic force, and aerodynamic power are plotted with each of the four snapshot locations indicated. (a) the top of the upstroke, (b) the point of maximum lift production, (c) the bottom of the downstroke, and (d) the midpoint of the upstroke.

https://doi.org/10.1371/journal.pone.0207613.g015

of lift production in flapping flight means that the vertical position of the bat's body moves slightly up and down during flight.

Spanshot (c) from Fig 15 is taken at the bottom of the downstroke. Lift production drops rapidly towards the end of the downstroke—from (b) to (c) there is a nearly 90% drop in lift.

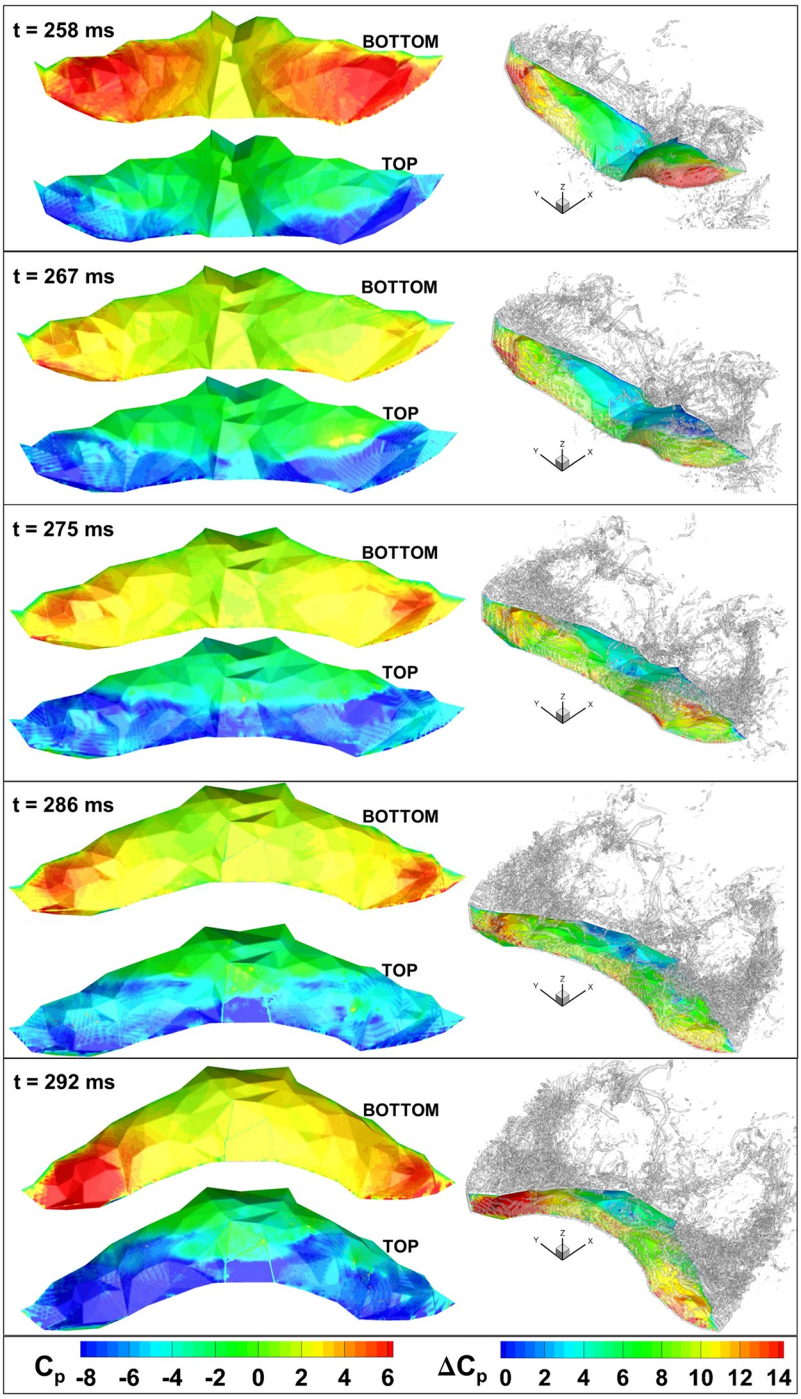

Fig 16. Left: Aerodynamic pressure on the top and bottom of the bat wing is shown at 5 instances during the downstroke. Right: Pressure difference is shown on the wing surface with iso-surfaces of coherent vorticity.

https://doi.org/10.1371/journal.pone.0207613.g016

The prominent TiVs can be seen convecting downstream into the wake, yet have little impact on the flight once they are shed and are significantly distanced from the wing surface. The bat begins to rotates its wings aligning them to the flow and drawing the wing tips together. At time (c) the span is about 33 cm compared to the maximum span of 52 cm. Despite the wingtip

velocity dropping to zero at the bottom of the downstroke, the power expenditure is still around 1 watt, likely due to wing inertia and elastic potential being converted to aerodynamic power as the wings stop and reverse direction. The vertical velocity of the bat body is near maximum at this point, and then begins to reverse.

Spanshot (d) from Fig 15 corresponds to the mid-upstroke. The upstroke is shorter in duration than the downstroke, which allows the bat to quickly reset the wing position and prepare for the next downstroke where the majority of lift and thrust are generated. During the upstroke, the bat positions its wing perpendicular to the flow to mitigate negative lift. In fact, the lift force never drops below zero during the upstroke. The vortex structures in the flow can be seen to be minimal at this point. The planform area drops to a minimum of around 260 cm^2 midway through the upstroke after which it starts increasing again.

Fight power analysis

Power consumption is a particularly important metric in flight because the flight fuel must be held aloft by the flying animal or vehicle. This results in a non-linear feedback between weight and power consumption—more fuel requires more lift power which in turn requires even more fuel. Bats store fuel from food to efficiently power their wing muscles. Pennycuick [58] and others [59–63] conducted early research into the power requirements of animal flight using respiratory experiments and fixed wing airfoil theory. Other attempts to understand flapping flight power consumption involved measuring metabolic power during flight [12,64], and measuring kinetic energy in the wake of a flying animal using PIV [64].

Aerodynamic simulations offer a straight forward and direct method to calculate power usage by a flying animal regardless of the complexity of the wing kinematics. At each instant in time, the aerodynamic power equals the instantaneous rate of work done by the wing on the fluid, and can be determined by,

$$P = \frac{dW}{dt} = \int_S (p\hat{n} - \vec{\tau}) \cdot \vec{v}_{wing} \, dS \tag{9}$$

where p is fluid pressure, $\hat{n}$ is the wing surface normal, $\vec{\tau}$ is the viscous stress tensor, and $\vec{v}_{wing}$ is the velocity of the wing surface. In the context of the immersed boundary method, Eq (9) is evaluated by summing $\vec{F} \cdot \vec{v}$ over the discrete surface elements comprising the wings. The resulting power is shown for two complete flap cycles in Fig 17.

The cycle averaged power expenditure was 1.00 W and 1.10 W for the two flaps respectively. Peak power output reached 3–3.5 W in the second half of each downstroke. In the present analysis, the wing inertia and elastic strain energy are assumed to have minimal impact on power, in line with the findings of other researchers [64]. This is largely because the wing velocity diminishes to zero at the top and bottom of the stroke, thus the inertial energy is returned to the flow. Similarly, the wing stretches during the downstroke thereby storing potential energy, but as the membrane relaxes on the upstroke the energy is returned to the flow. These factors may impact the temporal accuracy of the power values, but should not affect the cycle averaged results.

Conclusion

Aerodynamic simulations of bat flight allow for the direct investigation of the fluid phenomena responsible for generating of lift and thrust by a flexible flapping membrane. The ability to analyze transient flow fields alongside detailed wing kinematics can advance the understanding of flapping flight beyond prior methods. Previous work in the field has leaned on the well-

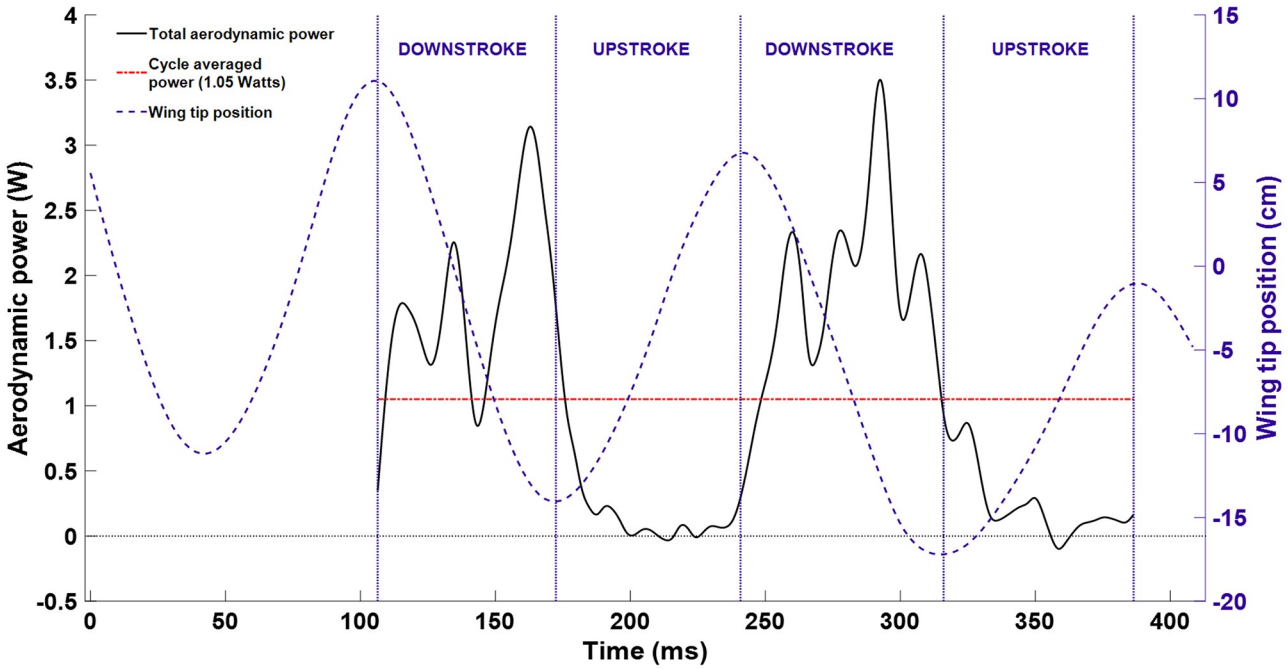

Fig 17. Aerodynamic power is plotted for two complete flap cycles along with wing tip position for context. Power expenditure was maximum during the second half of each downstroke at around 2.5 to 3.5 Watts. The cycle averaged value over both flaps was 1.05 Watts.

https://doi.org/10.1371/journal.pone.0207613.g017

known theory of conventional airfoils which is not always applicable to bat flight. For example, the angle of attack, camber, and chord length vary significantly both along the span of a bat wing as well as temporally throughout the flap cycle in contrast to the well-defined and predictable behavior of a conventional airfoil. Other research has used PIV methods to measure the flow field in the wake of the bat, however this method has restrictions on the size of the bat and the ability to study flight maneuvers. Additionally, pseudo-steady wake models for force calculations rely on the frozen vortex hypothesis which does not always hold in animal flight.

Conducting aerodynamic simulations to numerically obtain the flow field around bat wings during flight is an attractive alternative to other methods of analysis. However, both high spatial resolution motion capture, as well as the numerical simulations remain a technical challenge. In the present work, 108 discrete marker points were tracked in order to fully capture the many degrees of freedom of the bat wings. After motion capture, the kinematic data was interfaced with a Navier-Stokes solver using the immersed boundary method as well as LES. A fluid grid of 88.1 million cells was used to resolve the unsteady flow of Re = 11,680.

Aerodynamic forces and the associated power were directly calculated from the resulting flow field using surface integrations. Coherent vorticity visualization was used in conjunction with wing area, force, and power data to investigate some of the underlying mechanism of bat flight. For example, while still in the upstroke, the bat starts generating lift due to wing rotation which results in the formation of a LEV. However, the majority of lift is generated during the downstroke when the LEV mitigates massive flow separation from the wing. During the upstroke, negative lift is completely avoided by virtue of wing rotation and a drastic reduction in planform area providing a net performance benefit.

There are still many challenges and open questions to be considered in the field of bat flight. For example, what is the interplay between wing elasticity and unsteady flow features? How do different bat wing morphologies manifest as optimizations to different types of flight (speed

versus maneuverability versus efficiency)? What is the underlying control scheme to actuate flapping flight? How are bats so adept at maneuvering flight? Computational modeling can be a critical tool in uncovering answers to these and other open questions in the realm of bat flight. The 3D motion capture and computational framework described and validated in this study has the potential to analyze a wide variety of bat flights, including the study of maneuvering bat flight.

Supporting information

S1 CSV File. Time series of force and power data from the bat flight simulation.
(CSV)

S1 Video Frames. Series of images from the bat flight video. Images are provided from the view of two separate cameras. Each successive frame is separated by 1/120 seconds. The cameras were synchronized in their recording (i.e. frame 380 represents the same moment for both cameras).
(RAR)

Acknowledgments

The financial support of the NSF CBET Grant No. 1510797, NSF IRES Grant No. 1658620, support from VT ICTAS/BIST Center, National Natural Science Foundation of China (Grant Nos. 11374192 & 11574183), Chinese Ministry of Education Tese Grant for international faculty exchange is gratefully acknowledged. The authors would also like to acknowledge the computational resources provided by Advanced Research Computing (ARC) at Virginia Tech.

Author Contributions

Conceptualization: Peter Windes, Danesh K. Tafti.

Data curation: Xiaozhou Fan.

Investigation: Peter Windes.

Resources: Matt Bender, Rolf Müller.

Supervision: Danesh K. Tafti, Rolf Müller.

Writing – original draft: Peter Windes.

Writing – review & editing: Peter Windes, Matt Bender, Danesh K. Tafti, Rolf Müller.

References

1. Shyy W, Aono H, Chimakurthi SK, Trizila P, Kang CK, Cesnik CES, et al. Recent progress in flapping wing aerodynamics and aeroelasticity. Prog Aerosp Sci. Elsevier; 2010; 46: 284–327. https://doi.org/10.1016/j.paerosci.2010.01.001
2. Shyy W, Berg M, Ljungqvist D. Flapping and flexible wings for biological and micro air vehicles. Prog Aerosp Sci. 1999; 35: 455–505. https://doi.org/10.1016/S0376-0421(98)00016-5
3. Lentink D, Jongerius SR, Bradshaw NL. The scalable design of flapping micro-air vehicles inspired by insect flight. Flying Insects and Robots. 2010. pp. 185–205. https://doi.org/10.1007/978-3-540-89393-6_14
4. Ho S, Nassef H, Pornsinsirirak N, Tai YC, Ho CM. Unsteady aerodynamics and flow control for flapping wing flyers. Progress in Aerospace Sciences. 2003. pp. 635–681. https://doi.org/10.1016/j.paerosci.2003.04.001
5. Chin DD, Lentink D. Flapping wing aerodynamics: from insects to vertebrates. J Exp Biol. 2016; 219: 920–932. https://doi.org/10.1242/jeb.042317 PMID: 27030773

6. Norberg UM, Rayner JM V. Ecological Morphology and Flight in Bats (Mammalia; Chiroptera): Wing Adaptations, Flight Performance, Foraging Strategy and Echolocation. Philos Trans R Soc B Biol Sci. 1987; 316: 335–427. https://doi.org/10.1098/rstb.1987.0030
7. Swartz SM, Konow N. Advances in the study of bat flight: the wing and the wind. Can J Zool. 2015; 93: 977–990. https://doi.org/10.1139/cjz-2015-0117
8. Hedenstrom A, Johansson LC. Bat flight: aerodynamics, kinematics and flight morphology. J Exp Biol. 2015; 218: 653–663. https://doi.org/10.1242/jeb.031203 PMID: 25740899
9. Hedenström A, Johansson LC, Spedding GR. Bird or bat: comparing airframe design and flight performance. Bioinspir Biomim. 2009; 4: 15001. https://doi.org/10.1088/1748-3182/4/1/015001 PMID: 19258691
10. Kunz TH, Fenton MB. Bat Ecology. the University of Chicago Press. 2003. pp. 107–112.
11. Hartman F a. Some Flight Mechanisms of Bats. Ohio J Sci. 1963; 63: 59–65.
12. Thomas SP, Suthers RA. The physiology and energetics of bat flight. J Exp Biol. 1972; 57: 317–335.
13. Bullen R, McKenzie NL. Bat airframe design: Flight performance, stability and control in relation to foraging ecology. Aust J Zool. 2001; 49: 235–261. https://doi.org/10.1071/ZO00037
14. Norberg UM. Aerodynamics, kinematics, and energetics of horizontal flapping flight in the long-eared bat Plecotus auritus. J Exp Biol. 1976; 65: 179–212. PMID: 993701
15. Rayner JM V, Aldridge HD. Three-dimensional reconstruction of animal flight paths and the turning flight of microchiropteran bats. J Exp Biol. 1985; 118: 247–265.
16. Aldridge HD. Kinematics and aerodynamics of the greater horseshoe bat, Rhinolophus ferrumequinum, in horizontal flight at various flight speeds. J Exp Biol. 1986; 126: 479–97. PMID: 3806000
17. Aldridge HD. Turning flight of bats. J Exp Biol. 1987; 128: 419–425. PMID: 3559468
18. Aldridge HD. Body accelerations during the wingbeat in six bat species: the function of the upstroke in thrust generation. J Exp Biol. 1987; 130: 275–293.
19. Aldridge HD. Flight kinematics and energetics in the little brown bat, *Myotis lucifugus* (Chiroptera: Vespertilionidae), with reference to the influence of ground effect. J Zool. 1988; 216: 507–517. https://doi.org/10.1111/j.1469-7998.1988.tb02447.x
20. Aldridge HD. Vertical Flight in the Greater Horseshoe Bat Rhinolophus Ferrumequinum. J Exp Biol. 1991; 157: 183–204.
21. Norberg UM, Kunz TH, Steffensen JF, Winter Y, Von Helversen O. The Cost of Hovering and Forward Flight in a Nectar-Feeding Bat, Glossophaga Soricina, Estimated From Aerodynamic Theory. J Exp Biol. 1993; 182: 207–227. PMID: 8228780
22. Tian X, Iriarte-Diaz J, Middleton K, Galvao R, Israeli E, Roemer A, et al. Direct measurements of the kinematics and dynamics of bat flight. Bioinspir Biomim. 2006; 1: S10–S18. https://doi.org/10.1088/1748-3182/1/4/S02 PMID: 17671313
23. Riskin DK, Willis DJ, Iriarte-Diaz J, Hedrick TL, Kostandov M, Chen J, et al. Quantifying the complexity of bat wing kinematics. J Theor Biol. 2008; 254: 604–615. https://doi.org/10.1016/j.jtbi.2008.06.011 PMID: 18621062
24. Hedenstrom A, Johansson LC, Wolf M, von Busse R, Winter Y, Spedding GR. Bat Flight Generates Complex Aerodynamic Tracks. Science (80-). 2007; 316: 894–897. https://doi.org/10.1126/science.1142281 PMID: 17495171
25. Muijres FT, Johansson LC, Barfield R, Wolf M, Spedding GR, Hedenstrom A. Leading-Edge Vortex Improves Lift in Slow-Flying Bats. Science (80-). 2008; 319: 1250–1253. https://doi.org/10.1126/science.1153019 PMID: 18309085
26. Johansson LC, Wolf M, von Busse R, Winter Y, Spedding GR, Hedenström A. The near and far wake of Pallas' long tongued bat (*Glossophaga soricina*). J Exp Biol. 2008; 211: 2909–18. https://doi.org/10.1242/jeb.018192 PMID: 18775928
27. Johansson LC, Wolf M, Hedenström A. A quantitative comparison of bird and bat wakes. J R Soc Interface. 2010; 7: 61–66. https://doi.org/10.1098/rsif.2008.0541 PMID: 19324669
28. Hubel TY, Hristov NI, Swartz SM, Breuer KS. Time-resolved wake structure and kinematics of bat flight. Anim Locomot. 2010; 371–381. https://doi.org/10.1007/978-3-642-11633-9_29
29. Hedenström A, Muijres FT, Von Busse R, Johansson LC, Winter Y, Spedding GR. High-speed stereo DPIV measurement of wakes of two bat species flying freely in a wind tunnel. Animal Locomotion. 2010. pp. 361–370. https://doi.org/10.1007/978-3-642-11633-9_28
30. Spedding GR, Hedenström A. PIV-based investigations of animal flight. Animal Locomotion. 2010. pp. 187–201. https://doi.org/10.1007/978-3-642-11633-9_16

31. Gutierrez E, Quinn DB, Chin DD, Lentink D. Lift calculations based on accepted wake models for animal flight are inconsistent and sensitive to vortex dynamics. Bioinspir Biomim. 2016; 12: 16004. https://doi.org/10.1088/1748-3190/12/1/016004 PMID: 27921999

32. Dabiri JO. On the estimation of swimming and flying forces from wake measurements. J Exp Biol. 2005; 208: 3519–3532. https://doi.org/10.1242/jeb.01813 PMID: 16155224

33. Dong H, Koehler C, Liang Z, Wan H, Gaston Z. An Integrated Analysis of a Dragonfly in Free Flight. AIAA J. 2010; 1–10.

34. Li C, Dong H. Wing kinematics measurement and aerodynamics of a dragonfly in turning flight. Bioinspir Biomim. 2017; 12: 26001. https://doi.org/10.1088/1748-3190/aa5761 PMID: 28059781

35. Wan H, Dong H, Gai K. Computational investigation of cicada aerodynamics in forward flight. J R Soc Interface. 2014; 12: 20141116–20141116. https://doi.org/10.1098/rsif.2014.1116 PMID: 25551136

36. Liu G, Dong H, Li C. Vortex dynamics and new lift enhancement mechanism of wing–body interaction in insect forward flight. J Fluid Mech. 2016; 795: 634–651. https://doi.org/10.1017/jfm.2016.175

37. Ren Y, Dong H, Deng X, Tobalske B. Turning on a dime: Asymmetric vortex formation in hummingbird maneuvering flight. Phys Rev Fluids. 2016; 1: 50511. https://doi.org/10.1103/PhysRevFluids.1.050511

38. Song J, Luo H, Hedrick TL. Three-dimensional flow and lift characteristics of a hovering ruby-throated hummingbird. J R Soc Interface. 2014; 11: 20140541–20140541. https://doi.org/10.1098/rsif.2014.0541 PMID: 25008082

39. Viswanath K, Nagendra K, Cotter J, Frauenthal M, Tafti DK. Straight-line climbing flight aerodynamics of a fruit bat. Phys Fluids. 2014;26. https://doi.org/10.1063/1.4864297

40. Deetjen ME, Biewener AA, Lentink D. High-speed surface reconstruction of a flying bird using structured light. J Exp Biol. 2017; 220: 1956–1961. https://doi.org/10.1242/jeb.149708 PMID: 28348041

41. Tobalske BW, Warrick DR, Clark CJ, Powers DR, Hedrick TL, Hyder GA, et al. Three-dimensional kinematics of hummingbird flight. J Exp Biol. 2007; 210: 2368–2382. https://doi.org/10.1242/jeb.005686 PMID: 17575042

42. Altshuler DL, Dickson WB, Vance JT, Roberts SP, Dickinson MH. Short-amplitude high-frequency wing strokes determine the aerodynamics of honeybee flight. Proc Natl Acad Sci U S A. 2005; 102: 18213–8. https://doi.org/10.1073/pnas.0506590102 PMID: 16330767

43. Bozkurttas M, Mittal R, Dong H, Lauder G V., Madden P. Low-dimensional models and performance scaling of a highly deformable fish pectoral fin. J Fluid Mech. 2009; 631: 311. https://doi.org/10.1017/S0022112009007046

44. Bender MJ, McClelland HG, Bledt G, Kurdila A, Furukawa T, Mueller R. Trajectory Estimation of Bat Flight Using a Multi-View Camera System. Model Simul Technol Conf SciTech 2015. 2015; 1–13.

45. Bender MJ, McClelland HM, Kurdila A, Mueller R. Recursive Bayesian Estimation of Bat Flapping Flight Using Kinematic Trees. AIAA Model Simul Technol Conf. 2016; 1–12.

46. Svoboda T, Martinec D, Pajdla T. A convenient multicamera self-calibration for virtual environments. PRESENCE teleoperators virtual Environ. 2005; 14: 407–422. https://doi.org/10.1162/105474605774785325

47. Fan X, Windes P, Tafti D, Sekhar S, Bender M, Kurdila A, et al. Proper orthogonal decomposition of straight and level flight kinematics in an insectivorous bat. 2018 AIAA Model Simul Technol Conf. 2018; 1–22.

48. Tafti DK. GenIDLEST: A scalable parallel computational tool for simulating complex turbulent flows. ASME-PUBLICATIONS-FED. 2001. pp. 347–356.

49. Tafti DK. Time-accurate techniques for turbulent heat transfer analysis in complex geometries. In: Amano R, Sunden B, editors. Computational Fluid Dynamics and Heat Transfer. Southampton, UK: WIT Press; 2011. pp. 217–264.

50. Germano M, Piomelli U, Moin P, Cabot WH. A dynamic subgrid-scale eddy viscosity model. Phys Fluids A Fluid Dyn. 1991; 3: 1760–1765. https://doi.org/10.1063/1.857955

51. Najjar FM, Tafti DK. Study of discrete test filters and finite difference approximations for the dynamic subgrid-scale stress model. Phys Fluids. 1996; 8: 1076–1088. https://doi.org/10.1063/1.868887

52. Nagendra K, Tafti DK, Viswanath K. A new approach for conjugate heat transfer problems using immersed boundary method for curvilinear grid based solvers. J Comput Phys. 2014; 267: 225–246. https://doi.org/10.1016/j.jcp.2014.02.045

53. Wolf M, Johansson LC, von Busse R, Winter Y, Hedenstrom A. Kinematics of flight and the relationship to the vortex wake of a Pallas' long tongued bat (*Glossophaga soricina*). J Exp Biol. 2010; 213: 2142–2153. https://doi.org/10.1242/jeb.029777 PMID: 20511529

54. Hubel TY, Riskin DK, Swartz SM, Breuer KS. Wake structure and wing kinematics: the flight of the lesser dog-faced fruit bat, Cynopterus brachyotis. J Exp Biol. 2010; 213: 3427–3440. https://doi.org/10.1242/jeb.043257 PMID: 20889823

55. Hubel TY, Hristov NI, Swartz SM, Breuer KS. Wake structure and kinematics in two insectivorous bats. Philos Trans R Soc B Biol Sci. 2016; 371: 20150385. https://doi.org/10.1098/rstb.2015.0385 PMID: 27528775

56. Hubel TY, Hristov NI, Swartz SM, Breuer KS. Changes in kinematics and aerodynamics over a range of speeds in Tadarida brasiliensis, the Brazilian free-tailed bat. J R Soc Interface. 2012; 9: 1120–1130. https://doi.org/10.1098/rsif.2011.0838 PMID: 22258554

57. Muijres FT, Johansson LC, Winter Y, Hedenström A, Muijres FT, Johansson LC, et al. Comparative aerodynamic performance of flapping flight in two bat species using time-resolved wake visualization. J R Soc Interfac Interfac. 2011; https://doi.org/10.1098/rsif.2011.0015 PMID: 21367776

58. Pennycuick C. Bird Flight Perfomance. Oxford University Press; 1989.

59. Withers BYPC Timko PL. The significance of ground effect to the aerodynamic cost of flight and energetics of the black skimmer (Rhyncops Nigra). J Exp Biol. 1977; 70: 13–26.

60. Rayner JM V., Viscardi PW, WARD S, Speakman JR. Aerodynamics and energetics of intermittent flight in birds. Am Zool. 1999; 39: 4A–5A. https://doi.org/10.1668/0003-1569(2001)041[0188:AAEOIF]2.0.CO;2

61. Rayner JM V. A new approach to animal flight mechanics. J Exp Biol. 1978; 80: 17–54.

62. Ellington C. Limitations on animal flight performance. J Exp Biol. 1991; 91: 71–91.

63. Ellington CP. The Aerodynamics of Hovering Insect Flight. I. The Quasi-Steady Analysis. Philos Trans R Soc B Biol Sci. 1984; 305: 1–15. https://doi.org/10.1098/rstb.1984.0049

64. von Busse R, Waldman RM, Swartz SM, Voigt CC, Breuer KS. The aerodynamic cost of flight in the short-tailed fruit bat (*Carollia perspicillata*): comparing theory with measurement. J R Soc Interface. 2014; 11: 20140147. https://doi.org/10.1098/rsif.2014.0147 PMID: 24718450

4. Analysis of a Great Roundleaf Bat in Turning Flight

Reprint of, "Kinematic and aerodynamic analysis of a bat performing a turning-ascending maneuver"

The following chapter is a reprint of a paper submitted to *Bioinspiration & Biomimetics* (submitted March 2020). This paper analyzes the kinematic and aerodynamic features of a bat conducting a sweeping turn maneuver over the course of 5 wingbeat cycles. As discussed in the introduction of this paper, the existing literature on bat flight maneuvering is very limited, and there is not a good understanding of the kinematic and aerodynamic mechanisms which allow bats to achieve a high level of maneuverability. This topic is particularly important in the context of understanding bat flight since maneuverability is one of the most impressive aspects of bat flight. In the paper, the computational methods discussed in Chapters 2 and 3 are applied to a sweeping turn where the bat is also ascending. A body-fixed coordinate system appropriate for analyzing non-straight flight is introduced along with a framework for calculating a temporally varying stroke plane for the right and left wings independently. The computational analysis framework from Chapter 3 is also extended by including a calculation of aerodynamic moments acting on the bat. In addition, a more detailed framework for estimating total power consumption, which accounts for not only aerodynamic power, but also the rate of change of potential and kinematic energy, is introduced. These additions are essential when analyzing a maneuvering flight where the vertical position and flight velocity are not constant in contrast to steady straight flight.

Kinematic and aerodynamic analysis of a bat performing a turning-ascending maneuver

Peter Windes[1], Danesh K. Tafti[1,2], Rolf Müller[1]

Abstract

The flapping flight of many bat species is characterized by a high degree of maneuverability and provides fertile ground for biomimetic design. However, there has been little prior work towards understanding bat flight maneuvers, particularly using a coupled kinematic and aerodynamic framework. Here, wing kinematic data of a large insectivorous bat (*Hipposideros armiger*) in straight and turning flight is investigated. Fundamental to turning flight are asymmetries in the wing kinematics and consequently asymmetries in the aerodynamic forces. Forces were calculated from the wing kinematics using aerodynamic numerical simulations. Aspects of the wing kinematics in the turn that were distinguishable from straight flight were an increase in stroke plane deviation angle, nominal increase in flapping amplitude, and a decrease in the horizontal stroke plane angle of the wing inside the turn. While prior work on the mechanics of turning flight in animals has focused on classifying a turn as either banking or yawing, in the present work we show evidence of simultaneous and synergistic banking and yawing mechanisms. During the initiation of the turn, the bank angle was low, and elevated thrust by the outside wing generated a significant yaw rotational moment during both the upstroke and downstroke. Later in the turn, the bank angle increased to approximately 25 degrees tilting the net force vector towards the inside of the turn providing centripetal acceleration thereby turning the bat. Understanding the details of the turning mechanism—combined yaw and bank—provides useful design and control principles for biomimetic flapping MAVs.

Keywords: bat flight, bat maneuvering, unsteady aerodynamics, motion capture, computational fluid dynamics, flapping flight, animal flight

[1] Department of Mechanical Engineering, Virginia Tech, Blacksburg, VA, United States of America
[2] Corresponding author: dtafti@exchange.vt.edu

1. Introduction

For many species of flying animals, agility in the air is an important component of survival. The ability to change direction rapidly is critical for capturing prey, avoiding predators, or navigating cluttered habitats. Agility or maneuverability encompasses the ability to rapidly initiate a turn, the ability to execute a turn within a tight radius of curvature, and the ability to re-orientate the body within a short duration of time. Depending on an animal's habitat and feeding behavior, various aspects of maneuverability may be more or less critical for that given species.

Bioinspired micro air vehicles (MAVs) incorporate structural and control components borrowed from flying animals with the objective of inheriting desirable flight capabilities—for example, speed, efficiency, quietness, endurance, durability, weight reduction, or agility. Bats in particular present a compelling model for an MAV which requires maneuverability as certain bat species are especially agile in the air. Bats that pursue maneuverable insect prey on the wing must be able to deal with evasive maneuvers. In addition, bat species living in cramped or cluttered environments such as winding cave passages or dense forests require exceptional maneuverability to navigate.

Prior research on bat flight aerodynamics has primarily focused on understanding different aspects of straight bat flight—specifically, wing and bone structure [1]–[4], efficiency and performance [5]–[10], kinematic complexity [11], [12], and wing aerodynamics [13]–[19]. While this research has provided tremendous insight into bat flight, straight flight is an atypical mode of flight for bats in their natural habitat. During flight, bats are primarily performing some form of maneuver. Although there are many inherent challenges to effective investigation of maneuvering bat flight, there have been a few studies focused on its understanding [20]–[24].

Norberg conducted a study in which two bats (the common noctule, *Nyctalus noctula*; and the large-eared free-tailed Bat, *Otomops martiensseni)* were filmed performing a 180° roll maneuver and a sideslip [20]. Since a single camera was used, no 3D kinematic data was generated. However, from the film, the bats were observed to initiate both maneuver types by pronation of one wing and supination of the other wing. In 1986, Aldridge conducted a study on bat maneuvering by recording the flight of six bat species in a flight tunnel outfitted with multiple cameras [24]. The body trajectories of several turns were reconstructed in 3D. Correlations were conducted between turning radius and morphological parameters of the bats.

Iriarte-Díaz and Swartz investigated 90° turns of fruit bats in an L-shaped tunnel with 3D motion capture [22]. From the detailed kinematic data, they were able to observe a combination of banking and yawing turn mechanisms. Various kinematic parameters were reported throughout the duration of the turn—specifically, vertical and horizontal stroke plane angles, body orientation angles, and angle of attack. Change in body heading was seen to occur primarily during the upstroke and appeared to initiate lateral redirection of the flight path.

Henningson et al. investigated basic sideways maneuvers of brown long-eared bat in a wind tunnel using particle image velocimetry (PIV) and 3D motion capture [23]. This method allows for coupled analysis of kinematics and aerodynamic force. Inside the wind tunnel, bats were enticed off their straight flight path by mealworms. This stimulus resulted in a mean lateral displacement over the course of several trials of 10.7 ± 0.97 cm from their straight flight path inside the wind tunnel. The resulting lateral velocity was 0.18 ± 0.04 m/s corresponding to a change in heading of 4°. Initiation of a given maneuver was more often observed during the upstroke than the downstroke and most commonly using asymmetries in drag/thrust than in lift. Time histories of wing amplitude, lift, thrust, wing length, angle of attack, and body orientation were reported for several successive turns.

These studies also outline some of the challenges for studying maneuvering bat flight. Specifically, the collection of flight kinematic data in a wind tunnel restricts the ability of a bat to perform turns with a significant change in bearing. The use of a static flight tunnel such as the one used by Iriarte-Díaz et al. [22] allows complex maneuvers to be observed; however this configuration does not allow for the use of PIV flow measurements. Numerical simulation of the flow using the wing kinematics as input provides a compelling option for the simultaneous analysis of kinematic and aerodynamic data during complex flight maneuvers, thus we have adopted a computational approach in the present study. Computational techniques are widely used in the study of insect flight aerodynamics and have been previously applied to bat fight in a few prior studies [12], [18], [19], [25], [26].

In this paper we identify the kinematic and aerodynamic mechanisms used by a great roundleaf bat (*Hipposideros armiger*) in a right turn ascending maneuver. Of particular interest is,

- How do force asymmetries arise?
- Are lift, thrust, or drag asymmetries more prevalent during the turn?

- Do kinematic and force asymmetries differ between the initiation of the turn and the remainder of the turn?
- Is the turn achieved primarily through banking, yawing, or a combination of both?
- Is the upstroke or downstroke more important in turning and what is the relative contribution of the two phases during the wingbeat cycle?
- What is the energy cost of turning and how does it differ from straight flight?

Investigation of these questions is accomplished by kinematic measurements of flight and detailed computational analysis of the aerodynamic forces generated during the turn compared to straight flight of the same bat under similar conditions. The wing kinematic data is collected in a static flight tunnel using 3D optical motion capture. The numerical simulations are run using the wing kinematic data as time-varying boundary conditions in order to calculate the air flow-field around the bat's wings. Aerodynamic forces and rotational moments are derived from the flow field and analyzed in both the global frame and in a body fixed local reference frame. Using this framework, we are able to investigate the underlying mechanisms causing the body rotations and turning force. The current method gives access to accurate spatially and temporally resolved force data on the entire surface of the wings at each moment throughout the maneuver.

The approach taken in the current study focuses on the detailed kinematic and aerodynamic mechanisms driving the observed turning ascending maneuver. In any study, there is a tradeoff between the number of samples studied and the detail of the investigation. For example, Norberg and Rayner (1987) studied 257 bat species, but only collected high level morphological data such as mass, wingspan, and typical flight velocity [27]. That approach is useful for making broad generalizations, but provides limited insight into the mechanisms bats use to fly. Iriaite-Diaz et al. (2008) studied four individual bats of one species executing 53 turning flights of 90° from a single bat species and collected detailed kinematic data [22]. This allowed for more detailed analysis of the turning kinematics, but was limited in scope to a particular bat species and a particular type of turn. In addition, no aerodynamic data was collected. Henningsson et al (2018) collected kinematic and aerodynamic data over ten flights of bats executing a 4° sideways maneuver—this approach yielded even more detailed insight on the maneuvering mechanisms, but was more limited in generalizability due to the single bat species studied and the limited range of maneuvers observed [23]. Our study exists at the far end of this spectrum by providing a high level of both kinematic

and aerodynamic detail to robustly examine the turning mechanisms used by the bat, but is limited in generalizability due to single bat used and the sample size of the flights examined in this study.

2. Methods

Kinematic data collection was conducted using an optical 3D motion capture setup inside an open-ended 1.2 m × 1.2 m flight tunnel. Inside the tunnel, 28 synchronized video cameras (GoPro Hero4 Black) recorded the bat flying through the tunnel performing different types of flight maneuvers. Recording was conducted at 120 frames per second and in 1920 × 1080 resolution. The camera calibration was conducted using the Svoboda multi-camera self-calibration method [28]. Additional details related to the motion capture setup are outlined in our prior paper [12].

In the present study, the subject was an adult male great roundleaf bat (*Hipposideros armiger*) with a mass of 54.5 g and a wingspan of approximately 52 cm. *H. armiger* is a large insectivorous bat that occurs in parts of South, Southeast, and East Asia. Before and after data collection, the bat was housed in a large climate controlled aviary with a group of other individuals. Ethical housing and handling procedures were followed under oversight from Virginia Tech's Institutional Animal Care and Use Committee (protocol number 15-067).

During data collection, 240 small white non-toxic markers (approximately 3 mm diameter) were affixed to the bat's wings and tail for 3D tracking. The resulting reconstructed points are shown at one instant during a representative downstroke in Figure 1a. Of several recorded flights, a sweeping turn (68 video frames), and a straight section of flight (42 video frames) were selected for detailed analysis. Stereo triangulation was performed using a custom MATLAB code to achieve (240 points)×(68 frames) = 16,320 total 3D points for the turning flight, and (240 points)×(42 frames) = 10,080 total 3D points for the straight flight. Occlusion of a point in all cameras simultaneously was very rare (0.37% in the turning flight, and 0 in the straight flight), but when no 3D point was reconstructed the point was filled using a temporal spline curve. The low rate of occlusion was due to the large number of cameras capturing many perspectives of the bat wings at each frame. 3D reconstruction of the kinematic data from the video frames was conducted using a MATLAB code in which point correspondences were defined using a hybrid of manual and automatic techniques—specifically, the correspondences were initially predicted using several different prediction methods and correctness was verified manually by a researcher. The basic

prediction scheme involved fitting periodic functions to the wing points in spherical coordinates using kinematic data generated from a previously analyzed flight. Then a spatially recursive method was used to fit the new wing data starting with the body trajectory, moving to the bones, and finally the membrane.

Characterizing error in the kinematic data is challenging as there is no known ground truth values for comparison. One method to provide validation of the 3D point reconstructions was to calculated the length of the relatively rigid forearm bone over the course of each flight. The distance between the elbow joint and the wrist join approximates this bone length and was found to be 87.40 mm ± 0.26 mm for the right forearm and 85.94 ± 0.43 mm for the left forearm. The low standard deviation between temporal measurements provides confidence in the fidelity of the reconstructions. The difference between the right and left wing was 1.46 mm and was likely due to the precise placement of the white markers on the wings which have a diameter of 3.0 mm. That is, the difference between the right and left wing measurement was just half the diameter of the markers themselves. In addition, the validation of the forces (Section 3.3) provides indirect validation of the kinematic data since the kinematics are an input to the force calculation. Error in the kinematic data would be amplified in the resulting force calculations, so kinematic error is bounded as some smaller subset of the force error.

2.1 Reference Frames

Two reference frames were defined for the purpose of analyzing maneuvering bat flight—a global ground-fixed frame and a local body-fixed frame. Robustly defining these coordinate systems is critical for subsequent kinematic and aerodynamic analysis since the stroke plane, angles of attack, and local aerodynamic forces and moments are calculated relative to the time varying body-fixed frame. The ground coordinate system $\langle x_g, y_g, z_g \rangle$ is a fixed, inertial reference frame defined relative to the physical orientation of the flight tunnel and gravity. In the ground frame, x_g points axially along the tunnel, z_g upward (opposite gravity), and y_g points laterally, normal to x_g and z_g.

A second body-fixed frame, $\langle x_b, y_b, z_b \rangle$ is defined relative to the bat body, and moves with the bat as it flies as shown in Figure 1b. Since the bat accelerates and turns during flight, the body-fixed frame is non-inertial. The origin of the body frame, $\langle x_b, y_b, z_b \rangle$, follows the approximate center of mass of the bat. The basis vector y_b points laterally towards the left wing.

Mathematically, it was defined as the mean of three unit vectors, 1) pointing from the right wingtip to the left wingtip, 2) pointing from the right wrist to the left wrist, and 3) pointing from the right elbow to the left elbow. The basis vector, x_b, was defined as a vector pointing along the axis of the body nominally in the direction of forward flight. Specifically, x_b points from the mean of the two hip points and the tail base towards the mean of the two shoulder points and the neck point—additionally, this vector was projected into a plane normal to y_b to enforce perpendicularity between the basis vectors x_b and y_b. The third basis vector z_b was defined as the cross-product of x_b and y_b and nominally pointed upward. Thus, all three basis vectors were unit length and mutually orthogonal and conformed to the right-handed convention as depicted in Figure 1b. Euler rotations about the body fixed axes are designated as roll, pitch, and yaw as shown in Figure 1b. Note that pitching up is defined as a negative pitch angle since it is a rotation about the y_b axis.

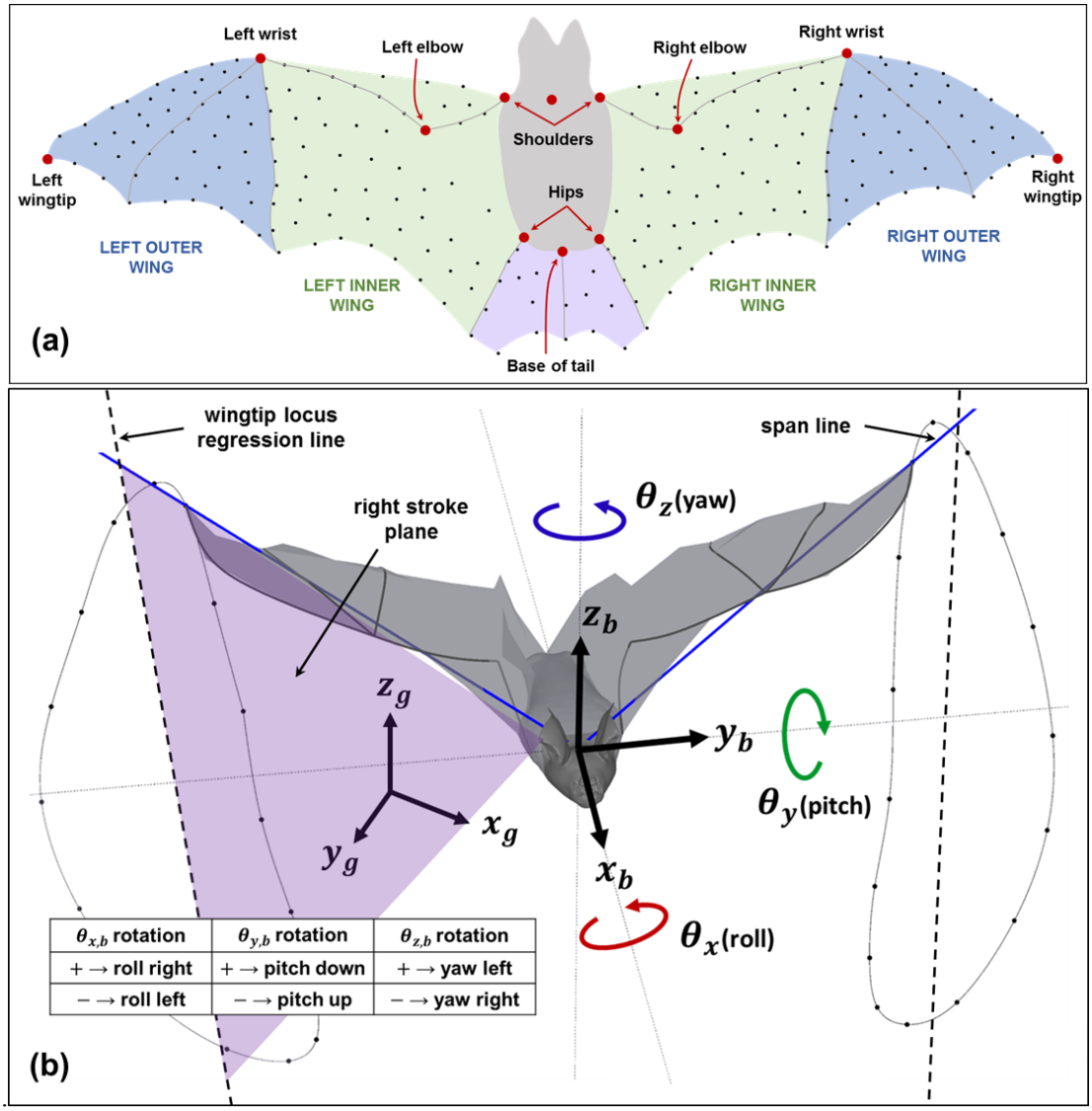

Figure 1. (a) Each of the 240 marker points are represented by black dots. Key points are indicated by red dots and labeled accordingly. The total wing surface is divided into inner wing, outer wing, and tail as shown. (b) The bat is shown oriented in the body-fixed coordinate system at an arbitrary point during the flight. The span line connects the shoulder and wingtip and is represented in blue. Two regression lines are fit through the right and left wingtip loci, and are used to define the respective stroke plane. Rotations about $\theta_{x,b}, \theta_{y,b}, and\ \theta_{z,b}$ are designated as roll, pitch, and yaw respectively.

2.2 Kinematic Analysis

In the present study we focus on key kinematic parameters—the vertical and horizontal stroke plane angles, the flap angle, and the stoke plane deviation angle. These four parameters provide an organized summary of highly complex configurations which a flexible bat wing can effectuate.

i. The stroke plane is defined as the plane formed by a linear regression line passing through the loci of wing tip points from a complete wingbeat cycle and the root of the wing. A

separate stroke plane is calculated for the right and left wings using the respective right and left wingtip loci. The vertical stroke plane angle is defined by projecting the regression line onto the body-fixed $x_b - z_b$ vertical plane and is the angle between the line and the x_b axis. The vertical stroke plane angle varies from 0 to 90 degrees where higher angles support more thrust generation and lower angles support more lift production. Additionally, a new vertical stroke plane is calculated each wingbeat cycle, thus it is a time-varying parameter.

ii. The horizontal stroke plane angle is defined by first projecting the wingtip locus regression line onto the body-fixed $x_b - y_b$ plane. Then the angle between the projected regression line and the x_b axis is taken as the horizontal stroke plane angle, and is representative of the lateral movement of the wingtip. This angle also varies between 0 and 90 degrees and controls the lateral direction of the thrust/drag force. Symmetric horizontal stroke planes angles are associated with straight flight, while asymmetries in the right and left horizontal stroke planes will generate asymmetries in force.

iii. The flap angle of each wing is calculated by projecting the time-varying spanline onto the stroke plane and calculating the angle between the spanline projection and the body-fixed $y_b$axis.

iv. The stroke plane deviation angle is calculated as the angle between the actual spanline and the projection of the spanline onto the stroke plane. The stroke plane deviation angle is calculated separately for each wing and varies smoothly over the wingbeat cycle. Positive values of stroke plane deviation represent the wingtip moving in front of the stroke plane, while negative values represent the wingtip moving behind the stroke plane. Since the respective stroke planes cut through the middle of the right and left wingtip loci, the values nominally oscillate around a zero mean.

2.3 Aerodynamic Analysis

After the collection of kinematic data, aerodynamic flow simulations were conducted using the incompressible Navier-Stokes (N-S) solver, GenIDLEST [29]. The immersed boundary method (IBM) was used to impose moving boundary conditions representing the wing kinematics. In the IBM, a surface mesh is embedded in the background fluid grid and represents the location of the wing in the airflow. At each integration time step, the location of the wing mesh is updated

based on the motion of the wings. During the solution of N-S at each time step, a no-slip velocity boundary condition is imposed at the location of the embedded wing mesh. Validation of the general IBM implementation within the flow solver was robustly conducted in a prior study [30], and has been successfully used in several other subsequent studies investigating a wide range of flow conditions. Further details about the computational setup, including a grid independence study, are discussed at length in the author's recent prior works [18], [19]. In the present work, a grid containing 62.9 million fluid cells was used, in which the grid cell size in proximity to the bat wings had an edge length of chord/46. That is the mean chord distance spanned 46 fluid grid cells. The simulation was run in a moving reference frame which followed the mean velocity of the bat at a fixed velocity. Thus, the reference frame did not accelerate or rotate but remained inertial. This caused the bat wings to remain nominally near the middle of the fluid domain and only translate based on perturbations from the mean flight velocity. Since the bat was moving nominally forward and upward, the moving reference frame had a predominately forward velocity and a smaller upward velocity. In the simulation reference frame, the orientation was rotated about the simulation z-axis such that the initial and final x-position of the body was zero. In post-processing, the moving reference frame velocity was added back and the data was rotated back into the (x_g, y_g, z_g) global reference frame for analysis.

Additionally, we previously established that we had a sufficient resolution of the wing kinematics, by calculating the sensitivity of the simulation results to the number of kinematic markers used during motion capture [12]. For the present study, verification of the model was performed by comparing the simulated aerodynamic loads to the expected loads based on the observed flight trajectories (see Section 3.3). This analysis bounds the total force error which is made up of error resulting from kinematic error and numerical error from the grid discretization. Prior analysis has indicated that the kinematic error dominates the total error and that the numerical discretization error is approximately an order of magnitude smaller in most cases. This is because driving down numerical error is relatively straight forward and is achieved by refining the grid to the level we selected. However, bounding the total error is of greater importance for reliability of the results, so this was the focus of our validation for this particular study.

3. Results

The results from two separate flights are presented and contrasted here—the first flight is a straight and mostly level flight consisting of 2.5 wingbeat cycles (42 video frames), and the second flight is a turning flight consisting of 5 wingbeat cycles (68 video frames). While our primary interest is on the maneuvering flight, the straight flight is provided to establish a baseline for nominal flight behavior. Since bats are living animals, there are always small irregularities in wing motion from flap to flap. Comparing the turn to a straight flights allows us to distinguish between the significant differences between the two flights while ignoring the small irregularities.

3.1 Morphological Parameters

A single individual was used for both the straight and turning flights to allow a direct comparison between the two modes of flight without introducing extraneous variables. Measurements of the morphological parameters of the bat are provided in Table 1. The span is measured as the maximum wingtip to wingtip distance averaged over the several wingbeat cycles. The wing area is the maximum total surface area during the downstroke also averaged over the several wingbeat cycles. The planform area is the area of the wing projected onto the local body-fixed $x_b - y_b$ plane. The three derived parameters are calculated using the standard definitions—mean chord is planform area over span; aspect ratio (AR) is span squared over planform area; wing loading is weight over planform area. The species used in the present study was larger in both mass and wingspan when compared to prior work on maneuvering bat flight by Iriarte-Díaz et al. (mass of ~33 g), and Henningsson et al. (mass of ~10 g), [22], [23].

Table 1. Morphological parameters of the subject.

Mass (g)	Span (cm)	Wing Area (cm^2)	Planform area (cm^2)	Mean chord (cm)	AR	Wing loading (N/m^2)
54.5	51	434	398	7.8	6.5	13.4

3.2 Quantitative Description of Flights

The body trajectory of both the straight and turning flights are shown in Figure 2. During the turning flight, the bat first displaces very slightly to the left by 1-2 cm, and then enters the sweeping right turn during the second flapping cycle. Over the course of the flight the bat travels

approximately 80 cm and travels laterally by about 32 cm. The bat slightly descends for one and a half wingbeat cycles before climbing increasingly steeply for the latter two thirds of the flight especially during the fourth and fifth flap cycles. During the straight flight, the bat does not displace at all laterally, but descends by about 11 cm.

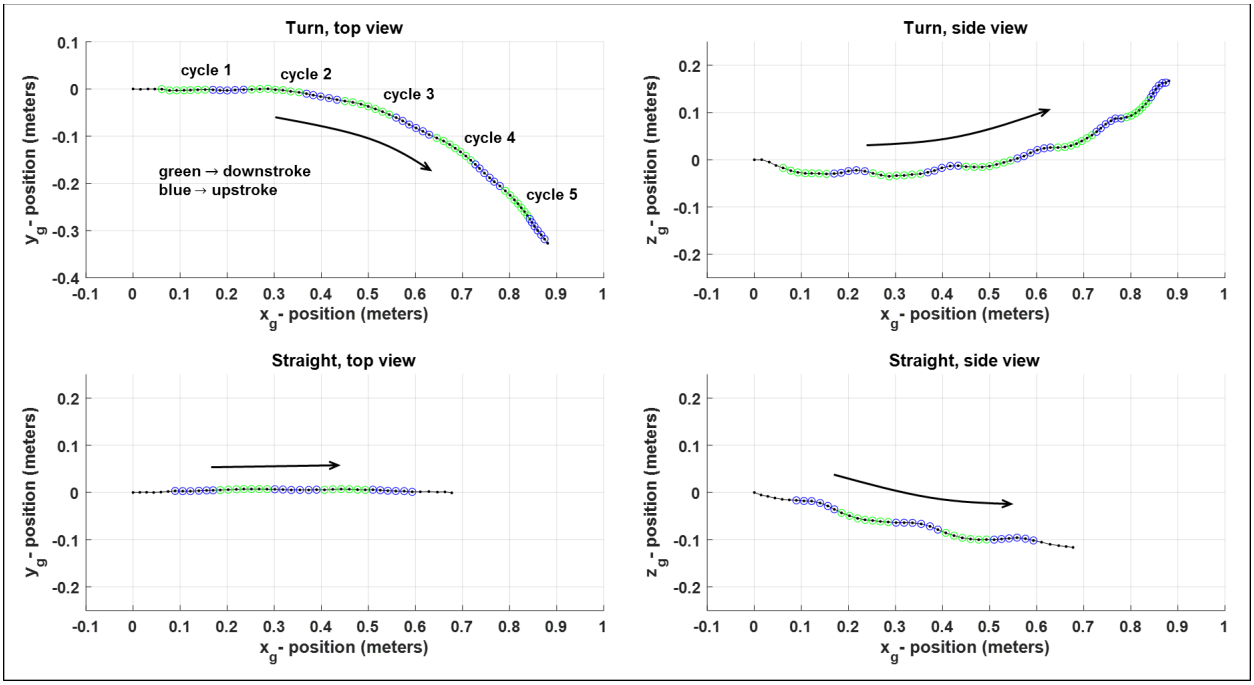

Figure 2. Trajectories of the two flights projected onto the ground frame $x_g - y_g$ plane (top view) and the $x_g - z_g$ (side view) plane. Each dot represents one frame of the video recording. For both flights, the flight begins at the global origin (0,0,0).

The flight parameters for the two flights are provided in Table 2. The wingbeat frequency does not differ much between the two flights, although it is about 3% higher in the turning flight. During each of the two flights, the wingbeat frequency remains relatively constant—a plot of the temporal variation of the wingbeat frequency for each flight is provided in the supplementary information (Figure S1). The bat is flying about 10% faster in the straight flight and also is accelerating, while during the turning flight the bat is decelerating along its curved path. The 1.81 m/s mean turning flight velocity in the present study was similar to the 2.0 m/s mean velocity observed by Iriate-Díaz et al. during 90 degree turns of a fruit bat, as well as the wind tunnel velocity of 2.5 m/s used by Henningsson et al. when studying maneuvers of a brown long-eared bat [22], [23]. The similarity in observed velocity between the bats in prior works and the present study eliminates nominal flight velocity as a differentiating factor when comparing turning

mechanics between studies. Although the flight velocities are similar, other parameters such as body mass, wing aspect ratio, and wing loading may factor into the comparison, so generalization should be approached cautiously. The velocities provided for the present study are not intended to be generalizations for the particular mode of flight observed—straight or turning. Both straight and turning flight can be executed at a wide range of velocities.

Table 2. Flight parameters for the straight and turning flights.

	Wingbeat frequency (Hz)	Flight duration (s)	N wingbeat cycles	Mean velocity (m/s)	Mean acceleration (m/s^2)
Straight Flight	9.4	0.342	3.2	2.02	0.76
Turning Flight	9.7	0.558	5.4	1.81	-0.86

3.3 Flight Kinematics

The wing kinematics—defined as the time-varying shape and orientation of the bat wings—fully encompass the mechanisms by which a bat generates lift and thrust to stay aloft as well as the forces and moments which allow it to turn. In order to present the kinematic data in an organized format, several parameters which were derived from the wing motion are provided. The wings flap such that the right and left wing tips nominally fall within two planes—the right and left stroke planes. The orientation of these planes control the approximate direction of forces generated by each wing and are described by the vertical and horizontal stroke planes angles (as defined in Section 2.2).

The vertical and horizontal stroke plane angles for the two flights are shown in Figure 3. During the straight flight, the vertical stroke plane angle is approximately 40 degrees and is symmetric between the right and left wings. This value is quite close to what was reported by Sekhar et al. for a Pratt's roundleaf bat (*Hipposideros pratti)* in straight flight ($\gamma_v = 53°;\ m = 55\ g;\ span = 52\ cm$) [19], and Iriarte-Díaz et al., for a lesser short-nosed fruit bat (*Cynopterus brachyotis*) performing a 90 degree turn ($\gamma_v = 52.7°;\ m = 32.8\ g;\ span = 23\ cm$) [22]. Since the bat was descending slightly during the straight flight, gravity can augment thrust production and a priority can be given to lift resulting in a marginally lower vertical stroke plane angle. During

the turning flight, there is slight asymmetry in the vertical stroke plane angle between the wings during the initial two wingbeat cycles with a minimally larger stroke plane angle for the right wing.

With regard to the horizontal stroke plane angle, again approximate symmetry can be seen during the straight flight; however during the turning flight, the left horizontal stroke plane angle is substantially larger than the right. During the turning flight, the left horizontal stroke plane angle varies between 75 and 80 degrees, slightly larger than both wings during the straight flight, while the right wing has a much lower angle between 40 and 65 degrees. A similar phenomenon was observed by Iriarte-Díaz et al. in which they identified that the horizontal stroke plane angle between the right and left wings differed substantially during a 90 degree turning flight [22].

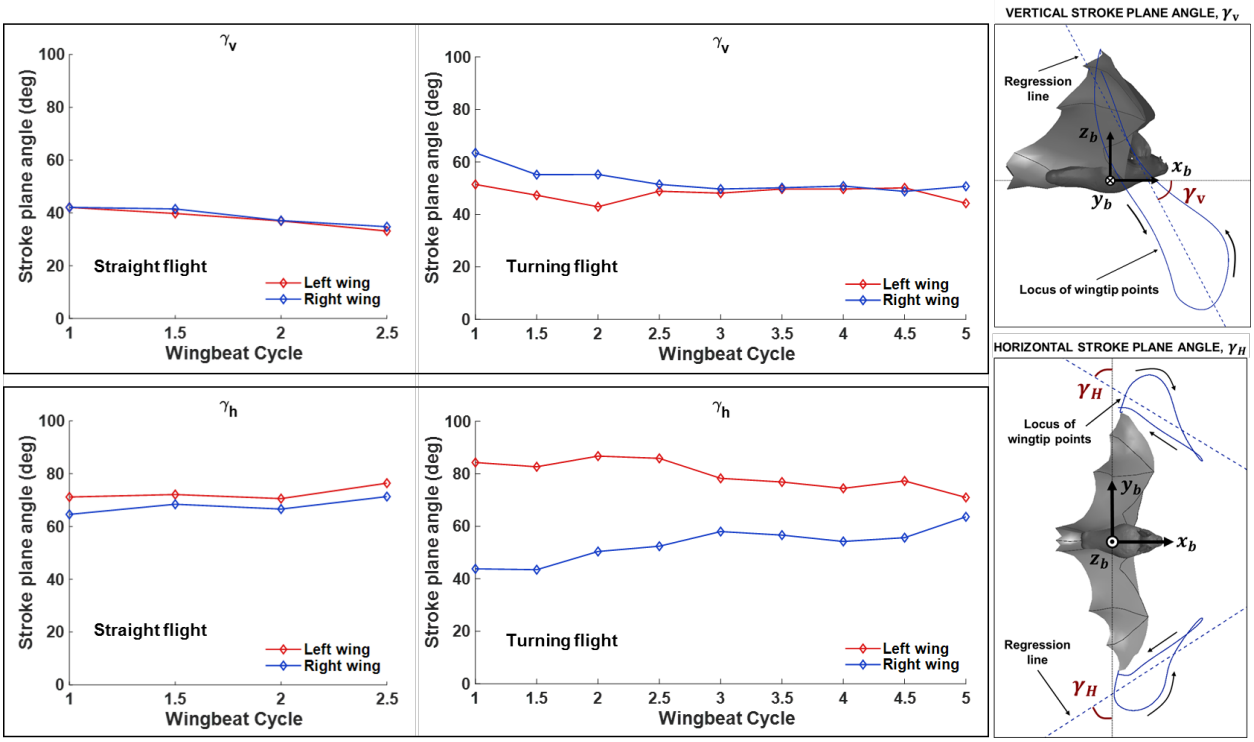

Figure 3. The vertical and horizontal stroke plane angles for the right and lefts wings are shown for the straight and turning flights. The stroke plane is defined at each half-stroke of the flight.

Wing motion relative to the stroke plane is captured in the wing flap angles, stroke plane deviation angles, and half-span distance. These parameters are shown for the two flights in Figure 4. During the straight flight, the wings flap between approximately -50 degrees and 50 degrees with close symmetry between the right and left wings. During the turn, the right wing has a greater flap angle amplitude by 10 to 20 degrees manifesting during the transition between the upstroke

and the downstroke. While the flap angle measures the orientation of the wing inside the stroke plane, the stroke plane deviation angle measures the degree to which the wing flaps outside of the stroke plane. The stroke plane deviation angle varies between -10 and 10 degrees during the straight flight with the greatest deviation occurring during the upstroke. During the turning flight, the right wing experiences larger positive deviation during the mid-upstroke. Directly comparing the two flights, there is minimal difference between the two wings during the straight flight—in contrast, the right wing deviates substantially from the stroke plane compared to the left wing during each mid-upstroke of the turning flight.

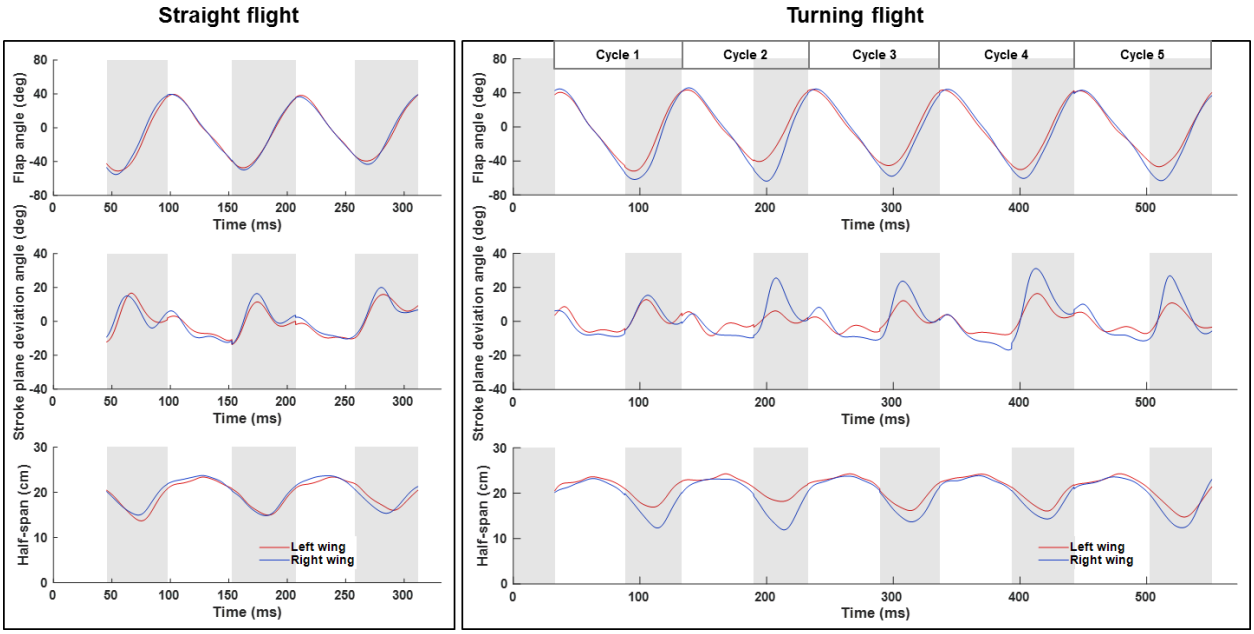

Figure 4. The wing flap angle, stroke plane deviation angle, and the half-span are shown for the right and left wings for the straight and turning flights. The upstroke is designated by the shaded regions, while the downstroke is designated by white.

The half-span, measuring the instantaneous distance between the shoulder and respective wing tip, varies between 12 and 22 cm for both the straight and turning flights. During the downstrokes, the half-span is maximum and relatively constant. As the wings pull inward and rotate during the upstroke the half-span drops by around 50%. In turning flight, during the first two flapping cycles, the half span of the right wing is notably smaller than the left wing indicating the right wing tip is retracted much closer to the body during the upstroke. As the bat settles into the turn, the differences reduce in magnitude but still persist.

A more holistic comparison of the kinematic variations between straight and turning flight can be made by comparing the trajectory of the wrist and wing tip points projected on to the body-coordinate planes in Figure 5. At the initiation of the turn during cycle-2, the right wing has a much broader sweep area in the $(y_b - z_b)$ plane than the left wing. While the lateral extension of both wings during the downstroke, as indicated by the wrist and wing tip, are the same, the left wing does not retract towards the body as much as the right wing which retracts more than what it would normally do in straight flight. This is supplemented by the left wing limiting the forward movement of the wing tip during the upstroke and the right wing extending further out ahead of the body than normal (see projection in $x_b - z_b$ plane). Collectively, the wing motions translate to the larger stroke plane deviation of the right wing during upstroke, the smaller horizontal stroke plane angle of the right wing, and the smaller half span of the right wing during the upstroke in Figure 4. Other flapping cycles are shown in supplementary Figure S2. It is noted that as the bat proceeds into the turn, the right wing tip maintains nearly the same trajectory, while the left wing trajectory approaches that of straight flight.

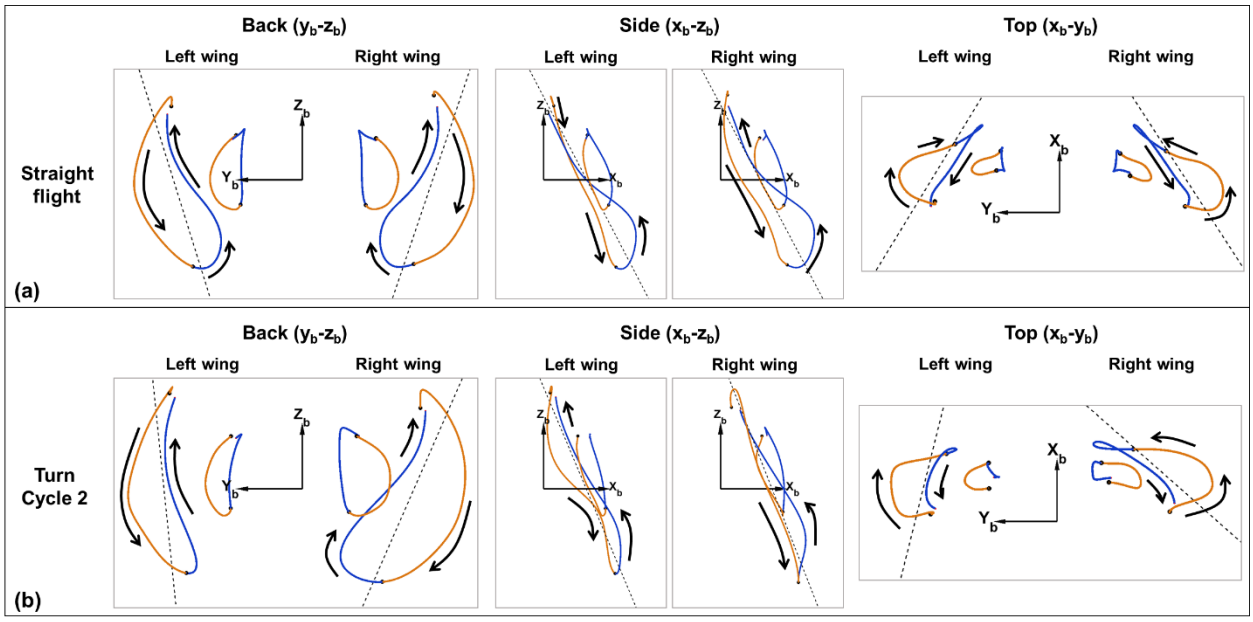

Figure 5. Comparison of wrist and wingtip trajectories for straight flight (a), and flap-2 of turning flight (b). The downstroke is designated by orange, and the upstroke is designated by blue. The wingtip locus regression line used to define the stroke plane is shown by the dashed line in each sub figure.

3.4 Aerodynamic Simulation Results

Two aerodynamic simulations were run, one for each flight using the previously described computational scheme. The aerodynamic force of the air on the bat wing is derived from the pressure and velocity fields from the simulation output. The normalized aerodynamic force coefficients for both the straight and turning flight are shown in Figure 6 in the body-fixed frame. The normalization of the force was done using the following equation,

$$C = \frac{F}{\frac{1}{2}\rho {U_\infty}^2 S}$$

where ρ is the air density, U_∞ is the mean flight velocity, and S is the maximum planform area. The body frame allows analysis of the lift coefficient ($C_{z,b}$), thrust coefficient ($C_{x,b}$), and lateral force coefficient ($C_{y,b}$) regardless of the global orientation of the bat. The body frame x_b-direction is aligned with the direction of the bat's body, thus the x_b-component of the force is the net of thrust ($+x_b$) and drag ($-x_b$). It is noted that even in level flight the body orientation does not coincide with the forward velocity vector. The forces plotted are only the aerodynamic forces and exclude the gravitational force on the bat's body.

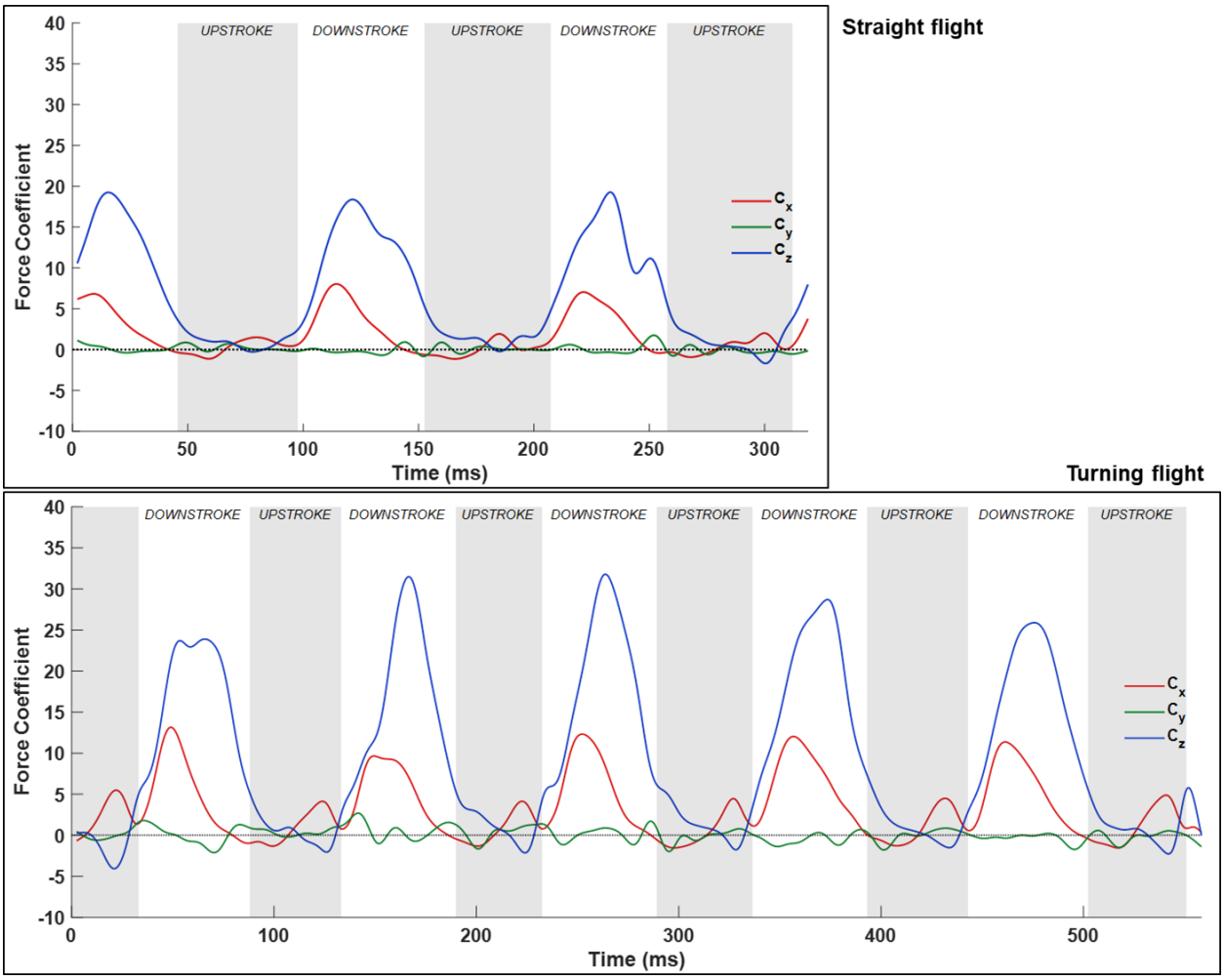

Figure 6. Normalized force coefficients for the straight and turning flights in the body-fixed frame.

The z_b-component of the force can be seen to be substantially larger than the other two components in order to support the weight of the bat. If the bat is flying perfectly level, the cycle averaged lift should be equal to the bat's weight. Examining $C_{x,b}$ for each of the two flights, a positive value (thrust > drag) persists during the downstroke of each flight. During the straight flight, the bat is accelerating thus $C_{x,b}$ must be positive. In contrast, during the turning flight the bat is decelerating; however, since the bat is climbing as well as turning, a positive thrust force must be generated to oppose gravity. Since the bat is decelerating, the gravitational force is overwhelming the thrust force despite the thrust being larger than drag throughout the turn. A trend in thrust production across the two flights is that the maximum in thrust production precedes maximum lift production at the middle of the downstroke. Because of the articulated wing rotation

and inward folding of the outer wing, a positive lift force is maintained for most of the upstroke while some drag is experienced at the beginning of the upstroke.

The lateral force in the body frame, $C_{y,b}$, is nearly zero for both flights. This is expected for the straight flight since there should be no net lateral force. However, the lack of lateral force in the turning flight is unexpected—$C_{y,b}$ oscillates around zero, but has a very small cycle averaged value. This suggests that turning is achieved by a reorientation of the body thus redirecting the lift and thrust as opposed to a lateral force being generated in the body frame. In order to determine the precise mechanism of turning, examination of the force moments as well as the forces acting on different locations of the wing is required.

As described in the Methods section, the numerical solver used in the present study has been evaluated for simulating bat flight in several prior studies [12], [18], [19]. However, in order to establish confidence in the aerodynamic forces calculated for this particular study, a straight forward lumped mass dynamics analysis was conducted. From Netwon's second law, acceleration of the bat is the net force divided by mass. For this analysis, the bat is approximated as a point mass and the forces are obtained from the numerical flow simulations. Integrating the predicted time-varying acceleration twice provides predicted position. That is, we get the expected path of the bat's body (given the simulation results) which can be compared to the observed path of the bat from the motion capture data. The results are shown in Figure 7.

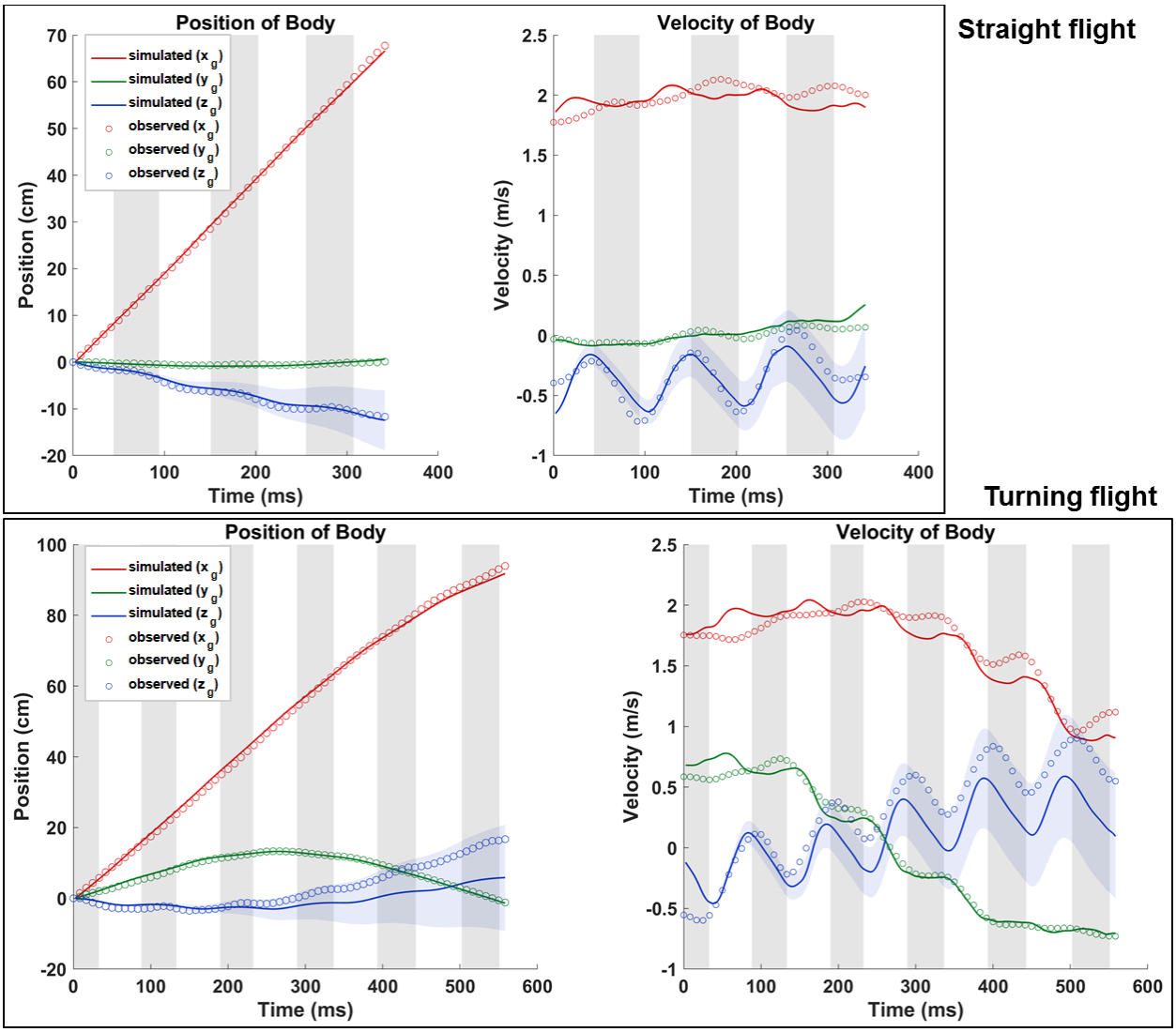

Figure 7. Lumped mass dynamics validation for straight and turning flight. The shaded region around the z-direction estimate represents a ±10% force band.

Good comparison between the predicted and observed values can be seen for the straight flight in all three directional components over the duration of each flight. Due to inertial oscillation of the wings, the trajectories will not necessarily match within a single wingbeat cycle, but should match over several wingbeat cycles. The reason for the difference is that the simulated trajectory tracks the center of mass while the observed trajectory tracks a fixed point on the center of the bat's body which approximates the center of mass. As the wings flap, the center of mass can oscillate due to changes in inertia of the wings. However, the mean trajectory measured over several wingbeat cycles is dictated by external influence only, namely the aerodynamic force. For

the turning flight, the x_g- and y_g-components closely match the observed values of velocity and position. In the z_g-direction, the under prediction of the vertical velocity and consequently the vertical position indicates that the z_g-direction force is under predicted by the simulation model. Since the velocity and position are calculated via temporal integration of acceleration, any discrepancy between the observed and predicted values will accumulate in time. In order to illustrate this effect, a shaded blue region is shown which encompasses the possible positions and velocities admitting to a possible ±10% over or under prediction of z_g-direction force. Since the observed position and velocity is within this envelope, we can conclude that the under prediction of z_b-force by the model is limited to 10%. The 10% bound value was selected based on a survey of literature on this specific topic. Calculating the force generated by live flying animals with complex wing structures and wing motion has been demonstrated to have many potential sources of error [31]. The challenge of precisely measuring force in flying animals was investigated by Gutierrez et al., in which they found that measured lift, when compared to the animal weight, routinely deviated ±10% from expected values across over 40 studies (though often up to ±20%) [23], [31]. Based on review of this meta-analysis, we selected 10% as a reasonable and acceptable bound for our calculated forces.

3.5 Turning mechanics

In order to initiate and sustain a turn, a bat must generate a force directed towards the center of the radius of the turn. In order to illustrate this mechanism, the net force vector was broken into three perpendicular components which are plotted in Figure 8 on a half-cycle averaged basis. When the force and flight trajectory are projected onto the horizontal $x_g - y_g$ plane the components directed tangentially to the flight path and radially to the flight path can be calculated. The third force component, the vertical force, is normal to the $x_g - y_g$ or alternatively parallel to the z_g-axis.

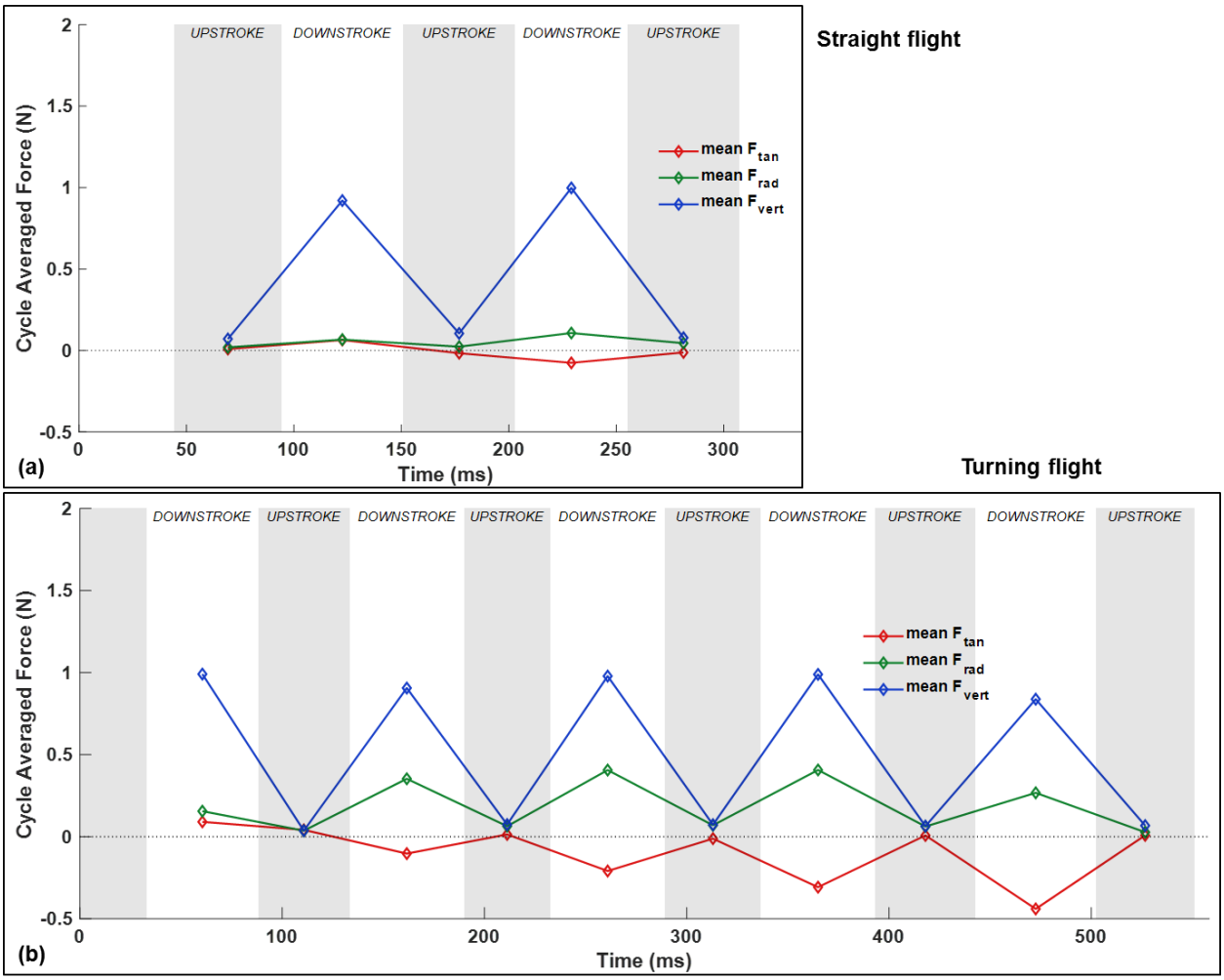

Figure 8. Cycle-averaged force components from the straight flight (a) and turning flight (b) oriented tangent to the flight path (red), radially towards the inside of the turn radius (green), and vertically aligned with the gravity vector (blue).

A positive tangential force will accelerate the bat along the flight path, a positive radial force will cause the bat to turn tighter or more gradually depending on the magnitude, and a positive vertical force is necessary to keep the bat aloft. During the first downstroke the tangential force is positive corresponding to the slight acceleration observed in the beginning of the flight. The subsequent four downstrokes show increasingly negative tangential force matching the deceleration into the turn from 2.1 m/s down to 1.6 m/s. Peak radial force was observed during the third and fourth downstrokes where the radius of curvature of the turn was tightest. The radial force magnitude can be estimated based on the expected centripetal acceleration,

$$F_{rad} = m\,a_c = \frac{m{v_{tan}}^2}{r} \approx \frac{(0.0545\ kg)\left(1.7\frac{m}{s}\right)^2}{0.8\ m} = 0.2\ N$$

where m is the total bat mass, a_c is the centripetal acceleration, v_{tan} is the approximate flight velocity magnitude averaged over the portion of the flight where the turn is the tightest, and r is the approximate radius of curvature averaged over the same timeframe. Although the bat is not in a steady state, constant velocity turn, this calculation provides an estimation of the anticipated radial force. From Figure 8 it can be seen that the radial force is about 0.05 N during the middle two upstrokes and 0.4 N during the middle two downstrokes averaging to about 0.2 N providing adequate turning force to the bat. The half-cycle mean forces provide the clearest visualization of the radial turning force; however, the transient force curves are also provided in supplementary Figure S3.

The net radial force provides a satisfactory explanation of how the bat follows a curved trajectory during the turn, yet the cause of the radial force requires deeper investigation. The most significant driver of the direction of the net force vector is the rotational orientation of the bat in space. The angular rotation of the bat throughout the turning flight is represented as the relative orientation of the local body-fixed frame to the ground described by three Euler angles—the roll, pitch, and yaw as shown in the schematic in Figure 2b. The two main results of the bat changing its angular orientation in space is to redirect the forward flight path in a new direction (through yaw), and re-orienting the force vector to achieve a radial acceleration (through roll). Since pitch is defined as rotation about the y_b-axis, negative values represent pitching upward.

A subtle but important distinction should be made between the orientation of the bat's body, and the direction in which it is flying. Especially during turning flight, deviations may exist between the instantaneous flight velocity vector and the long axis of the bat's body, x_b. That is, the flight direction does not always perfectly coincide with the direction the bat is facing. For this reason, it is necessary to introduce two additional angles, bearing angle and climb angle, which describe the direction of the flight velocity vector. The bearing angle is defined as the angle between the bat's initial flight direction and its current flight direction both projected on the horizontal $x_g - y_g$ plane. It differs from the heading or yaw in that it is based on the flight direction, not the orientation of the bat's body. The difference between the heading and bearing

angles can be important for understanding turning mechanics. The climb angle is simply the inclination of the velocity vector with respect to the horizontal.

Figure 9 shows both the Euler rotation angles of the bat's body (roll, pitch, and yaw) along with the orientation of the velocity vector (bearing and climb angle). The negative pitch angle, referred to as the "elevation", is presented in place of pitch for clarity such that positive values represent an upward inclination of the body. The last angle reported is the bank angle which is closely related to the roll angle except that it is defined as the absolute angle between y_b and the horizontal, and is not an Euler angle. Euler rotations are applied sequentially such that the roll angle contains effects of the pitch and yaw whereas the bank angle does not. At small pitch angles, the roll and bank angles will be nearly identical as is found in the early part of the turning flight and throughout the straight flight.

A persistent difference exist between the elevation angle of the bat's body and the inclination angle of the velocity vector, such that the body orientation of a level flying *H. armiger* bat (horizontal velocity vector) is inclined upward at about 20 degrees. The data show a relatively constant 20 degree offset in the elevation angle such that, for example, the bat climbing at 10 degrees will have an elevation angle of about 30 degrees. Figure 9 shows a -10 degree climb angle (equivalent to 10 degree descent) in the straight flight corresponding to a body elevation angle of about 10 degrees of upward pitch. The climb angle during the turning flight varies from -20 to 30 degrees corresponding to body elevation angles between 0 and 50 degrees. During both the straight and turning flights, within a single wingbeat, a strong and persistent trend was observed that the bat pitches up during the downstroke and pitches down during the upstroke. To achieve a climb, the downstroke upward pitching must exceed in magnitude the upstroke downward pitching, which is indeed observed in the present data.

As previously illustrated in the radial force data, the bat is achieving a turn by reorienting the net force vector through body rotation. While the most obvious way to tilt the force vector laterally is through banking, a combined yaw-bank maneuver is even more effective. A roll with zero yaw can effectuate a gradual turn, but does not optimally redirect the net force vector for a tight turn—conversely with roll and yaw the center of the radius of the turn will be shifted back resulting in a tighter turn. Yaw in absence of roll is also suboptimal since the lift force would remain vertical and only the smaller thrust force would have a radial component. In the actual turn we see the combined synergistic effect of yawing and rolling. Yaw is especially important in the

early stage of the turn since subsequent roll is performed around a rotated axis. When observing the overhead flight trajectory of the turn (i.e. in Figure 2), at first glance it seems that the bat is not yawing in the early stage of the turn. However, by comparing the bearing and heading curves in Figure 9, it can be seen that the heading of the body (yaw angle) in fact changes rapidly towards the inside of the turn (to the right) during the first one and a half wingbeat cycles despite the bearing angle remaining close to zero. The roll angle during the turn increases rapidly during the first wingbeat cycle to around 25 degrees and is sustained throughout the remainder of the turn. Once substantial banking is reached at the end of the second cycle, the bearing angle aligns with the heading. Thus, the yaw angle appears to augment the impact of the bank, and would be rather ineffective alone without banking. Once into the turn, the roll and bank angles remain nominally constant at about 20 degrees with a very gradual straightening out. Similarly, the heading and bearing remain aligned (velocity vector and body orientation) till the start of the fifth flapping cycle when the bat enters into a steeper climb, during which the bearing (velocity) deviates from the heading.

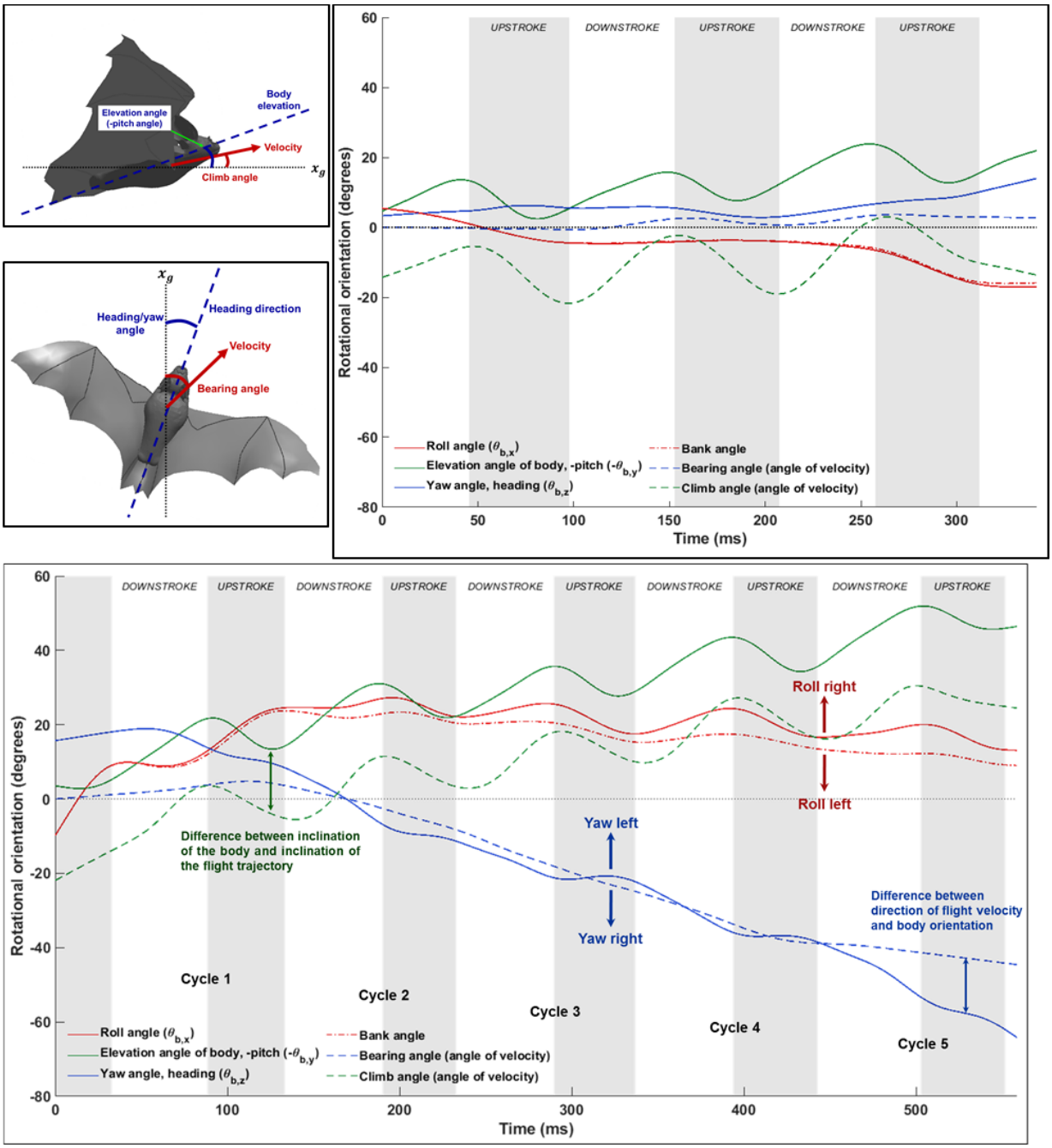

Figure 9. The angular attitude of the bat's body relative to the ground for the straight flight (top) and the turning flight (bottom) are shown. The slope of each line indicates the angular velocity while the concavity indicates the angular acceleration.

Thus far, it has been shown that the bat achieves turning by generating a lateral force resulting in centripetal acceleration. The lateral force arises from a re-orientation of the net force vector by combined yawing and banking body rotations. In order to provide insight into the cause of the body rotation, force asymmetries between the right and left wings can be investigated. Prior

work on flapping flight maneuvering has identified several possible mechanisms for generating body rotations—namely, lift imbalance during the downstroke, thrust/drag imbalance during the upstroke, and thrust/drag imbalance during the downstroke [23]. The aerodynamic simulations conducted in the present study provides, for the first time, the full spatial variation of force on the bat's wings during a maneuvering flight. In Figure 10, the aerodynamic forces in the body-fixed local frame are shown separated by net force on each of the right and left wings, as well as net force acting on the inner and outer region of each wing as specified in the schematic in Figure 1a.

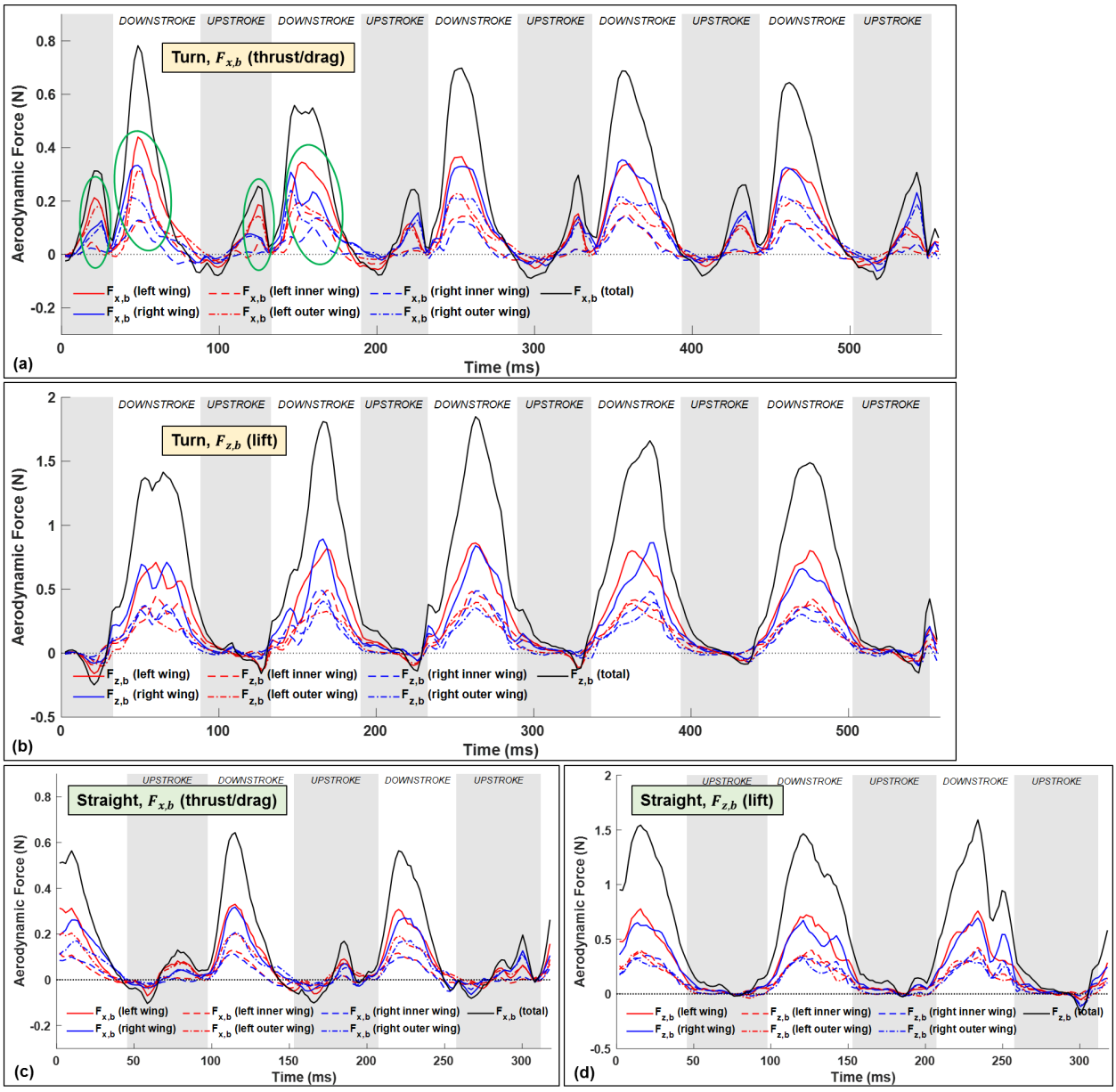

Figure 10. $F_{x,b}$ and $F_{z,b}$ components of aerodynamic force broken down by the section of the wing it is acting on for the turning flight (a) (b) and the straight flight (c) (d). All forces are provided in the body frame. Specification of precisely what comprises each section of the wing is shown in Figure 1a.

Figure 10a shows $F_{x,b}$ for each region of wing for the turning flight. $F_{x,b}$ reflects the difference between thrust and drag where positive values indicate thrust being greater than drag and negative values reflect drag being greater than thrust. Of particular interest are asymmetries arising in the first one to two cycles where the greatest yaw angular acceleration was observed in the body orientation data. The circled regions of the plot show strong evidence of excess thrust being generated by the left wing, which is positioned on the outside of the turn, during both the

upstroke and downstroke phases. During the upstroke, the left outer wing is responsible for nearly all of the thrust, while during the downstroke, it accounts for about half the thrust. During the turn, the bat does not appear to employ the strategy of creating excess drag on the inside wing—rather the yaw acceleration is effectuated almost entirely by thrust. Also of note is that the bat generates thrust asymmetry exclusively early in the turn. Once a yaw rotation is induced, the bat can continue to rotate at a constant angular velocity about the yaw axis without any further moment. It is significant that the yaw is induced in the initiation of the turn since subsequent roll rotation will be relative to a rotated longitudinal axis.

Relative symmetry can be seen in the $F_{z,b}$ shown in Figure 10b. Since the bat already has a substantial roll velocity in the first cycle, shown by the slope of the roll angle curve in Figure 9, this is not unexpected. This indicates that during the main phase of the turn, defined as the region of primary bearing angle change, the bat maintains relatively nominal lift generation patterns and relies on a significant yet constant magnitude roll to effectuate the majority of net bearing angle change. There does exist slightly elevated lift on the left wing (outside the turn) during flaps three, four, and five which appears to serve as stabilization, recovering lost roll from the upstroke phase maintaining the positive right roll angle.

$F_{y,b}$ is omitted since the magnitudes are very small and oscillate about zero. This is expected since prior work on bat maneuvers and flapping flight maneuvers have not predicted body-frame lateral force imbalances to be a mechanism for turning. Near zero $F_{y,b}$ denotes that the net force vector remains in the $x_b - z_b$ plane which bisects the bat's back. While lateral forces in the body-fixed frame are near zero, banking of the bat tilts the frame causing a global lateral (radial) force, which as previously discussed is highly critical for centripetal acceleration into the turn.

Force asymmetries, specifically elevated thrust on the left wing during both the upstroke and downstroke in the initiation of the turn provide solid indication of how the bat initiates the turn. However, additional verification of this conclusion can be shown by calculating force moments. Full spatial variation of force across the bat's wings allows for estimation of the net rotational moment relative to the bat's center of mass. The clearest representation of the moments can be seen by plotting half-cycle averaged moments as shown in Figure 11. Additionally, the transient curves have also been provided in supplementary Figure S4. The moments acting on the bat provide an angular acceleration, which is a change in angular velocity, to the bat. In order to

more easily visualize how the angular velocity is changing with time, half-cycle mean angular velocities are provided in Figure 11.

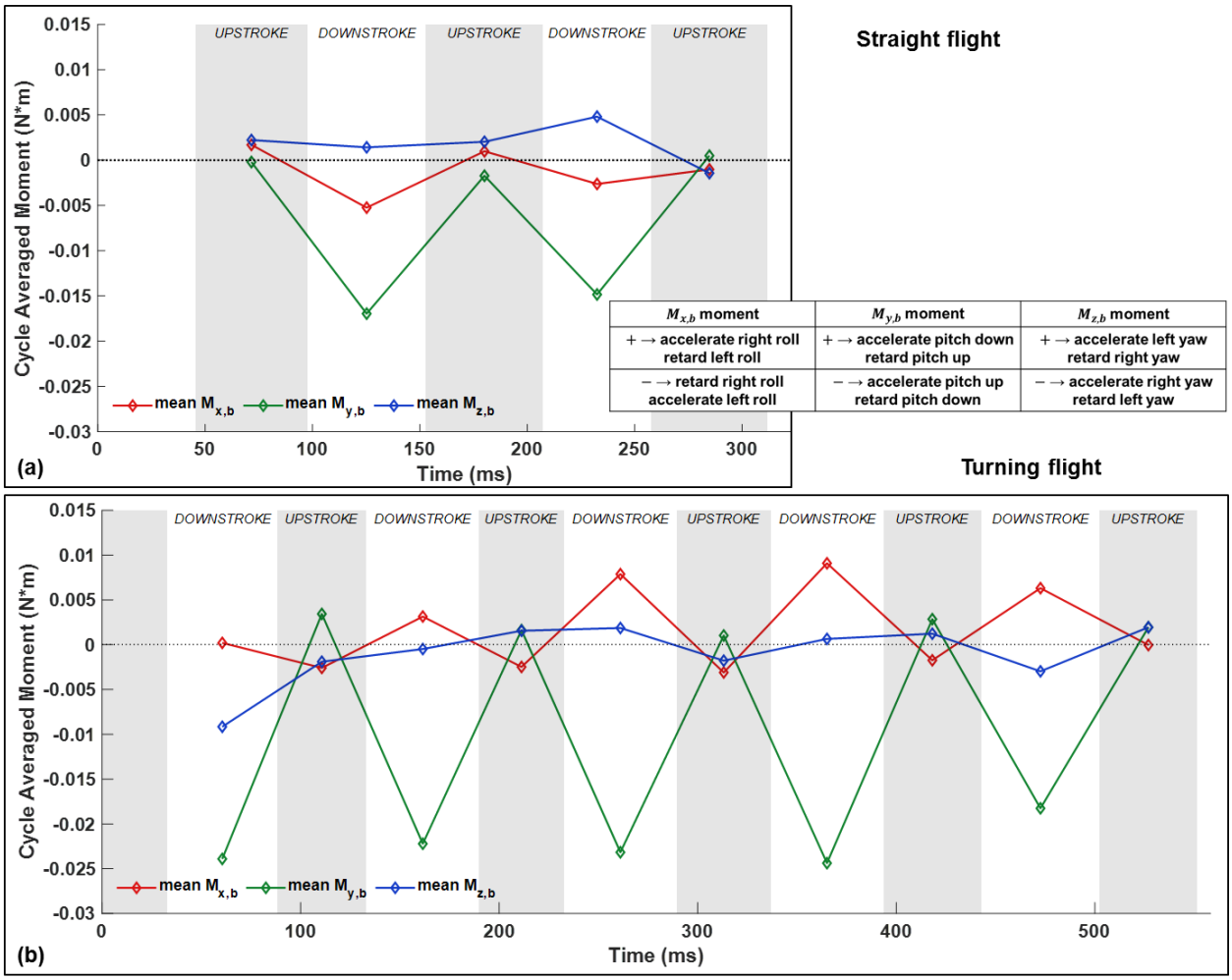

Figure 11. Rotational moments about the body-frame axes relative to the estimated center of mass are shown for the straight flight (a) and the turning flight (b).

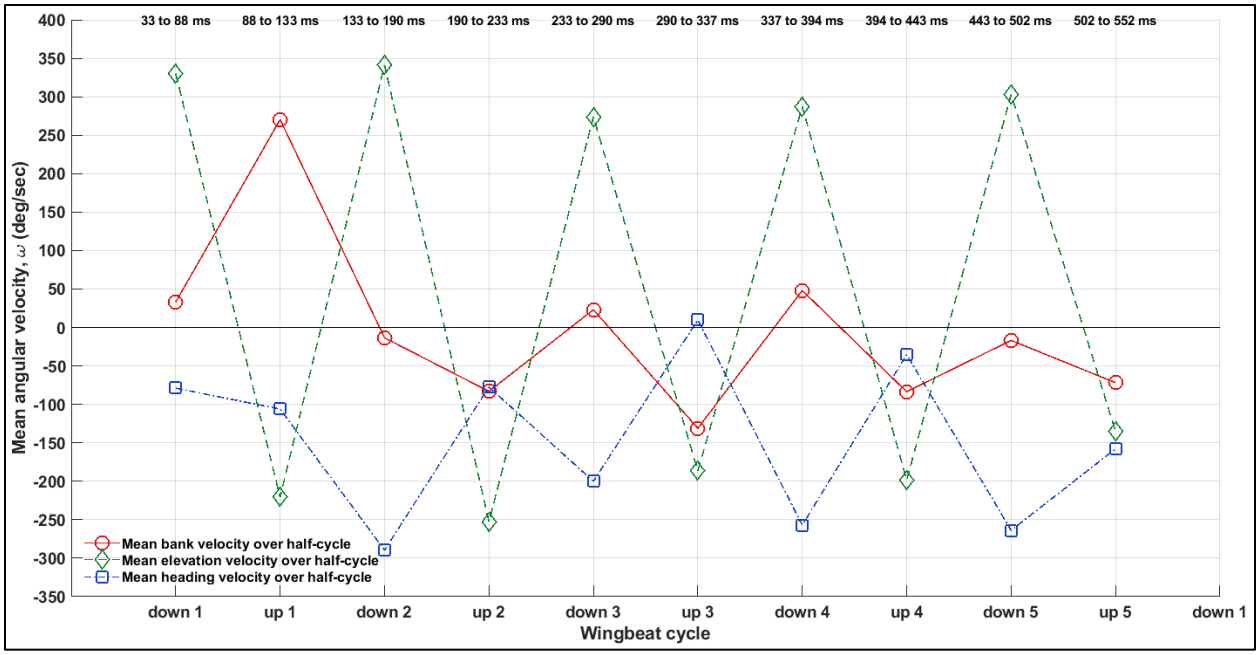

Figure 12. Half-cycle mean angular velocities are shown for the turning flight. The changes in angular velocity represent angular accelerations and are caused by aerodynamic moments, inertial moments, or a combination of the two.

When the moments and angular velocities are analyzed in conjunction with the forces partitioned by the region of the wing on which they act, a few important trends emerge. The elevated thrust by the left wing in the initiation phase of the turn correlates well to the yaw moment in Figure 11b. In addition, the heading (yaw) angular velocity magnitude in Figure 12 increases in the first three consecutive half-strokes to 300 degrees per second of yaw rotation which is the peak over the turn. The pitch moment oscillates within each wingbeat cycle such that the bat pitches up during downstroke and pitches down during upstrokes. The magnitude of the pitch moment decreases slightly, but steadily throughout the turn mirroring the trend observed in the rotational velocity plot. Although the bat climbs steadily during the later phase of the turn, the pitching angular velocity decreases slightly towards the end. Once the bat enters the middle phase of the turn, the roll and yaw angular velocities can be seen to oscillate with the frequency of the wingbeat. Right roll angular velocity is induced by a roll moment during each downstroke, and subsequently drops off during the following upstroke. Since aerodynamic forces are relatively low during the upstroke, it suggests that inertia may induce counterproductive left roll during the upstroke which is subsequently corrected during the following downstroke to maintain a constant roll angle.

The aerodynamic forces acting on the wings arise from a pressure difference between the top and bottom surfaces of the wings. The magnitude of the force is equal to the strength of the

pressure difference, and the direction of the force is normal to the surface. In order to visualize this, contours plots of pressure coefficient differential are shown in Figure 13 along the flight trajectory in the global coordinate system. The net force vector resulting from the pressure differential acting on each wing is shown at the right and left wingtip for each time snapshot. The instant in time at which each snapshot is taken is shown in Figure 13c—the snapshots were chosen as the point in the downstroke at which lift is maximum and the point in the upstroke in which thrust is maximum. During the downstroke (Figure 13a), the wing surface is colored by the magnitude of the differential pressure coefficient, ΔC_p, between the bottom and top surface of the wings per standard aerodynamic convention. During the upstroke (Figure 13b), the pressure differential plotted is the pressure on top of the wing minus the bottom due to the rotation of the wing.

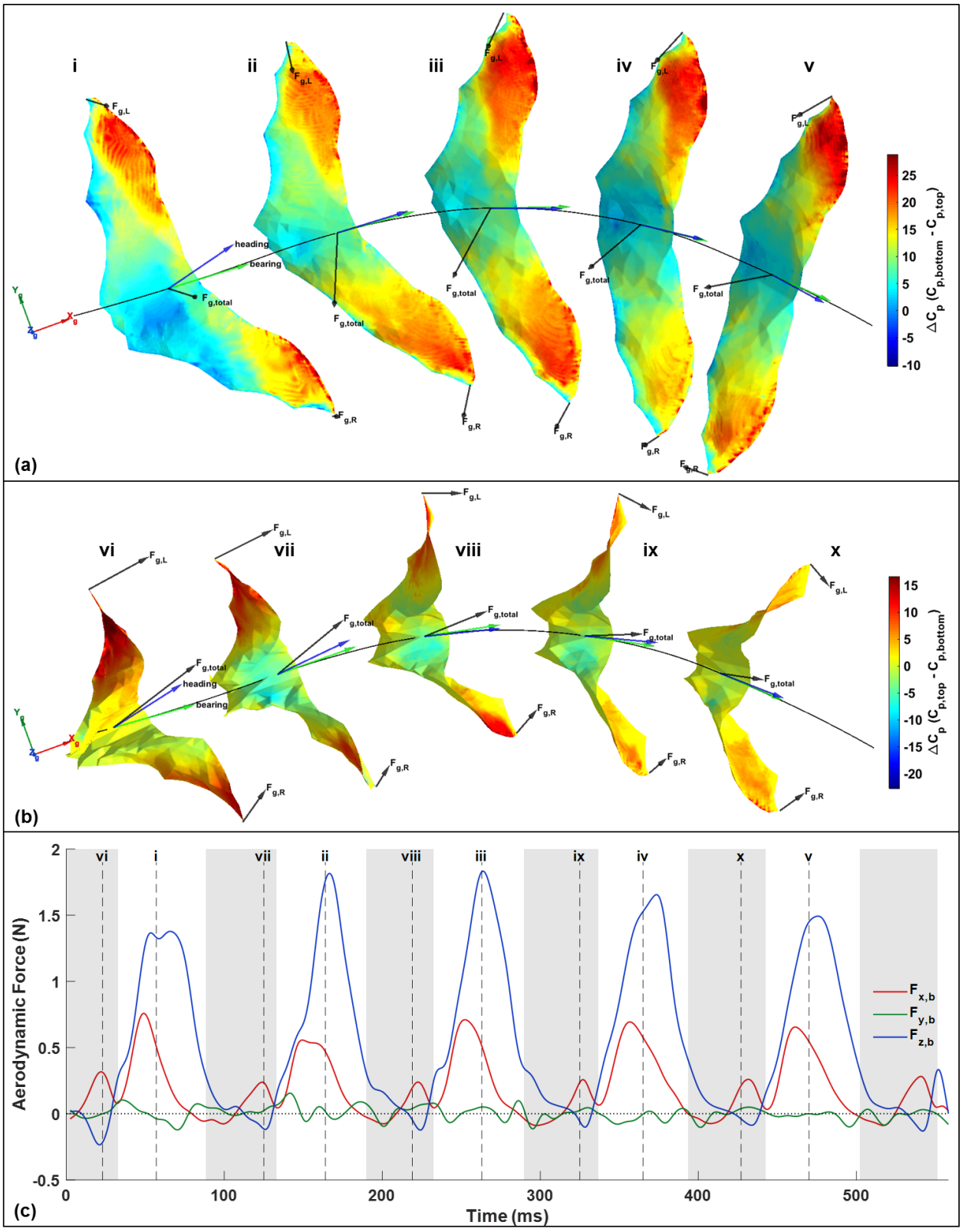

Figure 13. Wing surface plots colorized by the local strength of pressure differential during each downstroke (a), and each upstroke (b). Force vectors show the total force as well as the force acting on the left and right wings independently. The point in time at which each surface is plotted is designated in (c).

Figure 13a shows the elevated thrust generated by the left wing during the first downstroke which is critical in generating the yaw moment in the initiation of the turn. Comparing the subsequent snapshots with the first, the re-orientation of the bat heading relative to the velocity vector (bearing) is apparent. During the main phase of the turn (i.e. where the radius of curvature is minimum), it can be seen how the banking of the bat redirects the net force vector radially. Furthermore, the magnitude of the radial force reaches a maximum when the bearing angle is changing most rapidly (cycles 2, 3, and 4). Elevated pressure differential can be seen on the left wing during cycles 3, 4, and 5 generating a stabilizing roll moment to sustain right roll throughout the flight. The tangential component of the force, directed along the trajectory, decreases throughout the flight consistent with the deceleration observed in the flight. This is caused by the roll redirecting the force vector laterally, and the pitch redirecting the force vector rearward. The bat compensates by generating additional thrust as it climbs, but the magnitude of the additional thrust is lower than what would be required to maintain a constant flight speed. This illustrates the trade-offs at play when executing a complex maneuver. In this specific instance, the bat elects to sacrifice some velocity to achieve the turn and climb.

Figure 13b shows the same trajectory but the selected snapshots correspond to the point in the upstroke where thrust is maximum. Thust is generated during the end of the upstroke by flicking the wingtips up and back—while lift during the downstroke is generated by elevated pressure under the wing and reduced pressure on top of the wing, thrust during the upstroke is generated by elevated pressure on the top surface of the wing. For this reason, the contour plot of ΔC_p in Figure 13b shows $C_{p,top} - C_{p,bottom}$ (negative of what is plotted in Figure 13a). The pressure difference can be seen to be maximum during the first two upstrokes on the left wing, resulting in an increased force magnitude and consequently thrust by the left wing. Throughout the entire flight, some amount of thrust is generated during each upstroke. An additional important feature of the configuration of the wings during the upstroke is the wing rotation orienting the surface vertically to mitigate negative lift. Since nearly all of the lift is generated during the downstroke, the ability to re-set the wings in preparation for the subsequent downstroke without generating negative lift is a major asset to the flight performance of the bat. An animation of the flight including the pressure on the wing surface and iso-surfaces of coherent vorticity is included in supplementary information (Video S1).

3.6 Power Analysis

Throughout the flight, the bat expends power to stay aloft and to propel itself through the air. The baseline power expenditure for straight flight includes overcoming lift-induced drag (cost of staying aloft), and overcoming profile and parasitic drag (cost of forward movement). Additional power in excess of the baseline must be expended to turn or climb.

In order to evaluate the power cost of the ascending turn maneuver, a total energy analysis was conducted. First, the aerodynamic power was calculated from the flow simulation results. Aerodynamic power for a differential element on the wing is calculated as $P=F.v$ which is then integrated over the surface of the wing at each point in time throughout the flight. The result represents the rate of work done on the air by the wing. The aerodynamic power is not always equivalent to the power expended by the bat. Since both the vertical position and the velocity of the bat change throughout the flight, the changes in kinetic and potential energy effect the power output required by the bat relative to the aerodynamic power calculated. When the bat descends or decelerates, the change in energy proportionally reduces the power load on the bat. Conversely, when the bat ascends or accelerates, the power load is increased. The net power expenditure by the bat (Figure 14) is thus the aerodynamic power plus or minus the rate of PE and KE gained or lost.

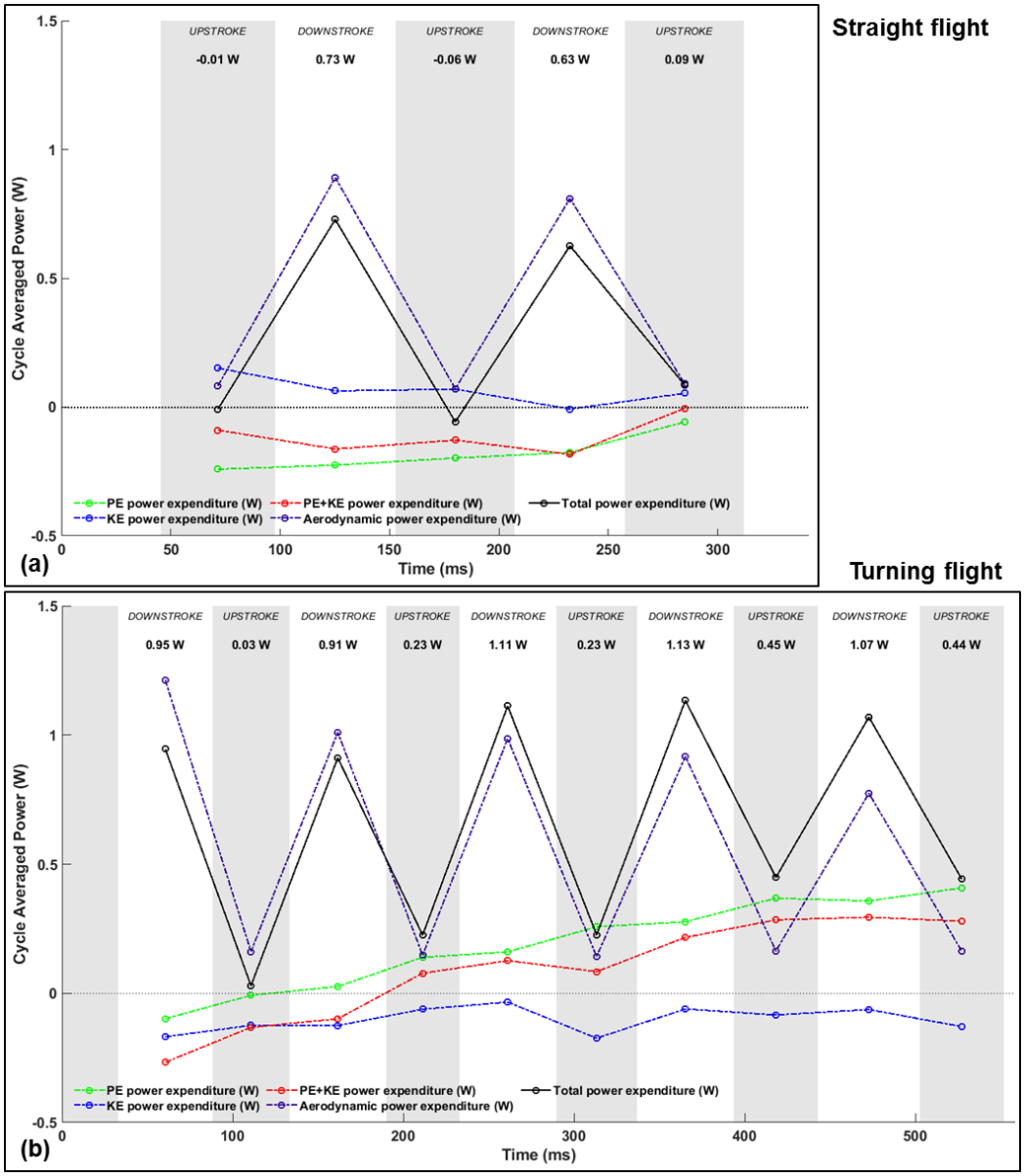

Figure 14. Total power expenditure during the straight (a) and turning (b) flights defined as the net of the aerodynamic power and the rate of gain/loss of potential and kinetic energy.

Power expenditure for the straight flight is shown in Figure 14a. The cycle averaged power expenditure for the straight flight was 0.34 W. Straight flight represents power expenditure near the base case with slight deviation due to the fact that the bat is descending (power gain) and accelerating (power loss). Since the rate of conversion of potential energy into flight energy is higher than the loss resulting from the acceleration, the calculated aerodynamic power is less than the total power expenditure during the flight by approximately 0.1 W. The cycle mean total power expenditure is about 0.34 W. Since the bat is flying relatively straight, the wings can flap

symmetrically in typical patterns which provides the most energy optimal mode of flight. Additionally, no extraneous lateral forces or excess lift is required in this mode of flight.

During the turning flight, power expenditure represents the base requirement plus the cost of turning and climbing. Figure 14b shows elevated power expenditure throughout the flight. During wingbeat cycles 1 and 2, the bat is not yet climbing, so the elevated power requirement can be attributed to the generation of yaw moment in the initiation of the turn. Cycles 3, 4 and 5 represent the additional power required both to climb and maintain the turn. Since the bat is slowing down, kinetic energy is being converted into flight power; however, the amount of energy required to effect the change in potential energy more than exceeds this gain. Thus, once the bat enters the climbing phase of the flight, the total power expenditure is elevated. The mean power expenditure over the entire maneuver is 0.66 W which represents a 91% increase compared to the straight flight. Looking at the different phases of the turn, the mean power requirement during the initiation of the turn is 0.48 W (40% more than straight), while the requirement during the climb and main phase of the turn is 0.72 W (110% more than straight). From this analysis, it is clear that both turning and climbing require significantly elevated energy expenditure.

Total power expenditure is critical for evaluating the power required for a bat to execute a flight; however, the metabolic power burned by the bat to fuel the flight will be somewhat higher due to energy losses resulting from the actuation of the wings. This loss factor is referred to as metabolic efficiency and has been investigated in a few prior studies. Metabolic efficiency in bats is difficult to measure experimentally, but estimates range between 5% and 40% [9]. Given a particular estimate for metabolic efficiency, energy burned for a flight will be total power expenditure divided by the efficiency.

4. Discussion

In this investigation of maneuvering bat flight, we have shown how several different mechanisms work simultaneously and synergistically to achieve the desired flight trajectory. This illustrates the importance of analyzing the flight holistically as no single mechanism is sufficient to fully explain the resulting maneuver. Through this process it was found, in summary, that asymmetries in the kinematics drive force imbalances which reorient the bat thereby redirecting

the net force vector laterally. During the maneuver, both roll and yaw rotations were used and in addition both the upstroke and downstroke were active.

4.1 Method selection considerations

Key in unraveling the various aspects of the maneuver, is the ability to analyze the kinematics and aerodynamics in parallel. To achieve this, a novel method for collecting and analyzing high spatial resolution kinematic data in conjunction with aerodynamic data for maneuvering bat flight was employed. The optical motion capture setup used was derived from systems routinely used to study animal flight with a few important augmentations—the number of cameras was increased to 28 (from a typical 3-6) extending the capture volume to be able to recorded maneuvers taking place over several wingbeat cycles. In addition, a higher than normal density of points on the wings was tracked including points on the membrane as well as the skeleton. The elevated spatial resolution of the captured wing kinematic data could then be used to run numerical simulations of the flow around the bat's wing. Use of simulations provides detailed flow data from which forces, moments, and power can be calculated.

Historically, the study of bat flight aerodynamics has been dominated by PIV and related methods. These are useful methods and have yielded some important studies, but have different advantages and disadvantages relative to computational methods. Comparing PIV-based methods to computational methods for studying bat aerodynamics, both methods start with a fairly direct measurement of the 3D wing kinematics; from the kinematics, computational methods calculate forces based on experimentally measured kinematics using Navier-Stokes, while PIV methods measure airflow in the animal's wake and calculate the forces from conservation of momentum. Both methods calculate aerodynamic force from measurements using different strategies. In computational methods, error can result from poor model construction, while in PIV methods, error can result from the calculation of forces from the wake (as summarized by Gutierrez et al., 2016). PIV-based methods have the advantage of directly measuring airflow in a bat's wake and do not require detailed kinematic data of the membrane deformation to calculate force. That is, there is no dependency between the kinematic and aerodynamic calculations, and any error in the kinematics do not propagate into the force calculations. In addition, the ability to set the wind tunnel velocity allows more direct control of the bat's flight velocity in contrast to free flight. A key limitation of PIV methods is that studies must be run in wind tunnels, so studying maneuvers

is challenging. Additionally, wake decay from viscous dissipation in the flow may result in under prediction of force insomuch as the frozen wake hypothesis is violated during a real flight. Computational methods have the advantage of calculating flow velocity in the entire vicinity of the wings including the critical near-wing region where the flow interacts with the wing. The major challenges with computational studies are that more robust and careful validation is required, and also generating datasets from a large number of flights is currently untenable using present algorithms. This is a result of higher fidelity kinematic data being required for input to the simulations, as well as high computational cost to simulate each flight. For these reasons, it is advantageous to have studies on bat flight using both methods to better elucidate a broad range of questions related to bat flight.

Since force calculations using computational methods have dependency on the accuracy of the kinematic data, it is important to understand the source of error in generating 3D point reconstructions. The source of the uncertainty in the kinematics results from imperfection in the camera calibrations which are used to generated the 3D reconstruction of the wing points. Small deviations exist between the idealized pinhole camera model used for stereo triangulation and real cameras. In addition, the radial and tangential distortion models differ from the exact manufactured lens shape of each camera used. During the calibration, the mean re-projection error of each camera was monitored, but there is no standard method of propagating re-projection error through to calculate specific uncertainties of the kinematic points or trajectories which would be required to include error bars on kinematic plots. However, the lumped mass dynamics analysis which was primarily conducted to validate the simulations, indirectly validates the kinematics as well since the kinematics are the input into the simulations. There is a theoretical ground truth flight trajectory which is not known but exists somewhere relative to the “simulated” and “observed” trajectories that are shown in Figure 7. Since the “observed” and “simulated” trajectories fall quite close to each other, one can reasonably infer that the unknown ground truth trajectory lies somewhere between these two. The unknown true flight trajectory likely lies close to the “observed” trajectory based on the error dependencies. That is, the “observed” trajectory contains only 3D reconstruction error, while the “simulated” trajectory contains numerical error as well as error resulting from any deviation between the actual wing kinematics and the 3D reconstructed kinematics.

4.2 Generalization of results

The primary focus of the present study was to elucidate kinematic and aerodynamic mechanisms driving a sample turning flight in comparison to a nominally straight flight at a detailed level. A secondary consideration of how typical the observed mechanisms are, is an interesting question related to extending the work. Undoubtedly, some broader generalization to typical turning mechanisms exists, but it must be approached cautiously. A quantitative characterization of generalizability is beyond the scope of this study. However, we identify a few factors to consider when attempting to generalize. First, the geometry of the flight tunnel and setup of the experiment influences the bat's flight behavior. Since it is not feasible to setup up camera arrays in a bat's natural habitat, the artificial environment of the flight tunnel remains should be considered when attempting to generalize the results to *in situ* flight behavior. In this study, the bat's wingtip is relatively close to the tunnel wall at certain sections of the flight. From the flight animation (Supplementary Video S1), it can be seen that the wake primarily propagates backward and downward with limited lateral travel. This suggests that the present of the wall does not have a substantial aerodynamic effect, although it likely has a behavioral effect since the bat must navigate within the confines of the tunnel. Second, any individual bat may use slightly different turning mechanisms during each maneuver. This is analogous to how human gait is cyclical in nature, but slightly deviates each individual step. Third, different bat species have different mass and wing morphology which undoubtedly influences turning mechanisms. An open area for future studies would be to robustly characterized scaling laws for turning mechanisms, and to quantify the relationship between wing morphology and turning mechanisms.

5. Conclusion

Over the five wingbeat cycles comprising the maneuver, the kinematic data showed maximum right-left asymmetry early in the initiation phase of the turn. This was reflected in the elevated horizontal stroke plane angle of the left wing (more oriented toward the midline), as well as the extended flap amplitude and stroke plane deviation of the right wing. Also in the initiation phase of the turn, the body exhibited rapid yaw rotation preceding bearing change—that is, the direction the bat was facing changed prior to the portion of the flight where the trajectory curved. The yaw rotation was caused by elevated thrust on the outer wing during both the upstroke and downstroke. One important effect of early yaw is that subsequent roll is applied relative to a rotated roll axis. The roll angle reached a maximum of about 25 degrees during the second wingbeat cycle

at which point the bat began the majority of the change in bearing. The centripetal force causing the curved flight path was a result of the net force vector being tilted toward the radius of the turn due to the roll angle. Based on the mass of the bat, the flight velocity, and the radius of the turn, the radial component of the net force appears to explain the vast majority, if not the entirety, of the required turning force.

The bat also began to ascend around the second wingbeat cycle, achieved by upward pitching during the downstroke. Significant differences in both angular velocity and forces were observed between the upstroke and downstroke even at times opposing each other. The bat generated an upward pitching moment during the downstroke, but a downward pitching moment during the upstroke. The net result over several wingbeat cycles was determined by the relative magnitudes of the alternating effects. In this case, the upward pitching was more significant so over several cycles, the bat achieved a climb. A similar phenomenon was seen in the roll where stabilizing right roll was generated during the downstroke and counter roll (back toward neutral) was generated during the upstroke. The source of these mechanics was investigated by looking at the pressure difference across the wing at various points during the flight. Elevated lift on the left wing during the downstroke of cycles 3-5 strongly indicates that the source of the stabilizing roll is aerodynamic.

Since the net force vector is substantially larger during the downstroke, the majority of the radial turning force in the main phase of the turn was generated during the downstroke. Due to the low force magnitude during the upstroke, it can be tempting to conclude that the upstroke is aerodynamically inactive—however as a counter example, the asymmetric thrust during the upstroke in the initiation phase of the turn provides an important yaw moment impacting the entire turn. This indicates that there is a progression to the turn and that each flap comprising the turn is not identical. Certain mechanics may be present during a particular flap, but are not exhibited during subsequent flaps. While straight flight is essentially a repeating pattern of cyclical motion, maneuvers have much more of a transient nature.

Development of bioinspired micro air vehicles is currently being undertaken by researchers using a variety of model organisms. Bat represent a compelling model for vehicles on the order of 0.01 kg to 0.1 kg which prioritize maneuverability, flight efficiency, and load carrying capabilities. One of the key barriers to the design of such a vehicle is a detailed understanding of properly actuating the wings to mimic bat kinematics as well as understanding the expected force response

for the purpose of controller tuning. The data presented in the present work sheds light on both of these questions.

In the future, there is more work to be done investigating maneuvering bat flight. The data presented in the present work focuses on one particular turn; however a more comprehensive understanding of turning flight requires investigation of turns with other radii of curvature and at different flight speeds. Additionally, investigation of other species of bats with different masses, wing spans, and chord lengths should be conducted to gain a more generalized understanding of how kinematic asymmetries, aerodynamic forces and power requirements scale with the size and flight speed of the bat.

Acknowledgements

The authors acknowledge Matt Bender for help with computer vision and experimental setup; Josh Lesser for help with video processing; Yang Xu, Yuxian Ye, Mengfan Wang, Junyang Xu, Han Xu, and Xuchen Gu for help with data collection; and Dr Susheel Sekhar for brainstorming. In addition, the authors thank Advanced Research Computing at Virginia Tech for providing computational resources for the numerical simulations (URL: http://www.arc.vt.edu). This research received financial support from NSF CBET Grant No. 1510797, NSF IRES Grant No. 1658620, support from VT ICTAS/BIST Center, National Natural Science Foundation of China (Grant Nos. 11374192 & 11574183), and Chinese Ministry of Education Tese Grant for international faculty exchange.

References

[1] D. A. Swartz, S.M.; Middleton, K.M.; Iriarte-Diaz, J.; Lee, M.; Wofford, J.M.; Breuer, K.S.; Ritter, "Can bats actively control the mechanical properties of the wing membrane?," *Integr. Comp. Biol.*, vol. 44, p. 751, 2004.

[2] J. A. Cheney, N. Konow, A. Bearnot, and S. M. Swartz, "A wrinkle in flight: the role of elastin fibres in the mechanical behaviour of bat wing membranes," *J. R. Soc. Interface*, vol. 12, no. MAY, pp. 1–9, 2015.

[3] S. M. Swartz, "Skin and bones functional, architectural, and mechanical differentiation in the bat wing," in *Bat Biology and Conservation*, 1998, pp. 109–126.

[4] J. A. Cheney, J. J. Allen, and S. M. Swartz, "Diversity in the organization of elastin bundles and intramembranous muscles in bat wings," *J. Anat.*, vol. 230, no. 4, pp. 510–523, 2017.

[5] Y. Winter and O. Von Helversen, "The energy cost of flight: Do small bats fly more cheaply than birds?," *J. Comp. Physiol. - B Biochem. Syst. Environ. Physiol.*, vol. 168, no. 2, pp. 105–111, 1998.

[6] F. T. Muijres, L. C. Johansson, M. S. Bowlin, Y. Winter, and A. Hedenström, "Comparing aerodynamic efficiency in birds and bats suggests better flight performance in birds," *PLoS One*, vol. 7, no. 5, 2012.

[7] U. M. Norberg, T. H. Kunz, J. F. Steffensen, Y. Winter, and O. Von Helversen, "The Cost of Hovering and Forward Flight in a Nectar-Feeding Bat , Glossophaga Soricina , Estimated From Aerodynamic Theory," *J. Exp. Biol.*, vol. 182, no. April, pp. 207–227, 1993.

[8] A. Hedenström, L. C. Johansson, and G. R. Spedding, "Bird or bat: comparing airframe design and flight performance," *Bioinspir. Biomim.*, vol. 4, no. 1, p. 015001, 2009.

[9] R. von Busse, R. M. Waldman, S. M. Swartz, C. C. Voigt, and K. S. Breuer, "The aerodynamic cost of flight in the short-tailed fruit bat (*Carollia perspicillata*): comparing theory with measurement.," *J. R. Soc. Interface*, vol. 11, p. 20140147, 2014.

[10] F. T. Muijres, G. R. Spedding, Y. Winter, and A. Hedenström, "Actuator disk model and span efficiency of flapping flight in bats based on time-resolved PIV measurements," *Exp. Fluids*, vol. 51, no. 2, pp. 511–525, 2011.

[11] D. K. Riskin *et al.*, "Quantifying the complexity of bat wing kinematics," *J. Theor. Biol.*,

vol. 254, no. 3, pp. 604–615, 2008.

[12] P. Windes, D. K. Tafti, and R. Müller, “Determination of spatial fidelity required to accurately mimic the flight dynamics of a bat,” *Bioinspir. Biomim.*, 2019.

[13] L. C. Johansson, M. Wolf, and A. Hedenström, “A quantitative comparison of bird and bat wakes.,” *J. R. Soc. Interface*, vol. 7, no. 42, pp. 61–66, 2010.

[14] M. Wolf, L. C. Johansson, R. von Busse, Y. Winter, and A. Hedenstrom, “Kinematics of flight and the relationship to the vortex wake of a Pallas’ long tongued bat (Glossophaga soricina),” *J. Exp. Biol.*, 2010.

[15] F. T. Muijres, L. Christoffer Johansson, Y. Winter, and A. Hedenström, “Leading edge vortices in lesser long-nosed bats occurring at slow but not fast flight speeds,” *Bioinspiration and Biomimetics*, 2014.

[16] L. C. Johansson, M. Wolf, R. von Busse, Y. Winter, G. R. Spedding, and A. Hedenström, “The near and far wake of Pallas’ long tongued bat (*Glossophaga soricina*).,” *J. Exp. Biol.*, vol. 211, no. Pt 18, pp. 2909–18, 2008.

[17] A. Hedenstrom, L. C. Johansson, M. Wolf, R. von Busse, Y. Winter, and G. R. Spedding, “Bat Flight Generates Complex Aerodynamic Tracks,” *Science (80-.).*, vol. 316, no. 5826, pp. 894–897, 2007.

[18] P. Windes, X. Fan, M. Bender, D. K. K. Tafti, and R. Müller, “A computational investigation of lift generation and power expenditure of Pratt’s roundleaf bat (Hipposideros pratti) in forward flight,” *PLoS One*, vol. 13, no. 11, p. e0207613, 2018.

[19] S. Sekhar, P. Windes, X. Fan, and D. K. Tafti, “Canonical description of wing kinematics and dynamics for a straight flying insectivorous bat (Hipposideros pratti),” *PLoS One*, 2019.

[20] U. M. Norberg, “Some Advanced Flight Manoeuvres of Bats,” *J. Exp. Biol.*, vol. 64, pp. 489–495, 1976.

[21] A. J. Bergou *et al.*, “Falling with Style: Bats Perform Complex Aerial Rotations by Adjusting Wing Inertia,” *PLoS Biol.*, vol. 13, no. 11, pp. 1–16, 2015.

[22] J. Iriarte-Diaz and S. M. Swartz, “Kinematics of slow turn maneuvering in the fruit bat Cynopterus brachyotis,” *J. Exp. Biol.*, 2008.

[23] P. Henningsson, L. Jakobsen, and A. Hedenström, “Aerodynamics of manoeuvring flight in brown long-eared bats (Plecotus auritus),” *J. R. Soc. Interface*, vol. 15, no. 148, 2018.

[24] H. D. Aldridge, “Turning flight of bats,” *J. Exp. Biol.*, vol. 128, pp. 419–425, 1987.

[25] K. Viswanath, K. Nagendra, and D. Tafti, “Climbing Flight of a Fruit Bat Deconstructed,” in *52nd Aerospace Sciences Meeting*, 2014.

[26] S. Wang, X. Zhang, G. He, and T. Liu, “Lift enhancement by bats’ dynamically changing wingspan,” *J. R. Soc. Interface*, 2015.

[27] U. M. Norberg and J. M. V. Rayner, “Ecological Morphology and Flight in Bats (Mammalia; Chiroptera): Wing Adaptations, Flight Performance, Foraging Strategy and Echolocation,” *Philos. Trans. R. Soc. B Biol. Sci.*, vol. 316, no. 1179, pp. 335–427, 1987.

[28] T. Svoboda, D. Martinec, and T. Pajdla, “A convenient multicamera self-calibration for virtual environments,” *PRESENCE teleoperators virtual Environ.*, vol. 14, no. 4, pp. 407–422, 2005.

[29] D. K. Tafti, “GenIDLEST: A scalable parallel computational tool for simulating complex turbulent flows,” in *ASME-PUBLICATIONS-FED*, 2001, vol. 256, pp. 347–356.

[30] K. Nagendra, D. K. Tafti, and K. Viswanath, “A new approach for conjugate heat transfer problems using immersed boundary method for curvilinear grid based solvers,” *J. Comput. Phys.*, vol. 267, pp. 225–246, 2014.

[31] E. Gutierrez, D. B. Quinn, D. D. Chin, and D. Lentink, “Lift calculations based on accepted wake models for animal flight are inconsistent and sensitive to vortex dynamics,” *Bioinspir. Biomim.*, vol. 12, no. 1, p. 016004, 2016.

Kinematic and aerodynamic analysis of a bat performing a turning-ascending maneuver

Peter Windes , Danesh K. Tafti, Rolf Müller

Supplementary Material:

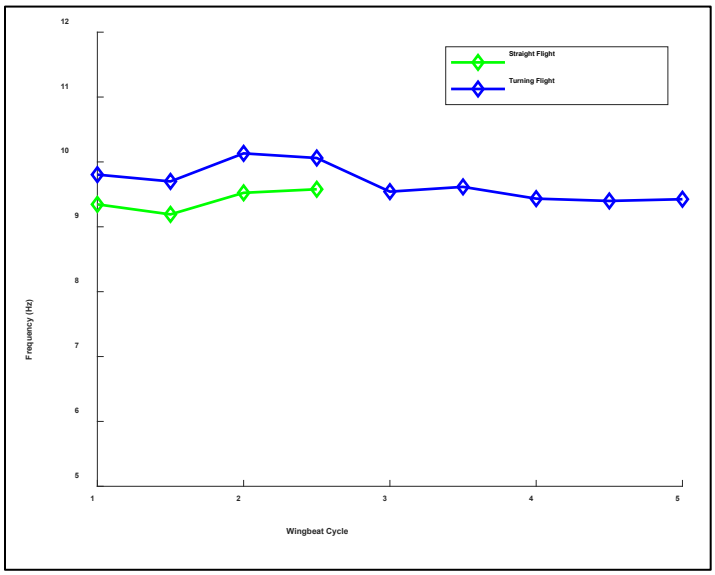

Figure S1. Temporal trend in wing beat frequency for the straight and turning flights. The frequency is shown at each half-cycle.

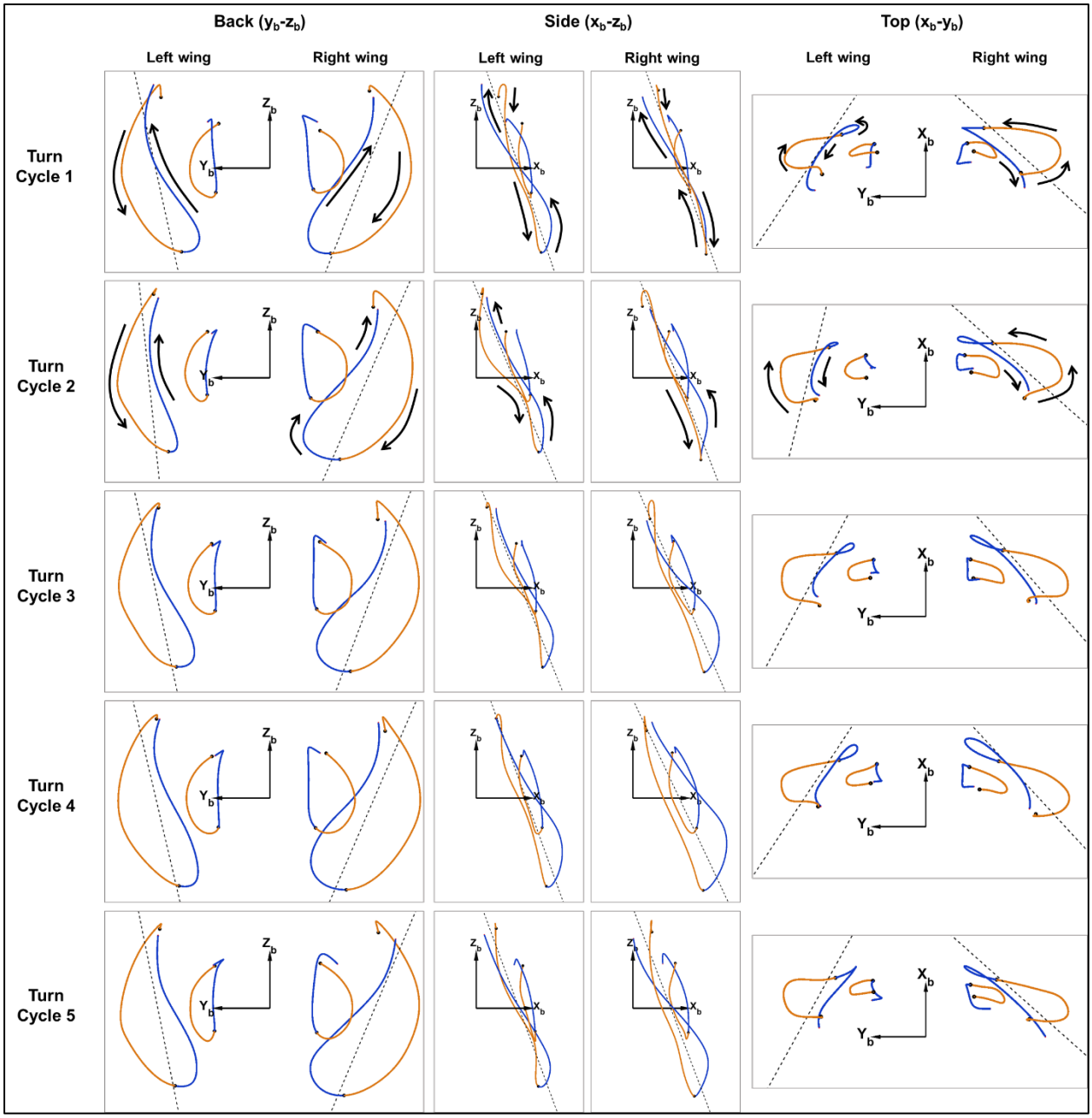

Figure S2. Wingtip and wrist trajectories for each of the 5 wingbeat cycles of the turning flight shown in three projections—back view, side view, and top view. The downstroke is designated by orange, and the upstroke is designated by blue. The locus regression line used to define the stroke plane is shown by the dashed line in each sub figure.

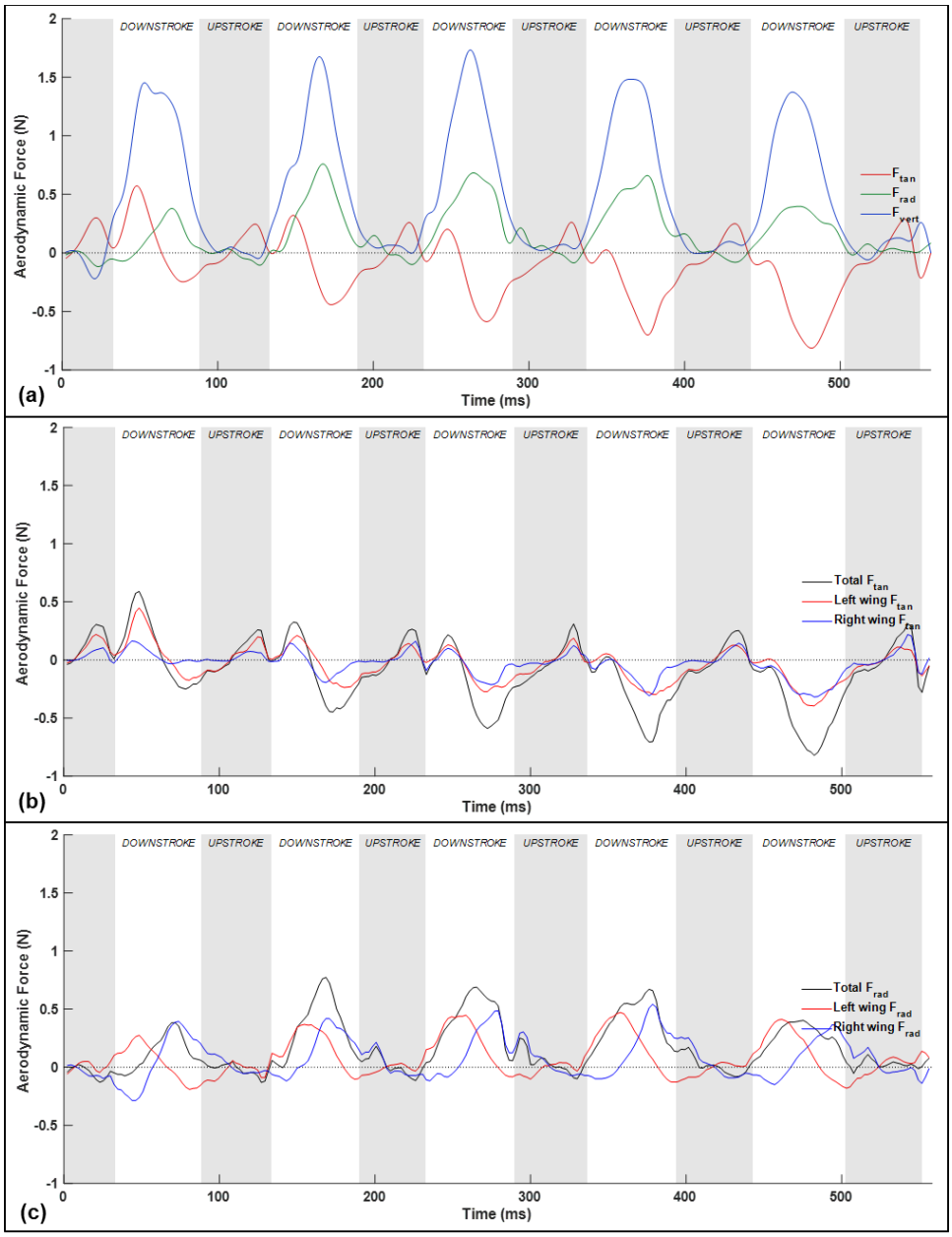

Figure S3. Tangential, radial, and vertical force for the turning flight (a). Also shown is the contribution of the left and right wing to the net tangential force (b) and net radial force (c).

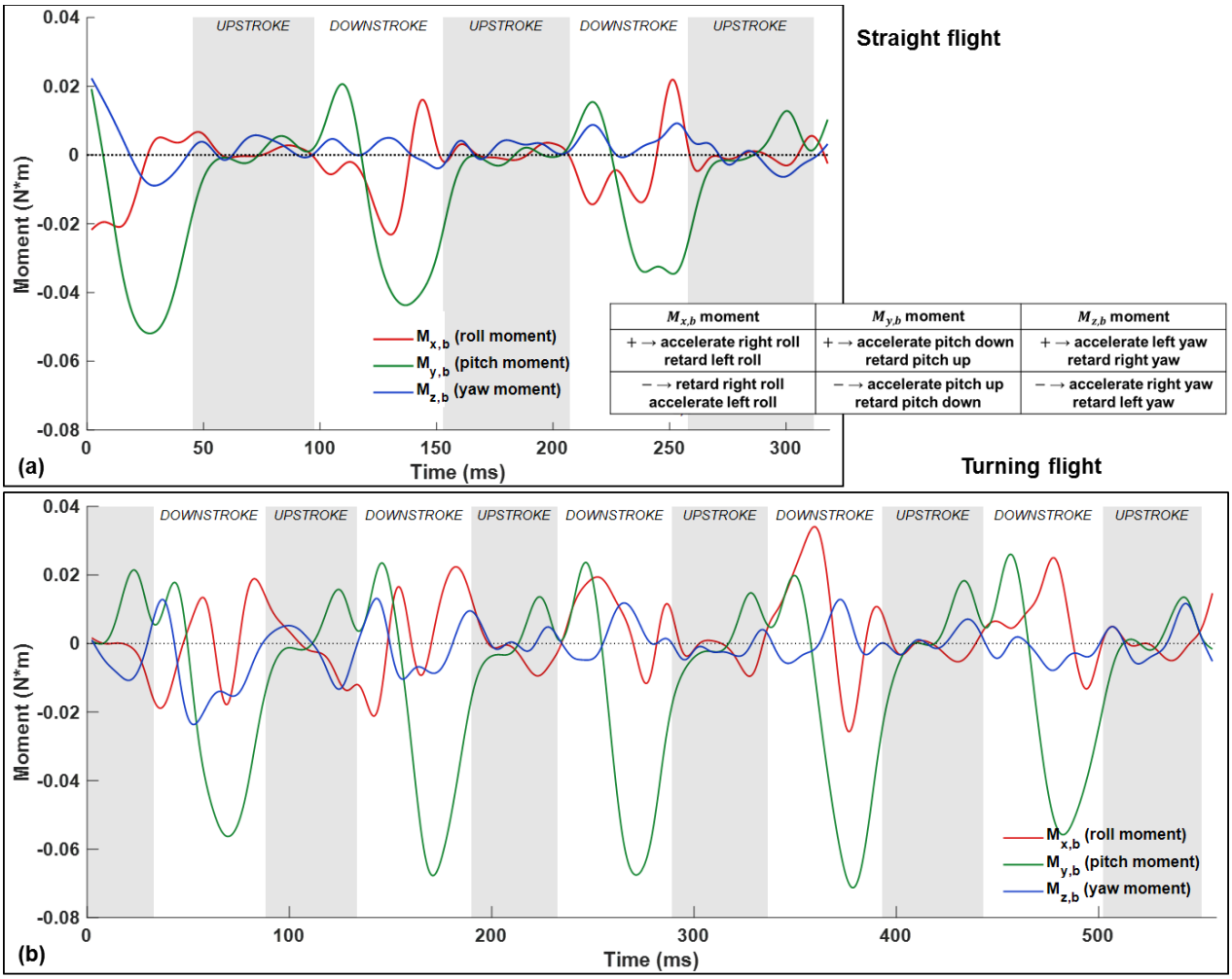

Figure S4. Transient rotational moments about the body-frame axes relative to the estimated center of mass are shown for the straight flight (a) and the turning flight (b).

Video S1. Animation showing pressure coefficient differential on the wing surface along with iso-surfaces of coherent vorticity.

5. Analysis of a U-turn Maneuver by a Great Roundleaf Bat

Reprint of, "Analysis of a 180-degree U-turn maneuver executed by a Hipposideros armiger bat"

The following chapter is a reprint of a manuscript which will be submitted to *PLOS ONE* (June 2020). The general analysis framework used in Chapter 4 was applied to a more complicated 180 degree U-turn maneuver. The study of rapid tight turns allows investigation of maneuvers near the upper limit of a bat's turning capability. Common methods of studying bat flight aerodynamics such as experimental particle image velocimetry (PIV) based techniques require the bat to fly in a wind tunnel and are thus unsuitable for investigating complex maneuvers. In contrast, our motion capture system operates in a static flight tunnel where a broader range of flight modes can be captured. This paper represents the first study to collect high spatial resolution wing kinematic data of a sharp turning maneuver as well as the first study to generate corresponding aerodynamic data through numerical simulations. Future work on this topic can include the calculation of rotational moments in addition to aerodynamic moments in order to achieve further understanding of maneuvering flight mechanisms.

Analysis of a 180-degree U-turn maneuver executed by a *Hipposideros armiger* bat

Peter Windes[1], Danesh Tafti[1,2], Rolf Müller[1]

Abstract

Bats possess wings comprised of a flexible membrane and a jointed skeletal structure allowing them to execute complex flight maneuvers such as rapid tight turns. The extreme limit of a bat's maneuvering capabilities is exhibited during a 180 degree U-turn. Prior studies have investigated more subtle flight maneuvers, but the kinematic and aerodynamic mechanisms of a U-turn have not been characterized. In this work, we use 3D optical motion capture and aerodynamic simulations to investigate a U-turn maneuver executed by a *Hipposideros armiger* bat (mass=55 g; span=51 cm). The bat was observed to decrease its flight velocity and gain approximately 20 cm of altitude entering the U-turn. By lowering its velocity from 2.0 m/s to 0.5 m/s, the centripetal force requirement to execute a tight turn was substantially reduced. Centripetal force was generated by tilting the lift force vector laterally through banking. During the initiation of the U-turn, the bank angle increased from 20 degrees to 40 degrees. During the initiation and persisting throughout the U-turn, the flap amplitude of the right wing (inside of the turn) increased relative to the left wing. In addition, the right wing moved more laterally closer to the centerline of the body during the end of the downstroke and the beginning of the upstroke compared to the left wing. Reorientation of the body into the turn happened prior to a change in the flight path of the bat. Once the bat entered the U-turn and the bank angle increased, the change in flight path of the bat began to change rapidly as the bat negotiated the apex of the turn. During this phase of the turn, the minimum radius of curvature of the bat was 5.5 cm. During the egress of the turn, the bat accelerated and expended stored potential energy by descending. Future work on this topic may focus on how a more diverse array of bat species achieve complex maneuvering flights. In addition, the interplay between aerodynamic moments and inertial moments are of interest in order to more robustly characterize maneuvering mechanisms.

[1] Department of Mechanical Engineering, Virginia Tech, Blacksburg, VA, United States of America
[2] Corresponding author: dtafti@exchange.vt.edu

1. Introduction

Of the three animal groups capable of powered flight—insects, birds, and bats—bats uniquely possess highly flexible wings composed of a jointed skeletal structure and a thin compliant skin membrane. This wing morphology allows a bat to perform complex flight maneuvers which are critical to navigating cluttered environments and capturing prey. Three fundamental factors in understanding the maneuvering flight of bats are the shape and structure of their wings (morphology), the motion of the wings during flight (kinematics), and the interaction of the wings with the surrounding air (aerodynamics).

Early work on characterizing the maneuverability of bats focused on wing morphology. In 1987 Norberg and Rayner investigated the relationship between bat wing morphology and flight capabilities such as maneuverability [1]. They studied 257 species of bats from 16 of the 18 families using multivariate statistical correlations in order to link morphological parameters to flight performance. Specifically, they investigated the relationship between mass, wing loading, wing aspect ratio, and wingtip shape index with flight efficiency, maximum flight speed, maneuverability, agility, and load carrying capability. It was found that across bat species, variations in morphology were closely correlated with optimization of different flight capabilities. Further, it was hypothesized that differing feeding strategies such as hunting for insects among vegetation, perching while seeking insect prey, fish catching, or foraging for fruit were a key driver of optimization of different flight abilities in different species of bats. In their analysis, low wing loading was correlated with increased maneuverability. While the scope of their study was constrained to bats, notably bats tend to have lower wing loading than birds and also tend to be more maneuverable. This study represented a material advance in the understanding of the factors that impact flight performance of bats including maneuverability; however, a limitation of the study was that specific mechanics of bat flight were not investigated. That is, morphological parameters were correlated with flight abilities, but the causal mechanism of the relationship remained unknown. Additionally, a portion of the analysis such as the investigation of flight efficiency relied on mathematical models based on fixed wing theory.

An early description of the turning radius of a flying animal as a function of mass, wing area, and bank angle was provided by Pennycuick [2]. However, two important factors in applying this framework had not been characterized by researchers—specifically, how do unsteady mechanisms impact lift generation in flying animals, and to what degree is banking utilized in

turning flight. Banking during both fixed wing flight and flapping flight tilts the lift force laterally providing a centripetal acceleration. Thus, both the bank angle and the magnitude of the lift force impact turning mechanics. It was long hypothesized that unsteady aerodynamic mechanisms may be an important aspect of lift generation in flapping flight, but the degree of impact was not known [3]. Unsteady mechanisms were first quantified in insect flight [4], [5], and subsequently bat flight [6], [7]. Since then, certain unsteady mechanisms such as enhanced lift by the leading edge vortex (LEV) have been shown to be nearly ubiquitous in flapping flight, while other mechanisms such as clap and fling are only observed in certain insects operating at smaller length scales.

In 1986, Aldridge studied the turning flight of six bat species—*Rhinolophus ferrumequinum*, *R. Hipposideros*, *Plecotus auritus*, *Myotis mystacinus*, *M. daubentoni*, and *Pipistrellus pipistrellus* [8]. All species were relatively small with masses ranging from 6 g to 22 g, and wing spans ranging from 21 cm to 36 cm. Each bat was trained to execute a U-turn in an open-ended flight tunnel, and 3D reconstruction of the body trajectories was conducted allowing calculation of the flight velocity and the minimum radius of curvature during each maneuver. All the bats were observed to decelerate significantly during the turn to a minimum flight velocity of 0.29-0.71 m/s depending on the species. Additionally, they were observed to climb as they entered the turn and subsequently descend while existing the turn. The bank angles during each turn were between 50 and 90 degrees. A lift coefficient for each fight was estimated using Pennycuick's formula. Considering variation between the bat species, Aldridge determined that the minimum radius of curvature was correlated with the mass of bat. Correlation was found between wing loading and curvature only when excluding results from *R. ferrmequinum,* and it was hypothesized that this bat was using a fundamentally different turning mechanism from the others. Due to the lack of specific kinematic and aerodynamic data provided, it is unclear what exactly this difference was.

While banking is the most obvious turning mechanism, it is not the only available method to achieve a turn during flapping flight. Fundamentally, some force asymmetry is required to turn; however, this may be achieved using either a thrust/drag asymmetry (yawing turn) or a lift asymmetry (banking turn). Iriarte-Diaz and Swartz studied the kinematics of a fruit bat (*Cynopterus brachyotis*) executing 90 degree turning maneuvers in an L-shaped flight tunnel [9]. They found that the use of a banking mechanism was significant but did not fully explain the turn. Heading rotation (change in body orientation) was observed to precede change in bearing (change

in flight direction), and occurred more significantly during the upstroke. Since aerodynamic force was not calculated, they hypothesized that either elevated thrust on the outer wing or increased drag on the inner wing may have been employed to achieve a change in heading.

Henningsson et al. (2018), conducted kinematic and aerodynamic analysis of a brown long-eared bat (*Plecotus auritus*) performing a basic sideways maneuver using particle image velocimetry (PIV) and 3D motion capture in a wing tunnel [10]. Although due to limitations of the wind tunnel setup that constrained the magnitude of the heading change during the maneuver to 4 degrees, some interesting observations were realized. It was observed that the bats were adaptable in selecting their turning mechanism, using both the upstroke and downstroke to initiate the turn. Additionally, both lift as well as thrust/drag asymmetries were employed. The most common method for generating a force asymmetry was in thrust/drag during the upstroke and was identified in 7 of the 10 observed maneuvers. In this study, the ability to simultaneously analyze the wing kinematics along with aerodynamic forces was pivotal towards understanding the maneuvers.

We previously investigated (Windes et al., 2020) the kinematics and aerodynamics of a sweeping turn maneuver of a great round-leaf bat (*Hipposideros armiger*) using 3D motion capture and aerodynamic simulations. Using the kinematic data along with numerical airflow simulations, we were able to couple the kinematic and aerodynamic analysis to show the bat using synergistic yawing and banking mechanisms. The initiation of the turn was dominated by yawing generated by elevated thrust on the outer wing during both the upstroke and the downstroke. As the bat progressed through the turn, the banking mechanism became much more dominate and generated a large lateral force imparting a centripetal acceleration.

These four studies on maneuvering bat flight—Aldridge (1988), Iriarte-Diaz and Swartz (2008), Henningsson et al. (2018), and Windes et al. (2020)—are challenging to unify due to significant differences in the maneuvers, size of the bats, as well as different data collection approaches. Limited inference on turning mechanisms can be derived from Aldridge (1988) since detailed kinematics were not collected and no aerodynamic measurements were taken. However, the data reported on flight velocity, radius of curvature, and bank angle may provide some general insight on the execution of a tight 180 degree maneuver over a range of bat species. Iriarte-Diaz and Swartz (2008), Henningsson et al. (2018), and Windes et al. (2020) all suggest that yawing in addition to banking is utilized across a diverse range of maneuvers from 4° to 90° heading change. Further, the upstroke was universally found to play at least some roll in executing a maneuver in

contrast to earlier notions that banking alone was used. The mode of turning analyzed by Iriarte-Diaz and Swartz and Windes et al., were similar and comparable mechanisms were observed in both studies—specifically the bat employed a combined yawing and banking mechanism with an emphasis on the upstroke. However, exact comparison between these two studies is challenging since aerodynamic data was not provided by Iriarte-Diaz and Swartz. Henningsson et al. observed both elevated thrust on the outer wing as well as increased drag on the inner wing, while Windes et al., only observed elevated thrust on the outer wing. Henningsson et al. also observed initiation of a maneuver using a banking mechanism.

Additional generalizations between the studies are unclear, and perhaps not appropriate. It is likely that while commonalties exist in the mechanisms used by different bats to maneuver, every maneuver will not be executed in the same way. From the limited data in the literature on the topic of maneuvering bat flight, early indications are that similar turning maneuvers across bat species share more commonalities than different maneuvers executed by similar bats. That is, the specific turning mechanisms used will be quite dependent on what the bat is trying to achieve, but for similar maneuvers commonalities may be observed across different bat species.

In trying to determine the limits of maneuverability of a bat, studying a tight U-turn can provide important insight. More gradual turns by definition do not represent the maximum possible turning capability of a bat. The data reported by Aldridge (1988) particularly illustrates the remarkable degree of maneuverability achievable by a bat. For example, *R. ferrumequinum* executed a U-turn with a minimum radius of curvature less than 1 cm. In the present work, we turn our attention to studying a similar type of turn executed by an *H. armiger* with the benefit of detailed kinematic and aerodynamic data collection and analysis tools. It is of particular interest to investigate any similarities or differences between the mechanisms used to execute a gradual turn versus a tight turn. During this analysis, we will address several key questions. What is the difference in wing kinematics between the right and left wings during the U-turn maneuver? How do the wing kinematics during a U-turn differ from straight flight? Do the wing kinematics during a U-turn primarily cause lift asymmetries, thrust asymmetries, or both? Is the U-turn achieved through banking, yaw rotation, or a combination of both? What is the relative contribution of the upstroke and downstroke during the U-turn? Comparing a sweeping turn with a U-turn, do the respective mechanisms differ in degree or in kind? What is the relative energy cost of a U-turn compared to straight flight or a sweeping turn?

2. Methods

Measurement of wing kinematic data of a great roundleaf bat (*Hipposideros armiger*) was taken inside a flight tunnel using an optical motion capture system of 28 synchronized cameras (GoPro Hero 4 Black). In order to aid wing tracking, 240 small white markers were affixed to the bat's wings. Video recording was conducted at 120 Hz and in 1920 × 1280 resolution. The large number of cameras in the setup served to both reduce self-occlusion of the wings by capturing more perspectives of the bat, as well as enlarging the capture volume. A minimum of two cameras is needed to observe a particular point in order to generate a 3D representation of that point; however, camera observation redundancy increases the robustness and precision of the measurements. The calibration of the cameras was preformed using the open source Svoboda Multi-Camera Self-Calibration toolbox [11].

The bat was allowed to fly freely inside the 1.2 m × 1.2 m tunnel, and a 180° U-turn flight was selected for analysis. Videos of the flight from each camera were processed using an in house MATLAB code to generate a time series of the 3D coordinates of the wings. The code applies standard methods of stereo triangulation coupled with a series of bat flight specific predictive motion models to aid the user in generating point correspondences. The most challenging and labor intensive aspect of collecting high spatial resolution bat wing kinematic data is establishing corresponding points between different cameras as well as between the time series of frames—referred to as the point "correspondence problem." Many of the automated methods which exist for automatically generating correspondences do not apply well to bat flight since bat wings are highly flexible and often twist and bend in unpredictable ways. Based on a survey of the literature most researches report using manual methods to establish correspondences when collecting bat flight kinematic data.

Since our aerodynamic analysis is conducted using computational simulations which require a relatively dense constellation of points to capture the wing kinematics, the use of purely manual methods for video processing is untenable. In order to address these challenges, we employ a hybrid user-supervised pseudo automated method. A fully automated correspondence method is attractive in principle but in practice introduces some problems with data quality. Since we do not have *a priori* knowledge of the correct kinematics, there is no reliable way of verifying

automatically identified correspondences. Manually checking the results of fully automated tracking becomes prohibitively labor intensive—for example, in the present work a time series of 90 frames captured by 28 cameras contains 2,520 discrete views collectively containing (240)×(2,520) = 604,800 image points to verify. In contrast, the user-supervised pseudo automated method used in the present work leverages a number of tools to maintain data fidelity while being able to process data considerably faster than a purely manual method.

After collection and 3D reconstruction of the kinematic data, we conducted numerical simulations of the airflow around the bat's wings which allow for the calculation of aerodynamic forces, moments, and power expenditure. The simulations were conducted using an incompressible Navier-Stokes solver [12] with the immersed boundary method (IBM) [13] to represent the wings in the flow. The IBM consists of embedding a surface mesh at the location of the bat wing inside the fluid domain and moving it at each integration timestep as dictated by the wing kinematic data. During solution of Navier-Stoke, a no-slip boundary condition is imposed at the location of the embedded wing mesh on both the top and bottom surface of the mesh. Further details on the implementation of the method are given in Windes et al., 2018 and Windes et al., 2019 [14], [15].

In the present study, a structured Cartesian fluid grid containing 69.1 million cells was used for the simulation. In the proximity of the bat, the fluid grid was refined to approximately 44 cells per wing chord length based on our prior grid independence analysis for similar simulations of bat flight [14], [16]. Validation of the computational method including selection of the grid refinement level is discussed further in the validation section.

During the simulation, the fluid domain was given a fixed reference frame velocity equal to the mean flight velocity of the bat to minimize the net displacement of the bat inside the domain. Since the bat performed a 180° U-turn partially returning toward the starting location, the net displacement was primarily a result of the initial 2-3 wingbeat cycles leading into the turn (see Figure 2a). In this context, the motion of the bat surface mesh relative to the background fluid grid represents the perturbation of the body location from the mean trajectory. The actual flight trajectory is recovered in post-processing by adding back the reference frame velocity to the perturbation. Since the bat travels back towards its initial position after the U-turn, there is less opportunity to constrain the size of the fluid domain by substantially moving the reference frame. Consequently, the computational cost of a U-turn simulation is larger than a straight flight of comparable duration.

The temporal discretization in the simulation was 20 microseconds per integration time step. Since this is significantly smaller than the video sample rate, intermediate point locations in the kinematic data were interpolated using piecewise cubic splines. The simulation was parallelized across 120 CPU cores using distributed memory message passing interface (MPI). The full simulation required approximately 44,000 CPU-hours to complete and was run on Intel Xeon E5-2680v3 2.5 GHz hardware.

In post-processing, two reference frames are used throughout the analysis—a ground fixed coordinate system and a body fixed coordinate system which rotates and translates along with the bat's body. The ground frame was defined such that z_g points upward exactly opposite to gravity and x_g points along the length of the flight tunnel. The body fixed frame was defined such that the origin follows the approximate center of mass of the bat body and the x_b direction remains aligned with the long axis of the bat's body and points forward. These coordinate systems are depicted in Figure 1.

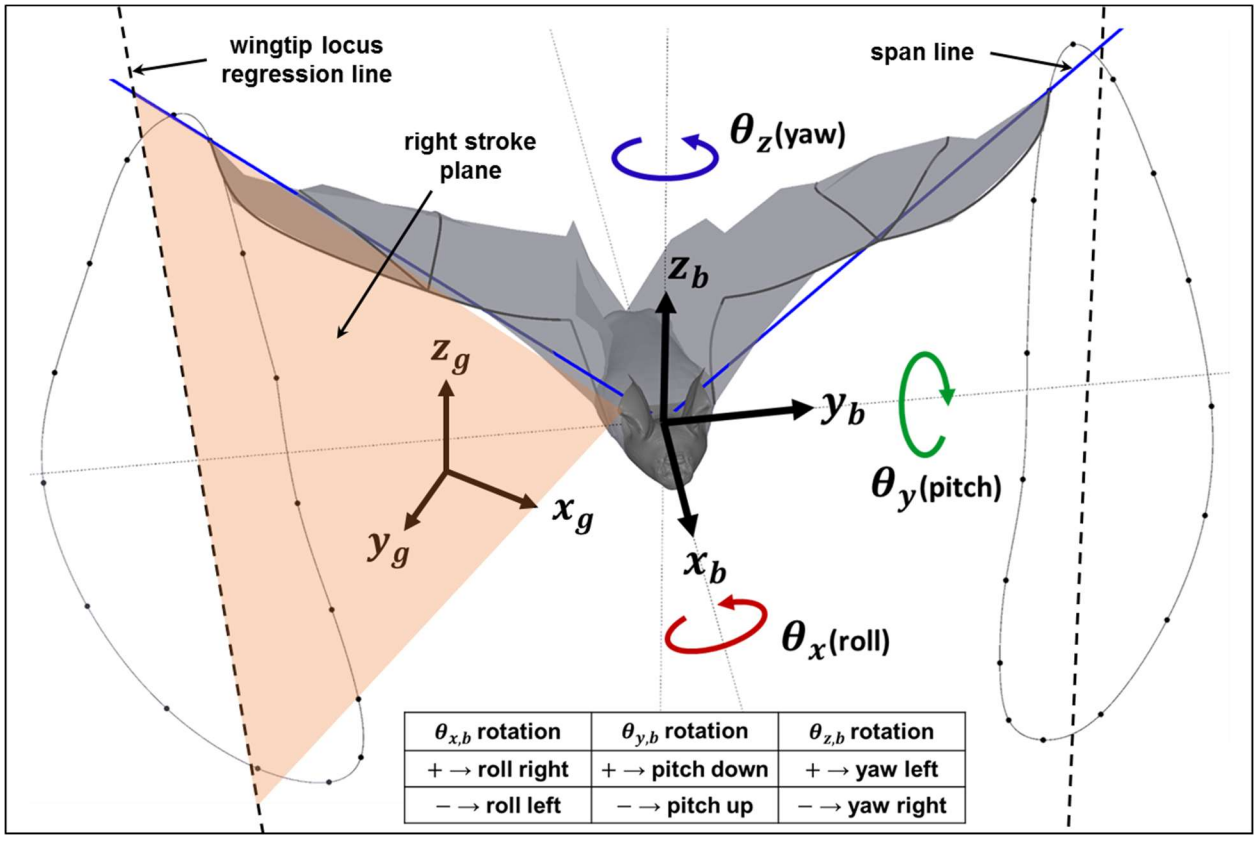

Figure 1. Ground and body coordinate systems. Rotations relative to the body frame are defined as roll, pitch, and yaw as depicted. A stroke plane is defined for the right and left wings separately by connecting the shoulder point with a regression line passing through the locus of wingtip points.

When analyzing the wing kinematic data of a non-straight flight, the right and left wings must be treated separately to identify asymmetries which drive the maneuver. A separate stroke plane is defined for each wing by joining the shoulder point to a regression line passing through the locus of points traced out by the wingtip (Figure 1). This calculation is done on the wingtip trajectory in the body fixed coordinate system. Since the stroke plane may vary temporally, a new stroke plane is calculated for each cycle updated every half cycle. A vertical stroke plane angle is defined by projecting the wingtip regression line onto the body-fixed $x_b - z_b$ vertical plane and is the angle between the line and the x_b axis. It is representative of the forward-backward movement of the wing – smaller the vertical stroke plane angle, larger is the fore-backward movement of the wing with respect to the flight direction. A horizontal stroke plane angle is defined by projecting the wingtip locus regression line onto the body-fixed $x_b - y_b$ plane and the angle between the projected regression line and the y_b axis is taken as the horizontal stroke plane angle. It is representative of the lateral movement of the wingtip. Motion of the wings relative to the stroke plane is quantified by the flap angle, stroke plane deviation, and half span. The flap angle represents in plane rotation of the spanline while stroke plane deviation represents out of plane rotation of the span line. The half span is the instantaneous distance between the shoulder and the wingtip.

The aerodynamic metrics calculated are force, moment, and power. The pressure and velocity fields in proximity to the wing surface which are generated by the simulation are used to calculate force on each discrete element of the wing $\left(\vec{F}_e\right)$ over the duration of the flight. Net aerodynamic force represents the surface integration of the surface element forces. The rotational moment is calculated relative to the middle of the bat's body by integrating $\vec{M}_b = \vec{r}_e \times \vec{F}_e$ over the surface of the wings. Aerodynamic power was obtained by integrating $P_{aero} = \vec{F}_e \cdot \vec{v}_e$ over the wing surface. Total power expenditure was calculated as the sum of aerodynamic power, rate of change of kinetic energy, and rate of change of potential energy.

3. Results

The bat studied is an adult male *H. armiger* weighing 54.5 g and has a maximum outstretched wingspan of 51 cm as measured during the downstroke from the kinematic data. Relevant morphological parameters are shown in Table 1.

Table 1. Morphological parameters of the subject.

Mass (g)	Span (cm)	Wing Area (cm^2)	Planform area (cm^2)	Mean chord (cm)	AR	Wing loading (N/m^2)
54.5	51	434	398	7.8	6.5	13.4

H. armiger is a somewhat larger bat in both mass and wing span compared to species previously investigated in prior studies of maneuvering bat flight [10], [17]. According to data reported by Norberg (1987), the majority of bat species fall between 5 and 100 g with extreme values ranging from 2 g up to 1 kg. Based on a correlation of body mass and wing area over 257 bat species, the wing surface area of *H. armiger* is slightly larger than other species of similar mass. The aspect ratio of *H. armiger* falls near the middle of the distribution. The kinematic and aerodynamic mechanisms driving a flight maneuver can be compared across bat species; however, one must consider the morphological differences between the bats when making the comparison.

3.1 General Description of U-turn Flight

The flight selected for the present analysis consists of six wingbeat cycles over a duration of 690 ms and includes both the approach to the U-turn in addition to the U-turn itself. Figure 2 shows the flight trajectory of the bat's body from the top view ($x_g - y_g$ projection) and the side view ($x_g - z_g$ projection). Over the course of the entire flight, the bat first begins to gradually turn and climb, then executes a tight U-turn, and lastly descends while exiting the turn. This sequence can be categorized into four phases:

- Phase 1, approach: Prior to entering the U-turn, the bat executes a gradual right turn, decreases its flight velocity, and begins to climb. This phase consists of wingbeat cycles 1 and 2.
- Phase 2, initiation of U-turn: The bat rapidly tightens the radius of the turn while continuing to climb and decelerate. This phase consists of wingbeat cycles 3 and 4.

- Phase 3, apex of U-turn: During the apex of the U-turn, the bat rapidly changes both heading and bearing angle. The bat reaches a maximum height, minimum radius of turn, and minimum flight velocity during this time. This phase consists of wingbeat cycle 5.
- Phase 4, U-turn egress: After the apex of the turn, the bat begins to accelerate, descend, and straighten out the flight trajectory. During the egress, the bat continues to turn, but the radius of the turn increases rapidly. The U-turn egress consists of cycle 6.

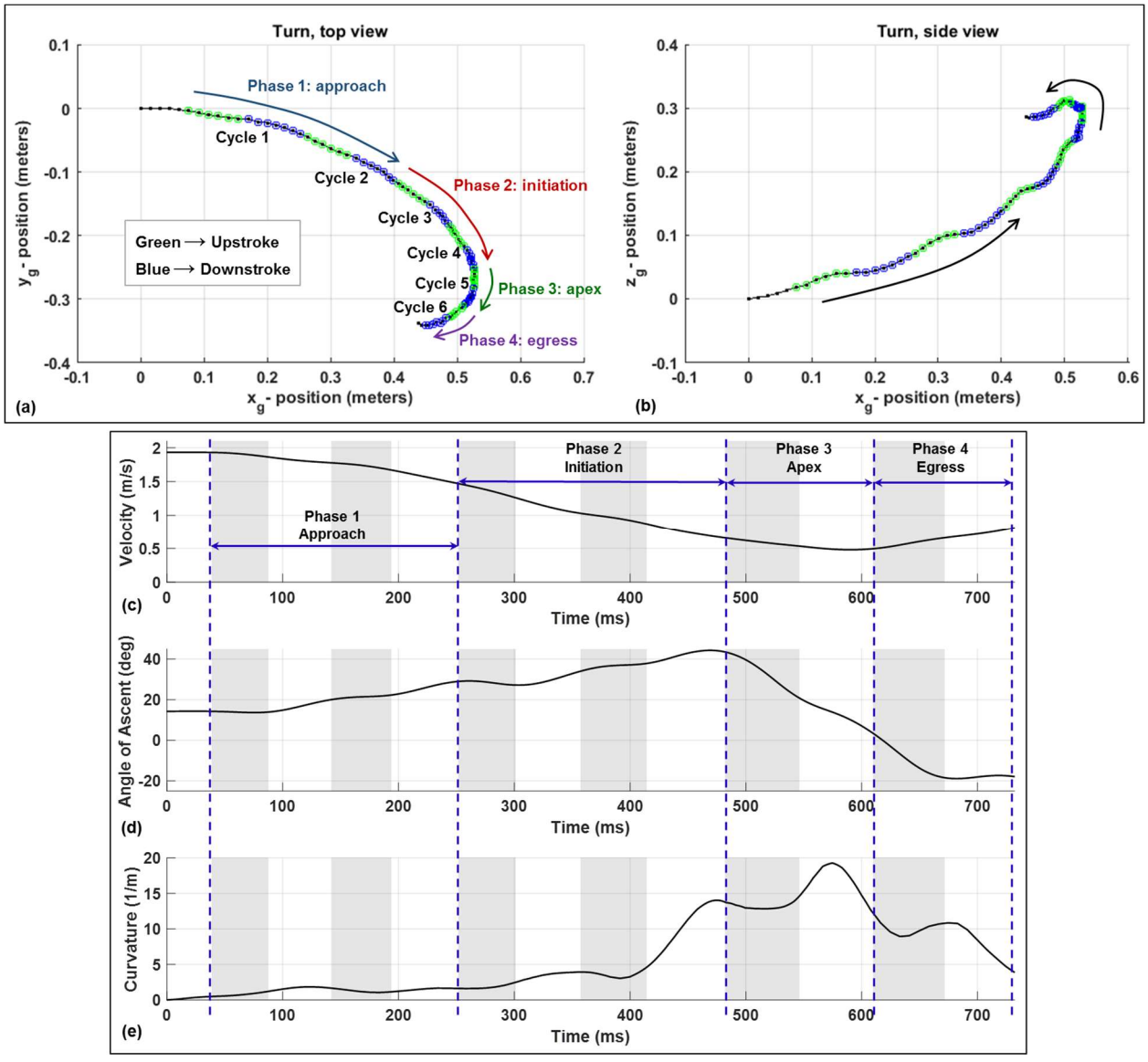

Figure 2. Top: Body trajectory of the bat during the U-turn flight from the top and side view. Bottom: Velocity, angle of ascent, and curvature of the turn. The curvature is defined using the standard definition: (radius of

curvature)$^{-1}$. The grey shaded regions denote upstrokes, and one complete wingbeat cycle consists of the upstroke+downstroke.

Phase 1, the approach, consists of a deceleration from 1.93 m/s to 1.47 m/s, and an increase in angle of climb from 14 to 30 degrees. Simultaneously, the radius of curvature decreases from 200 cm to 60 cm (curvature change 0.5 to 1.7 m^{-1}) and the bearing angle changes from 15 degrees to 28 degrees. During phase 2, the initiation, the bat continues to climb and decelerate, but more notably rapidly decreases the radius of curvature to 7 cm (curvature of 14 m^{-1}) towards the end of this phase. The bat reaches its maximum height, minimum turn radius of 5.5 cm (curvature of 18 m^{-1}), and minimum velocity of 0.48 m/s during phase 3, the apex of the turn. Between the upstroke and downstroke of cycle 5 the bat is oriented in the y_g- direction which is perpendicular to the long axis of the flight tunnel (x_g − direction). Subsequently, the bat egresses the U-turn during phase 4, accelerating from 0.49 m/s to 0.71 m/s, increasing its radius of turn from 6 cm to 93 cm (curvature change 17 to 1), and begins a descent. By the end of cycle 6, the bat is descending at an angle of 20 degrees and has dropped about 3 cm vertically (z_g- direction) from the apex of the U-turn.

Results from a previously analyzed straight flight (Windes et al., 2020) are included in the present paper for comparison where appropriate. The straight flight data comes from the same *H. armiger* bat flying at approximate 2.0 m/s and was collected using the same experimental setup and computational analysis methods.

The following sections present analysis of the wing kinematics as well as analysis of the aerodynamic forces calculated using numerical flow simulation.

3.2 Wing Kinematics Analysis

Aerodynamic force asymmetries which allow the bat to maneuver are generated by the wing kinematics during the flight. Figure 4 provides a high level characterization of the wing kinematics based on the orientation of the stroke plane. The vertical and horizontal stroke plane angles capture the orientation of the total wing motion over each half-cycle. A more granular representation of the wing motion is provided in Figure 4. The motion of the wings relative to the stroke ***plane are characterized by the flap angle, stroke plane deviation angle, and the half-span for the 180 degree U-turn flight (a) and a straight flight (b) for comparison.***—the flap angle, stroke plane deviation angle and

half span capture the instantaneous position of the right and left wingtips relative to the stroke plane. The difference between the stroke plane angles (Figure 3) and the wing position parameters (Figure 4) can be described as kinematic trends across flap cycles versus trends within a single flap cycle.

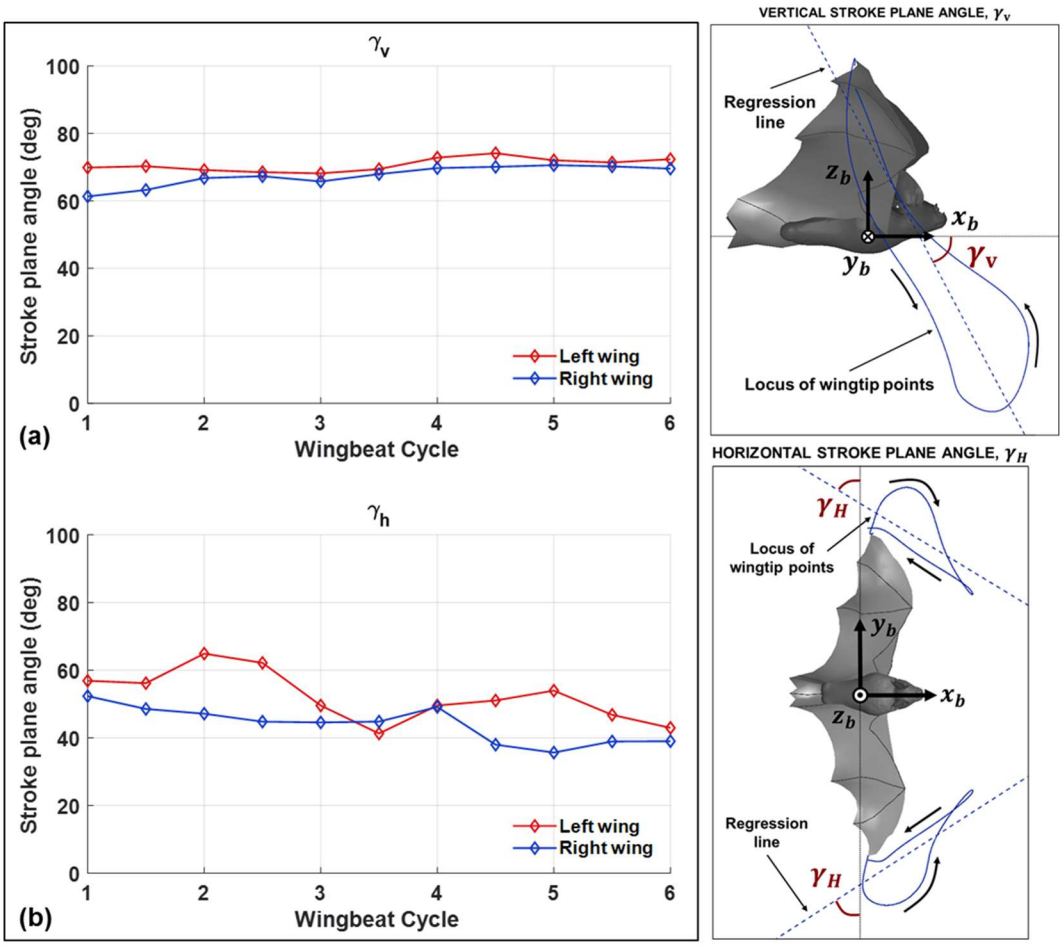

Figure 3. The vertical (a) and horizontal (b) stroke plane angle are shown for the right and left wing separately at each half-cycle as defined in the schematic above.

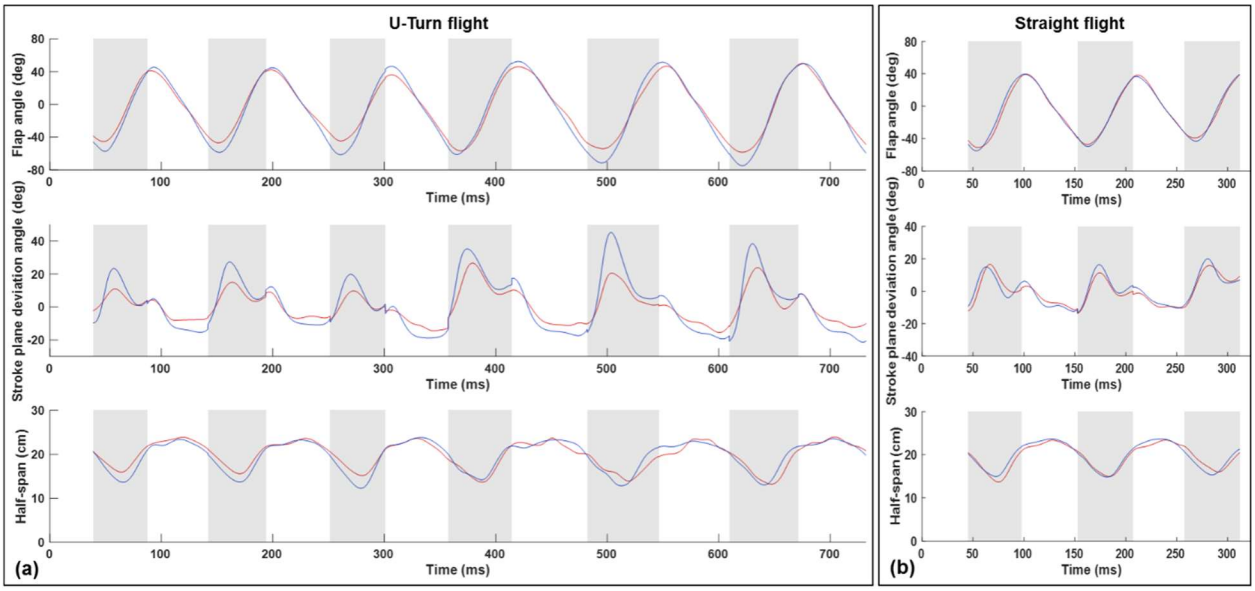

Figure 4. The motion of the wings relative to the stroke plane are characterized by the flap angle, stroke plane deviation angle, and the half-span for the 180 degree U-turn flight (a) and a straight flight (b) for comparison.

During straight flight, the right and left wings exhibit a high degree of symmetry. The flap angle varies between -50 degrees to 40 degrees, the stroke plane deviation angle is bounded by -15 degrees during the downstroke and 20 degrees during the upstroke, and the half span varies between a maximum value of approximately 25 cm to a minimum value of 14 cm during the upstroke when the wings are retracted towards the body. For the flight trajectory in this study, while relative symmetry exists in the vertical stroke plane angle, the horizontal stroke plane angle exhibits up to 30-40% difference between the right and left wings during portions of the flight. Specifically, the left wing on the outside of the turn has a higher angle relative to the right wing indicating that the right wing tip has stronger lateral movement. A similar trend was observed when analyzing a sweeping turn conducted by the same bat (Windes et al., 2020). In fact, during this flight, the right left asymmetry is not any greater during the U-turn (phases 2 to 4) when compared to the approach in phase 1 when the bat is gradually turning right. This indicates that modulation of the stroke plane orientation is not a major mechanism used by the bat to execute a tight U-turn compared to a gradual turn.

While the orientation of the stroke plane does not materially differ between gradual and tight turns, the wing motion relative to the stroke plane does differ significantly. During the initiation phase of the U-turn, the amplitude of the flap angle increases for both the right and left wings and the wingbeat frequency decreases simultaneously (Figure 5). Especially apparent in the

frequency plot, there is a sharp decrease in frequency between the third and fourth wingbeat cycles. This correlates closely with both a decrease in flight velocity as well as a rapid decrease in radius of curvature of the turn (Figure 2). The decrease in radius of curvature can be equivalently described as an increase in angular velocity about the body-fixed z_b- axis. A coordinated increase in flap amplitude and decrease in frequency allow the bat to maintain sufficient lift entering the U-turn. Throughout the flight, during both the approach and U-turn, the right wing to the inside of the turn exhibits a larger amplitude of flap angle relative to the left wing. This correlates with right/left asymmetry of the stroke plane deviation angle and is maximum during the early part of each upstroke. In the stroke plane deviation trend, a sharp change can be seen between cycles 1-3 and cycles 4-6. This indicates that the protracted motion of the right wing (inside the turn), which is a key marker of turning flight, increases proportionally to the tightness of the turn. The protracted motion is characterized by the wing tip exhibiting a larger downward and forward motion on the initiation of the upstroke than it normally does in level flight.

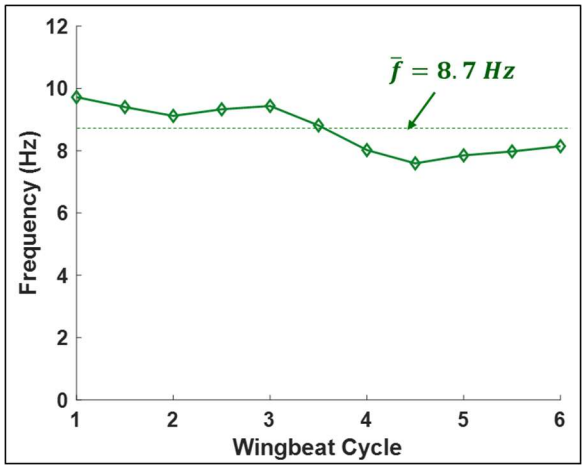

Figure 5. Wingbeat frequency by half-stroke. The mean frequency over the flight is 8.7 Hz.

In order to further examine the wing kinematic asymmetry driving the U-turn, the trace of the wingtips and wrists are provided in Figure 6. Equivalent kinematics of straight flight is also shown for comparison. The dash lines represent the projection of the stroke plane and represent the vertical and horizontal stroke plane angles in the side and top view, respectively. The general trace of the wingtip in the top view ($z_b - y_b$) identifies the full span of the wing as the bat stretches both wings out laterally during the downstroke, only to retract them inward towards the body on

the upstroke. As shown in Figure 4, the motion of the wing in z_b −direction denoted by the flap amplitude varies between -50 degrees to 40 degrees for straight flight. The side view $(z_b - y_b)$ shows that the wing sweeps back-to-front during the downstroke and front-to-back during the upstroke. As expected the straight flight exhibits a high degree of symmetry between the left and right wing motion. In contrast, during the gradual turning phase, modest but consistent right/left asymmetry can be observed throughout cycles 1-3; however, there is not much apparent temporal variation between the flaps. The asymmetry manifests as the right wing (inside of the turn) exhibiting a broader lateral traverse or larger stroke plane deviation. The inflection between the sweeping portion of the turn and the initiation of the U-turn occurs during the fourth cycle. During the fourth cycle not only does the right wing exhibit a large increase in stroke plane deviation as seen in the back view of the wingtip trace but also substantially increases the forward sweep of the wing during the upstroke as manifested in the side and top views. This is also accompanied by an increase in stroke plane deviation and forward sweep of the left wing but to a lesser extent than the right wing. As the bat approaches the apex of the turn in cycle 5, it retracts the right wingtip further towards it body during the upstroke resulting in still larger deviations from the stroke plane, while the left wing starts returning to its normal motion. This suggests that the left wing protraction may be marginally more impactful to the initiation of the U-turn while the right wing protraction is impactful to the execution of the U-turn. As the bat exits out of the U-turn in cycle-6, the left-right asymmetry still exists but returns to a state similar to that prior to cycles 4 and 5.

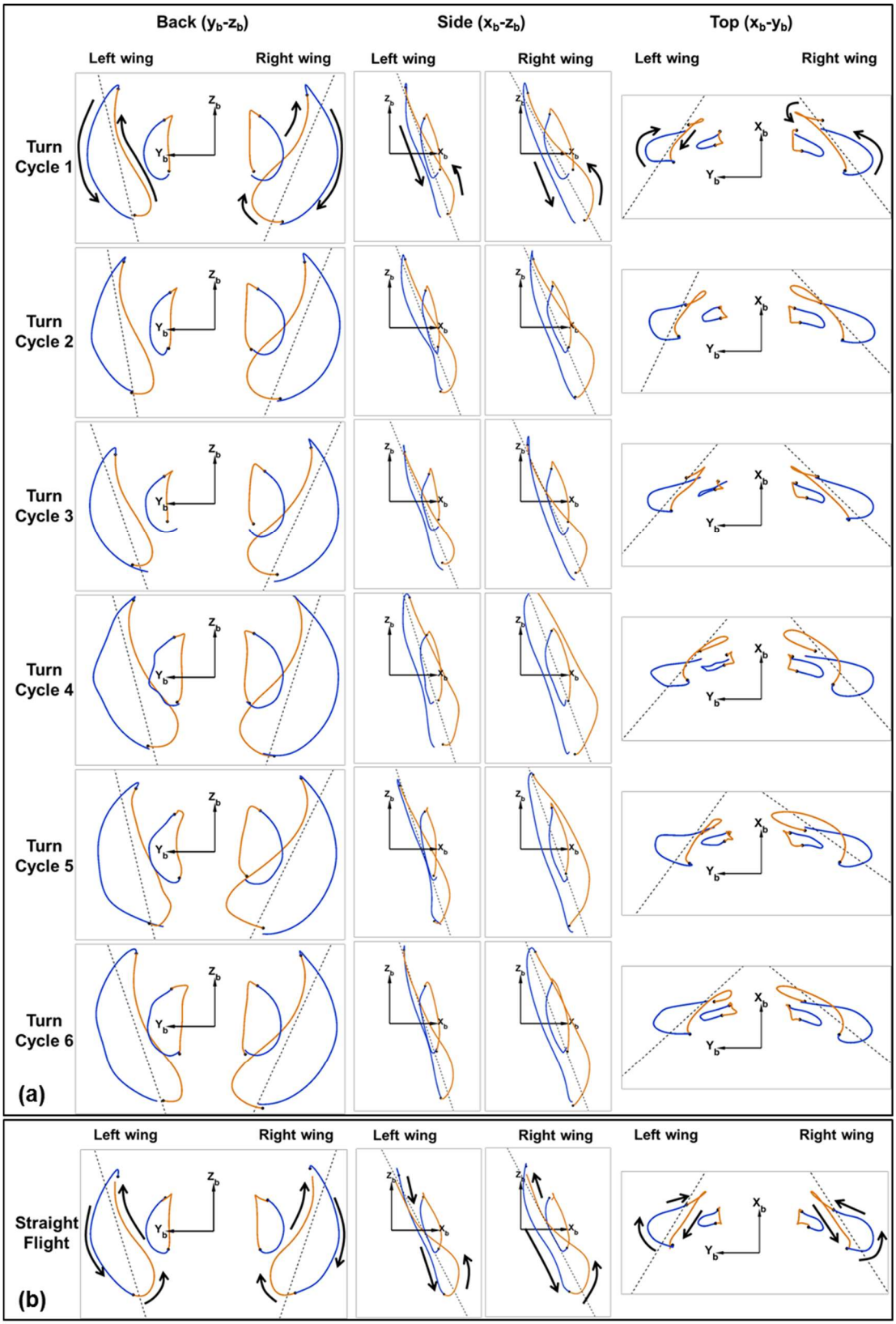

Figure 6. Trajectory of the wingtip and wrist for each wingbeat cycle of the U-turn shown in the body fixed coordinate system (a). A comparison from a representative straight flight is also provided (b).

In summary, from the kinematics we see a sharp reduction in wingbeat frequency and increase in stroke amplitude as the bat initiates the U-turn. This change persists throughout the U-turn. The stroke plane angle data—i.e. small right/left asymmetry—suggest that asymmetries within each wingbeat cycle relative to the stroke plane drive the U-turn maneuver as opposed to changes in the mean orientation of the stroke plane. The larger flap amplitude and larger stroke plane deviation of the right wing (towards the inside of the turn) relative to the left wing exists throughout the initiation of the maneuver and increases during the apex phase. From the wingtip traces, it can be seen that at the end of the downstroke and the beginning of the upstroke the right wing moves more laterally across the bat's body. The rotational inertia of wing can produce a counter rotation of the body into the turn to conserve angular momentum of the wing-body system. In order to further explore the turning mechanisms and to assess the relative importance of these observed inertia effects with aerodynamic mechanisms, we must investigate the aerodynamic forces generated by the wings during the maneuver.

3.3 Aerodynamic Simulation Results

Analysis of the aerodynamic forces during the U-turn allows us to examine how the wing kinematic asymmetries translate into turning forces and moments. Figure 7 shows the aerodynamic force coefficients throughout the flight in the body-fixed reference frame along with data from a straight flight (Windes et al., 2020) as a baseline for comparison.

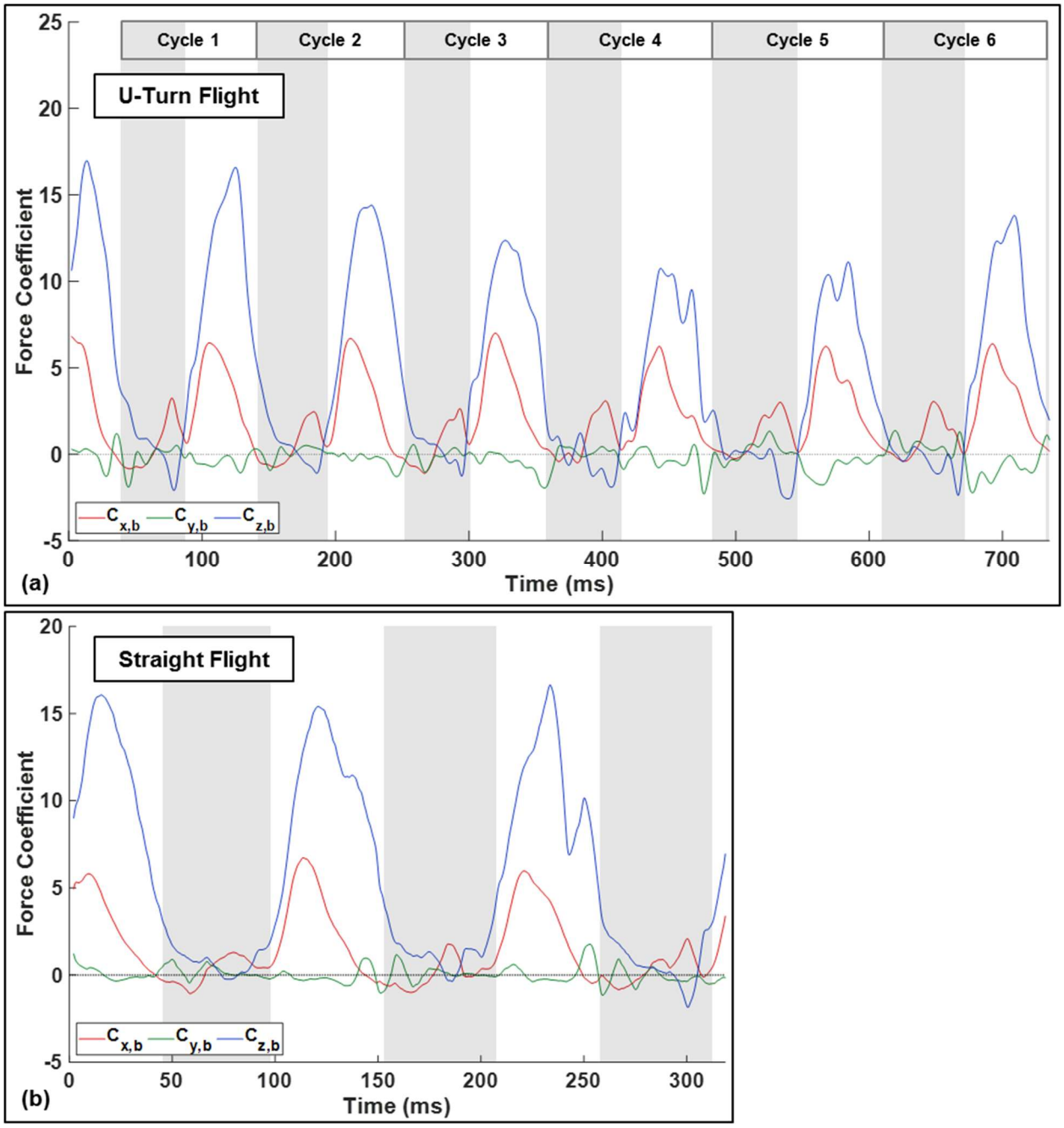

Figure 7. Force coefficients in the body frame for the U-turn flight (a). For comparison, results from a straight flight by the same bat is also provided (b).

In both flight regimes (straight and U-turn), the lift force, responsible for keeping the bat aloft, has the largest magnitude of the three components and peaks during the mid-downstroke. During the upstroke the bat avoids creating negative lift by retracting the wing inward towards its body and controlling the motion of the wing such that minimal fluid forces act on the wing. By

doing so, in normal straight flight not only is negative lift avoided but also very little drag is induced during the upstroke – in fact some thrust is produced at the end of the upstroke. Upstroke thrust has been observed many times in bat flight as the flexible outer wing moves upward and backward during pronation to position for the downstroke; however, it is not universally present in all modes of flight. In spite of the small amount of thrust produced by the wings during the upstroke, seemingly the sole purpose of the upstroke in straight flight is to position the wing for the downstroke during which the bulk of lift and thrust is produced.

During the recorded turning flight, the magnitude of lift force is largest during the approach phase in cycle-1 and steadily decreases till it increases in magnitude after cycle-4 as it initiates the tight U-turn and starts to ascend sharply. One important distinguishing factor from straight flight is the generation of negative lift towards the end of the upstroke in cycles 4 through 6 during the initiation and execution of the U-turn. While negative lift is produced during all six cycles, it is noticeably larger during cycle-4 and cycle-5. Not coincidental is the accompaniment of an increase in negative lift by an increase in positive thrust. Cycles 1-3 produce modest thrust (although noticeably larger than straight flight) near the conclusion of the upstroke and is accompanied by modest negative lift. This changes for cycles 4 and 5, which see relative larger magnitudes of thrust and negative lift during the upstroke. The bulk of thrust production occurs during the downstroke and peaks in value slightly earlier than the peak in lift. During turning flight, the magnitude of the thrust during the downstroke remains relatively constant for the first three cycles during the approach and initiation of U-turn, but increases in magnitude in cycle-4 and 5 during the U-turn and remains high in cycle-6. During the U-turn, upstroke thrust is accentuated and correlates with the decrease in radius of curvature. In order to achieve the elevated upstroke thrust, the bat allows larger negative lift.

The observed trends in kinematics and subsequent lift and thrust production point to the following scenario. Since the bat gains both height and vertical velocity during the approach and initiation of the U-turn, it down prioritizes lift during the tight portions of the U-turn in exchange for achieving rotation. In fact, we do see a decrease of vertical velocity, cresting, and subsequent decent during and after the apex of the U-turn clearly showing that the lift force drops below what would be required for maintaining altitude. This allows the bat to focus on generating excess lift entering the U-turn and subsequently prioritize rotation during the U-turn.

Contrary to lift and thrust, the lateral y_b- force oscillates around zero and the cycle mean remains near zero throughout the flight. This mirrors observations from prior turning flights in which yawing (moment generation about z_b) and banking (tilting the lift force laterally) primarily drive the turn as opposed to a y_b- force.

Validation of the computational framework for simulating bat flight has been conducted as a part of several of our prior studies (see [14]–[16]). However, in order to provide additional validation for this specific flight case, a mass dynamics analysis was run. The aerodynamic forces generated by the simulation were divided by the mass of the bat in order to get a predicted acceleration. The acceleration was integrated twice to obtain predicted position and velocity which is compared to the observed trajectory derived from the motion capture data. This is shown in Figure 8.

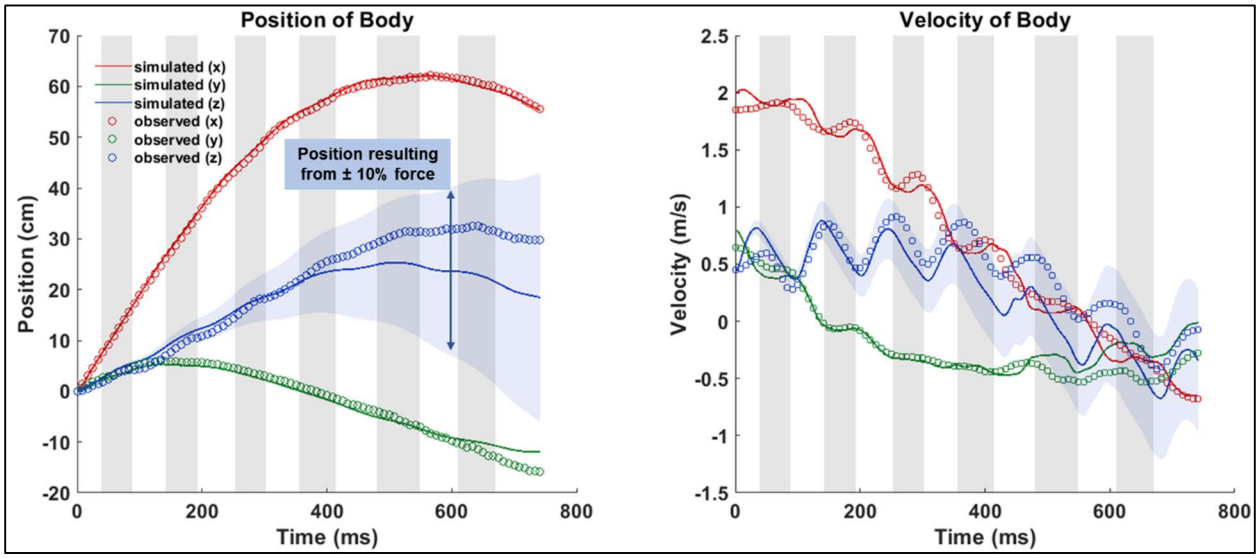

Figure 8. Comparison of observed and predicted position and velocity of the bat body.

Over the six wingbeat cycles, close agreement is seen in the global x and y-directions. The force in the z-direction is slightly under predicted but falls within a reasonable margin of error. Overlaid on the figure is an envelope containing the range of predicted z-position admitting to a possible ±10% over or under prediction of force. Due to the time integration, a constant force error accumulates substantially in the predicted position. Therefore, it is more appropriate to evaluate the predicted position relative to the envelop instead of the absolute deviation. Exact estimation of

aerodynamic force is challenging in live flying animals and the ±10% envelop represents a reasonable margin of error based on what is typically achievable using a range of techniques [18].

In order to characterize the progress of the maneuver over time, Figure 9 provides the temporal evolution of rotational orientation in three-dimensional space. Three orientation angles—roll, pitch, and yaw—characterize the rotation of the bat's body in space. However, the instantaneous direction of flight as represented by the orientation of the velocity vector does not always exactly coincide with the body orientation as previously recognized by Iriarte-Diaz et al., 2008 and Windes et al., 2020. The difference between the body orientation and velocity vector orientation is illustrated in two schematics in Figure 9.

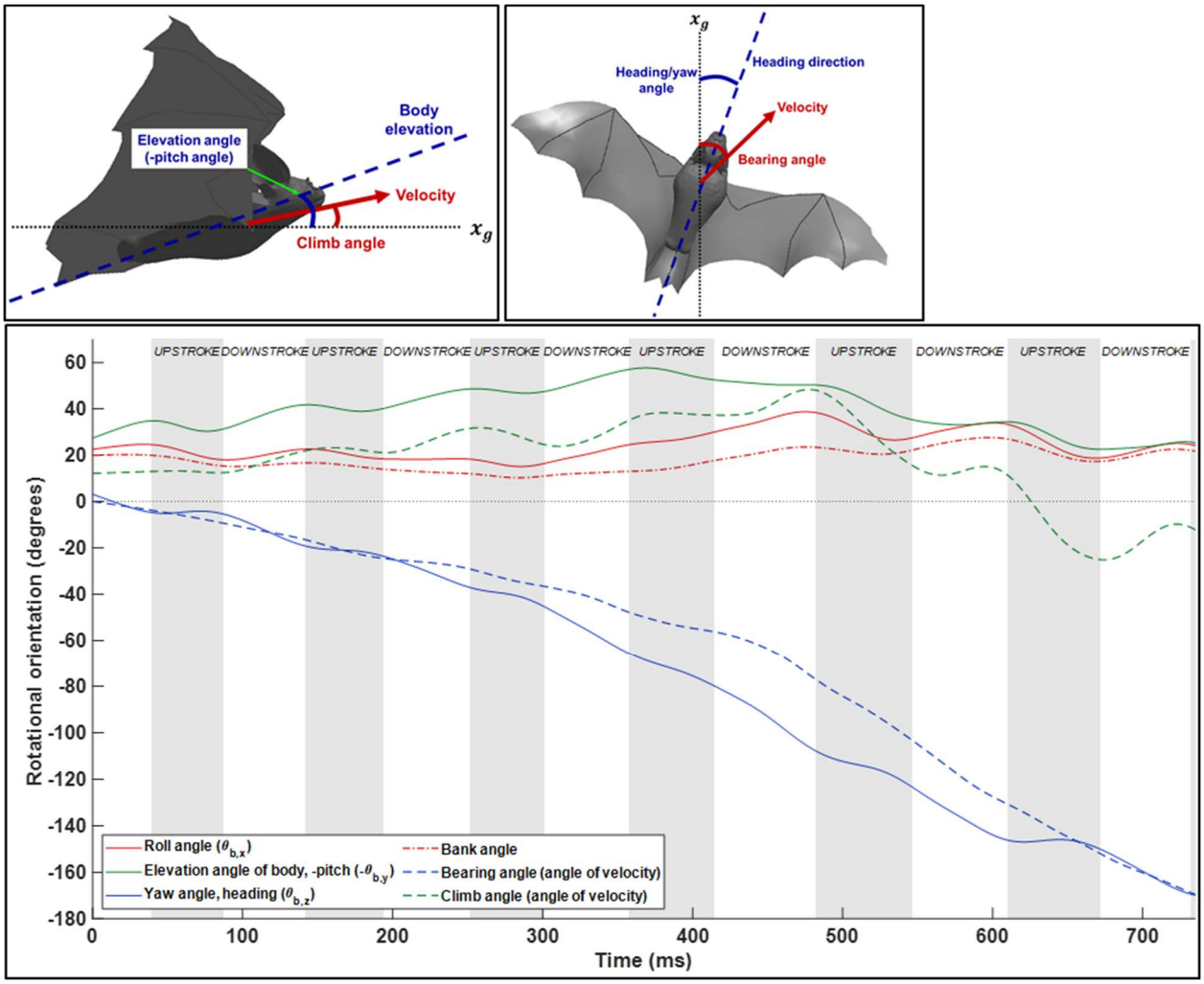

Figure 9. Rotational orientation of the bat using both body-based angles (roll, elevation, and yaw) and velocity-based angles (bearing angle and climb angle).

Figure 9 provides the three body orientation angles, yaw (or "heading") angle, elevation angle (negative pitch), and the roll or bank angle. The velocity vector orientation is described by the bearing and climb angle. Broadly speaking, the bearing angle characterizes the turning component of the maneuver, while the climb angle describes the increase in height throughout the flight. Both of these angles are calculated based on the instantaneous orientation of the velocity vector relative to the ground reference frame. In contrast, the bank angle describes not the turn itself but rather the mechanism by which the turn is achieved. The yaw or heading angle when viewed in relation to the bearing angle indicates the deviation between the direction the bat is facing relative to the direction of the velocity vector. As expected, the trend in heading generally corresponds to the trend in bearing angle. That is, the bat nominally flies in the direction its body is facing. However, small differences between these angles describe whether changes in body orientation lead or lag the reorientation of the flight path.

Throughout the approach, the difference between heading and bearing are negligible. Beginning in the initiation phase, the heading angle begins to change prior to change in the flight path. This suggests that the bat is using yaw rotation to reorient into the turn during the initiation phase of the U-turn. This closely mirrors observations seen by Iriate-Diaz et al., 2008 where turn initiation was mediated by yaw rotation [17]. The deviation between heading and bearing decreases during the apex of the U-turn and is eliminated during the egress. The trend between the heading and bearing angle shows that while the bearing angle undergoes a rapid change starting at cycle 4, the heading changes gradually over the whole U-turn maneuver. One explanation for why the heading change is more gradual over several flaps while the bearing change is comparatively more rapid, is that a change in the heading angle requires a yaw moment—the magnitude of the yaw moment is limited to some maximum value based on the upper limit of force asymmetry the wings can achieve. In contrast, the change in bearing angle can be partially achieved through tilting the net force vector by banking. Lift is the largest and most naturally generated force so simply redirecting this force through banking is less burdensome in comparison to generating large yaw moments.

The bat sustains a roll angle of approximately 20-25 degrees throughout the approach phase of the flight. This rapidly increases beginning at cycle 3 during the initiation phase of the U-turn to a final maximum of nearly 40 degrees. The peak roll angle is observed during end of the initiation phase and remains elevated throughout the apex before decreasing during egress. The

increase in roll angle from 20 to 40 degrees closely corresponds to the point at which the bearing angle begins to change rapidly during cycle 4. Taking the heading, bearing, and roll angle together, we can conclude that the bat begins yaw rotation early in the U-turn which persists throughout the entire U-turn, while in contrast the change in bearing is related somewhat to the yaw but more significantly to the increase in roll angle.

The elevation angle describes the upward inclination angle of the bat's body while the climb angle describes the inclination of the velocity vector. Prior studies have indicated that the elevation angle is persistently higher than the climb angle during all modes of flight (Windes et al., 2020). That is, the bat naturally flies with a slight body inclination of approximately 20 degrees during level flight. In the present flight, during the approach the bat initially climbs at 10 degrees increasing up to 30 degrees by the beginning of the initiation of the U-turn. The elevation angle is uniformly 20 degrees higher than the climb angle throughout the approach. During the initiation of the U-turn, the climb angle continues increasing from 30 degrees to the maximum of 43 degrees. Subsequently throughout the apex and egress, the climb angle rapidly decreases reaching zero (horizontal relative to the ground frame) in cycle 6. During the egress, the bat begins to descend (i.e. negative climb angle); however, the elevation angle of the body remains positive. One key result of this is that the lift force vector remains more vertically oriented. During decent, the bat is able to leverage gravitational force to accelerate and is not incentivized to use a large thrust force to achieve this.

Examination of the bat's body and velocity orientation angles suggests that rolling is responsible for a large portion of the bearing angle change during the U-turn. In order to further investigate this phenomenon, Figure 10 shows the net force in components of tangential, radial, and vertical force defined relative to the trajectory of the flight. Tangential force acts to accelerate or decelerate the bat along the trajectory, radial force acts perpendicular to the tangent of the trajectory and serves to change the bearing angle, and the vertical force opposes gravity keeping the bat aloft or allowing the bat to climb.

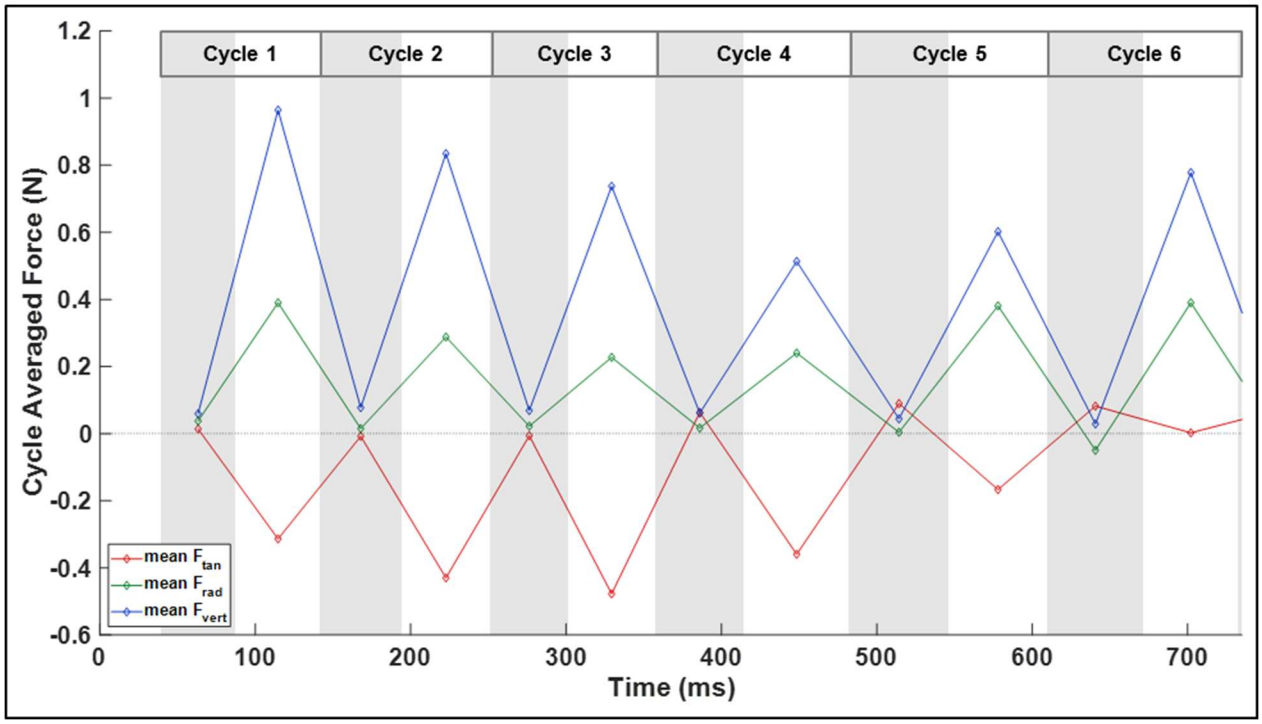

Figure 10. Tangential, radial, and vertical components of aerodynamic force relative to the flight trajectory.

The vertical force, although defined relative to the ground vertical axis, shows a similar trend to the body frame lift force. That is, when the bat begins to climb in the approach phase the vertical force is maximum. As the rate of height gain decreases throughout the initiation and apex phases, the vertical force decreases. As the bat egresses the U-turn, it arrests its rate of descent by slightly beginning to increase the vertical force to a magnitude which supports its weight. This serves to arrest its descent towards a more gradual downward trajectory preventing a precipitous loss of altitude. The tangential force remains negative over the first four cycles corresponding to the observed deceleration. This is critical to maneuvering a tight turn since it decreases the required centripetal force to achieve a given radius of curvature. For a bat of a given mass to achieve a turn of a particular radius of curvature, the radial force requirement increases with the square of the tangential velocity. That is, to achieve a turn with a radius of 6 cm, a bat flying at 1 m/s would need to achieve 4 times the radial force compared to a 0.5 m/s tangential flight velocity. For the present flight, the negative tangential force causing deceleration is minimum during the initiation phase of the U-turn, specifically during the third wingbeat cycle.

The radial force causes a centripetal acceleration of the bat causing a change in trajectory of the flight. This centripetal acceleration directly causes the change in bearing angle shown in

Figure 9. While it may be expected that the radial force would be maximum during the apex of the turn, it is critical to keep in mind the large impact that flight velocity has on the required radial force. Since the bat is decelerating throughout the initiation of the turn, the required radial force actually decreases substantially during the apex of the U-turn relative to the prior cycles. This is one additional explanation for why the lift force decreases during the apex of the U-turn—the lift force vector which is tilted radially by the roll angle does not need to be as high to turn the bat given the lower flight velocity.

The radial force as shown in Figure 10 explains the change in bearing angle and flight trajectory; however in order to investigate the change in body orientation—roll and heading—we need to view the action of rotational moments on the bat which re-orient the body. The aerodynamic force moments relative to the estimated center of mass of the bat are shown in Figure 11a. Moments on the bat induce angular accelerations which change the angular velocity of the bat's body. Thus, the angular acceleration is provided as well in Figure 11b. The center of mass for the purpose of calculating the moments was approximated as a fixed point on the middle of the bat's body. The aerodynamic moments and the angular accelerations are related by the moment of inertia of the body-wing system which is time-varying as the wings flap. While the trends in moment and angular acceleration should be similar, the plots should not be expected to match up completely since the moment of inertia varies temporally.

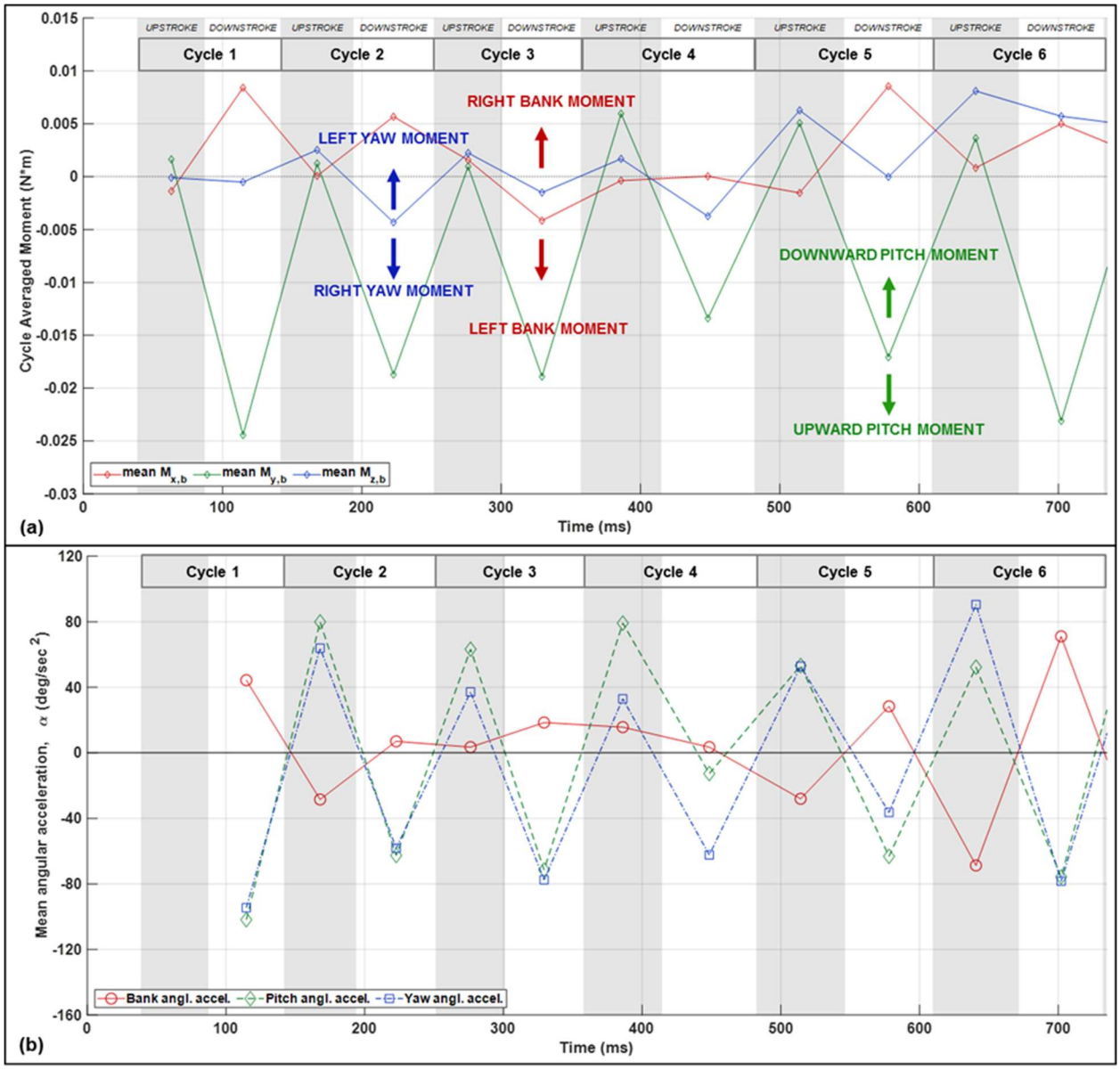

Figure 11. Half-cycle mean aerodynamic moments relative to the approximate center of mass calculated from the aerodynamic forces (a). Half-cycle mean angular acceleration of the bat body defined as rate of change of rotational velocity about the body-fixed coordinate axes (b).

Explanation of the moments is best conducted by observing general trends in the plots. This is because there are a few factors which contribute to the challenge of interpreting rotational moments in a very specific time-dependent manner. First, as the wings flap the location of the center of mass shifts thus the moments shown are only an estimate of the precise rotational moment. Second, the rotational moments are derived only from the aerodynamic forces. In addition, inertial moments may also contribute to reorienting the bat's body. Thus, the

aerodynamic moments are not guaranteed to explain 100% of the body rotation. However, despite these caveats, the trends in the aerodynamic moments are largely consistent with the observed changes in angular orientation. Additionally, comparing the aerodynamic moments and the angular acceleration can provide insight as to the relative contribution of aerodynamic mediated rotation versus inertia mediated rotation.

Negative yaw moment (right yaw) is observed during the downstroke of cycles 2-4 during the period of the turn when yaw angular velocity is increasing. Subsequently, during the later portion of the apex and moving into the egress, the rate of yaw rotation decreases and correspondingly the yaw moment becomes positive. This trend in the yaw moment corresponds to the trend observed in the angular acceleration. In addition, both yaw moment and yaw acceleration vary substantially between the upstoke and downstroke; during the downstroke, yaw moment and acceleration is directed into the turn while counter rotation is observed during the upstrokes. During the initiation, the magnitude of the right yaw during the downstroke is greater than the left yaw during the upstroke resulting in a net right rotation. The yaw rotational acceleration is slowed during the apex and egress of the U-turn. It is important to recognize that the yaw moment and angular acceleration describe the rate of change of the angular velocity—thus despite the rate of yaw rotation decreasing during the apex and egress, the yaw angular velocity maintains a right rotation through the duration of the flight. That is, the rate of right yaw rotation slows during the later portion of the maneuver but right rotation persists throughout the maneuver.

Both the roll and yaw moments are highly variable between the upstroke and downstroke. Generally for a right turn, right roll and right yaw are maximum during each downstroke and reverse during each upstroke. This provides two available mechanisms for increasing net moment across a complete wingbeat cycle. Either the downstroke moment may be elevated or the reverse moment during the upstroke may be mitigated. Thus despite the majority of the right roll and right yaw moment generation during the downstroke, modulation of the moment during the upstroke will contribute to the net moment experienced over the course of a full wingbeat cycle. An additional consideration is that roll rotation may be mediated by inertial effects. Roll moment is positive during downstrokes 1 and 2, indicating right roll; however, throughout the initiation phase (cycles 3-4), the aerodynamic roll moment does not appear to fully explain the roll angular acceleration shown in Figure 11b and the orientation shown in Figure 9.

In order to examine the source and nature of the aerodynamic moments at various points in the wingbeat cycle, the aerodynamic force in the body frame is broken up by the region of the wing on which it acts and is shown in Figure 12. Nominally, asymmetry in the x_b-force will cause yaw moments while asymmetry in the z_b-force will cause roll moments.

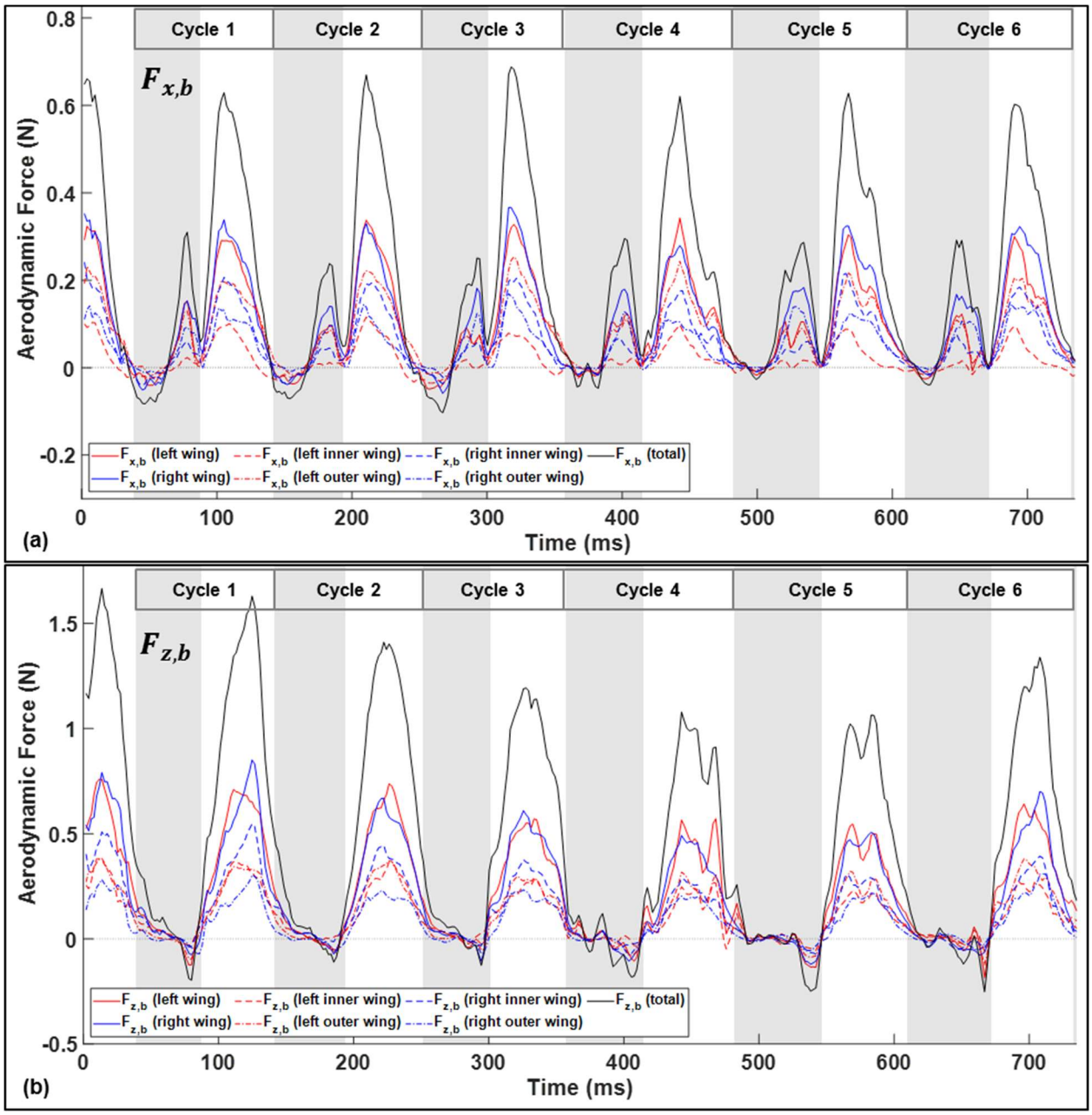

Figure 12. Thrust force (a) and lift force (b) calculated in the body-fixed frame partitioned by where the force is acting. Solid lines represent right and left wing totals. The dashed and dashed-dotted lines represent the force acting on the outer and inner right and left wings.

The thrust on the outer left wing relative to the inner left wing is elevated throughout the downstrokes of the initiation phase of the turn. In general, thrust generated by the outer wing will have a disproportionally larger contribution to aerodynamic moment relative to the inner wing since the moment arm is longer. The wingspan of around 50 cm is substantially longer than other dimensions of the bat such as the mean wing chord or the body length, so small asymmetries on the outer wing can have a large rotational effect. This appears to contribute to the yaw moment generated throughout the approach and initiation phase of the turn.

Lift force is overwhelming generated during the downstroke of each cycle. This aligns with the observation that right roll moment is generated almost exclusively during the downstrokes. Asymmetry in $F_{z,b}$ between the right and left wings is marginal throughout the flight; however, the specific location on the wing at which the force acts will change the length of the moment arm. During downstrokes 2-3, the lift generated on the right outer wing is depressed causing a net right roll moment corresponding to the increase in bank angle which occurs throughout the initiation phase of the turn.

3.4 Power and Energy Analysis

In order to investigate the power requirement of a tight U-turn maneuver, total power expenditure was calculated over the entire flight. Total power (Figure 13) is the sum of aerodynamic power, rate of change in potential energy (resulting from height change), and rate of change in kinetic energy (resulting from velocity change).

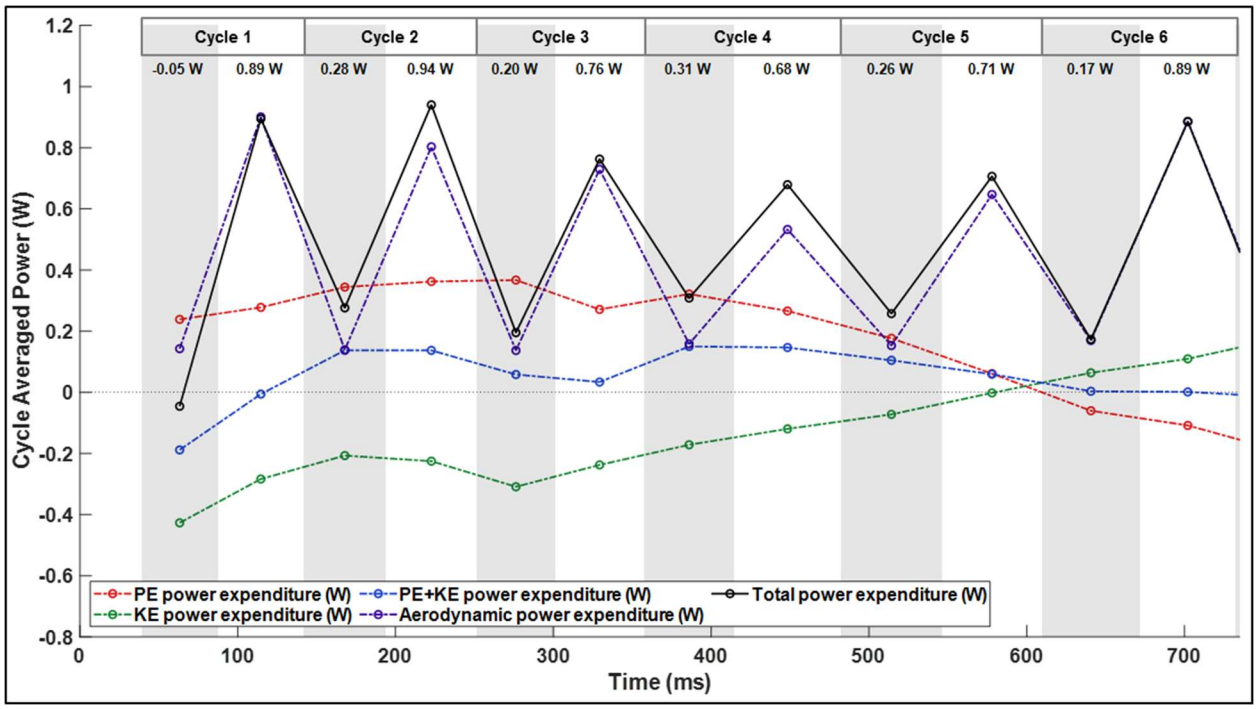

Figure 13. Total power expenditure defined as the sum of aerodynamic power, kinetic energy expenditure, and potential energy expenditure.

Table 2. Mean total power expenditure for a straight flight, sweeping turn, and U-turn.

	Cycle Mean	% Diff from Straight	Upstroke Mean	Downstroke Mean
Straight Flight	0.34 W	-	0.01 W	0.68 W
Sweeping Turn + Climb [15]	0.72 W	112%		
U-Turn Approach (flap 1-2)	0.56 W	65%		
U-Turn (flap 3-6)	0.67 W	97%		
U-Turn Initiation (flap 3-4)	0.63 W	85%		
U-Turn Apex (flap 5)	0.69 W	103%		
U-Turn Egress (flap 6)	0.73 W	115%		

Total power is elevated throughout the approach (cycles 1-2) corresponding with the time at which the bat is initiating its climb. This agrees with prior data which indicated that vertical height gain is a power intensive mode of flight. Total power expenditure remains elevated

throughout the maneuver when compared to the cost of straight flight. At the apex of the U-turn, the cycle mean power expenditure of 0.7 W is about double what has been previously calculated for the same bat in straight flight (cycle mean of 0.34 W). This suggest that even when the bat crests and ceases to climb, the cost of executing the U-turn is materially elevated relative to the straight flight baseline. Notably, the primary elevation in power relative to straight flight is observed during the upstrokes. This suggests that the bat is expending energy to generate elevated thrust and consequently yaw moments during the upstroke. Somewhat surprisingly, the maximum power expenditure (by a small margin) is observed during the egress of the turn. During the egress, both the downstroke thrust is maximum (Figure 7) and the tangential force becomes positive (Figure 10). Thus we can assign the primary power cost during the egress to acceleration out of the turn. While it is true that gravity aids the acceleration process, the observed positive tangential aerodynamic force indicates that thrust and gravitational force are used in concert.

4. Conclusion

Analysis of the wing kinematics in conjunction with aerodynamic parameters during each of the four phases of the flight provides several insights into the mechanisms the bat is using to execute a U-turn maneuver. During the initiation of the turn as the bat climbs and decelerates, the wingbeat frequency decreases and the flap amplitude increases. The right wing on the inside of the turn exhibits a greater flap amplitude compared to the left wing, and extends across the body toward the center axis of the body during the end of the downstroke and beginning of the upstroke. This phenomenon can be clearly seen in the wingtip locus visualization and manifests as a very high positive stroke plane deviation angle in the right wing during the initiation and apex of the U-turn. Lateral movement of the right wing causes an inertial effect causing counter rotation of the body to conserve angular moment. However, the presence of aerodynamic yaw moment suggests that the yaw rotation is not simply an inertia rotation but a combined aerodynamic and inertial mechanism.

The bat generates steady modest yaw rotation throughout the approach and initiation of the U-turn during both the upstroke and downstroke to reorient the body. Throughout the initiation phase the bank angle nearly doubles from 20 to 40 degrees causing a large lateral force. This causes the bearing angle to change rapidly throughout the fourth and fifth cycles eventually catching up

to the more gradually changing yaw angle in the sixth cycle. In addition to the high roll angle, the slower flight velocity allows the lateral force to more quickly turn the bat since the required centripetal force is lowered.

From this analysis, we can make several high level observations about the U-turn flight. The bat's ability to rapidly yaw appears to be limited to a degree so the yaw rotation began about one to two cycles before the rapid bearing angle change and was stretched out over many wingbeat cycles. During the apex of the turn, the bat combined a high roll angle with a low flight velocity magnitude to very rapidly redirect its bearing direction and negotiate a low radius of curvature flight trajectory. Right roll moments and right yaw moments were primarily generated during the down stroke phase of the wingbeat cycle. The general trends in aerodynamic moment and angular acceleration of the body were correlated, but they did not precisely match on an instantaneous basis suggesting a shared contribution of inertial and aerodynamic mediated rotation mechanisms.

In the future, further investigation of maneuvers executed by different bat species at different flight velocities and turning radii will allow a more generalized understanding of how bats turn. We believe this study highlights the importance of simultaneous kinematic and aerodynamic analysis in order to understanding the turning mechanisms being employed. A general model of how various different bat flight maneuvers are executed would be a valuable tool for both understanding bat biomechanics and enabling novel design of bat mimetic micro air vehicles.

Acknowledgements

The authors thank Advanced Research Computing at Virginia Tech for providing the computational resources which made this research possible (URL: http://www.arc.vt.edu). The authors also thank collaborators Susheel Sekhar, Matt Bender, Aevelina Rahman, Josh Lesser, Yang Xu, Yuxian Ye, Mengfan Wang, Junyang Xu, Han Xu, and Xuchen Gu. This research received financial support from NSF CBET Grant No. 1510797, NSF IRES Grant No. 1658620, support from VT ICTAS/BIST Center, National Natural Science Foundation of China (Grant Nos. 11374192 & 11574183), and Chinese Ministry of Education Tese Grant for international faculty exchange.

References

[1] U. M. Norberg and J. M. V. Rayner, "Ecological Morphology and Flight in Bats (Mammalia; Chiroptera): Wing Adaptations, Flight Performance, Foraging Strategy and Echolocation," *Philos. Trans. R. Soc. B Biol. Sci.*, vol. 316, no. 1179, pp. 335–427, 1987.

[2] C. Pennycuick, *Bird Flight Perfomance*. Oxford University Press, 1989.

[3] M. Dickinson, "Insect flight," *Current Biology*. 2006.

[4] C. P. Ellington, C. Den Van Berg, A. P. Willmott, and A. L. R. Thomas, "Leading-edge vortices in insect flight," *Nature*, 1996.

[5] M. H. Dickinson, "Wing Rotation and the Aerodynamic Basis of Insect Flight," *Science (80-.).*, vol. 284, no. 5422, pp. 1954–1960, 1999.

[6] A. Hedenstrom, L. C. Johansson, M. Wolf, R. von Busse, Y. Winter, and G. R. Spedding, "Bat Flight Generates Complex Aerodynamic Tracks," *Science (80-.).*, vol. 316, no. 5826, pp. 894–897, 2007.

[7] F. T. Muijres, L. C. Johansson, R. Barfield, M. Wolf, G. R. Spedding, and A. Hedenström, "Leading-Edge Vortex Improves Lift in Slow-Flying Bats," *Science (80-.).*, vol. 319, no. 5867, pp. 1250–1253, 2008.

[8] H. D. Aldridge, "Turning flight of bats," *J. Exp. Biol.*, vol. 128, pp. 419–425, 1987.

[9] J. Iriarte-Diaz, D. K. Riskin, D. J. Willis, K. S. Breuer, and S. M. Swartz, "Whole-body kinematics of a fruit bat reveal the influence of wing inertia on body accelerations," *J. Exp. Biol.*, vol. 214, no. 9, pp. 1546–1553, 2011.

[10] P. Henningsson, L. Jakobsen, and A. Hedenström, "Aerodynamics of manoeuvring flight in brown long-eared bats (Plecotus auritus)," *J. R. Soc. Interface*, vol. 15, no. 148, 2018.

[11] T. Svoboda, D. Martinec, and T. Pajdla, "A Convenient Multicamera Self-Calibration for Virtual Environments," *Presence Teleoperators Virtual Environ.*, vol. 14, no. 4, pp. 407–422, Aug. 2005.

[12] D. K. Tafti, "GenIDLEST: A scalable parallel computational tool for simulating complex turbulent flows," in *ASME-PUBLICATIONS-FED*, 2001, vol. 256, pp. 347–356.

[13] K. Nagendra, D. K. Tafti, and K. Viswanath, "A new approach for conjugate heat transfer problems using immersed boundary method for curvilinear grid based solvers," *J. Comput. Phys.*, vol. 267, pp. 225–246, 2014.

[14] P. Windes, X. Fan, M. Bender, D. K. K. Tafti, and R. Müller, "A computational

investigation of lift generation and power expenditure of Pratt's roundleaf bat (Hipposideros pratti) in forward flight," *PLoS One*, vol. 13, no. 11, p. e0207613, 2018.

[15] P. Windes, D. K. Tafti, and R. Müller, "Determination of spatial fidelity required to accurately mimic the flight dynamics of a bat," *Bioinspir. Biomim.*, 2019.

[16] S. Sekhar, P. Windes, X. Fan, and D. K. Tafti, "Canonical description of wing kinematics and dynamics for a straight flying insectivorous bat (Hipposideros pratti)," *PLoS One*, 2019.

[17] J. Iriarte-Diaz and S. M. Swartz, "Kinematics of slow turn maneuvering in the fruit bat Cynopterus brachyotis," *J. Exp. Biol.*, 2008.

[18] E. Gutierrez, D. B. Quinn, D. D. Chin, and D. Lentink, "Lift calculations based on accepted wake models for animal flight are inconsistent and sensitive to vortex dynamics," *Bioinspir. Biomim.*, vol. 12, no. 1, p. 016004, 2016.

3D Motion Capture of Bat Flight Maneuvers

Peter Windes,[a] Yang Xu,[b] Matt Bender,[a] Danesh Tafti,[a] Rolf Müller[a,b]

The flapping flight of bats is characterized by high maneuverability, efficiency, and load-carrying capacity in the low Reynolds number regime. These qualities make it an attractive model for advancing bio-inspired flight, e.g., for micro-air vehicles. A critical step in the process of deconstructing bat flight maneuvers is experimentally capturing the movement of the bat wings in three dimensional space and over time. Conventional motion capture systems are not well suited for bat flight since a bat wing contains many degrees of freedom, causing frequent self-occlusions, and high wing tip velocities. In the present work, an array of 26-34 GoPro cameras (1080p resolution at 120 fps) was placed inside a 1.2 meter wide tunnel that bats (*Hipposideros armiger*) were trained to fly through. The different view points of the cameras helped to mitigate self-occlusions of the bat wings during the wing beat cycle. Large numbers of calibration images were captured by recording a laser point that was moved though the flight tunnel for determining the intrinsic and extrinsic parameters of each camera in the array. After calibration, the three-dimensional trajectories of about 200-250 landmarks placed on the bat wings were recorded. In total, approximately 80 bat flights were captured using the camera system described above. Several u-turns, 360° turns, climbs, and upside-down landings were captured among all the flights observed. Future work will analyze this data in two ways: using non-linear dynamics to find low-dimensional representations for the complex wing motions and using computational methods to understand the unsteady fluid dynamics.

1 Introduction

Recently, there has been growing interest in understanding and optimizing low Reynolds number flight. One application is micro air vehicles (MAVs) which have been proposed as effective sensing and monitoring platforms [1]. Biological flyers also operate effectively in this regime, and can lend insight towards the design of MAVs. Biological flyers encompass a diverse array of insect, bird, and bat species.

Biological flight has been extensively researched for many years, but due to its inherent complexity, much of the field is still open for discovery. One hallmark of biological flight is that it remains effective at lower Reynolds numbers, 10^3 to 10^5, where the efficiency of fixed wing systems begin to decline [2]. Flow separation over an airfoil at high angles of attack leads to dynamic stall, that is, a very low lift to drag ratio [1]. Unsteady aerodynamics allows for much more versatility in controlling the behavior of vortices in the flow, and delaying the onset of stall. This translates to improved flight performance over a range of Reynolds numbers.

Some other attractive features of biological flight are that it operates at relatively low frequencies, it combines thrust and lift production in one motion, it can provide a high degree of maneuverability, and it is relatively efficient [3]. Thus, biologist and engineers frequently study various flying animal species to better understand flapping flight and unsteady aerodynamic phenomena.

[a] *Department of Mechanical Engineering, Virginia Tech, Blacksburg, Virginia, United States.*
[b] *Shandong University Virginia Tech International Laboratory, Jinan China*

1.1 Bat Flight

Bats, the only mammals capable of sustained flight, excel at maneuvers due to their high wing surface area and flexible wing membranes [4]. Additionally, bats have good load carrying capabilities and flight efficiency [5–8]. Bats are unique from other biological flyers due to their highly articulated wing structure and their ability to actively contour their wing membrane during flight. Compared with birds and insects, bats have a greater variation in wing surface area during flight, and have higher degree of freedom wings. These features are evidenced by their ability to weave through dense forests while flying, as well as chase and capture insects.

The goal of this research project was to experimentally capture the movement of bat wings in 3D during flight maneuvers using a video camera array. The data collected in the present work is currently being studied in detail using non-linear dynamics, and computational fluid dynamics (CFD) to better understand maneuvering bat flight.

2 Motion Capture of Bat Flight Maneuvers (Methods)

2.1 Mathematical representation of a bat wing

During flight, bat wings represent a continuous surface changing position and shape continuously in time. However like any experimental method, the measurement of a bat's wing position during flight is discrete. Discrete to continuous conversion (i.e. regression) can be preformed during post-processing only if the underlying data set has sufficient spatial-temporal

resolution. Since bat wings have many degrees of freedom, a high number of locations on the wing surface must be recorded to accurately reconstruct the surface.

Prior research has struggled to adequately spatially resolve the bat wing surface. For example, Riskin et al. (2008)[9] tracked 17 discrete points on the bones of the left wing of a *Cynopterus brachyotis* bat at 1000 observations per second. High frame rate digital cameras have made it easier to capture high temporal accuracy, however bats only flap at around 5-10 Hz. An order of magnitude above that, 100 Hz, is typically adequate to temporally resolve the bat wing. While other researcher have adequately temporally resolved bat flight, spatial resolution has been lacking.

There are 10 critical points on each wing of a bat–the shoulder, the elbow, the wrist, the end of each of the four digits, the ankle, and the knee. These can be considered discontinuities in the first derivative of a parametric space curve describing the skeleton or edge of the wing. Using just these points, a crude first order approximation of a wing may be constructed as shown in Figure 1. The 10 points can be used to construct a 3D piecewise linear parametric representation of the skeleton using 14 pieces.

As shown in Figure 1, 10 points do not well capture the proper wing area or edge shape. If 10 secondary observation points are added along each curved feature, the description improves dramatically as shown in Figure 1. These 20 points can be used to construct a 3D piecewise cubic spline parametric representation of the skeleton using 12 pieces. Qualitatively, this appears to be a good representation of the wing.

Thus for both wings, the lower bound for describing the wing *skeleton* may be considered approximately 40 points, however this will give no information regarding the deformation of the highly flexible wing membrane. Five additional membrane points are shown in Figure 1, as the minimum for a low order membrane representation. The material properties of the membrane are highly non-linear and anisotropic[10–12] so likely several more points are needed to resolve the contour of the membrane as it deforms during flight. 10-15 points on each wing are needed to construct a higher order membrane representation. In summary, for both wings, at least 20 total points are needed for a linear skeleton model, at least 40 total points are needed for a quadratic skeleton model, and at least 50-70 total points are needed to resolved both the skeleton and membrane.

These numbers only represent estimated lower bounds, using theoretical considerations. An additional factor to consider is that the outstretched wing as depicted in Figure 1 is the simplest pose of the wing. During flight, the twisting, bending, and stretching of the wing may motivate additional observation points to increase spatial resolution. Also the estimated number of observations above, assumes highly accuracy and precise measurement of each point. Occlusion of a point dur-

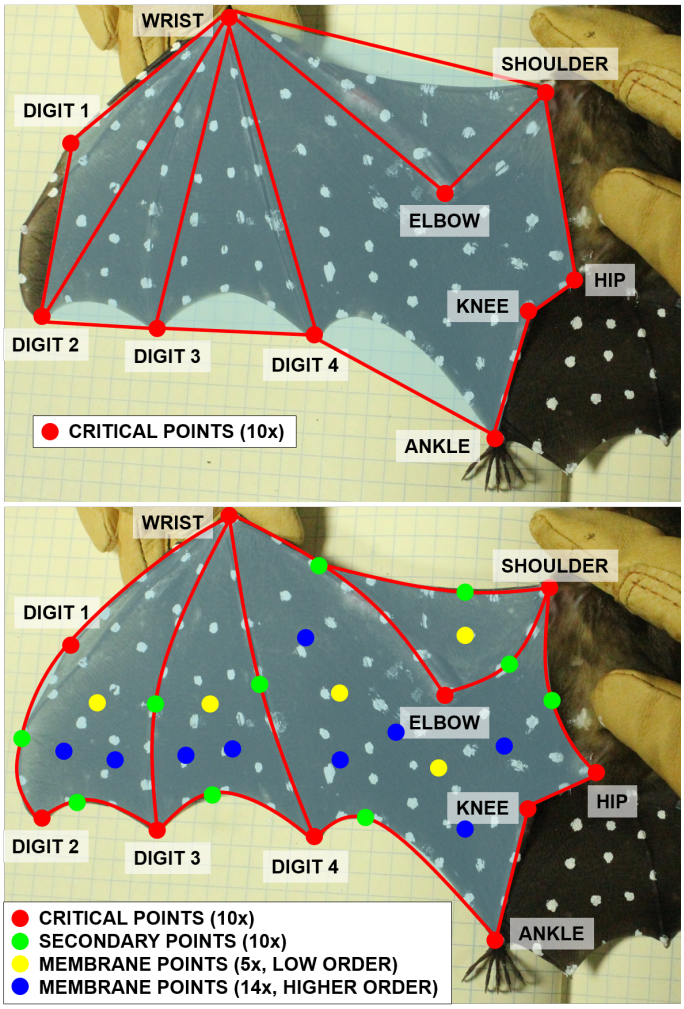

Fig. 1 Top: A lower order, linear representation of a bat wing skeleton using 10 points. Bottom: Adding 10 additional points leads to a much better representation of the wing skeleton. In addition, 5 more points must be included for a low order representation of the wing membrane, and 10-15 points should be added for a higher order membrane representation.

Fig. 2 The flight tunnel was configured for 3D motion capture of bat flight. An array of 34 cameras allowed for redundancy as well as mitigated occlusions of the wing landmarks. Six lights in the ceiling illuminated the subject during recorded to avoid motion blur. Gravity plumb lines establish an accurate gravity vector during post processing.

ing flight will result in a temporary loss of spatial resolution, thus increasing the number of points gives redundancy to the data set. In the present work, 200-250 landmarks across both wings and the tail were tracked to give robustness and redundancy to the data set. Points can always be discarded during post-processing, but additional points cannot be added retroactively.

2.2 3D motion capture camera array

In order to measure the location of the landmarks in 3D, an array of 26-34 action cameras (GoPro Hero4 Black) was placed inside a 1.2-meter-wide flight tunnel in which bats were trained to fly through. The different viewpoints of the cameras helped to mitigate self-occlusions of the bat wings during the wing beat cycle. Powerful lighting was required in order to reduce motion blur of the wings. Several plumb bobs were placed in the tunnel to establish the exact direction of gravity for later use during data analysis. The full setup can be seen in Figure 2.

The cameras were arranged in semi-rings of seven cameras. Depending on the experiment, 3-4 rings were placed down the span of the tunnel. Each camera was pointed towards the mid-line of the tunnel as shown in Figure 3. No cameras were positioned on the bottom of the tunnel pointing upward because they would not be able to focus on the bat with the light directly behind the subject. Ideally, some cameras observe the underside of the bat, but prior testing indicated that shooting footage into such bright light was not possible. The lowest

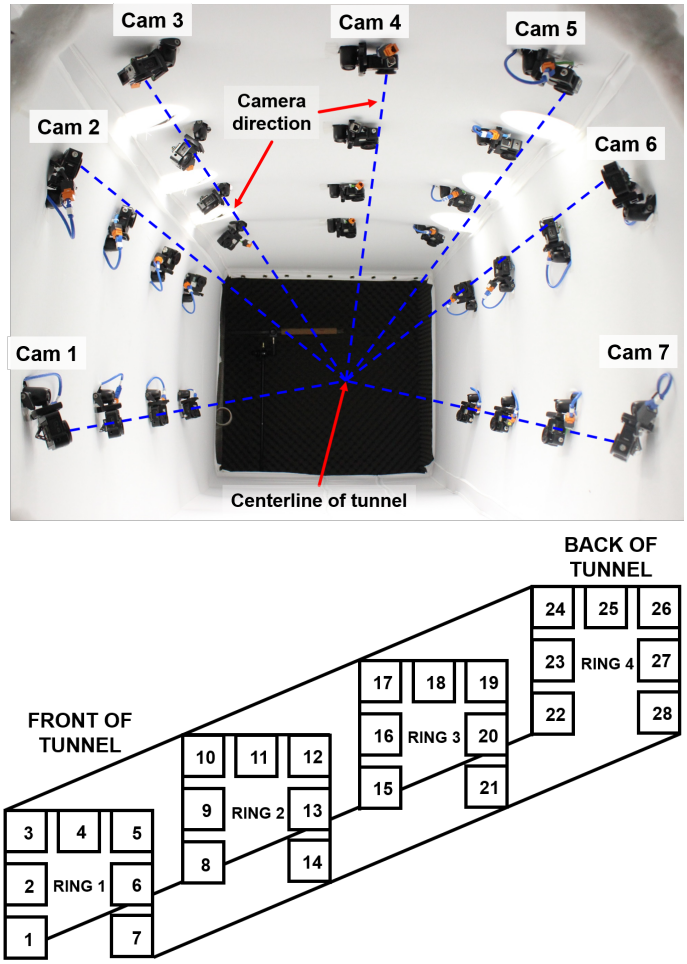

Fig. 3 Top: GoPros were grouped in rings of seven cams. Each group was comprised of four side cams, two corner cams, and one roof cam. Each cam was aimed toward the mid-line of the tunnel. Bottom: Depicted is the global cam numbering from a typical experiment using 28 cams.

two cameras on either side of the tunnel were slightly pointed upward by about 5-10 degrees, but not high enough to point into the lights. When the bat flew at the level or above cameras 1 and 7 (as numbered in Figure 3) the underside of the bat wing could be observed.

The cameras were mounted on swivel joints for easy positioning. The aiming of the cameras was important for the calibration process as will be discussed in a later section.

Additionally, the mounts needed to be very secure, because any wobbling of the camera would changes its orientation and would invalidate the camera's calibration. Robust steel mounts were used to house the cameras as shown in Figure 4.

The high frame rate of 120 Hz necessitated bright direct lighting on the subject. For comparison, cinematic features are typically shot at 30 Hz. When the frame rate is high, the

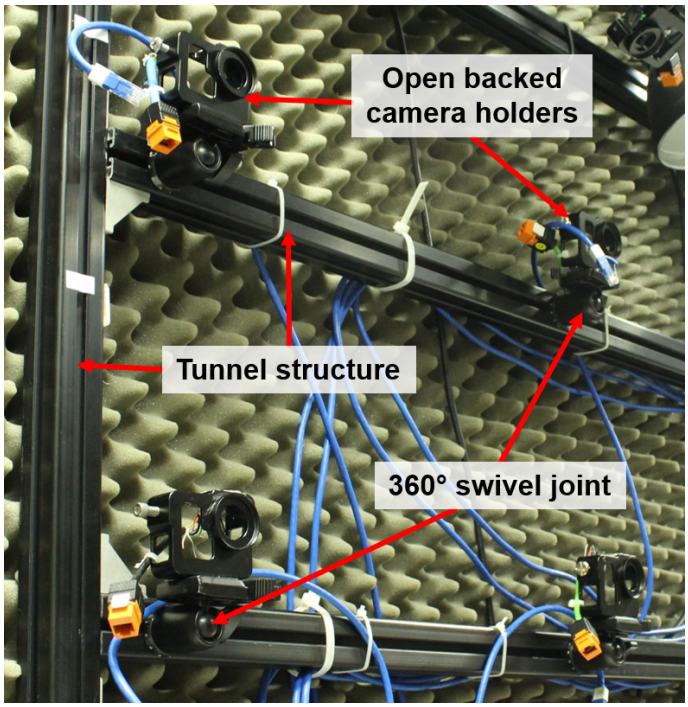

Fig. 4 The camera mounts were directly fastened to the steel frame of the flight tunnel. Securely mounted cameras prevented them from getting bumped which would compromise the calibration.

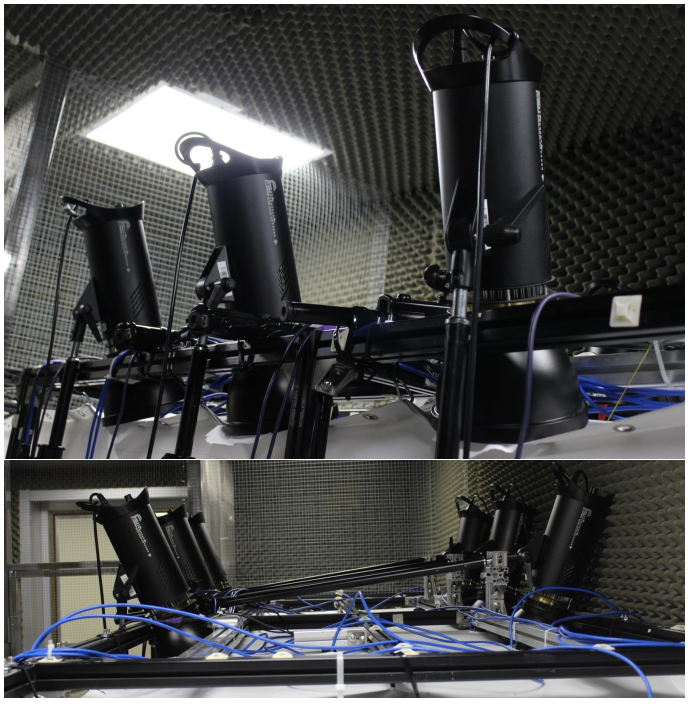

Fig. 5 Powerful lighting was needed to prevent motion blur of the fast moving bat wings. Six lights were mounted at the top of the tunnel for even, complete illumination.

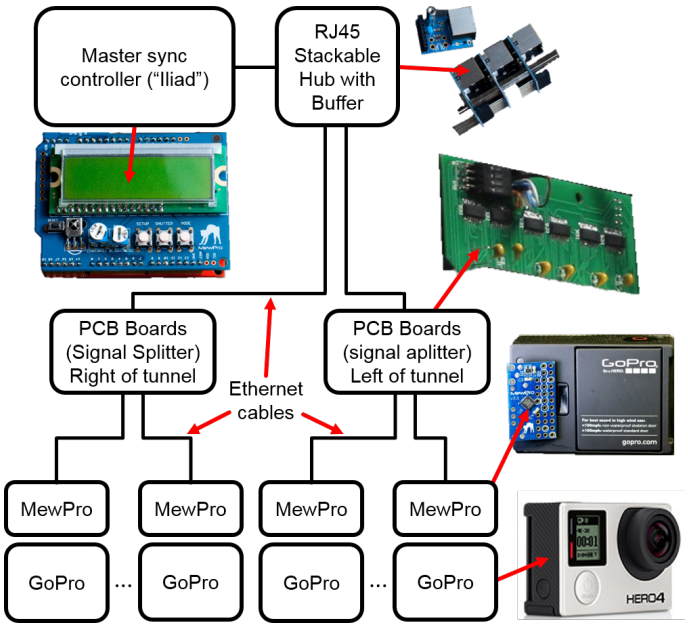

Fig. 6 The sync signal was distributed from the Iliad to the cameras via Ethernet cables. Two levels of branching were used–the stackable hub, and the PCB boards.

shutter is open for a shorter duration letting less light hit the sensor. Inadequate lighting would result in motion blur of the bat wings. Six lights were placed at the top of the flight tunnel as shown in Figure 5.

2.3 Synchronization Hardware

Synchronization of the camera array was critical to the camera calibration process, and stereoscopic reconstruction of the bat wing. This is because 3D triangulation requires the observation of a single point in space by two cameras. If the cameras are not capturing a moving point at the same instant in time, they are effectively observing two different points.

In order to achieve camera synchronization, a central unit (the ”Iliad”) distributed a trigger signal to all the cameras. The signal was split and then sent via Ethernet to custom Arduino boards (the ”MewPros”) attached to each camera. In order to verify camera synchronization, the lights were turned off and a high frequency strobe light was pulsed in the tunnel. Each of the synced cameras began recorded frames no more than $1x10^{-5}$ seconds apart from each other.

The synchronization hardware setup is shown in Figure 6. One line from the Iliad unit carried the sync signal to the stackable hub. The hub was purchased with the Iliad/MewPro kit and allowed for synchronization of 6 cameras (i.e. 6 lines out of the hub). In order to extend this capacity, the six signals from the hub were sent to PCB boards via Ethernet.

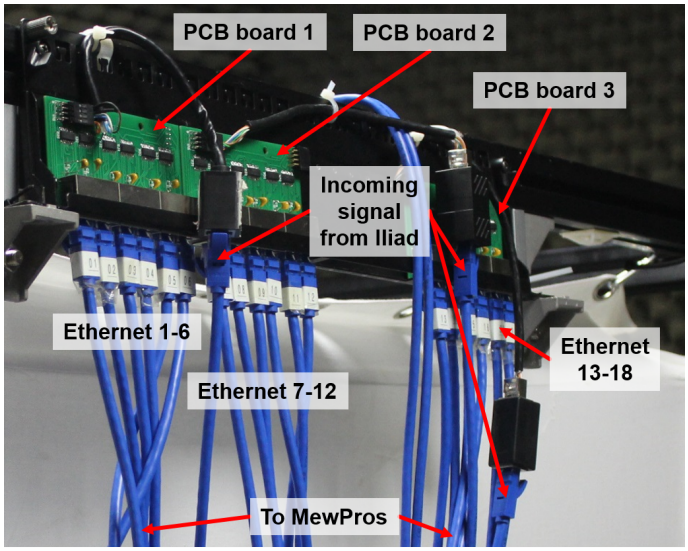

Fig. 7 Three PCB boards were mounted on the right and left sides of the flight tunnel. Each board received the sync signal and distributed it out to six MewPros.

Fig. 8 Several small white landmarks were placed on each bat wing. The number of points defines the spatial resolution of the final data set. Using simple approximations, a lower bound of 70 points should be used, however redundancy makes the data set quality less sensitive to occluded points. Too many points would lead to problems during post-processing, thus the approximately 200 points seen here represents a compromise.

Three PBC boards were mounted on each side of the tunnel as shown in Figure 7, and distributed out up to six signals to the MewPros. Each GoPro camera had one MewPro plugged into the back of it, and accepted a sync signal via Ethernet. The maximum total system capacity, as configured in the presented work, was 36 cameras.

2.4 Test Specimens

The bats used in this study were great roundleaf bats (*Hipposideros armiger*) indigenous to Southeast Asia. *H. armiger* are notably good flyers, and hunt insect prey by slow hawking and perch hunting. These hunting strategies require flight maneuverability to succeed.

The particular specimens used in this study ranged in weight from 55-65 grams. Their wingspans were around 55-60 cm. A typical wing aspect ratio was 6.5 to 7.0, and a typical wing loading was around 10 N/m^2 (1.0 kg/m^2). Inside the flight tunnel their typical flight velocities ranged from 2-4 m/s.

In between experiments, the bats were housed in a large climate controlled aviary in which they had plenty of space to fly around and exercise. The humidity and temperature in the enclosure were closely monitored. 3-5 meal worms were fed to each bat daily. A basin of water was provided allowing the bats to drink on the wing. Since bats are social animals, a minimum of two specimens were kept in each partition of the enclosure. Personal protective equipment was worn by anyone directly in contact with the bats during care or experimentation.

In order to track the surface of the bat wings during flight, small white landmarks were placed on the bat wings. Each landmark was approximately 3 mm in diameter, and negligible in weight. The optimal marking configuration is dense enough to fully represent the continuous wing surface by discrete points. However, if there are too many markers, it can lead to difficulty in post-processing. The ideal number of landmarks was determined to be around 200-250. The configuration for a typical experiment is depicted in Figure 8.

2.5 Experimental Procedure

An important aspect of data collection was establishing a standard procedure to follow during the flight experiments. To this end, a comprehensive checklist was developed so regardless of whoever was running the experiment, the proper protocol would be followed. Key aspects of the protocol are outlined here along with explanations. The complete checklist can be found in Appendix A.

1. **Specimen Preparation**

   (a) *Record bat name, species, and weight.* It is critical

to record the weight of the bat directly before running the experiment. This is because the weight of the bat may fluctuate day to day based on feeding and drinking patterns. An accurate weight will be needed for later dynamics analysis.

(b) *Place landmarks on dorsal and ventral side of wing.* Placing landmarks on the ventral side of the wing is a challenging step, however it materially improves the quality of the final data set. For example, on the upstroke often only the ventral side of the wing is observed. If there are no landmarks on the ventral side of the wing, the entire wing will be considered occluded. This may lead to problems, since the accuracy of 3D triangulation improves with more observances.

(c) *Photograph wings with DSLR camera.* This step is needed so there is a record of the configuration of the landmarks for the experiment being run. In post-processing, each landmark will be numbered, so this photograph is highly critical, and will server as the "map" for the landmark numbering.

2. **Setup Tunnel/Cams**

(a) *Check/aim lights.* Even lighting was essential to getting good quality video footage. Dim regions of the tunnel can cause motion blur of the bat wings. Since the lights were clamped in place, they typically did not need to be re-aimed each experiment. This step normally involved briefly checking all lights were in working order.

(b) *Install/check gravity plumb bobs.* The gravity plumb bobs consisted of a weighted string with 5-10 black beads evenly spaced along the string. The size of the beads needed to be large enough that they were clearly visible from several cameras. The black color ensured good contrast with the white tunnel wall. Preferably two or more gravity plumbs are used. During post-processing, the gravity vector from each plumb bob can be compared to the others to provide an indication of precision. If all vectors are parallel, the calibration has likely been quite accurate.

(c) *Install GoPros, MewPros, SD cards.* After each GoPro is mounted along with its associated MewPro and SD card, the following must be verified for each camera:

- Each camera must be securely installed into its frame holder. If the camera wobbles during data collection, it will change the calibration. Likely all data from that camera will have to be discarded.
- Each camera must be aimed in the proper direction. The camera calibration method used for this project requires all the cameras to be pointed towards the center line of the tunnel. Failure to properly aim the cameras may cause the calibration solver to diverge voiding the entire data set.
- Each camera must have adequate battery level. Repeated use of 30 or more batteries, charging cables, and USB charging hubs may result in degradation or failure of one piece of the battery system. Sometimes, a camera would be inadequately charged to complete the full experiment. Once the experiment is underway, the cameras cannot be touched to replace a battery because it may compromise the calibration of that camera.
- The lens of each camera must be wiped prior to the experiment to ensure clear video picture quality.

(d) *Verify that each camera turns on.* Once all the cameras are mounted and connected via Ethernet cable to the central controlling unit (the "Iliad"), it must be verified that all connections are working. A loose connection, broken solder joint, fried board, or corrupted firmware may cause one or more cameras at any given time to not respond to the Iliad's signal. Once all issues have been resolved, all cameras should turn on to their menu screen.

(e) *Calibrate camera with laser.* The Svoboda Multi-Camera Self-Calibration[13] requires video of a single laser dot moving through the capture volume in the dark. The calibration process will be discussed more in a later section of this report. For this step, the lights in the room were turned off, and a laser on a long pole was swept though the flight tunnel for 5-6 minutes. It is vitally important that the entire volume is covered by the sweep patter or else the calibration may diverge voiding the entire data set.

(f) *Move checkerboard through tunnel.* The checkerboard is used for scaling the data in post-processing. The Svoboda calibration does not independently solve for scale. Thus, a checkerboard was used to introduce a know scale into the data. The checkerboard was swept through the tunnel so that it could briefly be observed by each camera. The process took 45-60 seconds.

3. **Run Experiment**

(a) *Start the GoPros using the Iliad system.* Once the

Iliad started the cameras recording, a brief check was conducted to ensure that all the cameras were actually recording. The video duration showed in real time on the front display of each camera.

(b) *Speak the test number.* This step allowed for faster, more organized post-processing.

(c) *Allow the bat to fly through the tunnel.*

(d) *Make a brief note of what type of flight occurred.* Briefly noting the flight type during the experiment later helps finding specific flights more quickly in the video.

4. **Post-experiment Procedure**

(a) *Repeat item 2e (calibrate with laser).* Post-calibration was a safeguard against either a faulty pre-calibration or bumping/movement of any cameras. If the pre-calibration did not converge due to lack of laser points in the capture volume or a hardware malfunction, the post-calibration could be used instead.

(b) *Harvest the SD cards from the camera.* During harvesting of the SD cards, the number of each card was recorded on a diagram for future reference during post-processing.

(c) *Remove cameras and charge.*

5. **Finalization/Wrap-up**

(a) *Download data from SD cards (GoPro and DSLR).* All data was copied off the SD cards and backed up in two locations. Each SD card was wiped to make space for the next experiment.

(b) *Assess video quality.* This step was to ensure that all the cameras and lights were aimed properly. Any changes which needed to be made could be noted down for the next experiment.

Items 1 (Specimen Preparation) and 2 (Setup Tunnel/Cams) were worked on concurrently. Planning and timing was critical to ensure that the bat and cameras are ready to begin the experiment at the same time. Once the landmarks were placed on the bat, it could not remain in the bag for long. Once the cameras were installed and the calibration was complete, the batteries would begin to drain. Even if the cameras were powered off, the MewPro would slowly drain the batteries. Unplugging and replugging the MewPro, or swapping batteries could effect the calibration. The general guideline was not to touch the cameras, MewPros, cables, or the tunnel frame after calibration.

2.6 System reliability: challenges and solutions

There were three recurring reliability challenges during data collection which had to be overcome–MewPro failure, synchronization error, and the camera batteries expiring. A MewPro could fail due to loose solder joints, corrupted firmware, or overheating. Even if a single component has a low rate of failure, having many instances of the component increases the odds that at least one will fail. This simple probabilistic math, was realized over the course of the experiments. In order to increase the system reliability, the MewPro cables were tethered to the camera mounts in order to reduce mechanical stress on the solder joints. Also, the MewPro firmware was refreshed every 2-3 experiments. Both of these measures greatly reduced failure.

For unknown reasons, a low rate of synchronization error was discovered during the strobe light sync verifications. Approximately 1 in 15 cameras were found to have this issue. As both the cameras and the MewPros were 3rd party, "black box" hardware, it was impossible to troubleshoot. Fortunately, our system had enough redundancy the unsynced camera footage could be discarded in post-processing.

During some of the experiments, the batteries on the cameras ran low. Although this seems like a trivial issue, it was in fact a challenge. After calibration, the cameras cannot be touched to replace the batteries or the calibration may be compromised. One option would be to leave the charging cables plugged in during the experiment. However, this can lead to overheating of the MewPro boards. Additionally when the cameras were plugged in, the system tended to be less reliable. This may have been due to the charing somehow interfering with the sync signal. The best practice to mitigate these issues is to fully charge all batteries before beginning the experiment, and proceed with data collection as quickly as possible.

2.7 Tests completed

A series of bat flight experiments were run between May 31 and July 20, 2017 at the Shandong University Virginia Tech International Laboratory in Jinan, China. Table 1 outlines the experiments conducted.

Six preliminary test were run in order to iteratively improve on the setup and experimental protocol. Three full data sets using two different specimens were collected each containing 20-40 flights.

3 Video Recorded Flights (Results)

The *H. armiger* bats from the present study had a wing span of approximately 55 cm, and weighted around 60 g. The bats flew at velocities of 2-4 m/s. During straight flight, their flapping frequency was around 8 Hz. The bats were able to tra-

Table 1 The flight experiments which were conducted summer 2017 are listed below. Both bats were *H. armiger*. All cameras used were GoPros (Hero4 Black) shooting in 1080p at 120 fps. The calibration tests were done in order to test out the camera calibration process which did not require a bat. The pilot data was collected to test the entire system, dry run the experimental protocol, and improve system reliability. Each of the three full data sets contained several dozen flights.

Date	Bat	Type	Cams	Landmarks
May 31	No bat	Calibration test	14	NA
June 01	No bat	Calibration test	16	NA
June 03	"bat A"	Pilot test	16	sparse
June 21	"bat A"	Pilot test	28	sparse
July 02	"bat A"	Pilot test	30	sparse
July 06	"bat A"	Pilot test	29	bones only
July 11	"bat A"	Full data set	30	dorsal
July 18	"bat A"	Full data set	29	dorsal
July 20	"bat B"	Full data set	34	dorsal+ventral

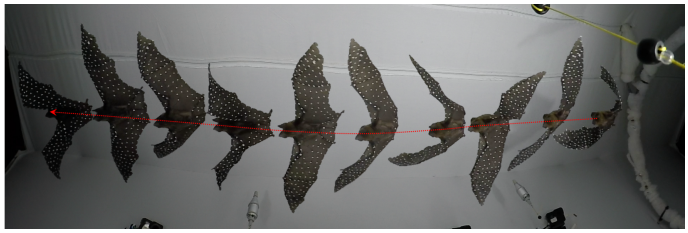

Fig. 9 During a straight flight, *H. armiger* bats were observed to fly at 2-4 m/s and flap at around 8 Hz.

verse the entire length of the flight tunnel in 1 sec. Five flight types were observed–straight flight, take-off, landing, the s-turn, and the u-turn. Examples of each are depicted below.

3.1 Straight and Level Flight

Maneuvering flight was the focus of the present work, thus straight flight served as the base line, or control case. For example, it may be insightful to compare the stroke plane angle of climbing flight with straight flight. Figure 9 depicts an image sequence of a typical straight flight.

3.2 Take-off Flight

Bats roost upside down, thus take-off consists of dropping from their roost, arresting their decent, and leveling off into straight flight. The bat is able to transition from free fall to level flight in less than a meter and with only 2-3 flaps. An image sequence of take-off is shown in Figure 10.

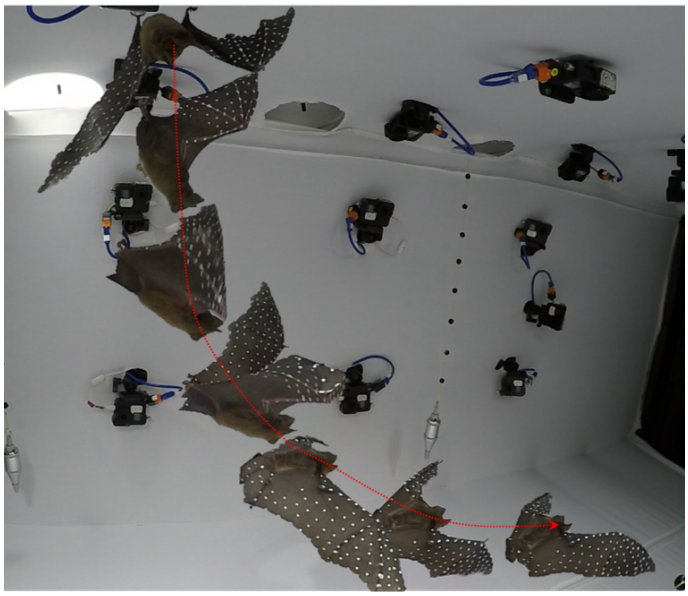

Fig. 10 Bats take-off by releasing their perch, arresting their fall, and leveling into straight flight.

3.3 Landing Flight

In order to land, a bat must rapidly climb, flip upside down, and grab the cave ceiling. Climbing at such a steep ascent is impressive for any flying vehicle. The bat is able to generate enough vertical inertia such that it can fold up its wings, flip upside down and still maintain enough velocity to continue moving upward so it can grab the surface of the ceiling. An image sequence of landing is shown in Figure 11.

3.4 S-turn Flight

Bats often must weave between obstacles in a forest, or quickly change direction while chasing prey. The s-turn observed here is a similar maneuver. Even half the s-turn–a simple banked turn–has not been explored much in the literature. Many experimental studies on bat flight are conducted in wind tunnels where turning flight is not possible. An image sequence of an s-turn is shown in Figure 12.

3.5 180° U-turn Flight

A tight u-turn in mid flight is a difficult maneuver to accomplish. In the distance of only a few body lengths, the bat was able to complete change direction. An image sequence of a u-turn is shown in Figure 13.

Fig. 11 In order to land, a bat accelerates upward, flips upside down, and grabs its perch.

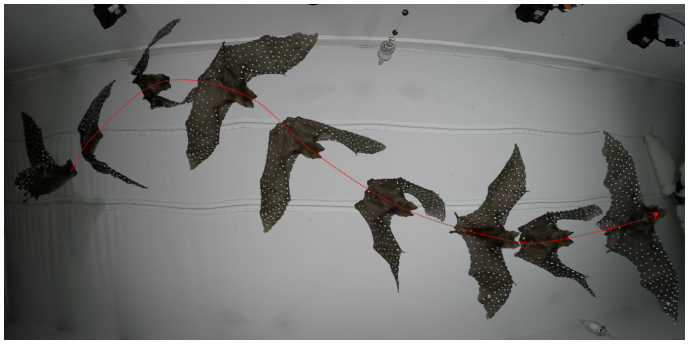

Fig. 12 An s-turn is comprised of subsequent sweeping turns as can be seen in this flight.

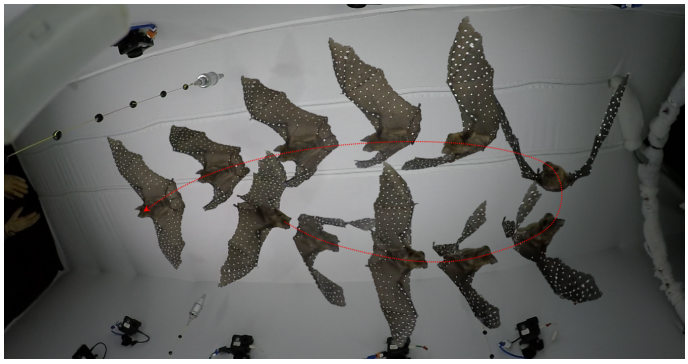

Fig. 13 A u-turn observed in mid flight.

4 3D Reconstruction of Wing Kinematics

In order to further study the bat flights which were video recorded, the 3D locations of all parts of the wing must be reconstructed using ray triangulation. This process is ongoing so only a brief summary will be provided in this report. 3D stereo reconstruction requires 2 steps–camera calibration and point triangulation.

4.1 Camera calibration

Camera calibration is defined as the determination of the location, orientation, and lens distortion of each camera in the array. "Extrinsic" calibration parameters define the location and orientation of a camera. "Intrinsic" calibration parameters define the lens distortion of a camera. Given the intrinsic and extrinsic calibration parameters from two cameras, a scene point common to images from both cameras may be triangulated. That is, an x,y,z vector location can be solved for relative to the camera locations.

Many calibration techniques use pairwise calibration. That is, two cameras will be calibrated relative to each other. A common method for pairwise calibration is to use a checkerboard of known size. For a small number of cameras, this technique has several advantages such as being able to explicitly solve for the calibration parameters.

However multi-camera calibration is more suitable for a large camera array. The advantage of multi-camera calibration is that any camera pair derived from the entire array will be calibrated together. For an array of 32 cameras, 496 individual pairwise calibrations would need to be done to achieve the same results.

The Svoboda Multi-Camera Self-Calibration [13] method was chosen to generate the calibration parameters. This method first requires sweeping a laser dot around the capture volume of the camera array. The resulting video is post-processed to generate a multi-camera calibration. The algorithm will be briefly described here at a high level, but the authors direct the reader to the reference [13] for more details.

1. Video record a laser point sweeping through the capture volume with the lights off (4-8 minutes of footage are needed depending on the size of the capture volume).
2. Extract image files (png or jpg) from the videos frames.
3. Inside the Svoboda Matlab package, run the script im2points.m in order to extract the 2D pixel location of the laser point in each image.
4. Inside the Svoboda Matlab package, set the calibration parameters in the configdata.m file.
5. Inside the Svoboda Matlab package, run the script go-cal.m.

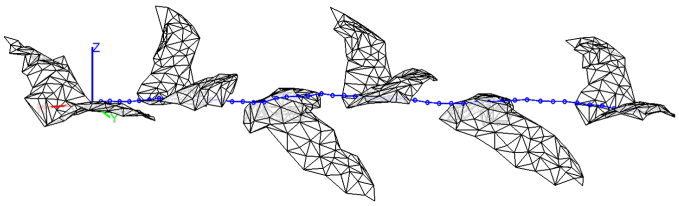

Fig. 14 A 3D reconstruction of a sample straight flight.

Often items 4-5 will need to be completed multiple times adjusting the calibration settings each time to achieve a successful calibration. A successful calibration will return intrinsic and extrinsic calibration parameters for each camera as well as mean and standard deviation calibration error in pixel units. Several things may lead to divergence of the calibration solver:

- Improper pointing of the cameras. The laser point should be seen by as many cameras as possible during calibration.
- Too few laser point locations, due to failure to sweep the entire capture volume.
- Improper configuration of the calibration parameters in configdata.m.
- One or more cameras not properly synchronized with the other cameras for whatever reason.

Any or some combination of the above issues may prevent successful calibration. In the event that no adjustment of calibration parameters leads to a successful calibration, one or more cameras may be excluded from the calibration process. Often an acceptable subset of the array may be then successfully calibrated, for example 26 out of 30 cameras could still lead to quality 3D reconstructions.

4.2 Point triangulation

After the calibration was complete, all the white landmark points on the bat wing were triangulated for each frame of the video. Due to time constrains during the project, point triangulation was not complete for the present data set. Figure 14 shows sample results from the authors' prior work on straight and level flight. The same process will be applied to the maneuvering flight data collected in the present work.

5 Conclusion

During the present work, great roundleaf bats (*Hipposideros armiger*) were released inside of a fight tunnel, and various flight maneuvers were captured by an array of 30+ cameras. In order to sufficiently resolve the surface of the wings, 200-250 small white landmarks were placed on the bat to be reconstructed in 3D. Synchronization hardware was employed in order to ensure that the cameras captured frames at the exact same moment. Over 80 flights of various classifications were observed including straight flights, take-offs, landings, u-turns, and s-shaped weaving turns. Multi-camera calibration was used to determine the intrinsic and extrinsic camera parameters. 3D reconstruction of the maneuvering flight data is ongoing.

5.1 Deconstructing Complex Flight Maneuvers (Future Work)

In the future, we plan to analyze the wing kinematic data which was collect using Gaussian processes dynamics. Additionally, the aerodynamics will be analyzed using computational fluid dynamics (CFD). Previously, we have analyzed straight and level bat flight using CFD to calculate lift, thurst, and aerodynamic power needed to sustain flight. Similar techniques will be applied to the maneuvering flight data collected during the present work.

Acknowledgments

The authors acknowledge the National Science Foundation International Research Experience for Students (IRES) for providing financial support for the present research. Additionally, the present research would not have been possible without the help of *list SDU undergrads here*.

References

1 W. Shyy, H. Aono, S. K. Chimakurthi, P. Trizila, C. K. Kang, C. E. S. Cesnik and H. Liu, *Progress in Aerospace Sciences*, 2010, **46**, 284–327.
2 W. Shyy, M. Berg and D. Ljungqvist, *Progress in Aerospace Sciences*, 1999, **35**, 455–505.
3 K. V. Rozhdestvensky and V. A. Ryzhov, *Aerohydrodynamics of flapping-wing propulsors*, 2003.
4 S. P. Thomas and R. A. Suthers, *Journal of Experimental Biology*, 1972, **57**, 317–335.
5 S. Swartz and N. Konow, *Canadian Journal of Zoology*, 2015, **93**, 977–990.
6 A. Hedenström and L. C. Johansson, *Bat flight*, 2015.
7 F. a. Hartman, *The Ohio Journal of Science*, 1963, **63**, 59–65.
8 U. M. Norberg, *Journal of Experimental Biology*, 1976, **65**, 179–212.
9 D. K. Riskin, D. J. Willis, J. Iriarte-D??az, T. L. Hedrick, M. Kostandov, J. Chen, D. H. Laidlaw, K. S. Breuer and S. M. Swartz, *Journal of Theoretical Biology*, 2008, **254**, 604–615.
10 S. M. Swartz, M. S. Groves, H. D. Kim and W. R. Walsh, *Journal of Zoology*, 1996, **239**, 357–378.
11 S. M. Swartz, *Journal of Morphology*, 1997, **234**, 277–294.
12 J. P. Madej, L. Mikulová, A. Gorošová, Š. Mikula, Z. ehák, F. Tichý and M. Buchtová, *Acta Zoologica*, 2012, n/a–n/a.
13 T. Svoboda, D. Martinec and T. Pajdla, *PRESENCE: teleoperators and virtual environments*, 2005, **14**, 407–422.

Appendix A

Experimental protocol checklist:

Test Number:_____ Name of note taker:_____ Date: _____

1. **Bat Preparation**
   - 1.1. Retrieve bat from aviary..... ☐
   - 1.2. Note down specimen number.....#_____
   - 1.3. Weight bat..... _____ grams
   - 1.4. Mark bat wings (dorsal /top side)..... ☐
   - 1.5. Mark bat wings (ventral/under side)..... ☐
   - 1.6. Photograph bat (flat with camera orthogonal)..... ☐
   - 1.7. Bag bat..... ☐

2. **Tunnel Setup/Camera Configuration**
   - 2.1. Check/aim lights..... ☐
   - 2.2. Install GoPros, MewPros, SD cards (fill out table below).....# of cams_____
   - 2.3. Turn on all cameras with Iliad, be sure all cams are on..... ☐
   - 2.4. Set camera settings with Iliad.....Frame rate_____, Resolution_____, ProTune?_____

Cam #	MewPro? ☑	SD card? ☑	Cam aimed? ☑	Cam stable? ☑	Wipe lens? ☑	Battery level (1-3)	Cam test? ☑
1	☐	☐	☐	☐	☐	___	☐
2	☐	☐	☐	☐	☐	___	☐
3	☐	☐	☐	☐	☐	___	☐
4	☐	☐	☐	☐	☐	___	☐
5	☐	☐	☐	☐	☐	___	☐
6	☐	☐	☐	☐	☐	___	☐
7	☐	☐	☐	☐	☐	___	☐
8	☐	☐	☐	☐	☐	___	☐
9	☐	☐	☐	☐	☐	___	☐
10	☐	☐	☐	☐	☐	___	☐
11	☐	☐	☐	☐	☐	___	☐
12	☐	☐	☐	☐	☐	___	☐
13	☐	☐	☐	☐	☐	___	☐
14	☐	☐	☐	☐	☐	___	☐
15	☐	☐	☐	☐	☐	___	☐
16	☐	☐	☐	☐	☐	___	☐
17	☐	☐	☐	☐	☐	___	☐
18	☐	☐	☐	☐	☐	___	☐
19	☐	☐	☐	☐	☐	___	☐
20	☐	☐	☐	☐	☐	___	☐
21	☐	☐	☐	☐	☐	___	☐
22	☐	☐	☐	☐	☐	___	☐
23	☐	☐	☐	☐	☐	___	☐
24	☐	☐	☐	☐	☐	___	☐
25	☐	☐	☐	☐	☐	___	☐
26	☐	☐	☐	☐	☐	___	☐
27	☐	☐	☐	☐	☐	___	☐
28	☐	☐	☐	☐	☐	___	☐
29	☐	☐	☐	☐	☐	___	☐
30	☐	☐	☐	☐	☐	___	☐
31	☐	☐	☐	☐	☐	___	☐
32	☐	☐	☐	☐	☐	___	☐

(page 2)

Test Number:_____ Name of note taker:_____ Date: _____

2.5. Install gravity plumb bob(s) with black beads.....How many?_____.....☐
2.6. Calibrate with laser COMPLETELY FILL VOLUME.....who?_____.....☐
2.6.1. Laser bright enough? .....☐
2.6.2. Ensure all cams running.....☐
2.6.3. 5 to 6 minutes?.....☐
2.7. Turn on big lights.....☐
2.8. Spatial calibration: checker board.....☐ circle board.....☐
2.9. Fully close the sheet.....☐

3. **Run Experiments/Video Capture**
3.1. Start the GoPros using the Iliad system
3.2. Say the test name/number
3.3. Release bat
3.4. Stop the GoPros using the Iliad system
3.5. Note type of flight (u-turn, dive, climb, hover, etc) and rate flight (0=garbage, 1=okay, 2=very good)
3.6. Repeat for as many tests, fill out form below for each test

Test	Rate	Describe flight
001		
002		
003		
004		
005		
006		
007		
008		
009		
010		
011		
012		
013		
014		
015		
016		
017		
018		
019		
020		
021		
022		
023		
024		
025		
026		
027		
028		
029		
030		
031		
032		

(page 3)

Test Number:_____ Name of note taker:_____ Date: _____

4. **Post-Experiment Procedure**
   - 4.1. Re-calibrate cameras
     - 4.1.1. Calibrate with laser COMPLETELY FILL VOLUME.....who?_____.....☐
   - 4.2. Re-weigh the bat....._____g
   - 4.3. Harvest SD cards (fill in out diagram below with SD card numbers).....☐
   - 4.4. Remove cameras.....☐
   - 4.5. Plug in all cameras.....☐

SD card labeling:

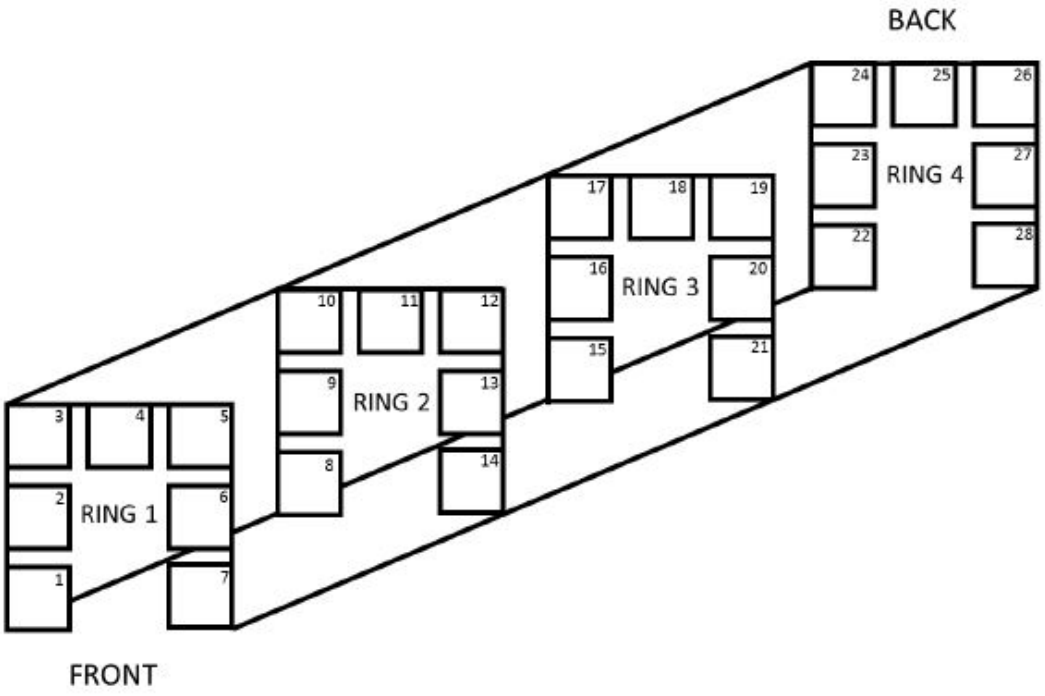

5. **End of Day**
   - 5.1. Download videos from SD cards.....☐
   - 5.2. Download wing marker pictures from DSLR camera.....☐
   - 5.3. Transfer files to external hardrive.....☐
   - 5.4. Delete videos from SD cards (use computer, *do not format SD cards from cam menu*).....☐
   - 5.5. Playback videos, assess video quality.....☐
   - 5.6. Check that data sheet is fully filled out.....☐
   - 5.7. Scan this document for records.....☐

PLOS ONE

RESEARCH ARTICLE

Canonical description of wing kinematics and dynamics for a straight flying insectivorous bat (*Hipposideros pratti*)

Susheel Sekhar, Peter Windes, Xiaozhou Fan, Danesh K. Tafti*

Department of Mechanical Engineering, Virginia Tech, Blacksburg, Virginia, United States of America

* dtafti@exchange.vt.edu

Citation: Sekhar S, Windes P, Fan X, Tafti DK (2019) Canonical description of wing kinematics and dynamics for a straight flying insectivorous bat (*Hipposideros pratti*). PLoS ONE 14(6): e0218672. https://doi.org/10.1371/journal.pone.0218672

Editor: Iman Borazjani, Texas A&M University System, UNITED STATES

Received: January 23, 2019

Accepted: June 6, 2019

Published: June 25, 2019

Data Availability Statement: Data related to the kinematic decomposition and aerodynamic simulations are within the manuscript and its Supporting Information files. Additional data related to motion capture are available from the authors' previous paper at https://doi.org/10.1371/journal.pone.0207613.s002.

Funding: The financial support of the NSF CBET Grant No. 1510797 to DKT and support from VT ICTAS/BIST Center is gratefully acknowledged. The funders had no role in study design, data collection

Abstract

Bats, with highly articulated wings, are some of the most agile flyers in nature. A novel three-dimensional geometric decomposition framework is developed to reduce the complex kinematics of a bat wing into physical movements used to describe flapping flight: namely flapping, stroke plane deviation and pitching, together with cambering and flexion. The decomposition is combined with aerodynamic simulations to investigate the cumulative effect of each motion on force production, and their primary contribution to the unsteady vortex dynamics. For the nearly straight and level flight of *Hipposideros pratti*, results show that the flapping motion by itself induced a moderate drag and lift. Stroke plane deviation increased lift, and nullified the drag. With the inclusion of the pitching motion into the kinematics, lift production further increased by a factor of more than 2.5, and exhibited a positive net thrust by virtue of the favorable wing orientation during the upstroke. The primary contribution of cambering, which included a maximum chord line displacement of ≈40% standard mean chord, was the stabilization of the leading edge vortex during the downstroke. This increased mean lift by about 35% at the expense of net thrust. Flexion was perhaps the most complex motion with maximum displacements of 75% standard mean chord. This was instrumental in reducing the negative lift during the upstroke by preventing the formation of strong leading edge vortices. The aerodynamic effective angle of attack emerged as a heuristic parameter to describe lift and net thrust production across movements.

Introduction

Flapping of wings is used by the smallest of insects on the millimeter scale to the largest of birds for generating both lift and thrust. Bats distinguish themselves from insects and birds by utilizing a membranous arm-wing that includes the shoulder joint, elbow, wrist, and fingers with phalanges [1], giving them an unparalleled capability to manipulate wing morphology and influence their flight dynamics. In all flying animals, at the most basic level, wing motion described by flapping combined with pitching is sufficient to describe the underlying aerodynamics that generates lift and thrust. Different flyers fine-tune these basic movements by using different phasing between flapping and pitching, deviations from the stroke plane, wing

and analysis, decision to publish, or preparation of the manuscript.

Competing interests: The authors have declared that no competing interests exist.

flexibility, passive and active cambering of the wing, wing twist, and so on, to achieve desired functionalities. While several studies have been conducted on insects [2–5] and birds [6] in identifying and isolating some of these physical movements, less progress has been made toward decomposing bat flight kinematics into simpler constituent movements. This can be chiefly attributed to the inherent complexity of bat wing kinematics, but also because of the lack of detailed wing kinematic data and appropriate aerodynamic analysis tools.

The lift and thrust forces generated by a flapping wing have been attributed to a number of fluid dynamic phenomena. Unlike stationary airfoils, which depend on attached steady flow to generate lift, flapping wings depend mostly on unsteady separated flow to generate the required lift and thrust forces. In these unsteady cases, out of the many mechanisms that have been theorized to generate lift and thrust, the most prominent is the mechanism of delayed stall. Here, the leading edge vortices (LEVs), which are generated during stall, are delayed from detaching from the wing surface, and are stabilized and harvested to create force-generating pressure differentials across the wing surface. The stability of the LEV and various factors that affect its longevity have been the topic of many investigations in the literature [7–15]. The most widely accepted explanation of LEV longevity in flapping flight is the presence of a spiral LEV that exhibits an axial flow (spanwise in wing coordinates) in the vortex core, which transports vorticity out of the core and keeps the LEV stable during a large part of the downstroke. While it is commonly acknowledged that most of the heavy lifting in force generation is done by the LEV that forms on the dorsal surface of the wing during the downstroke, other mechanisms such as rotational circulation [16,17], wake capture [18], and clap-and-fling mechanism [15] are also known to contribute to force generation. Rotational circulation generates forces during pronation and supination of the wing based on the Kramer effect. Similarly, wake capture is the process of harvesting wake vortices to generate forces on the wing surface, while clap-and-fling is the process by which vortices are generated at the beginning of the downstroke during pronation by very small insects.

Wing flexibility has been studied extensively in the literature, and has been shown to have a large impact on force generation in flapping flight. Flexibility often manifests as passive cambering and twisting of the wing by inertial and aerodynamic forces to enhance the interaction of the wing surface with the unsteady flow field. Aono et al. [19] showed both experimentally and numerically that in forward flight, passive deformation introduced a twist from the root to the tip, which enhanced thrust production. Wu et al. [20] conducted various experiments to measure the thrust generated by different wing configurations with passive wing deformation and twist. They actuated wings with a single-DOF rotary flapping motion, and found that a rigid wing generated little useful aerodynamic forces, but passive feathering, twisting, and bending of the membrane wings could provide meaningful thrust forces. They showed that chordwise stiffness needs to be orders of magnitude lower than spanwise stiffness to achieve thrust effectiveness and efficiency, and that spanwise stiffness needs to be optimized for different flapping frequency ranges and wing inertias to be efficient. Curet et al. [21] used an idealized wing model consisting of a cantilevered flat plate with a hinged trailing flap, and showed that passive oscillatory motion of this wing significantly increased lift (and drag) as a result of an attached LEV when the freestream velocity exceeded a certain threshold. Gopalakrishnan and Tafti [22] simulated the fluid-structure interaction of a rectangular membrane wing in flapping motion, and showed that spanwise and chordwise flexibility affected the lift and thrust generation. Specifically, they showed that between spanwise and chordwise flexibility, a higher flexibility in the chord yielded higher lift and thrust. The associated flow analysis demonstrated that wing deformation by aerodynamic forces introduced a streamwise camber, which increased the proximity of the LEV to the dorsal surface during the downstroke, increasing both lift and thrust production. Other independent studies [11,23] have also confirmed that

the 'phase lag' resulting from a purely passive deformation due to chordwise flexibility, where the trailing edge of the wing falls behind the motion of the leading edge, created an effectively larger projected area for the thrust forces to develop. Also in Ref. [11], spanwise flexible wings producing more thrust were associated with a larger effective angle of attack. In an *in vivo* experiment, Mountcastle et al. [24] artificially stiffened the wings of a bumblebee to restrict flexibility, and tested the vertical aerodynamic force production. Observing no significant difference in wingbeat frequency or stroke amplitude after the stiffening, they found that the more rigid wings had an 8.6% reduction in maximum lift in load-lifting trials.

Young et al. [2] and Walker et al. [3] demonstrated that camber and twist are important for desert locusts to achieve better power economy. Nakata et al. [4,25] used an FEM-based thin shell model to account for anisotropic wing stiffness of a hovering hawkmoth, *Manduca sexta*, and found that wing bending (or flexion) delayed the breakdown of the LEV near the wingtip, thus augmenting aerodynamic forces. Wing twist also increased aerodynamic efficiency by favorably orientating the wing. Most interestingly, they found that the spanwise kinematic variation was key to aerodynamic efficiency. Le et al. [26] studied the beetle wing in forward flight and found a similar result: that wing twist significantly increased lift, and that camber variation enhanced the power economy by reducing power consumption, as well as enhancing thrust. More specifically, Zheng et al. [5] pointed out in their comparative study of a Painted Lady butterfly, *Vanessa cardui*, that it was wing twist, not camber, that was the key to performance. Lucas et al. [27] focused their attention on the bending motion of animal wings and fins, and concluded through a statistical analysis across dramatically different taxa that the location of the axis of bending (flexion ratio) and the extent of bending (maximum flexion angle) cluster tightly around 0.65 and 27˚, respectively. More recently, Maeda et al. [6] reconstructed the wing kinematics of a hummingbird in terms of spanwise bending, twist and cambering that characterize the flexibility of the wing, along with three angles that describe the entire wing motion. This method allowed them to extract useful and detailed kinematic information about hummingbirds in flight, such as the change in wing area and the twist of the wing.

Compared to other animals, bats excel at maneuvering flight with their highly articulated skeletal structures and thin membranous wings serving as flexible aerodynamic control surfaces [28–30]. Whereas flapping-wing micro aerial vehicles (MAVs) that mimic other animals and/or insects have been extensively researched and adapted to miniaturized flying devices [31–34], equivalent studies and efforts for bat flight have seen very few practical implementations [35,36]. Recent advances in motion capture technology [37,38] have enabled detailed studies of bat flight. Tian et al. [39] experimentally measured the bat wing kinematics and performed a simple analysis of the wake structure for straight flight, which was the first quantitative experimental study that utilized advances in modern wind tunnel technology and developments in flow visualization techniques for bat flight. Muijres et al. [40] showed that a slow flying bat (*Glossophaga soricina*) uses an attached LEV to generate 40% of the lift, using DPIV-derived data. Hubel et al. [41] used a similar experimental approach to reveal four typical vortical structures across different flight speeds of lesser dog-faced fruit bats (*Cynopterus brachyotis*). They discovered that the proportion of the flight cycle without the presence of a tip vortex increased at high speeds, which contrasted with the continuous vortical structure found in bird flight. Subsequently, Hubel et al. [42] compared the kinematics of two insectivorous bats *(Tadarida brasiliensis* and *Myotis velifer*) and showed that they differ significantly in prey pursuit at slow flight. They inferred that *M. velifer* has a better flight efficiency for two reasons: a decreased disruption in lift generation between the body and wing, and a characteristic root vortex with diminished strength. Bender et al. [43] and Fan et al. [44] used a high marker density on the wing surface (up to 200 markers on both wings) of an insectivorous bat, Pratt's roundleaf bat (*H. pratti*), which allowed them to extract a more accurate description of the

kinematics. Their motion capturing system consisted of a large three dimensional array of 21 cameras (GoPro HERO3+ Black, 720p at 120fps) arranged along the walls of a rectangular flight tunnel. The high fidelity experimental data from this setup has been used to build the bat model in the present work.

Previous numerical studies of bat flight aerodynamics are few, although attempts to apply computational techniques have increased recently. Pivkin et al. [45] made an early attempt to simulate bat flight numerically using a spectral flow solver along with the arbitrary Lagrangian-Eulerian (ALE) method. In their effort, a flying *Pteropus poliocephalus* was simulated at Re = 100, however minimal quantitative analysis was provided from the simulation results. In 2014, Viswanath et al. [46,47] simulated the straight, climbing flight of a fruit bat (*C. brachyotis*) using the immersed boundary method. The kinematics of a single wing with 50 markers—borrowed from Riskin et al. [1]—was transformed into a periodic motion to ensure fully developed flow at two different Reynolds numbers (433 and 5625). Visualization of the flow structures provided detailed insight into the effect of the LEV on the generated lift and thrust. Nondimensional lift and drag forces were found to be independent of the Reynolds number in these simulations. Additionally, they showed that by decomposing the kinematics using proper orthogonal decomposition (POD) into the sum of a collection of modes, merely two modes could explain almost all of the resulting averaged forces. Though their decomposition of wing kinematics was based on a single wing, the overall strategy showed excellent potential to identify important kinematics in designing flapping wing MAVs based on bat flight data. In 2015, Wang et al. [48,49] used the immersed boundary method to simulate a slow flying bat at an intermediate Reynolds number (Re = 1000). The wing kinematic data for their simulations—borrowed from Wolf et al. [50]—consisted of only five markers points per wing. It is unclear if five points per wing is sufficient to capture the articulated wing structure and membrane deformation during flight. Additionally, the wing morphology of the model was derived from a *Pteropus poliocephalus* (wingspan ≈ 25 cm, mass ≈ 11 g, ref. [51]), while the kinematics were derived from a *Glossophaga soricina* (wingspan ≈ 117 cm, mass ≈ 770 g, ref. [51]), raising questions about the fidelity of the model. In 2018, Windes et al. conducted a numerical investigation of both aerodynamic power and forces of a straight flying *H. pratti* using the same kinematic data set as the present work. Time variation of surface area, aerodynamic loads, and aerodynamic power were analyzed in conjunction with vortex dynamics and wing surface pressure coefficient.

The objective of this paper is to decompose bat wing kinematics into the fundamental canonical descriptors of flapping flight, and investigate each movement's contribution to the cumulative force production during bat flight. The measured wing motion of an insectivorous *H. pratti* in nominally straight and level flight is used. The native wing motion is decomposed into a set of canonical descriptors such as stroke plane angle, flapping amplitude, stroke plane deviation angle, pitch angle, together with chordwise camber and wing flexion. With these synthesized kinematics, aerodynamic simulations of the modeled wing in flight are conducted, and details of how each component of wing motion dictates the underlying unsteady vortex dynamics through the manipulation of the LEV and effective aerodynamic angle of attack are investigated.

The paper is organized as follows: the decomposition paradigm is detailed in the Kinematics Decomposition and Analysis section. Each motion of flapping flight is expounded in terms of parameters that define it, and their incorporation into the kinematics is described in a model equation. This is done with an increasing level of complexity. Next, the Aerodynamic Analyses section introduces the governing equations, mesh set-up and the boundary conditions used in the simulations. The effective angle of attack is revisited for this study because it was identified as a key factor in understanding the aerodynamics. This is followed by

simulation results, where the effect of the synthesized wing kinematics on the unsteady flow field generated, and ultimately on force production, is investigated. Finally, conclusions are summarized in the Summary and Conclusions section.

Kinematics decomposition and analysis

Raw wing kinematic data was obtained from a prior study [43,52], in which a 3D optical motion capture system was used to record an adult male *H. pratti* in straight flight. The experimental setup consisted of an array of 21 cameras inside a flight tunnel with a cross section of 1.2 m × 1.2 m, and an approximate length of 4 m. The Svoboda multi-camera self-calibration open source MATLAB package was used for the calibration of the camera array [53]. Additional details related to the experimental facility, motion capture system and the kinematic dataset pre-processing set-up are described in the authors prior work [43,52].

A 1 m long flight path of a *H. pratti* that weighed 55 g, with a wingspan of 52 cm and a standard mean chord of 7.4 cm, over a duration of 0.42 s, was chosen for analysis. During the nearly three flapping cycles recorded, the bat moved laterally by about 5 mm, and descended by about 10 mm at an inclination of approximately 5˚. In the absence of any active maneuvers, the recorded flight is considered to be nominally straight and level. Fig 1 shows selected still-frames along the flight path.

Decomposition of bat wing kinematics using canonical descriptors

The wing kinematic data was decomposed into five types of motion—flapping, stroke plane deviation, pitching, camber, and flexion—which are described in more detail in later sections.

Wing kinematics terminology. The approximate midpoint between the bat's shoulders is defined as the origin, *O*, which translates through space along with the bat (see Fig 2). The two lines connecting *O* and each of the wingtips are referred to as the *span lines*. The right and left wings each have independent span lines that pivot about the shoulder as the bat flaps and flies.

A cross section of the wing in a plane perpendicular to the span line is referred to as an *airfoil section*, as shown in the inset in Fig 2. Each wing is discretized into a series of airfoils along the span. A straight line connecting the leading and trailing edge of each airfoil is referred to as the airfoil's *chord line*.

Coordinate systems used in kinematic decomposition. In order to clearly define the five components of motion, two coordinate systems are used. The first coordinate system, ($\mathbf{x_b}$, $\mathbf{y_b}$, $\mathbf{z_b}$), centered at *O*, is a body-fixed system that is defined relative to the stroke plane. Since the bat wings do not flap in a perfectly planar motion, the stroke plane defines the central tendency of the stroke. It is calculated by first projecting the locus of points traced by the two wingtips onto a vertical plane bisecting the bat's body, as shown in Fig 2. Then, a linear regression is performed on the projected points in order to obtain the slope of the stroke plane, β. The $\mathbf{x_b}$ and $\mathbf{y_b}$ axes of this body-fixed coordinate system lie in the stroke plane, as shown in Fig 3. The $\mathbf{y_b}$ axis is always horizontal, while the $\mathbf{x_b}$ axis points behind the bat. The $\mathbf{z_b}$ axis is perpendicular to both, and follows the right hand rule. This conforms to the convention used in Ref. [54].

A second frame of reference, ($\mathbf{x_a}$, $\mathbf{y_a}$, $\mathbf{z_a}$), which follows each given airfoil through movements about ($\mathbf{x_b}$, $\mathbf{y_b}$, $\mathbf{z_b}$), is also defined. Since both wings are discretized into multiple airfoils, there are as many ($\mathbf{x_a}$, $\mathbf{y_a}$, $\mathbf{z_a}$) systems as there are airfoil sections. The origin of this airfoil coordinate system is located on the span line, with the $\mathbf{y_a}$ axis remaining coincident with the span line as the wings flap. When the span line is horizontal at a zero flap angle, $\mathbf{x_a}$ is horizontal and $\mathbf{z_a}$ is vertical. As the wings flap, each airfoil coordinate system, ($\mathbf{x_a}$, $\mathbf{y_a}$, $\mathbf{z_a}$), shifts and re-orients based on the rotation of the span line as shown in Fig 3.

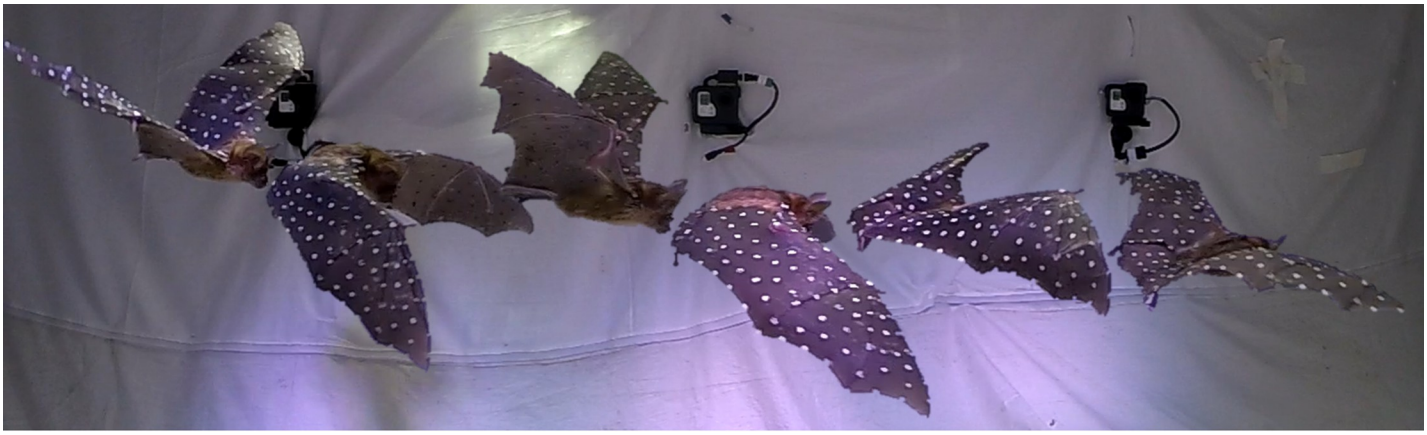

Fig 1. Still-frames showing flight path of *H. pratti* in tunnel: Wing marker points recorded and reconstructed to derive wing kinematics.

https://doi.org/10.1371/journal.pone.0218672.g001

Five wing motion components. First, the position of the wing span line is specified using two angles defined relative to the stroke plane. The first angle, ϕ, is the flapping angle in the stroke plane (Fig 3(B)), while the second angle, θ, captures the deviation of the wing from the

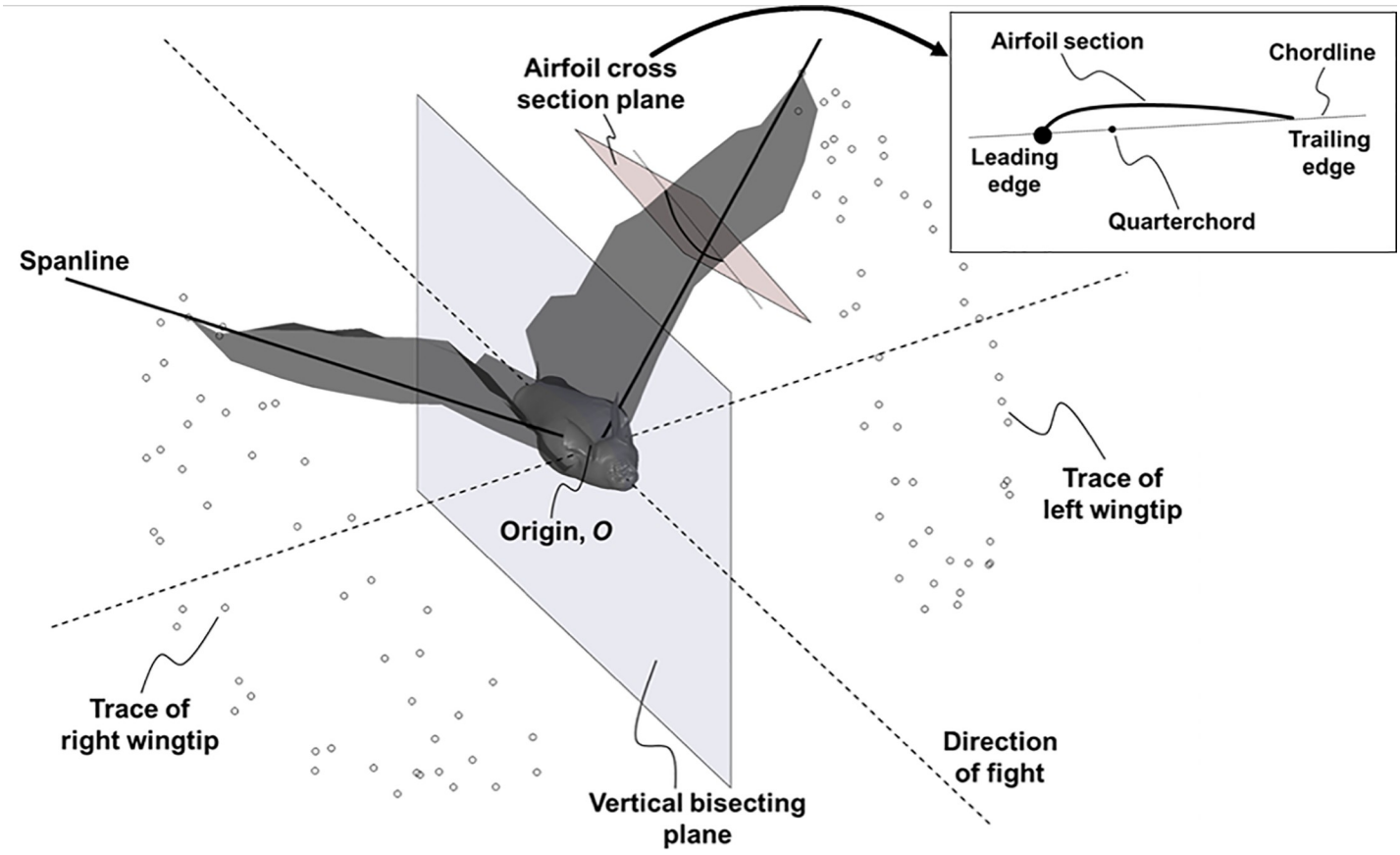

Fig 2. Terminology used in the kinematic decomposition: The right and left wingtips each trace out a locus of points that are projected onto the vertical bisecting plane to determine the stroke plane angle.

https://doi.org/10.1371/journal.pone.0218672.g002

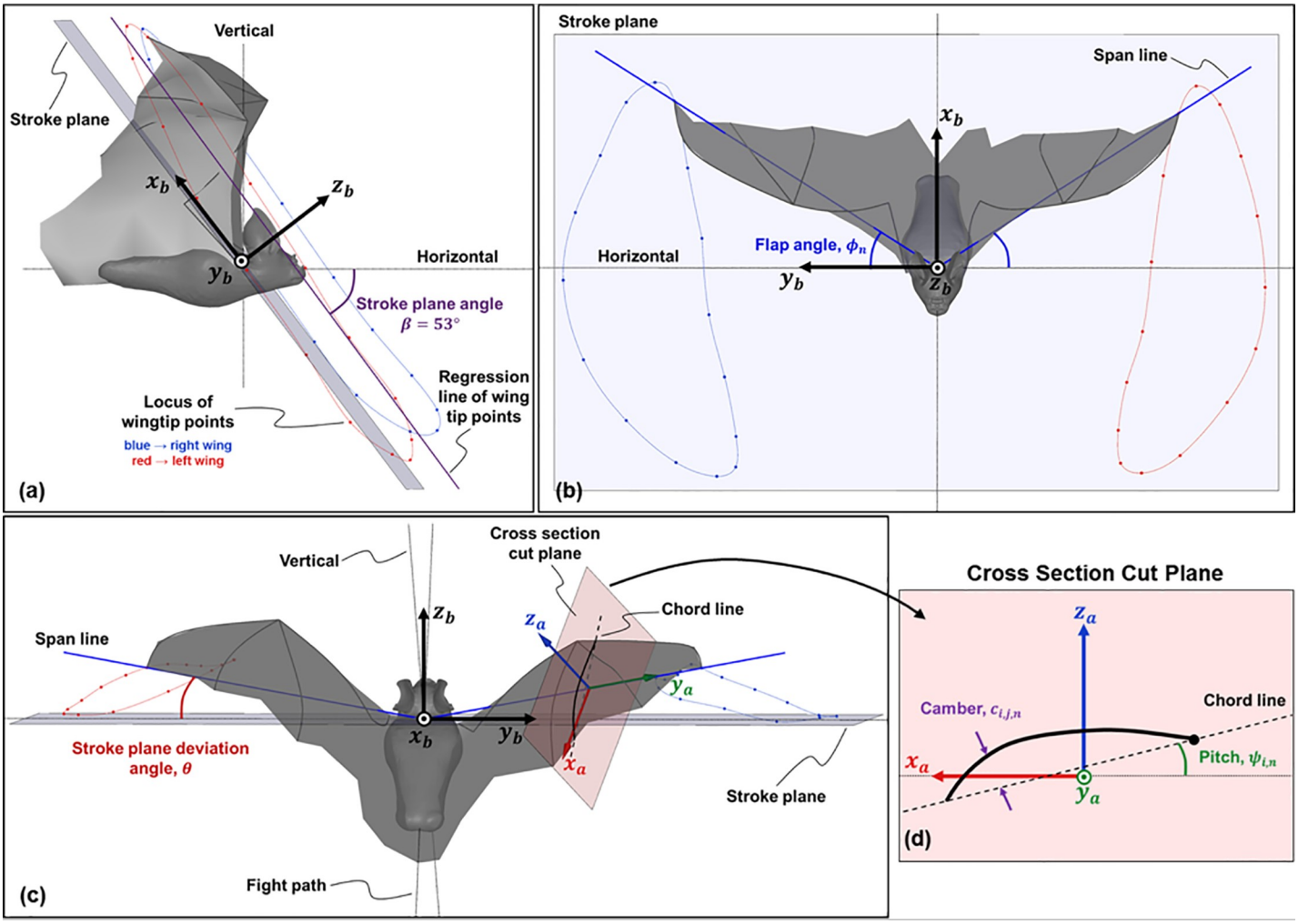

Fig 3. (a) Side view of the bat (view along the y_b axis) showing the stroke plane and the body-fixed stroke plane coordinate system (x_b, y_b, z_b), (b) view along the z_b axis, looking directly at the stroke plane: the flap angle, ϕ_n, controls the location of the span line and varies with time, (c) view looking down the stroke plane, along the x_b axis: the stroke plane deviation angle, θ_n, defines the position of the span line out of the stroke plane; a representative airfoil coordinate system, (x_a, y_a, z_a), is shown on the right wing, and highlighted in (d). The pitch angle, $\psi_{i,n}$, defines the rotation of the airfoil section about the span line, and varies along the span, 'i', as well as varies in time, 'n'. The camber, $C_{i,j,n}$, defines the displacement of the airfoil away from the span line, and varies along the span, 'i', chord, 'j', and in time, 'n'.

https://doi.org/10.1371/journal.pone.0218672.g003

stroke plane (Fig 3(C)). A third angle, ψ, defined in the airfoil reference frame, captures the rotation of each airfoil about the span line (Fig 3(D)). ψ represents the pitch angle of the wing, and can vary both temporally and spatially along the span. The curvature (or camber) of the wing is defined as the displacement of the airfoil from the chord line (Fig 3(D)). The camber can vary temporally, as well as spatially along the span and along the chord. Lastly, flexion of the wing captures the shift of each airfoil section relative to the span line, as shown in Fig 4. Flexion is necessary to properly define wing motion because the quarter-chord of each airfoil does not necessarily remain on the span line. Displacement of the quarter-chord from the span line in the $\mathbf{z_a}$ direction is shown in Fig 4(A), while displacement in the $\mathbf{x_a}$ direction is shown in Fig 4(B). The overall outline of the decomposition of native kinematics into the five wing motion components is presented as a step-by-step procedure in the Supporting information section (see S1 Text).

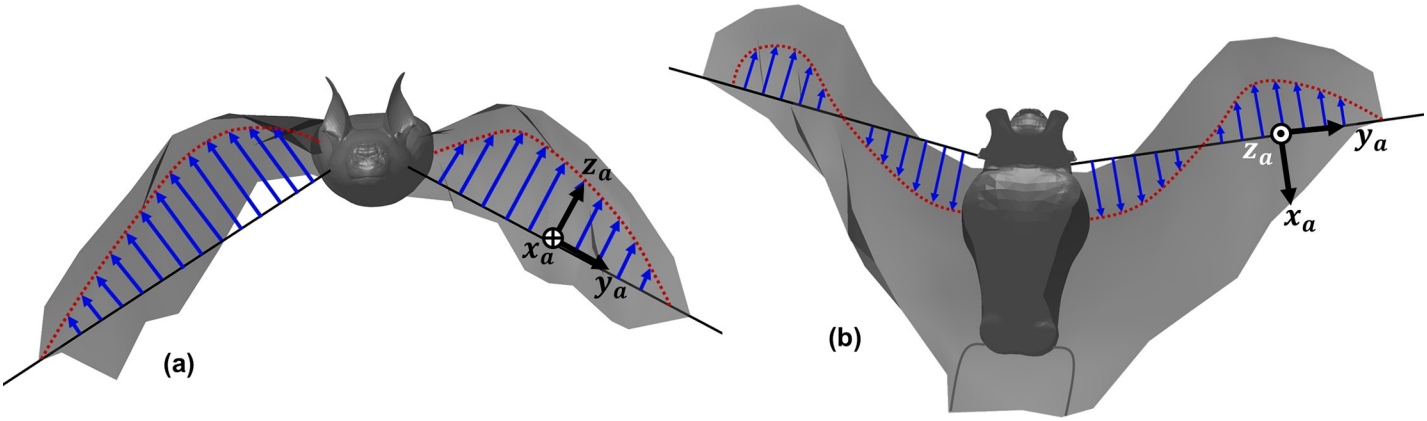

Fig 4. Wing flexion as defined as displacement of the quarterchord from the span line: (a) along the $\mathbf{z}_a$ axis, (b) along the $\mathbf{x}_a$ axis (refer Fig 3(d) for orientation information).

https://doi.org/10.1371/journal.pone.0218672.g004

Mathematically, the combination of all the aforementioned components is modeled as:

$$\mathbf{W}(t = t_n) = \mathbf{W}_{i,j,n} = \mathbf{R}_n(\phi)\mathbf{R}_n(\theta)\,\mathbf{R}_{i,n}(\psi)[\mathbf{P}_{i,j} + \mathbf{C}_{i,j,n} + \mathbf{D}_{i,n}] \quad (1)$$

Here, subscript 'n' signifies a discrete time instant, 'i' represents the index that identifies a chord line along the span, and 'j' denotes the discretization along each chord line to characterize camber. Thus, $\mathbf{W}(t = t_n)$ represents the combination of every modeled degree of freedom: $\mathbf{R}(\phi)$ represents the flapping motion of the wing, $\mathbf{R}(\theta)$ models stroke plane deviation, and $\mathbf{R}(\psi)$ denotes the pitching motion. It is evident from the equation that $\mathbf{R}(\phi)$ and $\mathbf{R}(\theta)$ vary with time, and are constants for each wing. $\mathbf{R}(\psi)$ is also time-dependent, in addition to varying along the span. $\mathbf{P}_{i,j} = [0, y_i, z_{i,j}]^T$ corresponds to the base state of the wings consisting of a collection of chord lines. To represent non-zero chordwise cambering, these chord lines transform into airfoil sections with the addition of $\mathbf{C}_{i,j,n} = [x_{i,j,n}, 0, 0]^T$. Additionally, $\mathbf{D}_{i,n} = [x_{i,n}, y_{i,n}, z_{i,n}]^T$ denotes wing flexion that represents the displacement of the quarter-chord of each airfoil away from

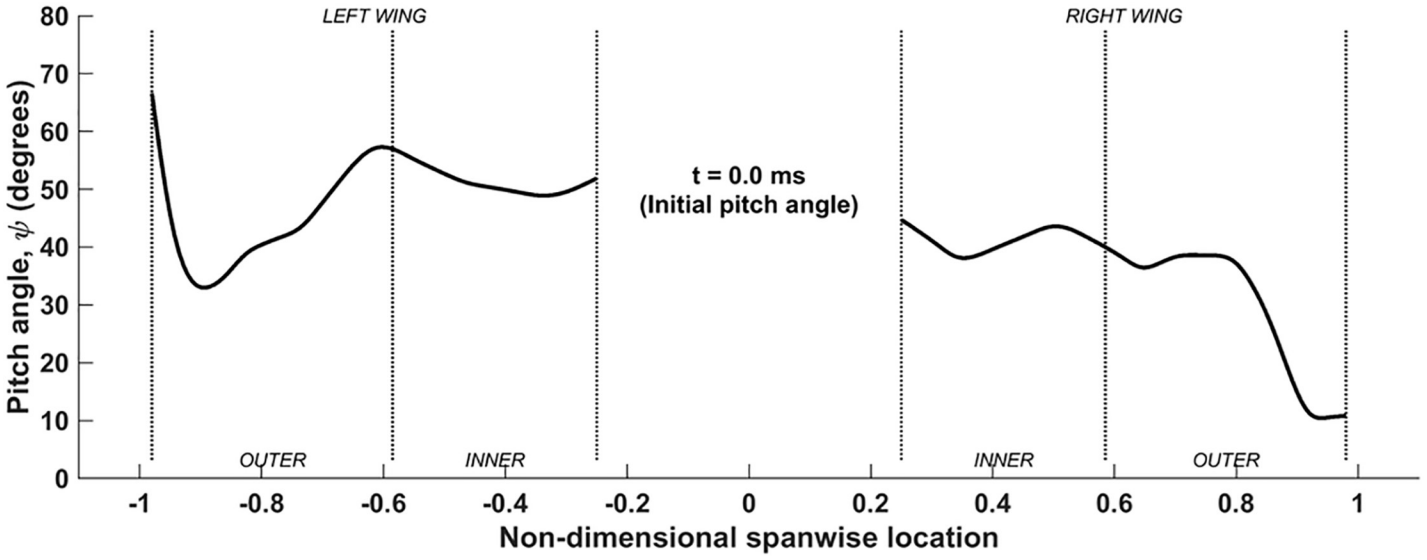

Fig 5. Spanwise variation of pitch angle (ψ) at base reference state (time-invariant).

https://doi.org/10.1371/journal.pone.0218672.g005

the span line within the airfoil plane ($x_{i,n}$,$z_{i,n}$), and the spanwise inward-outward movement of the wing ($y_{i,n}$).

The following sub-sections use the wing kinematic dataset for a 1 m long straight level flight of *H. pratti* to describe the progression from the simplest modeled motion to the most complex combination of movements in detail. For this dataset, the stroke plane angle was estimated to be $\beta = 53^{\circ}$ over the three flapping cycles.

Flapping motion. This motion constitutes the most fundamental of wing movements, flapping. Here, the wings do not deviate from the stroke plane, and the spanwise airfoils do not pitch, nor do they have any camber. Further, the wings do not flex, and thereby, the flapping motion only models the most significant rotational motion of the wing. The governing equation for this simplifies to:

$$\mathbf{W}(t = t_n) = \mathbf{W}_{i,j,n} = \mathbf{R}_n(\phi)\mathbf{R}_{i,n=0}(\psi)\,\mathbf{P}_{i,j} \tag{2}$$

Here, $\mathbf{P}_{i,j}$ is the time-invariant matrix of points that represents all the chord lines, and $\mathbf{R}_n(\phi)$ is the only time-evolving term. $\mathbf{R}_{i,n\,=\,0}(\psi)$ is the time-invariant pitching angle distribution along the span used to represent the base state of the wings (Fig 5). Nearly 80% of the left and right wings reveal pitching angles between 40˚ and 60˚ and 40˚ and 50˚, respectively. With $\beta = 53^{\circ}$, this sets up a nearly horizontal reference state for the wings. There are significant variations at the wingtips, with both wings exhibiting opposite trends in ψ. This combination results in the flapping of a rigid, but non-flat wing surface. At each time instant, both wings perform rigid body rotations, and the trajectory of the wingtips form arcs in the stroke plane.

In Fig 6(A), *t*/T denotes the nondimensional timestamp for one flapping cycle, and the corresponding dimensional time of flight starts at 53 ms and ends at around 182ms in the recorded kinematics. In Fig 6(B), the plot shows the temporal variations of ϕ about $\mathbf{y_b}$, with a mean amplitude of ≈90˚. This is comparable to the flapping amplitude of *C. brachyotis* (77˚), as noted by Viswanth et al. in their study of straight-climbing flight of fruit bats, and within the range expected of bat species of comparable weight (60˚-150˚ for bats weighing between 0.01-1kg; the *H. pratti* in the current study weighed 0.055kg) [47,52]. Whereas the flapping phases of both wings are in perfect synchrony, the angles are different between the right and left wings, with the overall amplitude remaining nearly the same for both. The instantaneous differences in ϕ between the left and right wings are attributed to the slight banking towards the left [52]. The overall shape of the temporal evolution of the flapping angle is sinusoidal, and the slope is steeper during the upstroke, which indicates a faster recovery movement.

Stroke plane deviation. The stroke plane deviation angle quantifies the extent of in-to and out-of stroke plane motion during the flapping cycles. The governing equation for the wing with this motion included is:

$$\mathbf{W}(t = t_n) = \mathbf{W}_{i,j,n} = \mathbf{R}_n(\phi)\mathbf{R}_n(\theta)\mathbf{R}_{i,n=0}(\psi)\mathbf{P}_{i,j} \tag{3}$$

Here again, $\mathbf{P}_{i,j}$ is time invariant and represents the chord lines, and $\mathbf{R}_n(\theta)$ is the only time-evolving term. Since flapping constitutes a fundamental motion of the wings, $\mathbf{R}_n(\phi)$ is included by default in this, and in subsequent canonical descriptors. The time-invariant reference frame pitching distribution, $\mathbf{R}_{i,n\,=\,0}(\psi)$, is also included in this combination.

This combination features each wing performing an additional rigid body rotation out of the stroke plane ($\mathbf{x_b}$, $\mathbf{y_b}$). Fig 7(A) shows the combined flapping and stroke plane deviation for the same cycle shown for flapping motion. In this case, the wingtips do not lie in the stroke plane, and continually move in and out of the ($\mathbf{x_b}$, $\mathbf{y_b}$) plane. The combined effect of these two movements (flapping and stroke plane deviation) results in crescent-shaped trajectories. The upstroke is characterized by a backward sweep of the wingtips, followed by a forward sweep

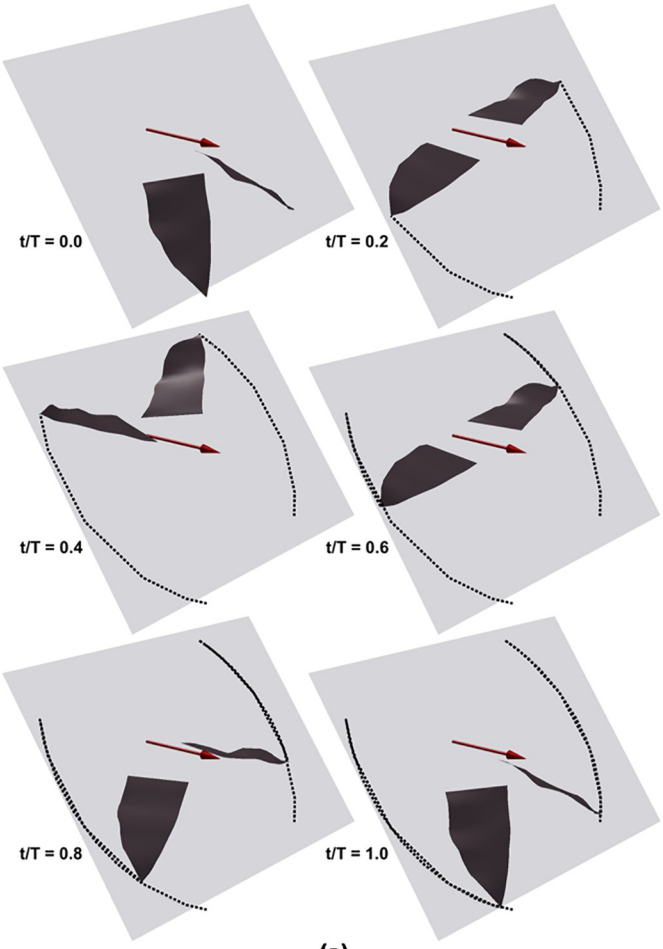
t/T = 0.0
t/T = 0.2
t/T = 0.4
t/T = 0.6
t/T = 0.8
t/T = 1.0

(a)

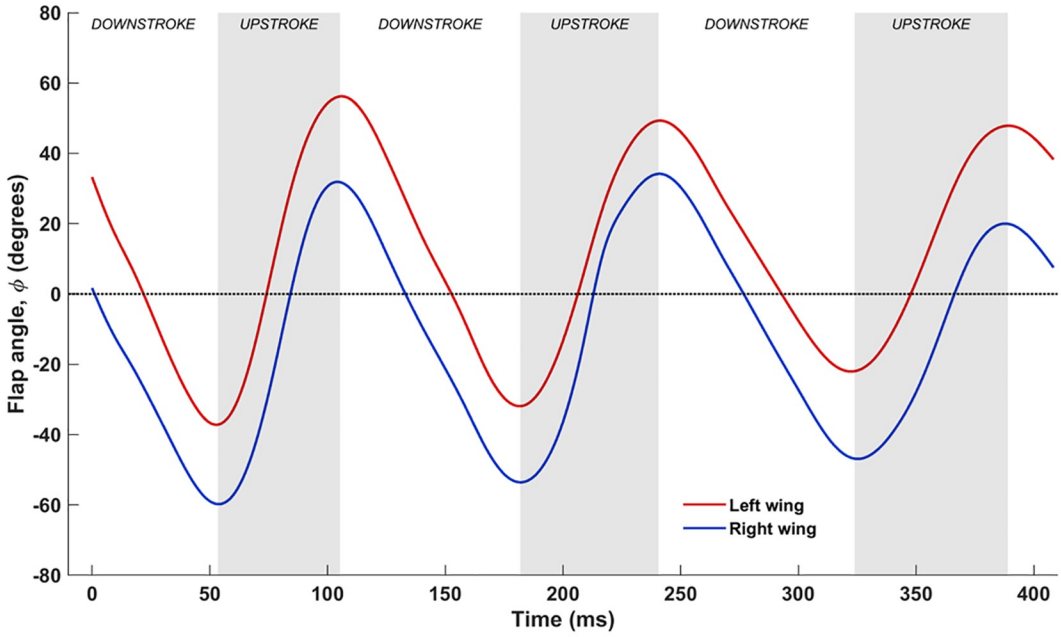
DOWNSTROKE
UPSTROKE
DOWNSTROKE
UPSTROKE
DOWNSTROKE
UPSTROKE
Flap angle, ϕ (degrees)
Time (ms)
Left wing
Right wing
80
60
40
20
0
-20
-40
-60
-80
0
50
100
150
200
250
300
350
400

(b)

Fig 6. (a) Flapping motion plotted for one flapping cycle (53ms to 182ms), with light-grey tiles representing the stroke plane (x_b, y_b) inclined at 53˚, dark-grey surfaces representing the wings, tip trajectories traced by dots, and maroon arrows denoting direction of flight; (b) temporal evolution of flapping angle (ϕ), with shaded areas representing upstroke.

https://doi.org/10.1371/journal.pone.0218672.g006

during the downstroke to complete the cycle. In Fig 7(B), substantial asymmetry exists between the left and right wings over the three flapping cycles. Peaks and troughs in θ occur during the middle of the upstroke and downstroke, respectively, with the left wing lagging behind the right wing. Over the three flapping cycles, the mean peak-to-trough amplitude for the left wing is approximately 13˚ about the stroke plane, and approximately 9˚ for the right wing, for nominal stroke deviation angles between ≈0˚ and 25˚ (positive angles by virtue of the stroke plane being located near the shoulder, and the wingtips lying ahead). It is notable here that in a previous work of a flapping and pitching 3D rigid flat plate with different stroke plane deviation profiles (O-profile and 8-profile) [55], it was found that the O-profile with θ between 10˚ and 20˚ produced a near steady thrust over the flapping cycle, leading to the conclusion that it was most suitable for steady forward flight.

Pitching motion. The governing equation for the wing kinematics when the pitching motion is included is:

$$\mathbf{W}(t = t_n) = \mathbf{W}_{i,j,n} = \mathbf{R}_n(\phi)\mathbf{R}_n(\theta)\,\mathbf{R}_{i,n}(\psi)\mathbf{P}_{i,j} \tag{4}$$

Here too, $\mathbf{P}_{i,j}$ continues to be time-invariant, whereas $\mathbf{R}_{i,n}(\psi)$ now varies with time, and along the span of the wing. $\mathbf{R}_n(\phi)$ and $\mathbf{R}_n(\theta)$ are carried over from the previous combination of movements.

The bat wing for this, and subsequent combinations, is assumed to be a flexible membrane that can twist along the span. As a result, different sections along the span exhibit different pitching angles. Fig 8 shows the demarcation of the inner and outer wing sections on both wings that are determined based on the instantaneous locations of the left and right wrists.

The pitching motion pertains to the orientation of the chord line of each airfoil section with respect to the stroke plane. Fig 9(A) shows the variation of the pitch angle (ψ) along the span during one flapping cycle, for the same time-period shown for the previous two movements (53ms to 182ms). Here, the color of the lines denotes the time lapsed from the beginning of the 1st upstroke until the end of the 2nd downstroke, making up one flapping cycle. Fig 9(B) shows the temporal evolution of ψ at different locations on the left and right wings identified as the mid-outer and mid-inner lines during the three flapping cycles.

Clearly, ψ varies not only with time (Fig 9(B)), but also along the span, which is representative of twist (Fig 9(A)). For much of the flapping cycle, extreme pitch angles are localized towards the ends of the wing (the root and the tip), and a somewhat monotonic and nonlinear variation of the pitching angle is established from the root to the tip, as can be seen in Fig 9(A). The overall variation of ψ is also larger in the outer wing (≈100˚ range) while it is less pronounced in the inner wing (≈60˚ range). Typically during the upstroke, there is more pronounced twisting of the wing towards higher pitch angles as the bat tends to align the wing with the direction of the upstroke to minimize negative lift [47]. This is apparent from the $t/T = 0$ and 0.2 curves (blue and green lines), which are limited to higher pitch angles. During this time, the pitch angle increases from the root to the tip, maintaining values between 100˚ to 130˚, such that the outer wing is more in alignment with the upward motion of the wings in the stroke plane. Near the end of the upstroke, this trend is reversed: not only do the pitch angles decrease in magnitude across the span of the wing, but now the inner wing exhibits higher pitch angles than the outer wing. From Fig 9(B), during the downstroke, the mid-outer wing reaches a smaller minimum pitch angle (approximately 35˚), whereas the minimum

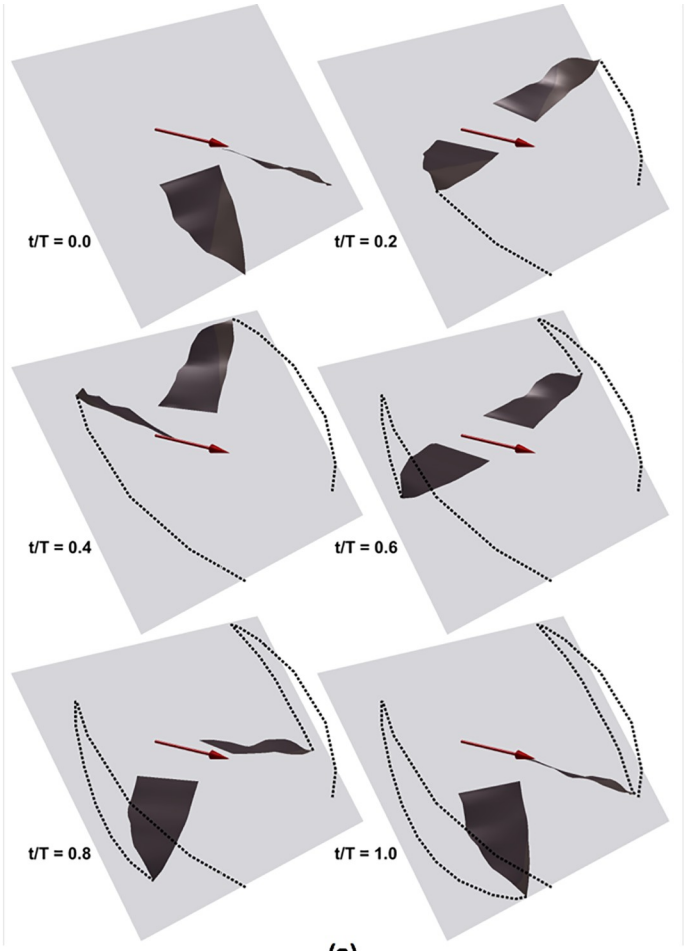
t/T = 0.0
t/T = 0.2
t/T = 0.4
t/T = 0.6
t/T = 0.8
t/T = 1.0

(a)

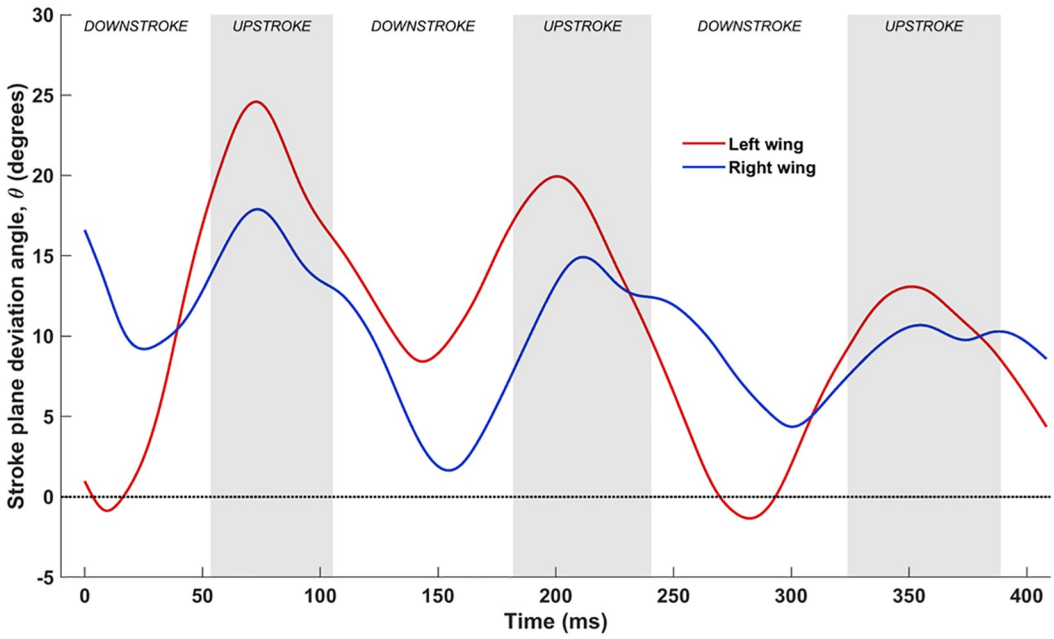
DOWNSTROKE
UPSTROKE
DOWNSTROKE
UPSTROKE
DOWNSTROKE
UPSTROKE
Left wing
Right wing
Stroke plane deviation angle, θ (degrees)
Time (ms)
30
25
20
15
10
5
0
-5
0
50
100
150
200
250
300
350
400

(b)

Fig 7. (a) Combined flapping and stroke plane deviation plotted for one flapping cycle (53ms to 182ms), with light-grey tiles representing the stroke plane ($\mathbf{x_b}$, $\mathbf{y_b}$) inclined at 53˚, dark-grey surfaces representing the wings, tip trajectories traced by dots, and maroon arrows denoting direction of flight; (b) temporal evolution of stroke plane deviation angle (θ)**, with shaded areas representing upstroke**.

https://doi.org/10.1371/journal.pone.0218672.g007

mid-inner wing ψ is at around 50˚. Between t/T = 0.8 and the end of the downstroke at t/T = 1.0, the wing undergoes rapid rotation, and it is during this time that the outer wing undergoes nearly 60˚ of rotation whereas the inner wing rotates by about 40˚. Also from Fig 9 (B), it is apparent that the wing undergoes advance rotation, i.e. the wing starts to pitch upwards before the end of the downstroke to optimize the upstroke motion, and starts to pitch downwards during the upstroke for a more effective downstroke. As will be shown later, wing twist has a significant effect on lift generation.

Cambering (chordwise). When chordwise cambering is included in the kinematics, the modeled equation describing wing motion is:

$$\mathbf{W}(t = t_n) = \mathbf{W}_{i,j,n} = \mathbf{R}_n(\phi)\mathbf{R}_n(\theta)\,\mathbf{R}_{i,n}(\psi)[\mathbf{P}_{i,j} + \mathbf{C}_{i,j,n}] \quad (5)$$

Here, the equation is nearly identical to the pitching motion, except that $[\mathbf{P}_{i,j}+\mathbf{C}_{i,j,n}]$ represents a cambered airfoil instead of the previous chord line ($\mathbf{P}_{i,j}$), and the camber varies with time. This is an additional degree of flexibility featured in the wing.

Fig 10 shows the temporal evolution of the shapes of four different airfoil sections on both wings, at the mid-inner and mid-outer wing locations defined in Fig 8. The leading edges are identified using a black dot at the (0,0) location in all the plots and both axes are in mm. During the downstroke (t/T = 0.6 to 0.8), the inner wing section exhibits a maximum chord length of approximately 100mm, whereas during the upstroke, the chord decreases to between 80mm and 90mm. The outer wing section, on the other hand, maintains a fairly constant chord length between 60mm and 70mm. There is a marked difference in the behavior of the inner wing and the outer wing sections on both wings: the variability in airfoil shape during the flapping cycle is significantly more for the outer wing sections, exhibiting a variety of shapes and much larger cambers than the inner wing section. The airfoil cutting planes in the outer wing

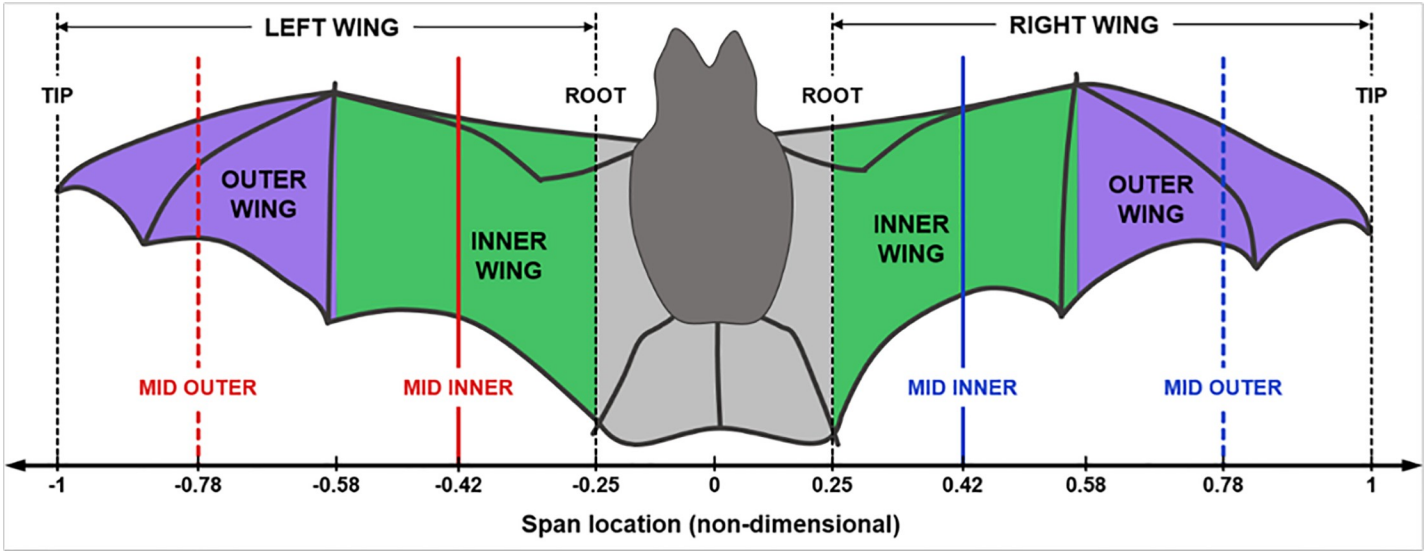

Fig 8. Demarcation of inner (green) and outer (purple) wings based on the instantaneous locations of the left and right wrists, and the location of cutting planes.

https://doi.org/10.1371/journal.pone.0218672.g008

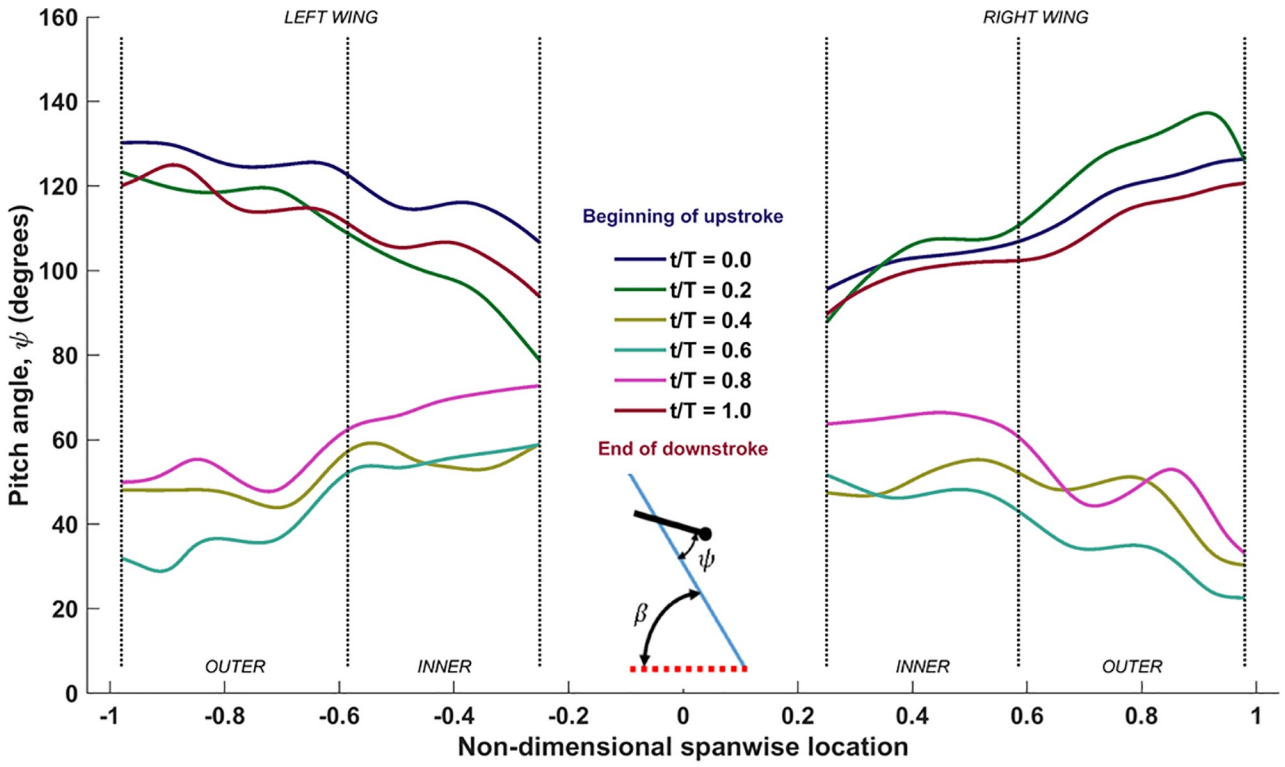
LEFT WING
RIGHT WING
Pitch angle, ψ (degrees)
Beginning of upstroke
t/T = 0.0
t/T = 0.2
t/T = 0.4
t/T = 0.6
t/T = 0.8
t/T = 1.0
End of downstroke
ψ
β
OUTER
INNER
INNER
OUTER
Non-dimensional spanwise location

(a)

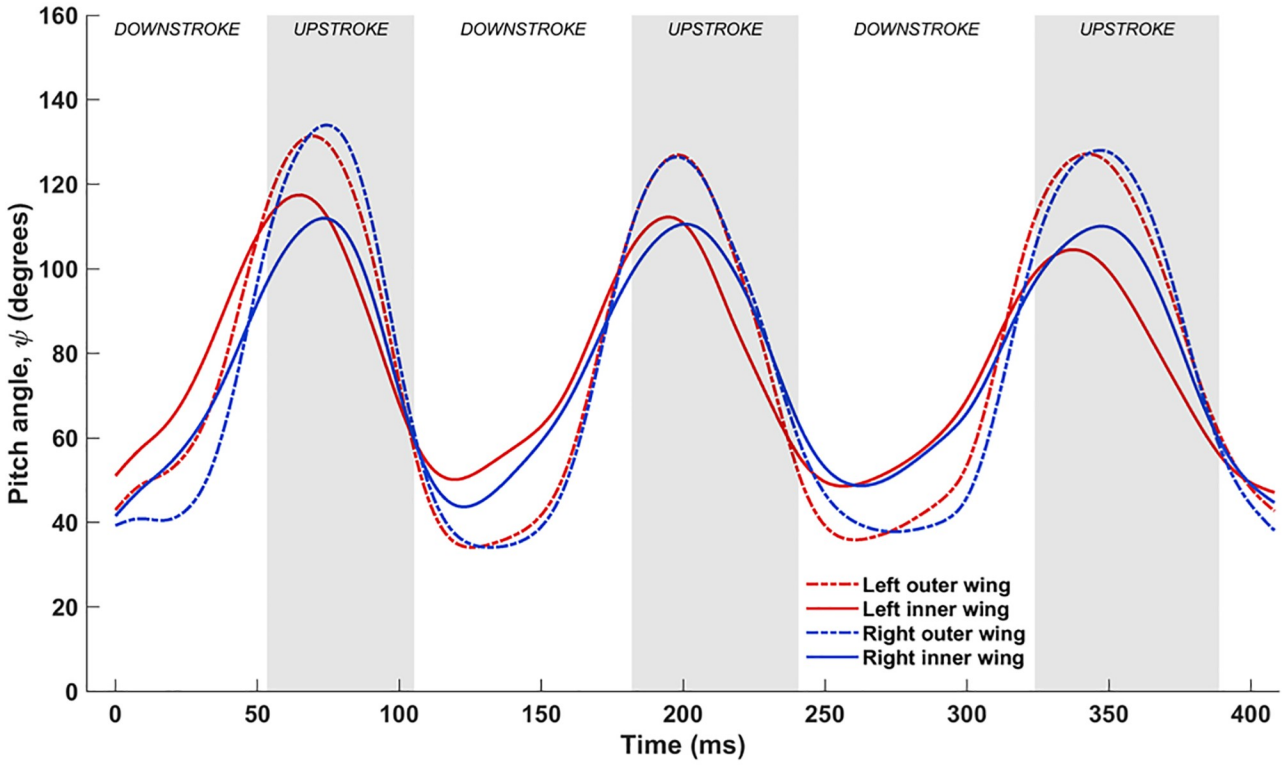
DOWNSTROKE
UPSTROKE
DOWNSTROKE
UPSTROKE
DOWNSTROKE
UPSTROKE
Pitch angle, ψ (degrees)
Left outer wing
Left inner wing
Right outer wing
Right inner wing
Time (ms)

(b)

Fig 9. (a) Spanwise variation of pitch angle (ψ) for one flapping cycle (53ms to 182ms) with inset showing the definition of pitch angle with respect to stroke plane angle (β) for an airfoil chord line; (b) temporal evolution of ψ at mid outer and and inner wing sections.

https://doi.org/10.1371/journal.pone.0218672.g009

pass through phalanges across different digits, which could alter airfoil camber considerably. The inner wing, on the other hand, assumes shapes more in line with conventional airfoils except at the start of the upstroke (t/T = 0 and 1.0). Here, the left wing shows a clear inflection point at 70–80% chord length, which is absent on the right wing. The outer wing sections on both wings behave rather independently, showing large variance in the camber values through the flapping cycle. The right outer wing shows a relatively consistent trend of having peak camber around the mid-chord, while the left wing behavior is more complex. These complex shapes can be attributed to the flexible membrane wing that stretches and relaxes during the flapping cycle depending on the aerodynamic and inertial forces acting on it.

In Fig 11, the time evolution of the maximum absolute chordwise camber over the measured flight at all span locations are shown as shaded regions. The lines (solid and dashed) are the maximum camber at the highlighted mid-sections of the inner and outer wing from Fig 8. Evidently, there is a wide spread in the maximum camber, which demonstrates the flexible nature of the wing, and the ability of bats to actively control wing morphology, as well as respond to both aerodynamic and inertial forces. For example, near the middle of the 2nd upstroke (≈200 ms), the maximum camber on the left wing reaches almost 29 mm and on the right wing, it reaches a local maximum of 23 mm. These represent deflections that are approximately 40% and 30% of the standard mean chord (74 mm).

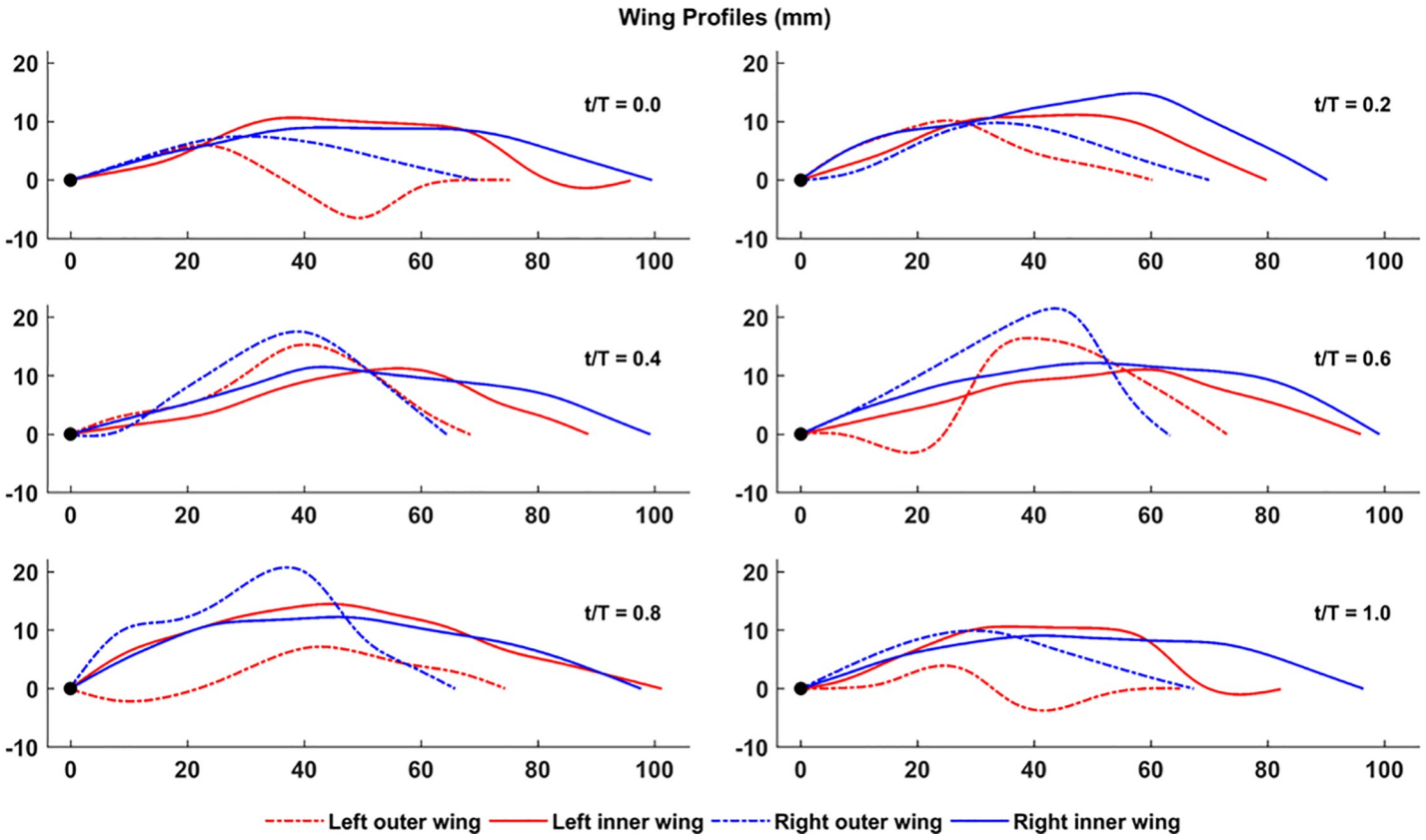

Fig 10. Temporal evolution of airfoil shape at mid-inner and outer sections on both wings over one flapping cycle (53 ms to 182 ms).

https://doi.org/10.1371/journal.pone.0218672.g010

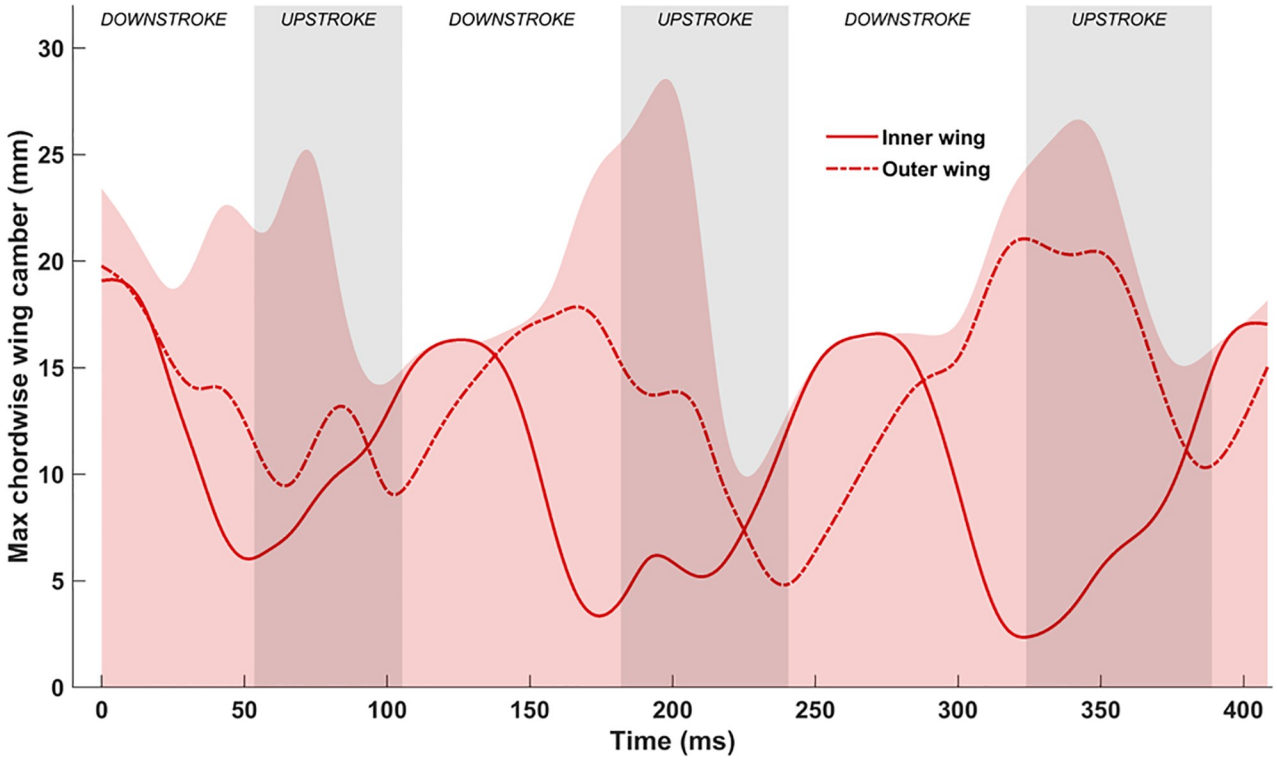
DOWNSTROKE
UPSTROKE
DOWNSTROKE
UPSTROKE
DOWNSTROKE
UPSTROKE
Inner wing
Outer wing
Max chordwise wing camber (mm)
Time (ms)
0
5
10
15
20
25
30
0
50
100
150
200
250
300
350
400

(a)

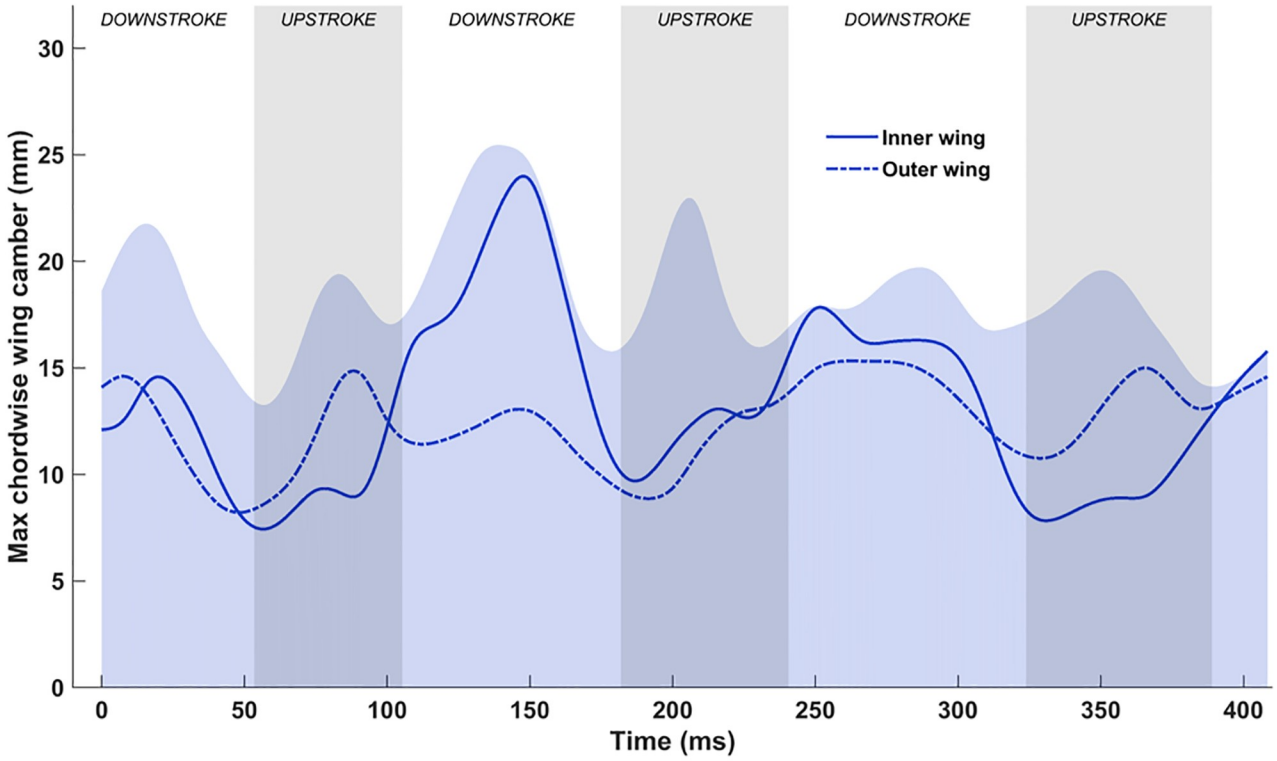
DOWNSTROKE
UPSTROKE
DOWNSTROKE
UPSTROKE
DOWNSTROKE
UPSTROKE
Inner wing
Outer wing
Max chordwise wing camber (mm)
Time (ms)
0
5
10
15
20
25
30
0
50
100
150
200
250
300
350
400

(b)

Fig 11. Temporal evolution of chordwise camber at different airfoil sections along the span: (a) left wing, (b) right wing.

https://doi.org/10.1371/journal.pone.0218672.g011

Temporally, the right wing shows a more consistent cambering trend between the inner and outer wing: except for out-of-sync cambering during the 2nd downstroke, both the inner and outer right wing follow the same cadence. The left wing also starts with a similar consistent cambering trend, but during and after the 2nd downstroke, the inner and outer left wing exhibit out of phase maximum cambering. Over the measured kinematics, the mean maximum camber over the full span of the wing is between 17 mm and 20 mm, which is approximately 25% of the standard mean chord.

Flexion. Incorporating wing flexion completes the integration of all the movements of bat wing kinematics. The modeled equation is the same as shown earlier (Eq 1):

$$\mathbf{W}(t = t_n) = \mathbf{W}_{i,j,n} = \mathbf{R}_n(\phi)\mathbf{R}_n(\theta)\mathbf{R}_{i,n}(\psi)[\mathbf{P}_{i,j} + \mathbf{C}_{i,j,n} + \mathbf{D}_{i,n}]$$

Here, $\mathbf{D}_{i,n}$ represents the time dependent displacement of each airfoil about its spanwise location, and this is allowed along all three axes.

Fig 12(A) shows the spanwise evolution of flexion of both wings during a single flapping cycle (53ms to 182ms) in terms of the off-span displacement: $|\mathbf{D}_{i,n}| = (x_{i,n}^2 + z_{i,n}^2)^{1/2}$. The high variability and the out-of-phase morphology between the left and right wings is testament to both the highly articulated nature of the wings and the inherent asymmetry in natural flight. It is noteworthy that the majority of flexion occurs towards the end of the downstroke (t/T = 0 and 1.0) and during the early part of the upstroke (t/T = 0.2), during which the bat retracts both wingtips towards the body, resulting in maximum flexion (≈50mm at t/T = 0.2) falling around the wrist on each wing. There is a marked reduction in flexion during the downstroke, when the bat extends the wing outwards to maximize the projected area, in addition to optimizing the planform using the pitch angle distribution (Fig 9(A)).

Fig 12(B) shows the temporal evolution of the maximum flexion of both wings during all three flapping cycles. The same trend of higher flexion magnitudes during the upstroke to reduce the planform area, and relatively lower magnitudes during the downstroke is evident throughout the flight path. Differences between the left and right wing flexion is further evidence that the bat uses multiple movements to optimize and effect even a simple near-straight and level flight. The mean maximum flexion over the three flapping cycles is approximately 35mm, which is ≈50% of the standard mean chord.

Aerodynamic analyses

The investigation into the cumulative impact of each physical movement on force production is presented here. The analysis first considers the basic flapping motion, and builds up complexity progressively by including additional movements to construct the complete native wing kinematics. Throughout this process, insight is gained into the effect of each motion on the unsteady flow field, and on force production.

Simulations setup

All simulations were performed using an in-house developed software, GenIDLEST [56] (Generalized Incompressible Direct and Large Eddy Simulation of Turbulence). It is a parallelized code developed for time-dependent fluid flow calculations that solves the incompressible Navier-Stokes equations in a generalized coordinate framework. Details about the formulation can be found in Ref. [57].

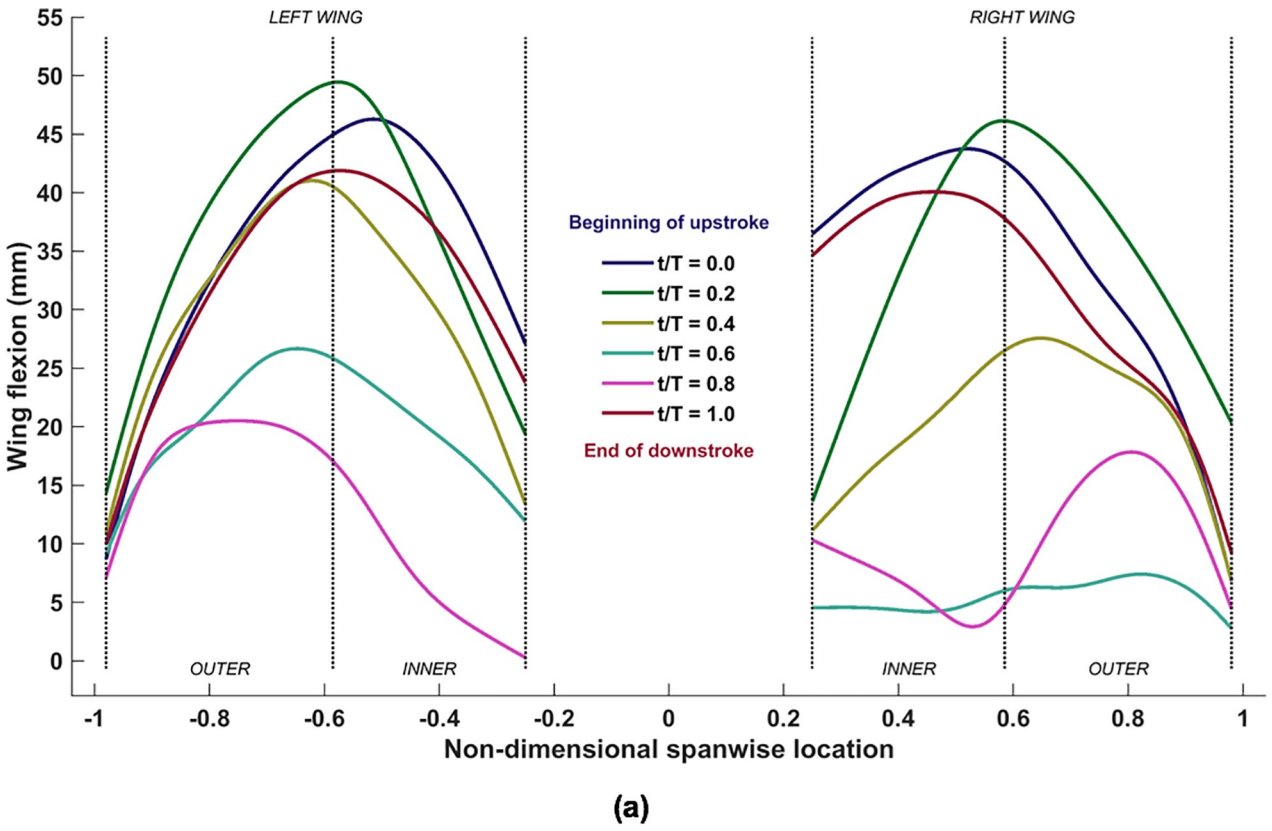

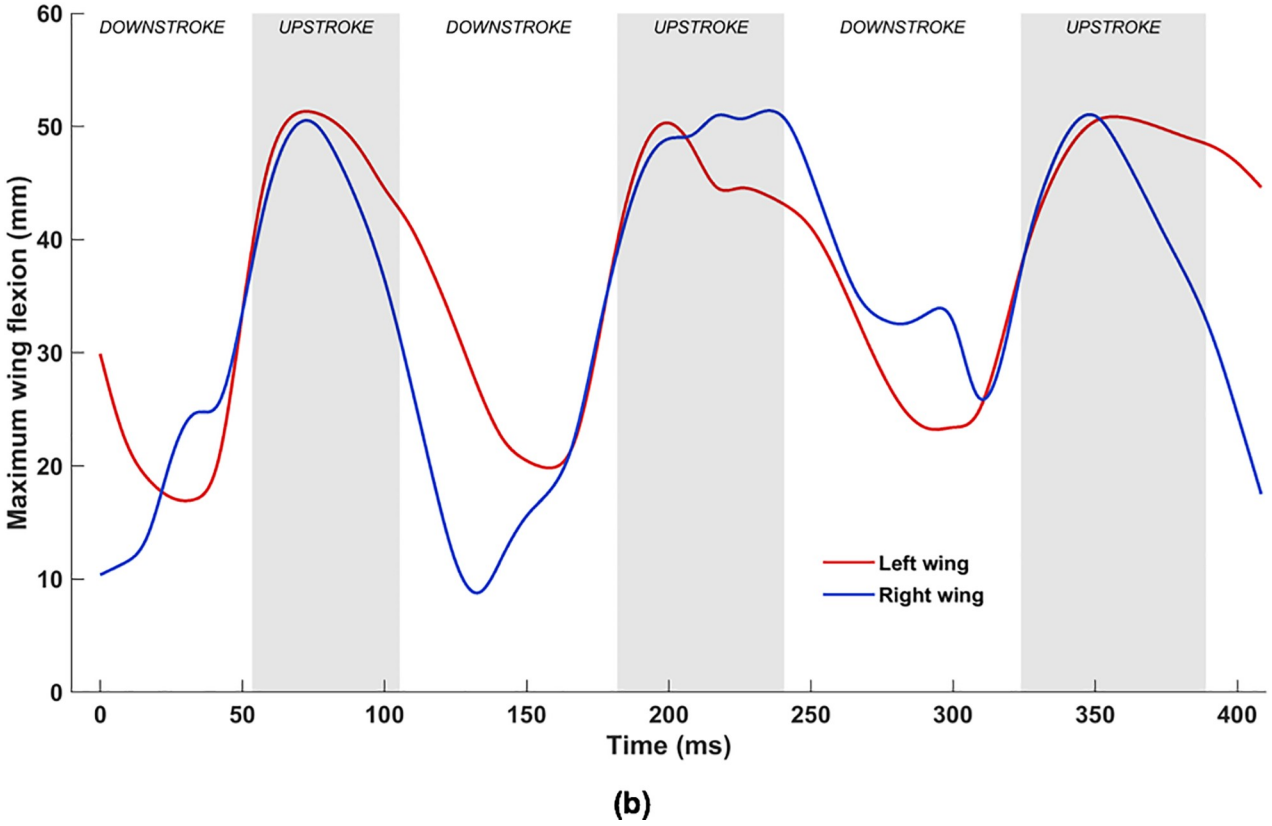

Fig 12. (a) Spanwise variation of flexion over one flapping cycle (53ms to 182ms), (b) temporal evolution of maximum flexion.

https://doi.org/10.1371/journal.pone.0218672.g012

Governing equations and methods. The nondimensional Navier-Stokes equations for incompressible flows in a generalized coordinate framework are:

$$\frac{\partial u_i}{\partial x_i} = 0 \tag{6}$$

$$\frac{\partial u_i}{\partial t} + \frac{\partial}{\partial x_j}\left(u_i u_j\right) = -\frac{\partial p}{\partial x_i} + \frac{\partial}{\partial x_j}\left[\frac{1}{\mathrm{Re}}\frac{\partial u_i}{\partial x_j}\right] \tag{7}$$

where the state variables are nondimensionalized as:

$$x_i = \frac{x_i^*}{L_{\mathrm{ref}}^*}; u_i = \frac{u_i^*}{u_{\mathrm{ref}}^*}; t = \frac{t^* u_{\mathrm{ref}}^*}{L_{\mathrm{ref}}^*}; p = \frac{p^* - p_{\mathrm{ref}}^*}{\rho_{\mathrm{ref}}^* u_{\mathrm{ref}}^* 2}; \mathrm{Re} = \frac{\rho_{\mathrm{ref}}^* u_{\mathrm{ref}}^* L_{\mathrm{ref}}^*}{\mu_{\mathrm{ref}}^*}$$

Here, the superscript '*' and the reference parameters are dimensional quantities, and subscripts '*i*' and '*j*' are indices according to the Einstein summation convention. In the present work, the standard mean chord $c = L_{\mathrm{ref}}^* = 0.074$ m, and $u_{\mathrm{ref}}^* = 2.57$ m/s is the average flight velocity. This standard mean chord is defined as the ratio of the maximum planform area of the bat to the tip-to-tip wingspan. Nondimensional forces coefficients are normalized as $C = F^* / \frac{1}{2}\rho_{\mathrm{ref}}^* u_{\mathrm{ref}}^* S^*$, where F^* is the dimensional force component, $\rho_{\mathrm{ref}}^* = 1.2$ kg/m^3 is the reference ambient air density, u_{ref}^* is the reference freestream velocity, and $S^* = 0.0385$ m^2 is the maximum planform area of the wing during the downstroke. Based on these conditions, the nominal flight Re ≈ 12,000. In a previous work [47], it was shown that the nondimensional forces (lift, thrust, etc.) are independent of the Reynolds number for the unsteady separated vortex dominated flows encountered, and noted that the flow structures are more coherent and amenable to physical interpretation at lower Re. Such clarity augments the analysis of flow features that develop from different combinations of movements, more so while establishing the paradigm for decomposing complex kinematics of flapping flight. Thus, simulations were conducted at an arbitrary low Re = 400. Evidence of the insensitivity of nondimensional forces to Reynolds number is presented in the form of comparisons of various computed force components at Re = 12,000, 1,200 and 400 in Fig 13. Additionally, supporting information S5 Video, S6 Video, and S7 Video show a comparison between Re = 400, Re = 1,200, and Re = 12,000.

The governing equations are solved using a finite-volume procedure with a second-order central difference operator used for the convection and diffusion terms. Linear systems resulting in the implicit treatment of the momentum equations and the solution of the elliptic pressure equation are solved using a preconditioned BiCGSTAB method.

Computational domain and boundary conditions. The computational domain, shown in Fig 14, consists of a rectangular region that represents the experimental flight tunnel (1.18 m × 1.18 m cross-section). Relative to the standard mean chord length, the domain extends $30c \times 16c \times 16c$ along the streamwise, lateral and vertical directions, respectively. Along the streamwise direction, from the inlet to the outlet, the background mesh is divided into three sections: (i) a relatively coarse section that extends 7*c* upstream, (ii) a refined section around the bat geometry to resolve flow around the wings that is 7*c* long, and (iii) a long coarsened section leading to the outlet that extends 16*c* downstream. A similar strategy was applied to the lateral and vertical directions. The simulation was run using a moving reference frame with an equal and opposite velocity to the nominal flight velocity. This allows the computational domain to follow the bat over a long flight path while only requiring a short computational domain.

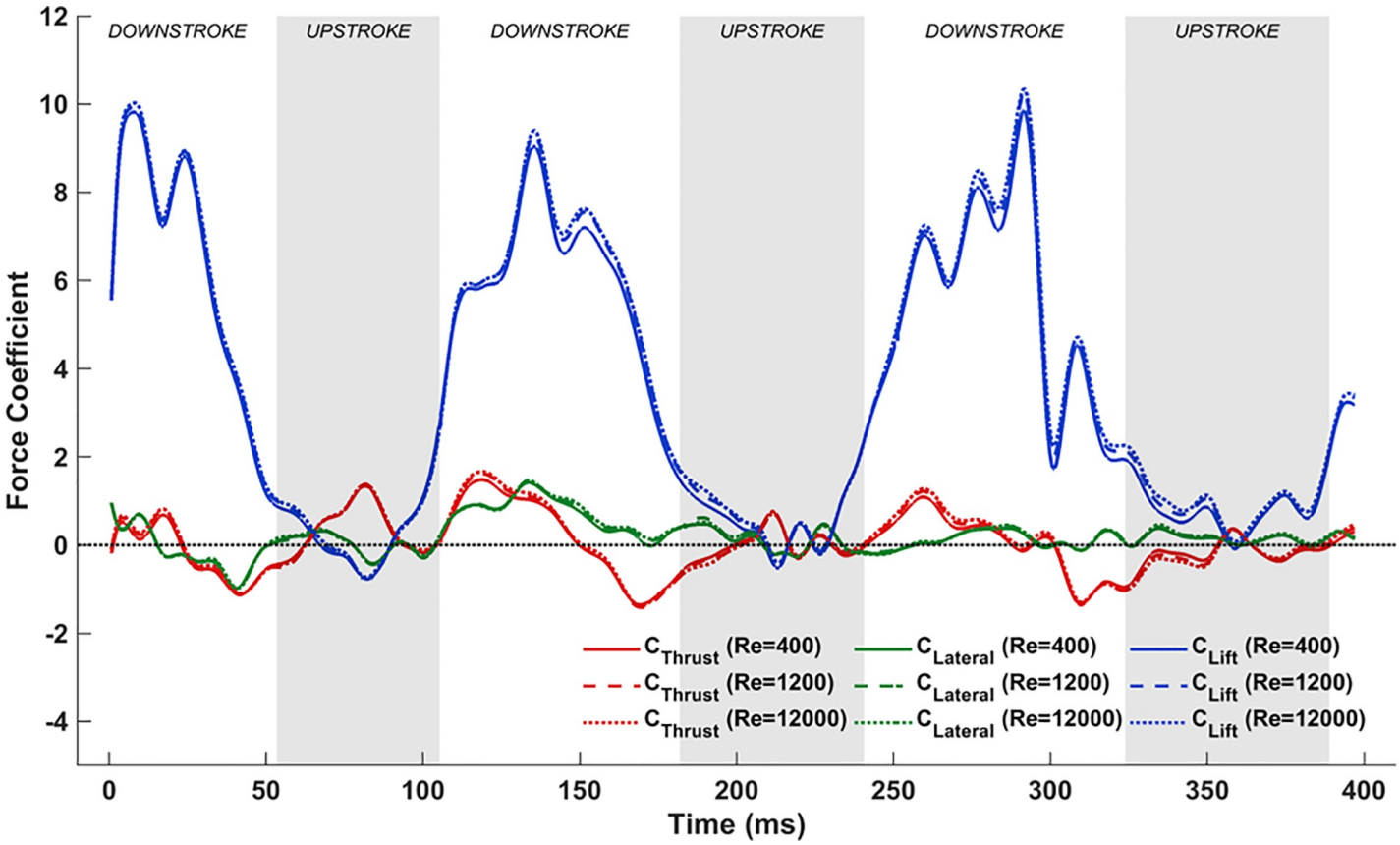

Fig 13. Comparison of force coefficients during bat flight (native kinematics) at three different Reynolds numbers (400, 1,200 and 12,000).

https://doi.org/10.1371/journal.pone.0218672.g013

The bat wing was represented as a moving immersed surface in a volumetric background mesh using an indirect-forcing sharp-interface IBM for infinitesimally thin surfaces. The wing was defined by a triangulated surface mesh. For the wing in motion, the fluid-solid interface was tracked in the flow at each time step based on the prescribed wing kinematics. The IBM procedure and implementation of boundary conditions are described in detail in Nagendra et al. [58]. The method was previously applied by Viswanath et al. [47,55] to bat flight, and by He and Tafti [59,60] to force and heat transfer calculations in particle suspensions. Most recently it was also applied by Windes et al. [52] to the native kinematics of the *H. pratti* in level flight.

The moving frame of reference was imposed using a constant inlet air velocity of 2.57 m/s and a sidewall slip velocity equal to the inlet velocity. The relative inlet and relative wall velocity of 2.57 m/s corresponds to zero velocity in a ground frame of reference. A zero-gradient condition was specified at the outlet of the domain noting that during the 0.42s of simulation time, the wake only extends up to 10*c* downstream of the bat and does not reach the outlet plane. The time-steps for all the simulations were approximately in the range of 25μs.

In all the cases presented, the wing surface was defined by approximately 70,000 triangular surface elements with a mean side of 1.26 mm. A grid independence study was carried out using four different Cartesian background meshes, ranging from 20-million to 70-million computational cells, while keeping the wing surface mesh the same. The results are tabulated in Table 1. The averaged differences (E_i) of the forces (F_i: net thrust, lateral force and lift) from

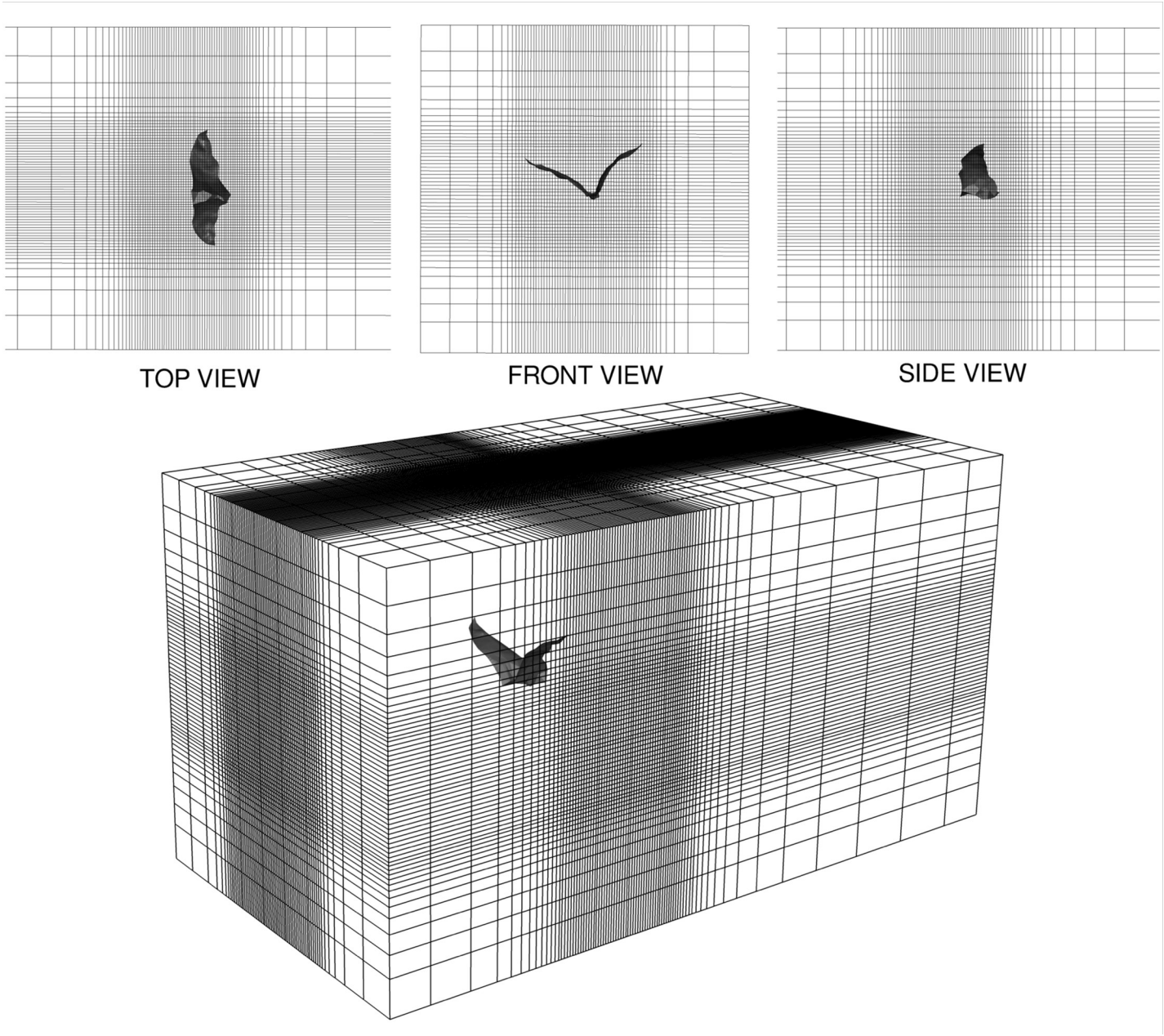

Fig 14. Perspective view of background mesh (plotting every 5th grid line of the $30c \times 16c \times 16c$ domain) for fluid simulation enclosing the bat, with orthographic projections of top ($18c \times 16c$), front ($16c \times 16c$) and side ($18c \times 16c$) views. The total cell count was 32 million.

https://doi.org/10.1371/journal.pone.0218672.g014

Table 1. Grid independence study.

Total number of cells	Length of cell in refined region	Aspect ratio of cell in refined region (Δx: Δy: Δz)	E_1(Net thrust)	E_2(Lateral)	E_3(Lift)
20×10^6	$c/28$	1 : 1 : 1	0.05%	1.6%	0.27%
32×10^6	$c/36$	1 : 1 : 1.5	0.03%	1.2%	0.05%
45×10^6	$c/36$	1 : 1 : 1	0.01%	1.1%	0.05%
70×10^6	$c/50$	1 : 1 : 1	-	-	-

https://doi.org/10.1371/journal.pone.0218672.t001

different meshes were calculated using:

$$E_i = \frac{1}{N}\sum^{N} \frac{|F_{i,n} - \hat{F}_{i,n}|}{|\hat{F}_{i,n}|} \quad (8)$$

Here, '*i*' represents different directional components of force, and '*n*' is the time-step. $\hat{F}_n$ is the baseline force calculated on the 70-million-cell background mesh. Estimated forces were grid independent for all meshes tested, with a maximum difference of 1.6% in the lateral force for the 20-million-cell background mesh. Related grid independency studies for the same flight of the *H. pratti* with native wing kinematics can be found in Windes et al. [52]. In the same study, dynamical analysis was provided to validate the calculated forces on the bat. There, it was shown that a trajectory predicted from the computed fluid forces matched well with the experimental flight trajectory.

Based on the results from this study, all simulations presented hereafter were performed on the 32-million-cell background mesh. A 3D representation of the grid showing every fifth cell is provided in Fig 14. The vortical structures in proximity to the wings, which directly impact force production, are well resolved in the refined region of the grid as shown in supporting S8 Video. Each was run on 120 Intel Broadwell processors at Virginia Tech's Advanced Research Computing facility, and took approximately 40hrs of wall clock time to complete the measured flight path of the bat.

Aerodynamics simulation results

Table 2 summarizes the time-averaged aerodynamic force coefficients from the simulations—net thrust is defined as the resultant forward force, lift is the net vertical force, and the lateral force is the third force component perpendicular to thrust and lift. It is evident that the flapping motion by itself produces a modest lift, and induces drag. The inclusion of stroke plane deviation increases lift by more than 40%, and more importantly, balances out the drag. The pitching motion further increases the mean lift by nearly 165%, and produces a net thrust force. Chordwise camber reduces net thrust by 20%, but increases lift by nearly 35%. Finally, the integration of all movements maximizes the lift force, reduces the net thrust to a modest value, and imparts a lateral force on the bat. These are in agreement with the small acceleration recorded during bat flight, and the nominal lateral movement off the straight flight path. Dynamic analysis using the native kinematics performed in Windes et al. [52] using the predicted instantaneous forces shows good agreement with the measured trajectory of the bat. Flight path animations showing the wing kinematics and isosurfaces of coherent vorticity are included as Supporting information (See S1 Video, S2 Video, S3 Video, S4 Video, S5 Video).

The following discussions elaborate on the unsteady flow physics that effects the results in Table 2. To interpret aerodynamic lift, which is the primary force of interest in the nominally straight and level flight of the *H. pratti*, an effective angle of attack ($\alpha_{\text{effective}}$) is defined. As will be shown, there is a strong correlation between the instantaneous lift force and the instantaneous

Table 2. Time-averaged forces over two flapping cycles (53ms to 324ms).

Forces	I	I+II	I+II+III	I+II+III+IV	I+II+III+IV+V
$\bar{C}_{\text{Thrust}}$	-0.23	0.00	1.23	0.97	0.13
$\bar{C}_{\text{Lateral}}$	-0.01	0.00	0.02	0.09	0.25
$\bar{C}_{\text{Lift}}$	0.61	0.87	2.30	3.09	3.47

(I–Flapping, II–Stroke plane deviation, III–Pitching, IV–Cambering, V–Flexion)

https://doi.org/10.1371/journal.pone.0218672.t002

effective angle of attack that allows for a distinctive interpretation of lift force production across different movements. The effective angles of attack are the angles that the local relative flow vector makes with each chord line of an airfoil section across the span of the wings. Thus, $\alpha_{\text{effective}}$ varies with time and along the span of each wing. The relative flow vector is the vector sum of the instantaneous forward flight velocity of the bat and the instantaneous velocity of the leading edge imposed by the kinematics in the stroke plane. A schematic interpretation of $\alpha_{\text{effective}}$ is shown in Fig 15. Similar to static airfoil theory, positive angles are indicative of positive lift production, whereas negative angles are detrimental and produce negative lift.

Using the aforementioned combinations of wing movements, the overall native kinematics of the wings are re-composed sequentially, from the simplest to the most complex and complete, and the associated aerodynamics are simulated and analyzed.

Flapping motion. Fig 16(A) shows the effective angle of attack ($\alpha_{\text{effective}}$) at the previously defined mid-inner and mid-outer wing sections, and Fig 16(B) is the plot of the simulated aerodynamic forces when flapping motion alone is included in the wing kinematics.

The effective angle of attack, $\alpha_{\text{effective}}$, can be used to explain the generation of lift for a large part of the flapping cycle by associating Fig 16(A) with Fig 16(B). During the downstroke, most of the airfoil sections (chord lines here) experience a positive $\alpha_{\text{effective}}$, and, thus, generate lift. Conversely, during the upstroke, $\alpha_{\text{effective}}$ is mostly negative, and results in a negative lift. During a brief time interval in the 2$^{\text{nd}}$ upstroke, between ≈215 ms and ≈225 ms, the aerodynamics show evidence of positive lift. Fig 6(B) provides some clues to this phenomenon. It shows that during the initial part of the upstroke, the right wing flapping angle increases rapidly at first until about 215 ms, followed by a sudden decrease in the rate of change. This is also reflected in the inflections in the $\alpha_{\text{effective}}$ curve in Fig 16(A), at 215ms on the outer wing and at 225ms on the inner wing. The faster upward movement of the right wing followed by the slow down creates a transient LEV on the dorsal surface of the wing resulting in lift production until the LEV dissipates away. This phenomenon is evident only in the second cycle. The averaged forces presented in Fig 16(B) reveal that merely flapping in the stroke plane ($\beta = 53^{\circ}$) induces a net drag on the bat, and a modest lift ($\bar{C}_{\text{Lift}} = 0.61$).

In order to understand the flow field in more detail, Fig 17 shows the 3D wings overlaid with isosurfaces of coherent vorticity, and nondimensional pressure contours on cutting planes positioned at $y/c = 1.75$ and $y/c = -2$ (approximate wrist locations of the fully stretched right and left wings, respectively) for two complete flapping cycles, from 53 ms to 324 ms. The coherent vorticity is educed from the flow field using the complex eigenvalues of the strain rate tensor [61]. Evidently, regions of low pressure are associated with coherent vortex cores that have a direct bearing on force generation on the wing surface.

At 53 ms, during the start of the upstroke, remnants of LEVs and tip vortices generated on the outer wings during the previous downstroke are still present in the wake. During the upstroke, by 63 ms, due to the negative $\alpha_{\text{effective}}$, LEVs form on the ventral side of the wings, which grow in strength until about 73 ms, when they detach from the surface and shed. During this period, $\alpha_{\text{effective}}$ extends its negative value, and the LEVs gather strength and increase the pressure differential between the dorsal and ventral sides of the wings, augmenting the negative lift. Subsequently, with the shedding of the first LEVs, weaker LEVs form on the ventral side, maintaining the negative lift, albeit of smaller magnitude. During the transition from upstroke to downstroke, beyond 94 ms, as $\alpha_{\text{effective}}$ becomes positive, the weaker LEVs separate from the ventral side, with the formation of a new set of LEVs on the dorsal surface of the wings. By 105 ms, the dorsal LEVs are firmly established, resulting in low-pressure regions on the upper wing surface and a positive lift force.

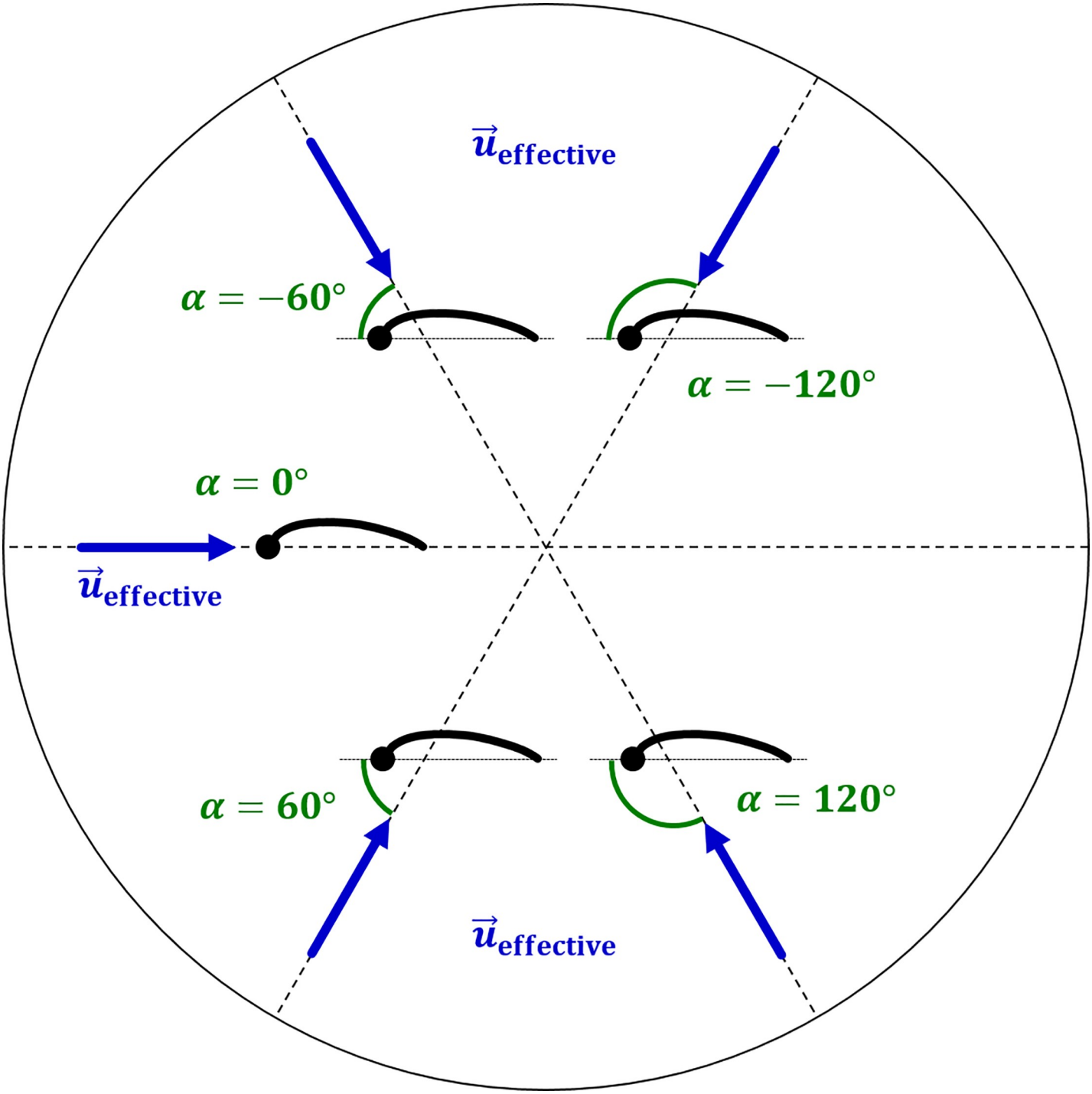

Fig 15. Interpretation of $\alpha_{\text{effective}}$ (or α).

https://doi.org/10.1371/journal.pone.0218672.g015

During the downstroke, which started at 105 ms, the LEVs on the dorsal side of the wing grow in strength and start to detach from the outer wing, as inferred from the vorticity isosurfaces at 129 ms. Soon after separation, a second set of LEVs start to form at the leading edge on the dorsal side of both wings, which are evident at 141 ms and at 156 ms. Towards the end of

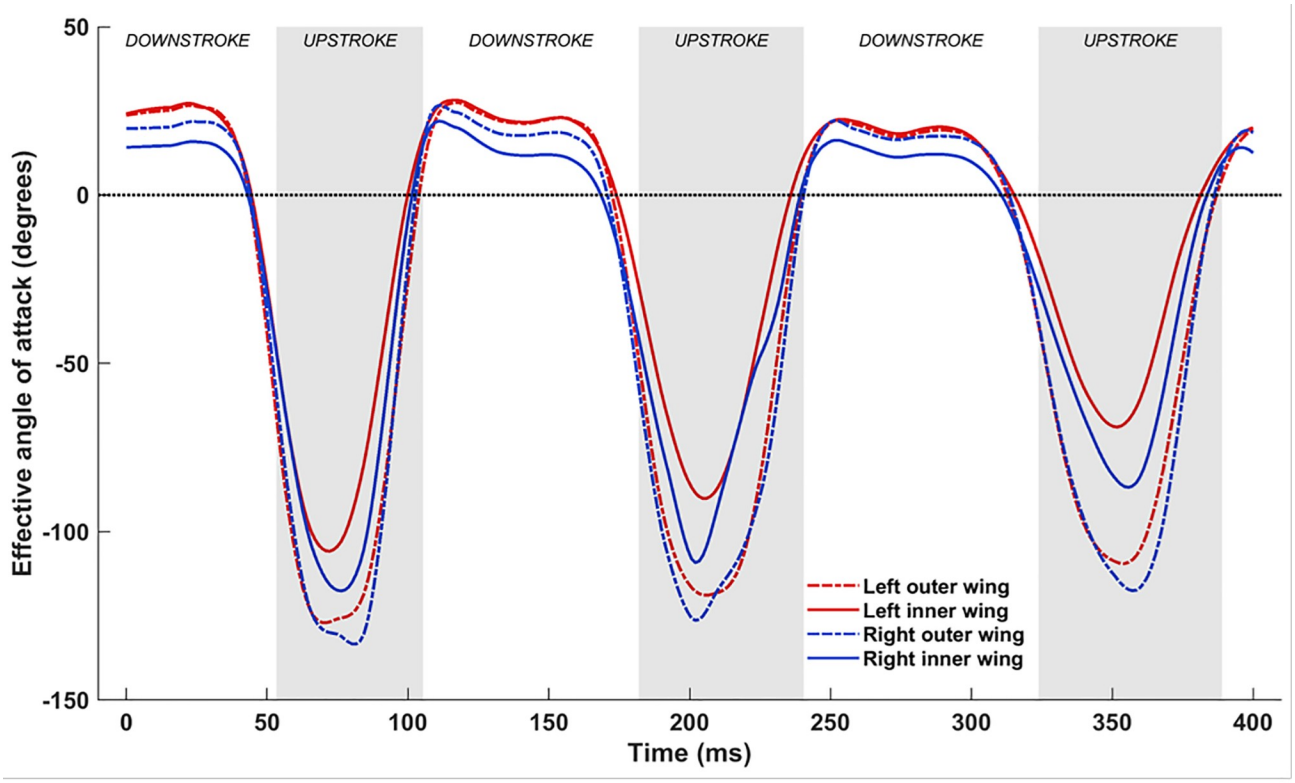
DOWNSTROKE
UPSTROKE
DOWNSTROKE
UPSTROKE
DOWNSTROKE
UPSTROKE
Effective angle of attack (degrees)
50
0
-50
-100
-150
0
50
100
150
200
250
300
350
400
Time (ms)
Left outer wing
Left inner wing
Right outer wing
Right inner wing

(a)

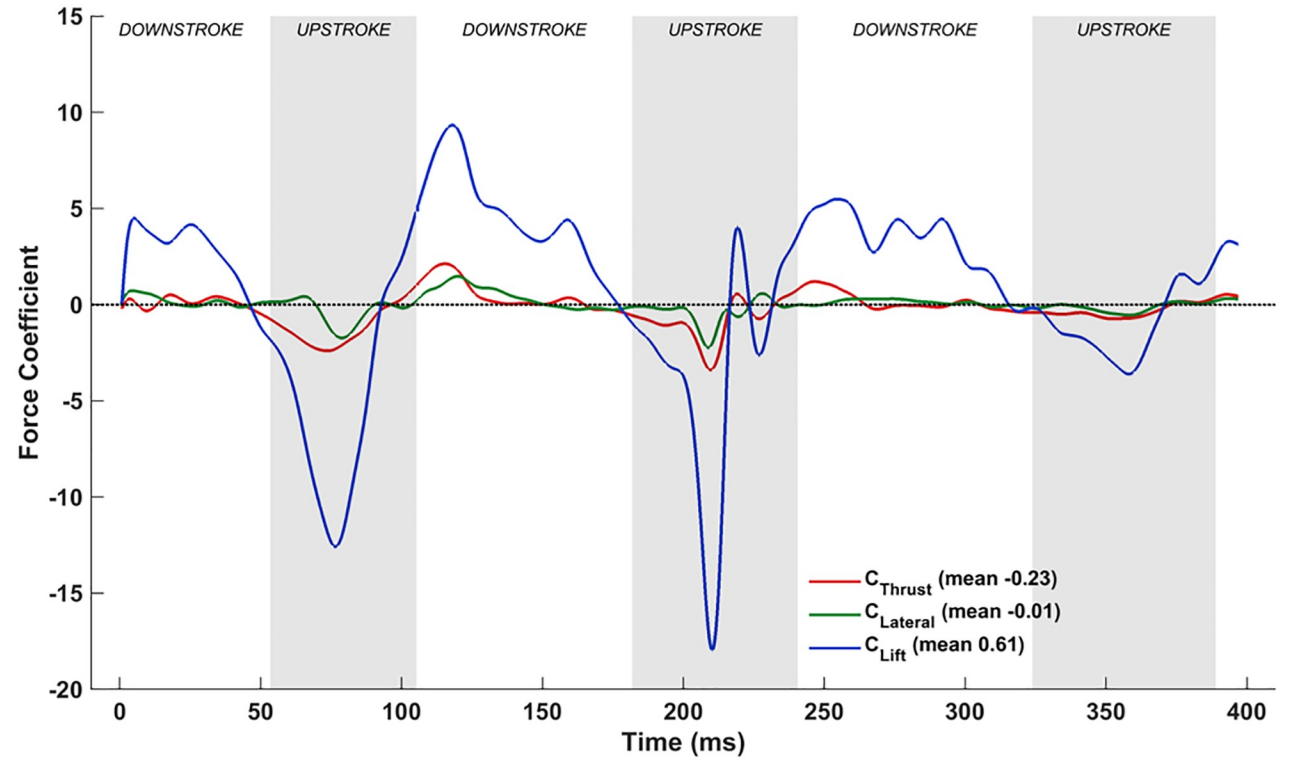
DOWNSTROKE
UPSTROKE
DOWNSTROKE
UPSTROKE
DOWNSTROKE
UPSTROKE
Force Coefficient
15
10
5
0
-5
-10
-15
-20
0
50
100
150
200
250
300
350
400
Time (ms)
C_Thrust (mean -0.23)
C_Lateral (mean -0.01)
C_Lift (mean 0.61)

(b)

Fig 16. Flapping motion: (a) Time variation of $\alpha_{effective}$, (b) Forces evolution averaged over two flapping cycles (53ms to 324ms).

https://doi.org/10.1371/journal.pone.0218672.g016

the downstroke, by around 169 ms, these LEVs have separated and the wings are ready to begin the upstroke at 182 ms with the formation of a new set of LEVs on the ventral side.

A similar overall trend of LEVs being formed alternatively on the ventral side during the upstroke and the dorsal side during the downstroke is evident during the 2nd flapping cycle (182 ms to 324 ms). The only notable difference starts at around 206 ms when the LEV from the ventral side appears to have been shed earlier than during the previous flapping cycle. Subsequently, at 216 ms, pressure contours on the right wing are quite different from the corresponding time-stamp in the 1st flapping cycle (84 ms). Whereas a clear pressure differential is established at 84 ms, which results in a consistent negative lift during this phase, at 216 ms the wing is enveloped by a low pressure bubble that gives way to a non-uniform pressure distribution at 228 ms. Here, the leading edge of the wing sees a low pressure region on the dorsal side, while the trailing edge sees a high pressure bubble. This uneven distribution is attributed to the acceleration and deceleration of the right wing, resulting in the weak inflection points in the $\alpha_{effective}$ curves.

The upstroke produces most of the negative lift, which is a direct result of negative $\alpha_{effective}$ throughout the span. Similarly, the positive $\alpha_{effective}$ produces positive lift during the downstroke. More specifically, the negative lift peak at around 74 ms is a result of the LEVs growing and subsequently separating from the surface. Similarly, the positive peak lift at around 115 ms is a result of the maximum strength of the LEVs on the dorsal side of the wing. These values are more inconsistent during the 2nd flapping cycle due to the spasmodic nature of the right wing kinematics, which leads to a less orderly behavior of the LEV. For thrust production, as the wing maintains the same pitch angle distribution throughout the flapping cycles (refer Fig 5), net thrust and lift are strongly correlated. As the wing starts with a slightly pitched down orientation and retains the pitch angle distribution throughout the flapping cycles, lift and net thrust are positively correlated, as seen in Fig 16(B).

Combined flapping and stroke plane deviation. Combining stroke plane deviation with the flapping motion does not have a significant impact on $\alpha_{effective}$, as evident when comparing Fig 18(A) with Fig 16(A). As a result, the underlying unsteady vorticity dynamics is only marginally affected by the inclusion of this motion (Fig 19 vs Fig 17). The noteworthy difference between the $\alpha_{effective}$ plots is at the start of each downstroke: whereas the flapping motion maintains a near constant $\alpha_{effective}$ during this phase, inclusion of θ (stroke plane deviation angle) into the kinematics results in a non-insignificant increase in $\alpha_{effective}$ at the beginning of each downstroke. This is most prominent on the left wing during the 3rd downstroke ($\approx$250 ms).

A more subtle difference is apparent during the 1st upstroke when comparing Fig 18(A) with Fig 16(A): between 73 ms and 84 ms, $\alpha_{effective}$ on the left outer-wing reaches the local minimum 10 ms later when compared to the flapping-only case, i.e., there is a more gradual attainment of the peak negative value when θ is included in the kinematics. This delay of $\approx$10 ms results in a weaker LEV and tip vortex on the left wing (Fig 17 and Fig 19, at 84 ms), which in turn reduces the magnitude of the peak negative lift during this phase of flight. This is also evident in the pressure contours at this time instant: whereas the low pressure on the ventral side of the left wing remains substantial for the flapping motion, when θ is added to the kinematics, a smaller low pressure bubble forms on the ventral side of the left wing. This is also the same time-period when θ changes direction for the left wing, after reaching a peak deviation of $\approx$ 25° off the stroke plane (Fig 7(B)). The combined effect of the movements results in a nearly 25% reduction in the peak negative lift. On the other side, the right wing maintains a

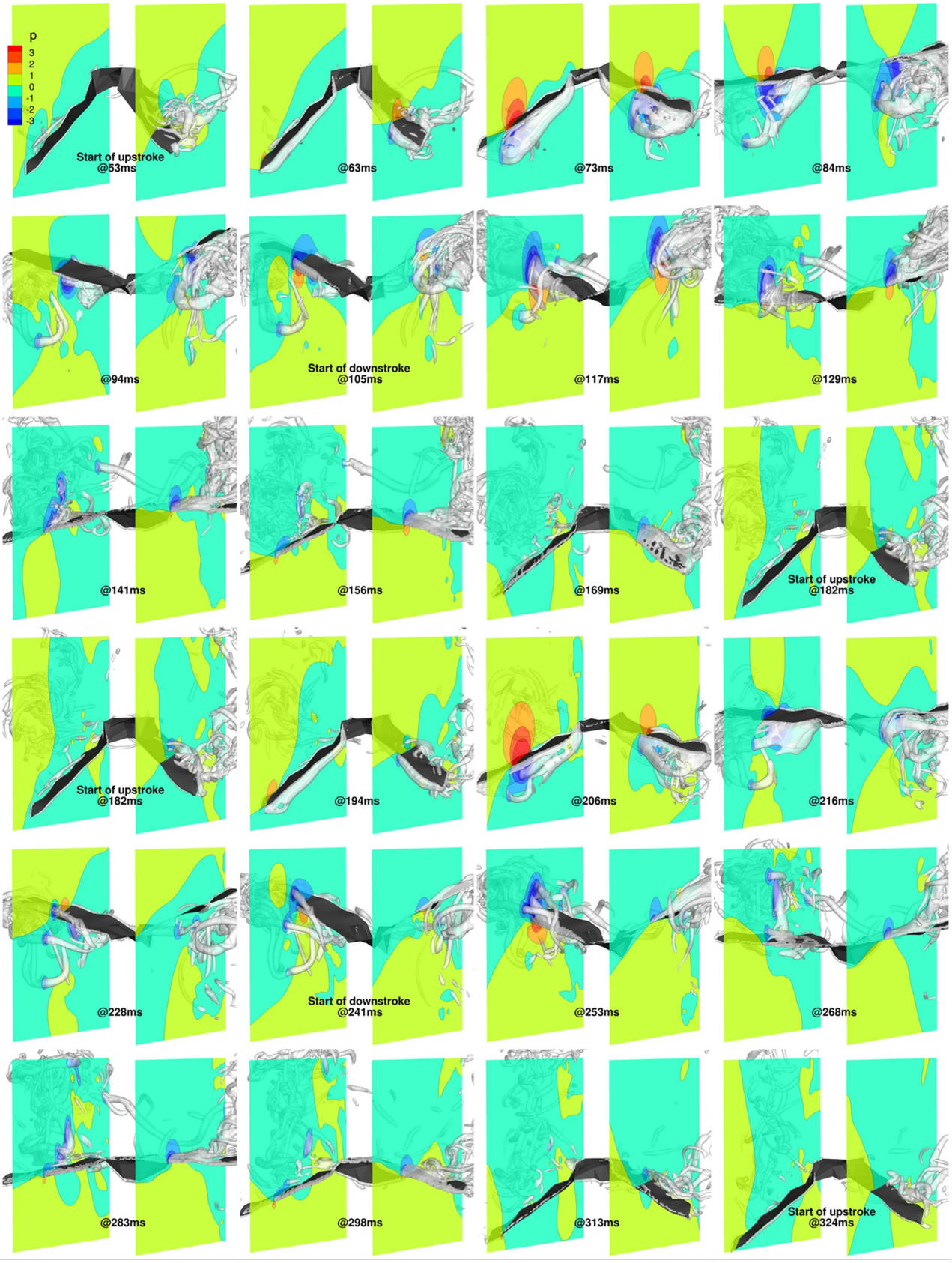
p
3
2
1
0
-1
-2
-3
Start of upstroke
@53ms
@63ms
@73ms
@84ms
@94ms
Start of downstroke
@105ms
@117ms
@129ms
@141ms
@156ms
@169ms
Start of upstroke
@182ms
Start of upstroke
@182ms
@194ms
@206ms
@216ms
@228ms
Start of downstroke
@241ms
@253ms
@268ms
@283ms
@298ms
@313ms
Start of upstroke
@324ms

Fig 17. Flapping motion (53 ms to 324 ms): 3D view of wing with pressure contours at y/c = 1.75 and y/c = -2, and isosurfaces of coherent vorticity (ω_c = 5).

https://doi.org/10.1371/journal.pone.0218672.g017

comparatively steady $\theta \approx 15^\circ$ deviation during this time period, and exhibits a similar pressure signature as the case without θ.

During the 2nd upstroke, the right wing stroke plane deviation increases from ≈7˚ to about 12˚, while the left wing θ decreases from ≈17˚ at the start of the stroke to 10˚ by the end of it. The out-of-phase stroke plane deviation between the left and right wings and the spasmodic nature of the kinematics during the 2nd upstroke seem to mitigate differences in the flow, and a similar clear distinction in lift is not evident during a similar stage of this stroke (at 216 ms). When integrated over the two flapping cycles, the cumulative impact of the differences during the upstroke and downstroke result in a noteworthy 40% increase in the average lift force, highlighting the impact of fine-tuned movements of the bat wing. The delicate movement of the left outer-wing during the 1st upstroke also reduces the peak negative net thrust during that time-period, and cumulatively nullifies the mean drag that was computed for the flapping-only simulation.

Combined flapping, stroke plane deviation and pitching. Incorporating pitching motion into the kinematics has a major impact on the force dynamics. In Fig 20(A), while the overall trend of $\alpha_{effective}$ is similar to that for the flapping and stroke plane deviation combination, there are significant differences in the magnitude of the angles during the upstrokes. When the pitching motion is included, $\alpha_{effective}$ for the mid-inner and mid-outer wing chord lines on both wings range from -50˚ to ≈35˚, whereas without the pitching motion, it varies from -125˚ to 25˚ on the outer wings and -100˚ to 20˚ on the inner wings. In addition to the differences in magnitude, which are prominent during the upstroke, the monotonic decreasing trend of $\alpha_{effective}$ during the downstroke is mitigated when the pitching motion is included: not only does the downstroke start with a high $\alpha_{effective}$ that decreases into the downstroke, but with pitching, $\alpha_{effective}$ subsequently increases to finish the downstroke as the inner and outer wing-sections start to supinate. One plausible explanation for the temporal variation of $\alpha_{effective}$ could be that the initial higher $\alpha_{effective}$ establish the LEVs early on during the downstroke, followed by a period of sustenance that necessitates lower $\alpha_{effective}$. Clearly, the pitching motion along the wing span (twisting of the wing) is used by the bat to maintain a nearly steady $\alpha_{effective}$ during the downstroke. Compared to the case without pitching, there is a more pronounced non-uniformity in $\alpha_{effective}$ between different sections of the left and right wings during the downstroke too, which is indicative of the wing pliability and ability to control force dynamics. During the 1st upstroke, both wings exhibit a mostly uniform distribution of $\alpha_{effective}$ across the span, though there is still a weak inflection point apparent on the right outer wing. This is still evident on the right outer wing during the 2nd upstroke, in addition to a stronger inflection point on the right inner wing at ≈225 ms.

The evolution of forces when pitching is added also differs significantly from the earlier settings. In Fig 20(B), towards the end of the 1st downstroke, the higher pitching angle here amplifies the projected planform area, and increases lift further (and the drag). This feature is apparent during the 2nd and 3rd downstrokes as well, where a more sustained higher lift coefficient is evident, in addition to a negative net thrust. The high lift, which occurs near the beginning of the 2nd and 3rd downstrokes for the cases without pitching, is sustained longer into the downstroke when pitching is included. This is attributed to better control of LEVs that form during each downstroke, and the pitch-up motion during supination at the end of each downstroke.

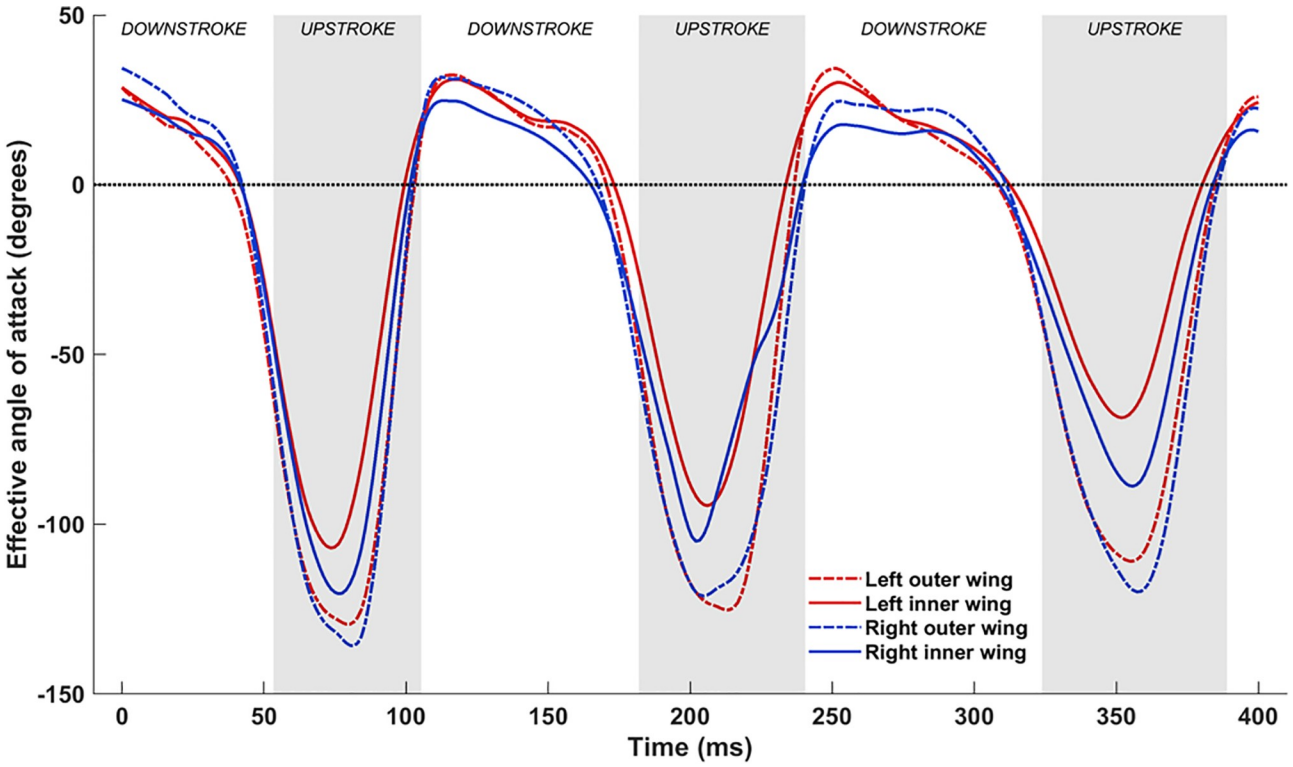
DOWNSTROKE
UPSTROKE
DOWNSTROKE
UPSTROKE
DOWNSTROKE
UPSTROKE
Effective angle of attack (degrees)
50
0
-50
-100
-150
0
50
100
150
200
250
300
350
400
Time (ms)
Left outer wing
Left inner wing
Right outer wing
Right inner wing

(a)

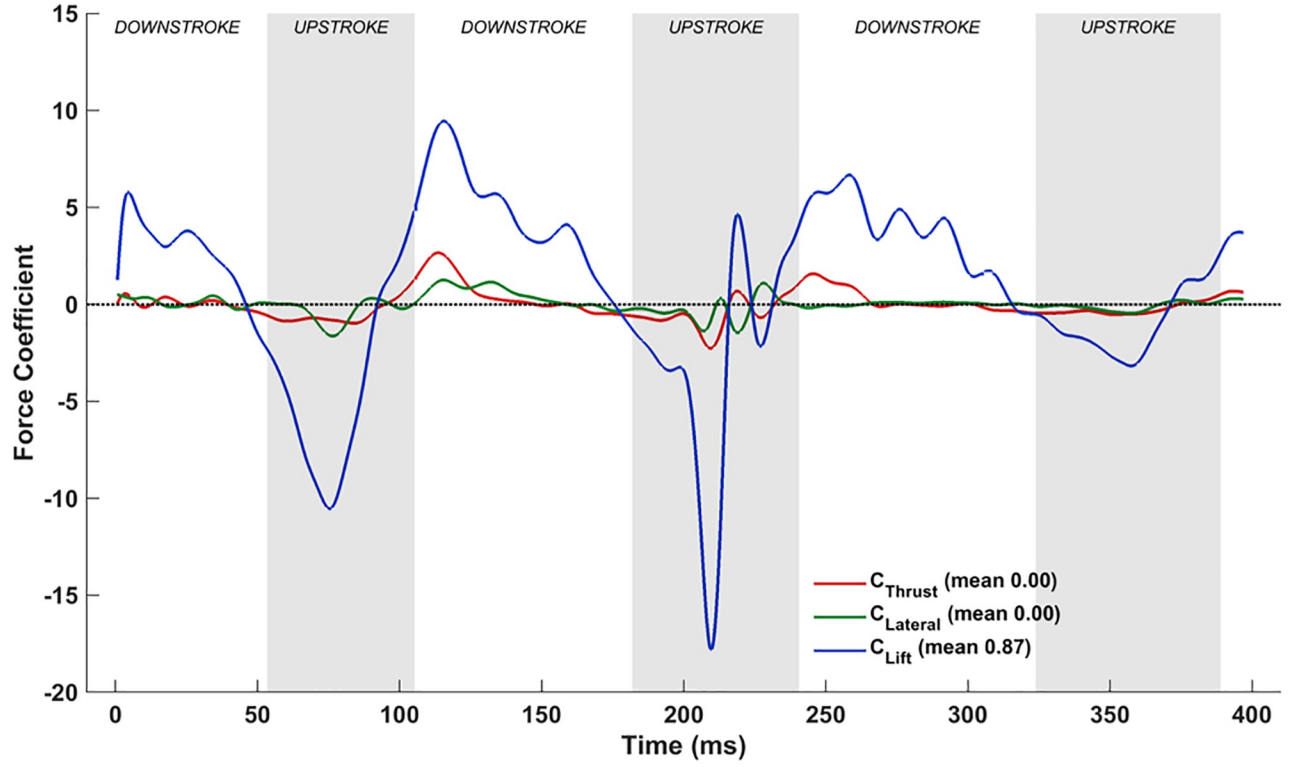
DOWNSTROKE
UPSTROKE
DOWNSTROKE
UPSTROKE
DOWNSTROKE
UPSTROKE
Force Coefficient
15
10
5
0
-5
-10
-15
-20
0
50
100
150
200
250
300
350
400
Time (ms)
C Thrust (mean 0.00)
C Lateral (mean 0.00)
C Lift (mean 0.87)

(b)

Fig 18. Combined flapping and stroke plane deviation: (a) Time variation of $\alpha_{effective}$, (b) Forces evolution averaged over two flapping cycles (53 ms to 324 ms).

https://doi.org/10.1371/journal.pone.0218672.g018

During the 1st upstroke, the magnitude of the negative lift is reduced by nearly 50%, while a significant net thrust is apparent. A similar reduction in peak negative lift is also seen during the 2nd upstroke, whilst an undulating variation in net thrust occurs during this time period. The most remarkable aspect of this upstroke is the large net thrust that is generated at ≈220 ms, which is attributed to the significantly higher $\alpha_{effective}$ on the inner right wing. The trend in the variation of lift and drag (or negative net thrust) are identical and opposite during the upstroke.

Fig 21 shows the wing surface, coherent vorticity isosurfaces and pressure contours on approximate mid-span cutting planes, similar to Fig 17 and Fig 19, for the two flapping cycles from 53 ms to 324 ms. At the beginning of the upstroke, at 53 ms, the wing has a much larger pitch angle compared to the flapping motion case with stroke plane deviation (15˚ vs -50˚). As a result, for a short amount of time (53 ms to ≈58 ms), the LEVs from the previous downstroke remain attached to the dorsal side of the wings. At 63 ms, the outer wings are pivoted almost vertically, and new LEVs form on the ventral side of the wings. From 63 ms to 73 ms, these LEVs grow stronger. From 73 ms to 84 ms, the wings undergo advanced rotation as they start to pitch down and translate upward to complete the upstroke. From 84 ms to 94 ms, the LEVs reduce in strength and are stabilized, during which the entire left and right wings are surrounded by relatively low pressure bubbles. Beyond 94 ms, up until 105 ms, the wings continue pitching down while flapping up, and in doing so, the LEVs weaken further and glide under the ventral side of the wings to form low pressure bubbles for the downstroke.

At the start of downstroke, at 105 ms, the wings have completed their pronation and their ventral sides are exposed to the freestream at a positive $\alpha_{effective}$. From 117 ms to 156 ms, the entire wing section pitches down, though non-uniformly. Both outer wings and the left inner wing change ψ gradually until about 169 ms, whereas the right inner wing exhibits a rapid decrease until 129 ms, followed by a gradual increase in ψ until 169 ms. During this period, the LEVs not only stay attached to the dorsal side of the wings, but they grow stronger. Beyond 169 ms, the rapid pitch-up motion on both wings cause the LEVs to slide off and separate out from the dorsal side of the wings. From 169 ms to 182 ms, towards the end of the downstroke, the wings perform a fast supination to transition to the next upstroke.

During the 2nd upstroke, from 182 ms up until 206 ms, there is a similar trend in the variation of $\alpha_{effective}$ as the 1st upstroke, where LEVs form on the ventral side and grow in strength. Over the next 10 ms, there is a vastly different trend in $\alpha_{effective}$ that translates to different pressure signatures over the wings: whereas the left inner and outer wings exhibit a more consistent change in $\alpha_{effective}$, the angle at the inner right wing suddenly increases at a faster rate than the outer wing. This results in a reduced projected area of the right wing, which mitigates the peak negative lift at 216 ms. At about this time, the inner right wing undergoes a sudden pitch up motion reducing $\alpha_{effective}$ from a high negative value to a positive value (this is not evident at 84 ms). As a consequence, the stagnation high pressure region forming near the dorsal trailing edge of the right wing at 84 ms does not materialize at 216 ms, thereby flipping the negative lift to a positive lift. Instead, a high pressure region materializes at 228 ms (but not at 94 ms), causing a sudden spike in net thrust. At around this time (still at 228 ms), the original LEVs also separate from the ventral side of the wings followed by the formation of weaker LEVs, which reinstate the negative lift and positive net thrust. This extent of unsteadiness is apparent only in the 2nd upstroke where the sudden pitch-up movement occurs at ≈220 ms. Towards the end of the upstroke, the wings rapidly pitch down to get ready for the downstroke. The

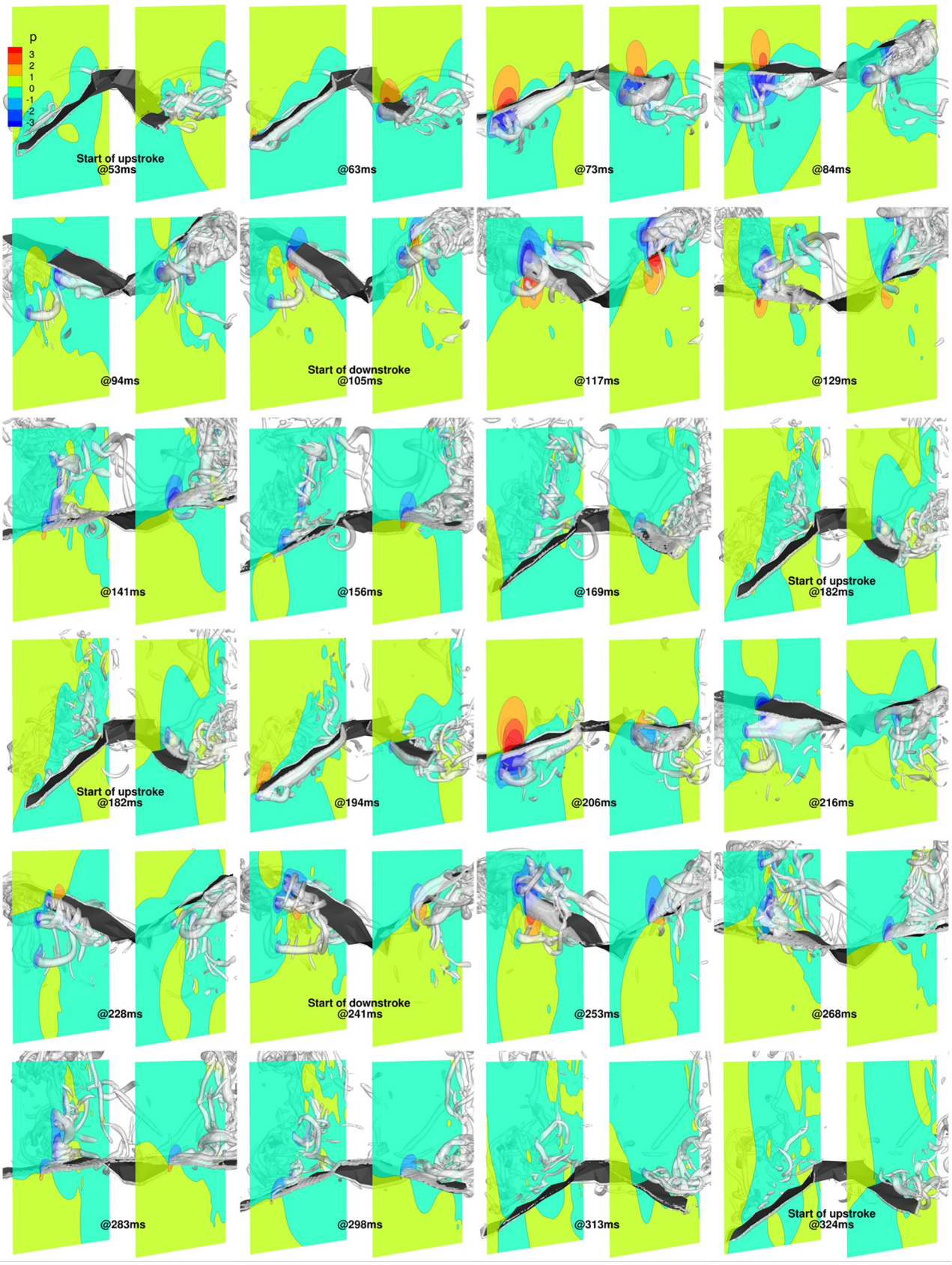
p
3
2
1
0
-1
-2
-3
Start of upstroke
@53ms
@63ms
@73ms
@84ms
@94ms
Start of downstroke
@105ms
@117ms
@129ms
@141ms
@156ms
@169ms
Start of upstroke
@182ms
Start of upstroke
@182ms
@194ms
@206ms
@216ms
@228ms
Start of downstroke
@241ms
@253ms
@268ms
@283ms
@298ms
@313ms
Start of upstroke
@324ms

Fig 19. Combined flapping and stroke plane deviation (53 ms to 324 ms): 3D view of wing with pressure contours at y/c = 1.75 and y/c = -2, and isosurfaces of coherent vorticity ($\omega_c = 5$).

https://doi.org/10.1371/journal.pone.0218672.g019

downstroke from 241 ms to 324 ms is nearly identical to the previous downstroke from 105 ms to 182 ms, and the inner right wing pitches in-phase with the rest of the wing, leading to a more steady distribution of positive lift.

Combined flapping, stroke plane deviation, twisting and cambering. By definition, the inclusion of chordwise camber ($\mathbf{C}_{i,j,n}$) does not change the temporal evolution of $\alpha_{effective}$, which remains the same as in Fig 20(A). However, similar to classical airfoil theory, the introduction of chordwise camber does impact force production, as seen by comparing Fig 22 and Fig 20(B). Although the trends in force production exhibited by the introduction of camber are very similar without it, there are subtle differences in the magnitudes. During the 1st upstroke (53 ms to 105 ms), when chordwise cambering is included, both negative lift as well as the peak net thrust are reduced. A similar trend is evident for the upstroke between 182 ms and 241 ms.

During the downstroke, the trends are similar to that without camber, but there is an increase in the lift force: the chordwise camber forces the LEVs to stay in close proximity of the dorsal surface to cover the majority of the bat wing, while the LEVs on wings without cambering separate more easily. Fig 23 shows this phenomenon during the downstroke between 105 ms and 129 ms. It is evident that the LEVs when $\mathbf{C}_{i,j,n}$ is included spread out more over the dorsal surface, resulting in lower pressure over a larger area of the wing (at 129 ms). The attached LEVs during the downstroke, together with the reduction in peak negative lift during upstroke, boost the average lift force by nearly 35% with the inclusion of camber. This was also observed by Gopalakrishnan [62] in his investigation of a flexible wing with aerodynamic force induced chordwise camber. It is noteworthy that camber decreases the net thrust by 20% for the same reasons that the negative lift decreases during the upstroke.

Combined flapping, stroke plane deviation, twisting, cambering and flexion. With the inclusion of flexion ($\mathbf{D}_{i,n}$), the complex wing kinematics of the *H. pratti* is represented in its entirety. Fig 24(A) shows the time evolution of $\alpha_{effective}$ at the previously defined four spanwise locations on the wings, and Fig 24(B) shows the corresponding force evolution in time. When comparing Fig 24(A) with the set-up without flexion (Fig 20(A)), a notable difference is the nearly universal positive $\alpha_{effective}$ at the inner wing during the upstroke when flexion is included.

To explain this in more detail, Fig 25 tracks the evolution of the wing surface and the orientations of the mid-inner and outer wing sections on both wings during the upstroke of the 1st flapping cycle. These are compared with snapshots at the same time instants without flexion. From 58 ms until 92 ms, both wings are brought inwards towards the body of the bat and flapped upwards. When flexion is not included, during the early stage of the upstroke at 58 ms, $\alpha_{effective}$ is ≈-30˚ for all wing sections (see Fig 20(A)). When flexion is incorporated, at the inner wing sections, $\rightarrow u_{effective}$ flips over to the opposite side of the chord line and changes sign, with a corresponding $\alpha_{effective}$ of about +15˚. This difference is more pronounced at 75 ms, when the wings are aligned to the direction of the upstroke, and slice through almost vertically upward in the stroke plane and backward. Whereas without flexion, $\alpha_{effective}$ is ≈-50˚ for all four airfoil sections, with flexion $\alpha_{effective}$ is ≈+5˚ at the inner wing sections. Towards the end of the upstroke, at 92 ms, the differences are marginal, and barely discernible in Fig 25. Thus, during the upstroke, flexion not only reduces the planform area of the wing but also works to achieve a positive angle of attack at the inner wing section. By orientating the inner

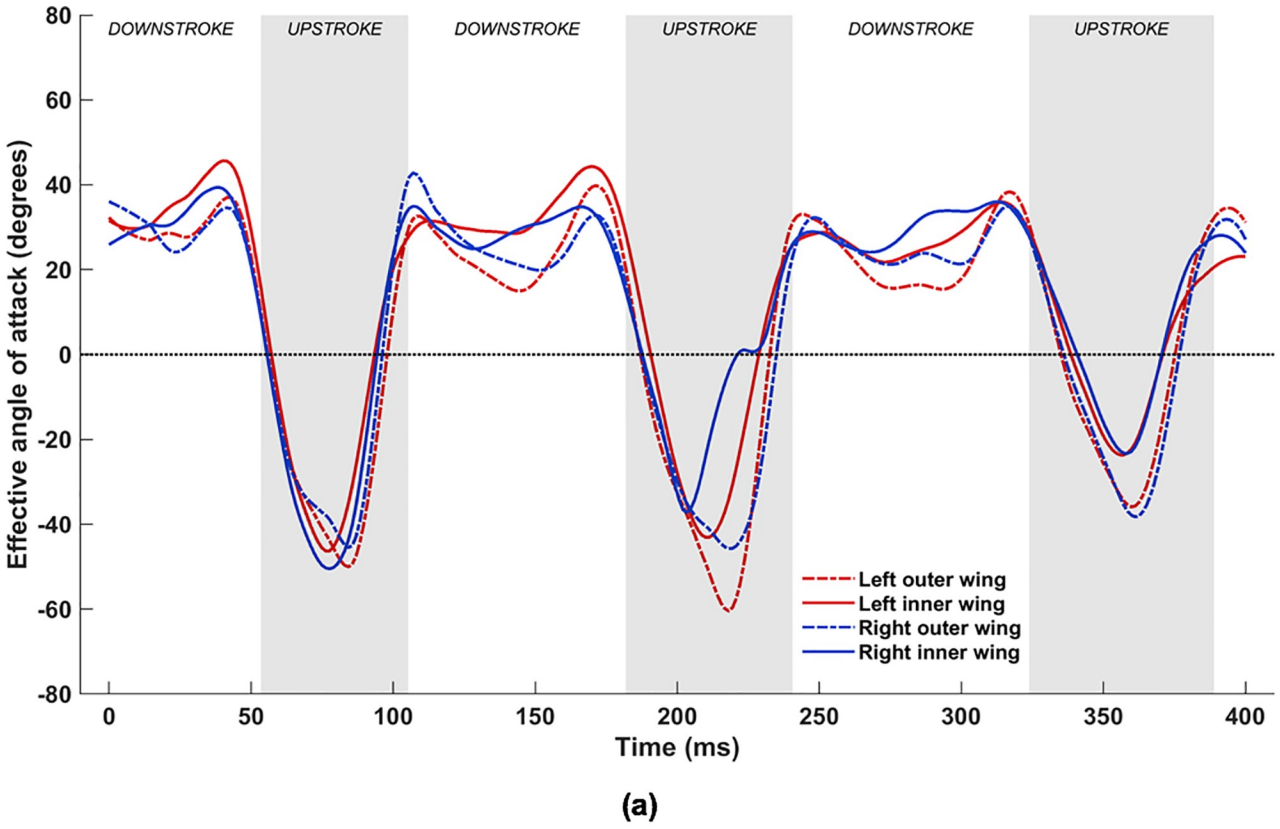
DOWNSTROKE
UPSTROKE
DOWNSTROKE
UPSTROKE
DOWNSTROKE
UPSTROKE
Effective angle of attack (degrees)
80
60
40
20
0
-20
-40
-60
-80
0
50
100
150
200
250
300
350
400
Time (ms)
Left outer wing
Left inner wing
Right outer wing
Right inner wing

(a)

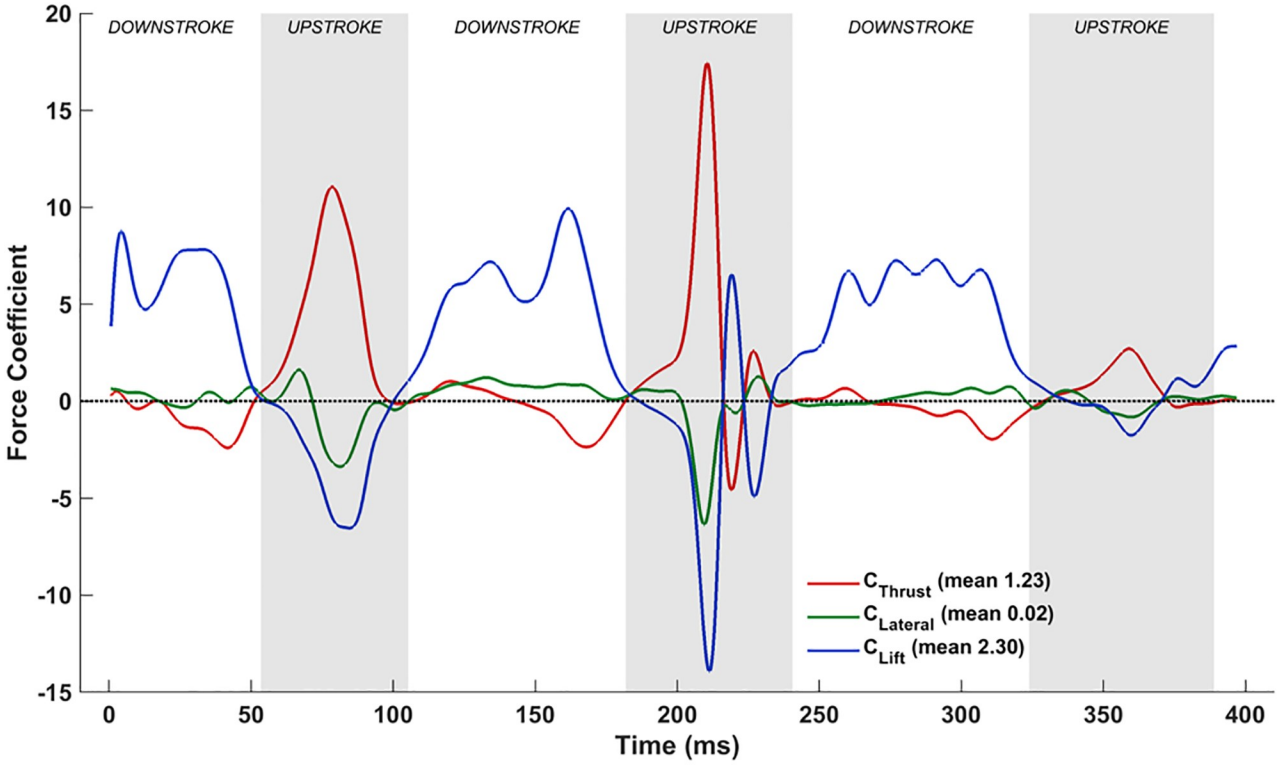
DOWNSTROKE
UPSTROKE
DOWNSTROKE
UPSTROKE
DOWNSTROKE
UPSTROKE
Force Coefficient
20
15
10
5
0
-5
-10
-15
0
50
100
150
200
250
300
350
400
Time (ms)
C_Thrust (mean 1.23)
C_Lateral (mean 0.02)
C_Lift (mean 2.30)

(b)

Fig 20. Combined flapping, stroke plane deviation and pitching: (a) Time variation of $\alpha_{effective}$, (b) Forces evolution averaged over two flapping cycles (53 ms to 324 ms).

https://doi.org/10.1371/journal.pone.0218672.g020

wing such that $\alpha_{effective}$ is positive on most of the wing, negative lift (and positive net thrust) are eliminated as evidenced in Fig 24(B).

An additional feature that stands out is the sharp drop in $\alpha_{effective}$ at the left mid- inner wing section at approximately 205 ms from a positive value of about 25˚ to a small negative value in a relatively short time span of ≈15 ms, followed by a rapid recovery back to 30˚ in the next ≈15 ms (Fig 24(B)). Interestingly, this coincides with about a 5˚ to 10˚ excursion in $\alpha_{effective}$ of the right inner wing section in the opposite direction. The consequence of these variations in $\alpha_{effective}$ on the left and right wings is that the oscillatory behavior of lift and net thrust in the middle of the upstroke (present in Fig 20(B) and Fig 22 at ≈220 ms) during the 2nd flapping cycle is eliminated. Thus, the oscillatory behavior of the forces at ≈220 ms without flexion is an artifact only because flexion was neglected in the kinematics. This aligns with the hypothesis that the instantaneous rate of flapping, pitching, and flexion work in tandem to effect a near zero negative lift penalty during the upstroke.

Fig 26 shows the vorticity and pressure contours from 53 ms to 324 ms for the combined kinematics that includes ϕ,θ,ψ, $\mathbf{C}_{i,j,n}$ and $\mathbf{D}_{i,n}$. For this case, at 53 ms and 184 ms, the wings start the upstroke with the tips drawn-in towards the body. From 53 ms to 84 ms (and 182 ms to 216 ms during the 2nd flapping cycle), the inner part of the wing reaches a nearly vertical orientation due to flexion. During this phase of motion, the outer part of the wing continues to benefit from the pitching motion, and maintains a nearly vertical profile for the initial part of the upstroke (53 ms to 73 ms and 182 ms to 206 ms during the 1st and 2nd upstroke, respectively, as explained previously when pitching is incorporated into the kinematics). Essentially, both pitching and flexion work in tandem to reduce the planform area and produce positive $\alpha_{effective}$ during the upstroke to minimize the peak negative lift by an order of magnitude of the value when both these movements are excluded (peak $C_{Lift} \approx$ -1 vs -10 during the 1st flapping cycle).

One of the distinguishing features of Fig 26 is the complete lack of extreme pressure fluctuations surrounding the wing during the upstrokes. During the upstrokes, although LEVs form on the ventral side of both outer wings, their lifespan is much shorter and strength much weaker than the LEVs that are formed without flexion. When combined with wing twist, the combined kinematics result in largely muted force fluctuations. Between the 1st and 2nd upstroke, the ventral LEVs on the outer wings are even weaker during the 2nd flapping cycle. The low-strength LEVs dissipate during the end of the upstroke.

Flexion also affects force production during the downstroke, but not as drastically as the upstroke. The multiple peaks in the lift forces from 105 ms to 169 ms and 241 ms to 313 ms (Fig 24(B)) result from the combination of multiple LEVs that form and shed during the downstrokes, the presence of tip vortices during the second half of the donwnstrokes and wing orientation, as discussed in some detail in Windes et al.[52].

Summary and conclusions

This paper investigates the nearly straight and level flight of an insectivorous bat (*H. pratti*). The relationship between flight kinematics and force dynamics is established through the decomposition of the complex 3D wing motion into basic descriptors of flapping flight. The novel framework reduces the kinematics into physical movements that include flapping, stroke plane deviation and pitching, together with cambering and flexion. To further elaborate on the aerodynamics, the effective angle of attack is revisited, and used as the basis for interpreting

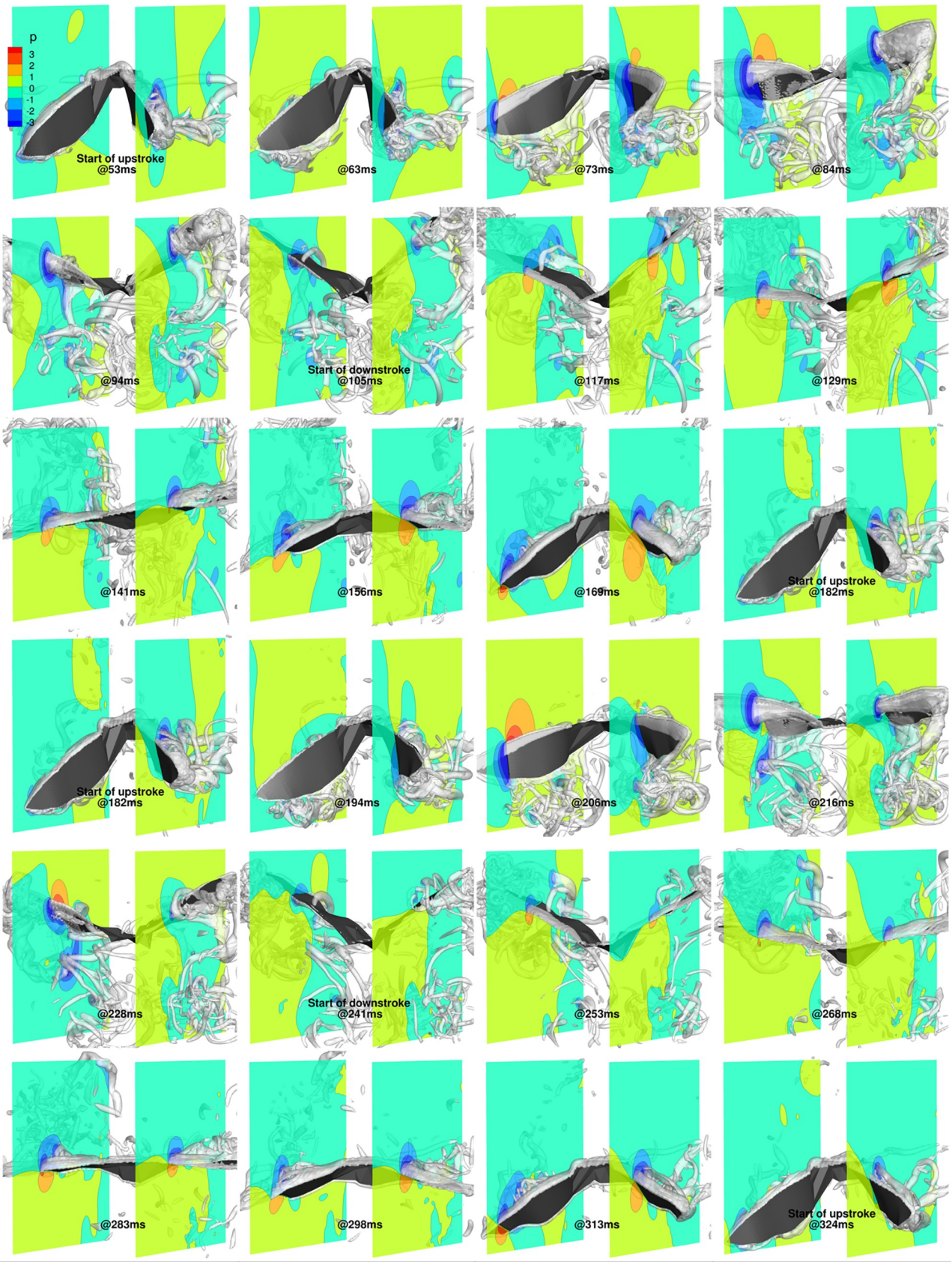

Windes, 190 of 200

Fig 21. Combined flapping, stroke plane deviation and pitching (53 ms to 324 ms): 3D view of wing with pressure contours at y/c = 1.75 and y/c = -2, and isosurfaces of coherent vorticity (ω_c = 5).

https://doi.org/10.1371/journal.pone.0218672.g021

the unsteady flow physics. While it is well known that bat wings are highly articulated and the kinematics, therefore, complex, this is the first attempt to break down the intricate motion into simpler physically relatable components of flapping flight. Both the left and right wings are initially considered rigid, and the first two movements, flapping (ϕ) and stroke plane deviation (θ), describe canonical flapping flight. The third movement (ψ) represents the twisting motion of the wing. Here, both wings are flexible, and are modeled as a collection of chord line sections incident at different pitching angles. This representation is further extended to account for cambering at each chord line. Finally, flexion models the displacement of each of these airfoils within the enclosing plane, and out of each plane. The decomposition is combined with aerodynamic simulations to investigate the cumulative effect of these movements on force production, and their primary contribution to the unsteady vortex dynamics.

For the nearly straight and level flight investigated, the stroke plane angle was calculated to be 53˚, with a stroke amplitude of around 90˚. The wing motion exhibited approximately ±9˚ and ±13˚ mean deviation from the stroke plane for the right and left wing, respectively, with the left wingtip subtending a clockwise crescent (looking outward from the body). The pitch angle varied substantially, both temporally and spatially along the span of the wing in the form of twist. During the downstroke phase, it decreased from varying between 50˚ and 75˚ at the

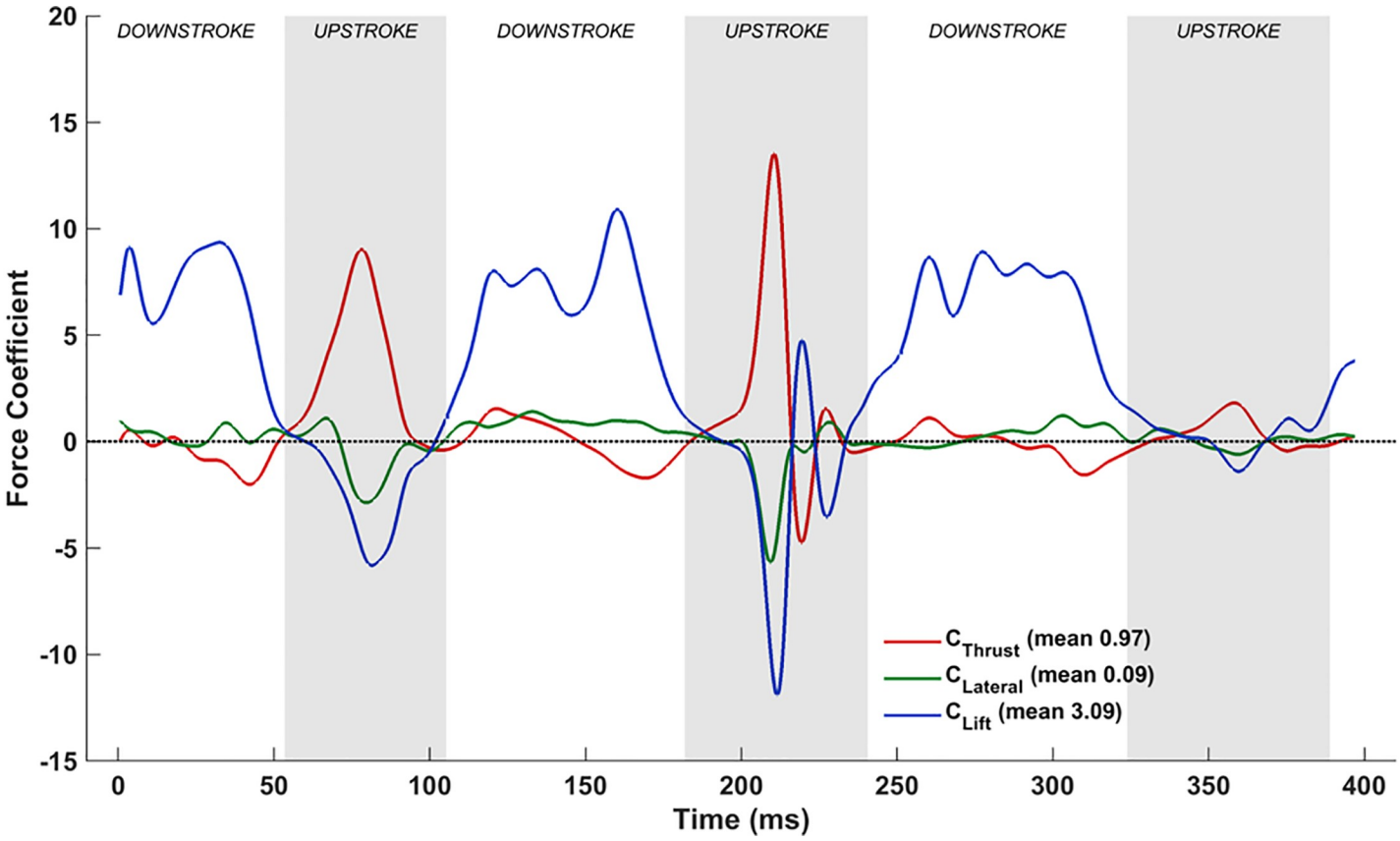

Fig 22. Combined flapping, stroke plane deviation, pitching and cambering: Forces evolution averaged over two flapping cycles (53 ms to 324 ms).

https://doi.org/10.1371/journal.pone.0218672.g022

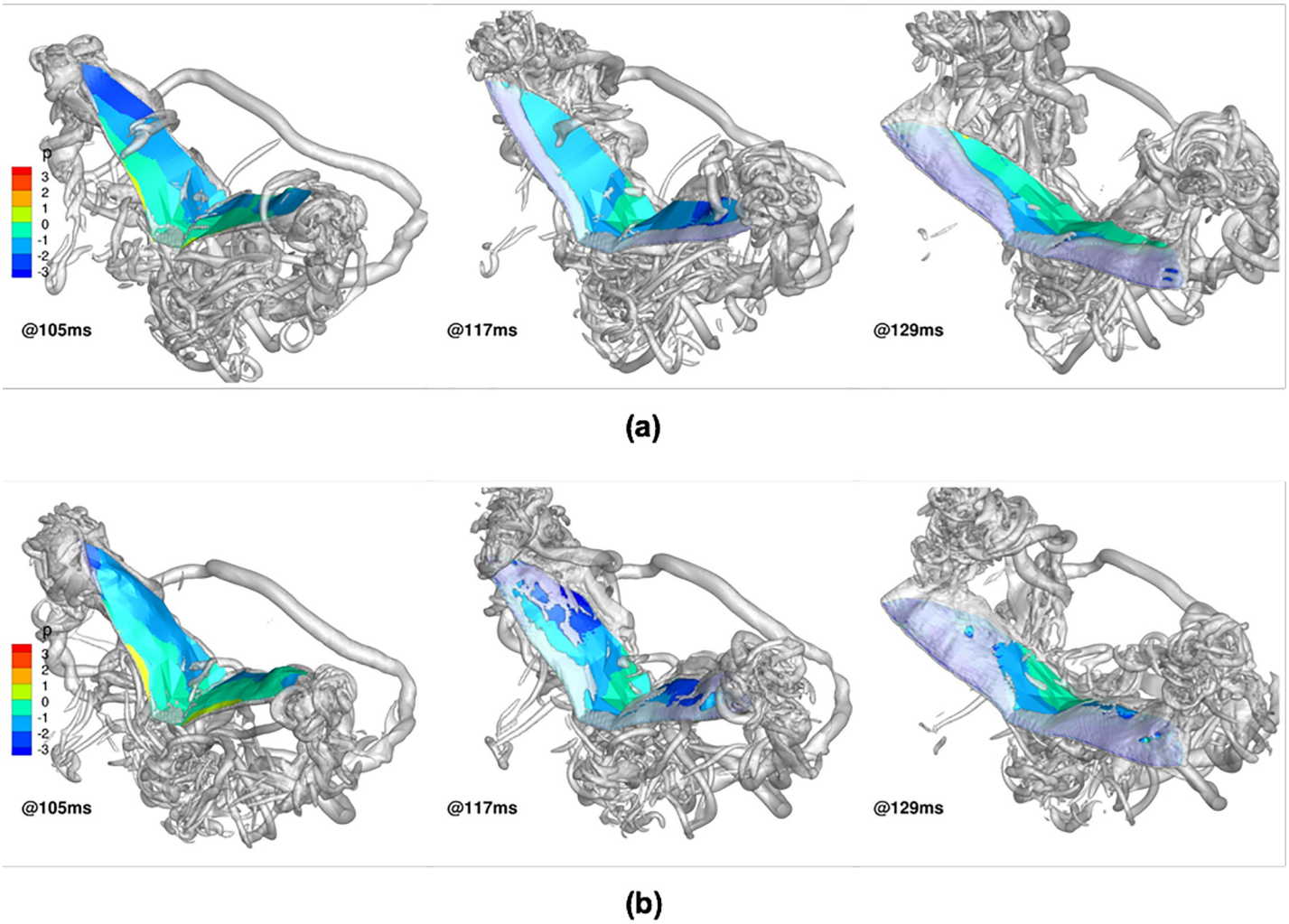

Fig 23. Effect of cambering on evolution of dorsal LEV during downstroke: wing surface colored by pressure, isosurfaces of coherent vorticity ($\omega_c = 5$): (a) without camber, (b) with camber.

https://doi.org/10.1371/journal.pone.0218672.g023

root to varying between 30˚ and 50˚ at the tip. Following the advanced rotation at the end of the downstroke, an opposite twisting trend was evident during the upstroke, when the pitch angle increased from varying between 80˚ and 110˚ at the root to varying between 125˚ and 130˚ at the tip. Cambering of airfoil sections along the wing span reached a maximum of 30–40% of the standard mean chord, while flexion varied between 10-50mm during the flapping cycles, with an average of approximately 35mm, and reached 50mm during the middle of the upstroke.

Aerodynamic simulations were performed using the IBM with a background mesh of 32 million cells and a wing surface defined by approximately 70,000 surface elements. By studying the cumulative aerodynamic effects of different physical movements, the following findings were substantiated for the nominally straight and level flight of *H. pratti*:

1. The flapping motion by itself was aerodynamically ineffective because of the large negative lift produced during the upstroke. Overall, this motion recovered only 17% of the mean lift generated by the native kinematics and produced a net drag force, which indicated that the

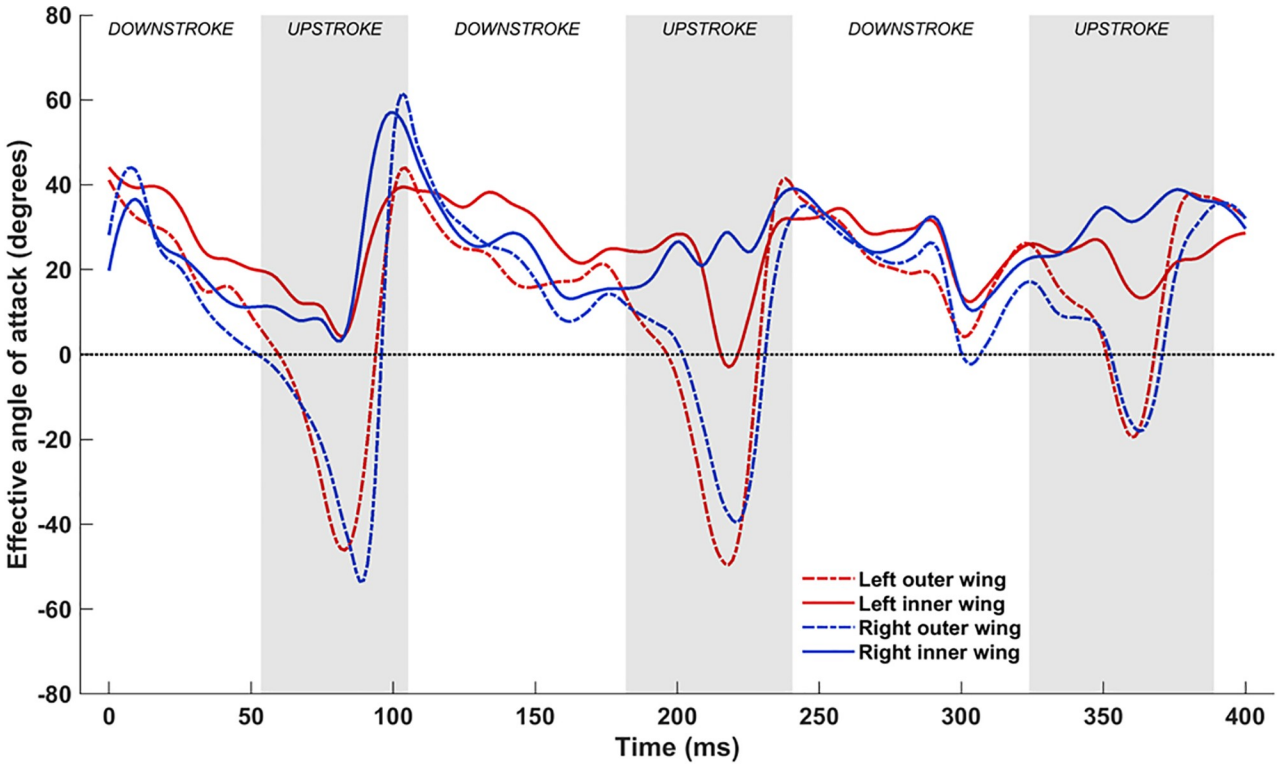
DOWNSTROKE
UPSTROKE
DOWNSTROKE
UPSTROKE
DOWNSTROKE
UPSTROKE
Effective angle of attack (degrees)
80
60
40
20
0
-20
-40
-60
-80
0
50
100
150
200
250
300
350
400
Time (ms)
Left outer wing
Left inner wing
Right outer wing
Right inner wing

(a)

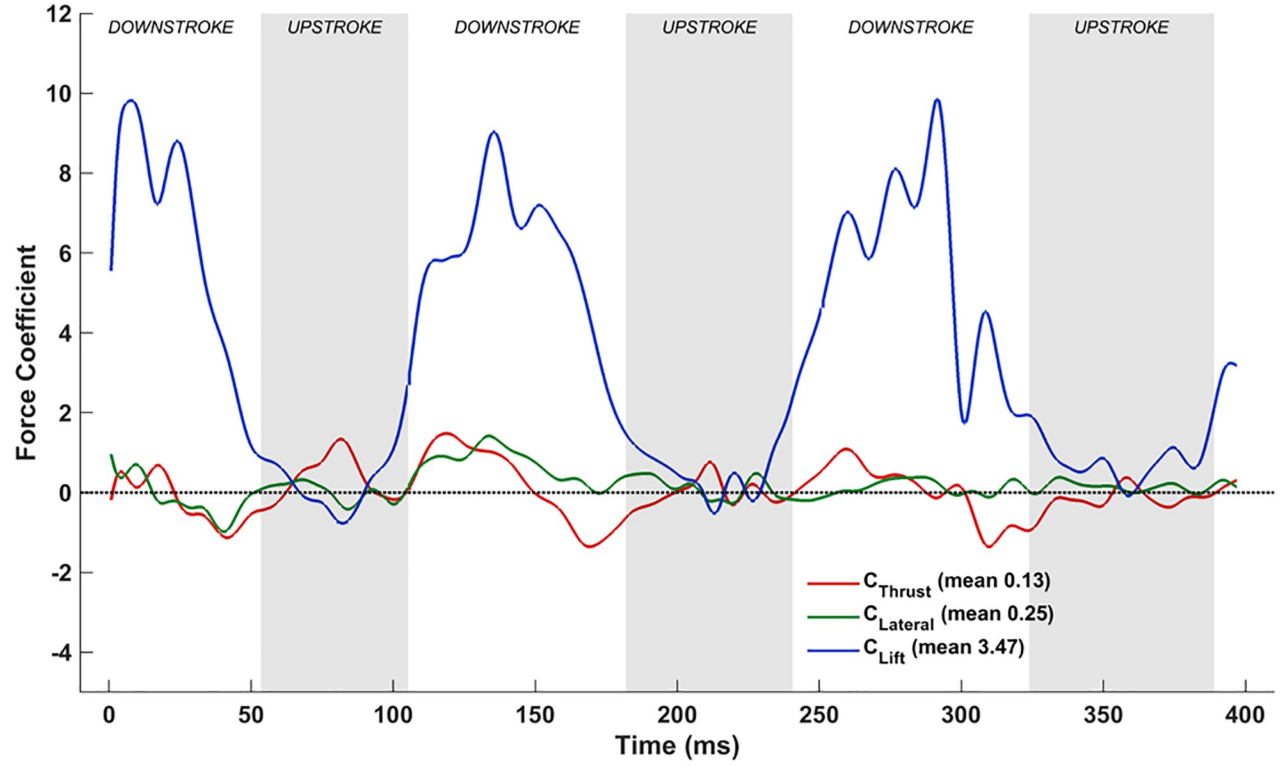
DOWNSTROKE
UPSTROKE
DOWNSTROKE
UPSTROKE
DOWNSTROKE
UPSTROKE
Force Coefficient
12
10
8
6
4
2
0
-2
-4
0
50
100
150
200
250
300
350
400
Time (ms)
C_Thrust (mean 0.13)
C_Lateral (mean 0.25)
C_Lift (mean 3.47)

(b)

Fig 24. Combined flapping, stroke plane deviation, pitching, cambering and flexion: (a) time variation of $\alpha_{effective}$, (b) Forces evolution averaged over two flapping cycles (53 ms to 324 ms).

https://doi.org/10.1371/journal.pone.0218672.g024

flapping motion by itself is not very effective, and requires other components of kinematics for effective flying;

2. Stroke plane deviation had a relatively small impact on lift when merged with flapping (combination accounted for 25% of the mean overall lift), but this motion managed to nullify the drag force generated by the flapping motion;
3. The addition of pitching and wing twist reduced negative lift during upstroke, and redirected some of the pressure differential to net thrust production. Supination allowed wings to position themselves such that the force components generated by the LEVs in the vertical direction were inconsequential, while at the same time produced a large component of net thrust. Another benefit of the pitching motion was the reduction of $\alpha_{effective}$ during the downstroke, which sustained the growth of LEVs on the dorsal side of the wing for longer periods of time. This motion combination accounted for 66% of the mean overall lift, and an effective mean net thrust that was nearly an order of magnitude higher than the overall value;
4. Cambering stabilized LEVs during the downstroke and allowed them to glide over the dorsal side of the wings, delaying separation from the surface. This combination accounted for nearly 90% of the mean overall lift;
5. Flexion allowed the bat to fine-tune $\alpha_{effective}$ during the upstroke such that the negative lift produced at the outer wing was nullified by the positive lift produced at the inner wing, resulting in a near zero lift during the upstroke;

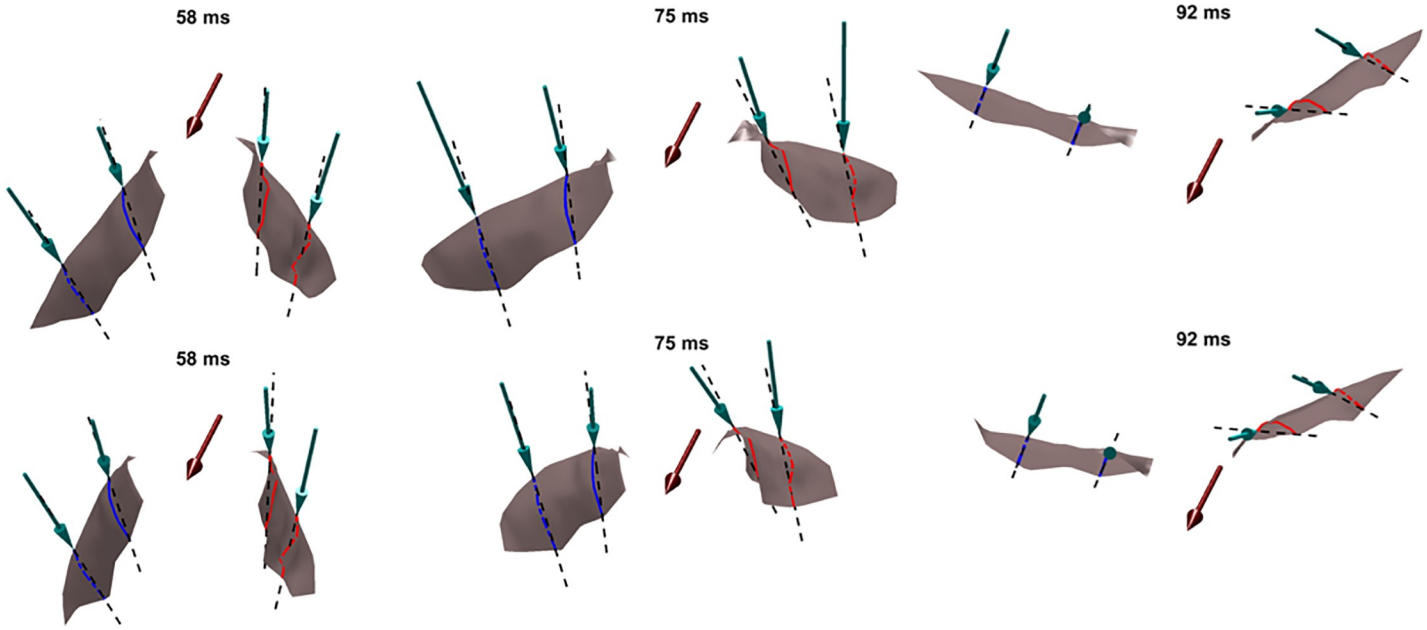

Fig 25. Effective angle of attack, $\alpha_{effective}$, at mid-inner and mid-outer wing locations (top–without flexion, bottom–with flexion), with maroon arrows denoting flight direction, green arrows denoting the direction of the local relative flow velocity at the leading edge of each airfoil, and dashed lines denoting extensions of chord lines at each airfoil section.

https://doi.org/10.1371/journal.pone.0218672.g025

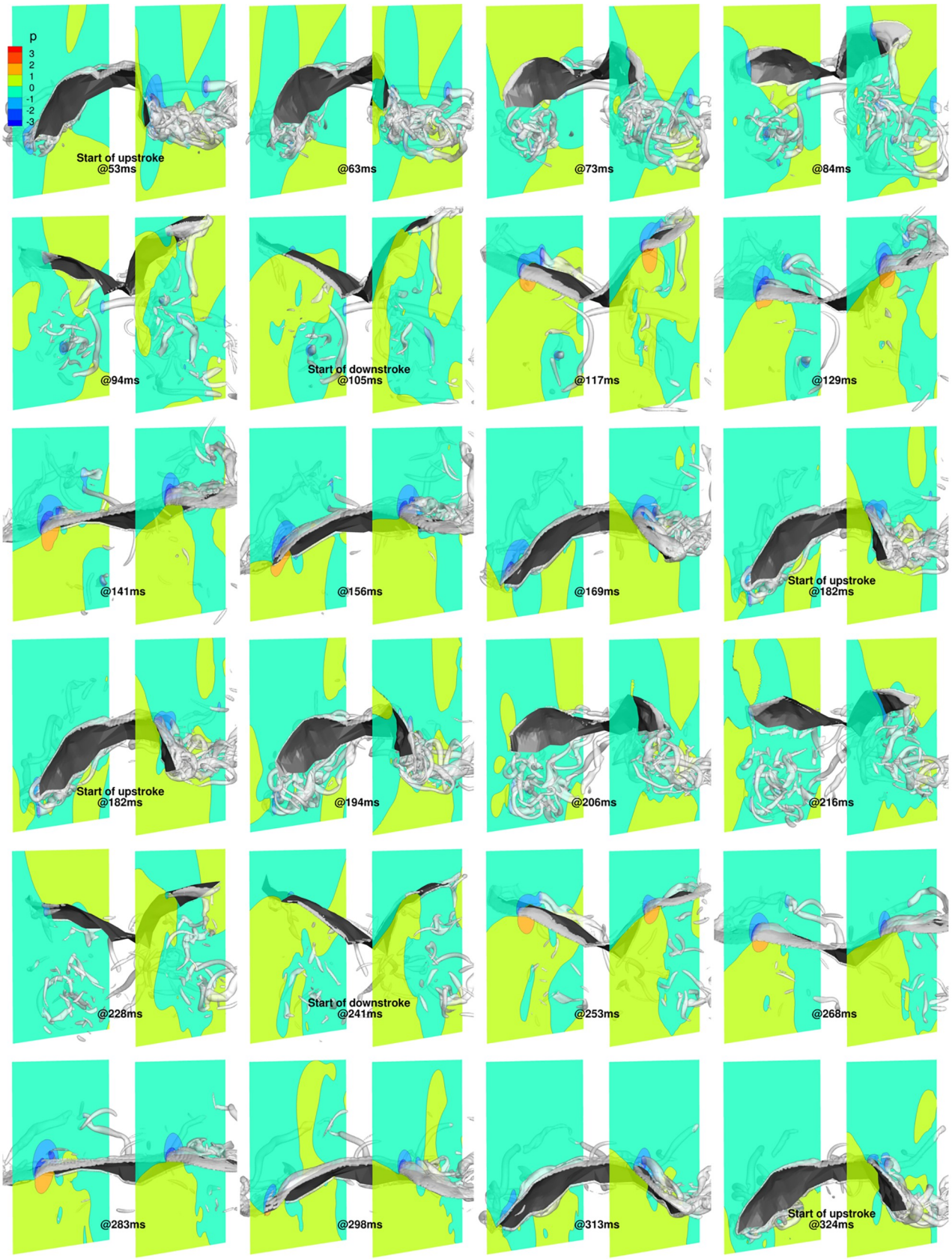

Fig 26. Combined flapping, stroke plane deviation, pitching, cambering and flexion (53 ms to 324 ms): 3D view of wing with pressure contours at y/c = 1.75 and y/c = -2, and isosurfaces of coherent vorticity ($\omega_c = 5$).

https://doi.org/10.1371/journal.pone.0218672.g026

6. From this study, it is notable that the aerodynamic effective angle of attack, $\alpha_{effective}$, emerged as the most significant parameter that affected the instantaneous lift and net thrust production.

Conclusions made regarding the contributions of each movement to force production are somewhat dependent on the order in which each motion is incorporated into the kinematics, and on the flight regime. The sequence followed in this paper is that of increasing complexity, from plain flapping motion to the complete complex kinematics. Many of the physical movements seem to work in synchrony, although each one individually may not have a favorable impact on the aerodynamics. However, such experimentation, which is made possible by the proposed decomposition, could result in novel combinations of movements for various flight regimes. The reduction to these foundational parameters from complex flight could facilitate comparison not only to the vast body of literature featuring canonical flight experiments and computations (flapping of rigid and flexible plates, pitching and/or plunging airfoils, etc.), but also comparison of wing kinematics and aerodynamics across different flying animals and flight regimes.

Supporting information

S1 Text. Outline for the decomposition of native kinematics. Information regarding motion capture of the flight kinematics is presented in Windes et al. [52]. The following is a step-by-step procedure to decompose the recorded native kinematics into different physical movements already described. This involves two main steps: first, the stroke plane location and orientation are determined based on the time-series of the wingtip points for both the left and right wings and the time-series of the shoulder points. This is followed up the decomposition process, which takes the instantaneous location information of the bat wings to isolate various components of motion:

1. Determining the stroke plane:
    a. Locate the time-series of should point positions, and determine the origin (O) of the body fixed coordinate system ($\mathbf{x_b}$, $\mathbf{y_b}$, $\mathbf{z_b}$)
    b. Locate the time-varying wingtip positions of both wings, and project the points onto the vertical bisecting plane
    c. Perform a linear regression on these points, and determine the stroke plane angle, β, and the stroke plane ($\mathbf{x_b}$, $\mathbf{y_b}$)
2. Decomposition of the native kinematics:
    a. Determine instantaneous span lines as the lines joining O and the wingtips
    b. Divide both span lines into a predetermined number of planes ($\mathbf{x_a}$, $\mathbf{z_a}$) that are perpendicular to the span lines
    c. Determine airfoil sections as the intercept of the wing surface and the previously identified planes
        i. The line joining the leading edge and trailing edge of each airfoil is the chord line
        ii. Flexion is determined as the offset of the quarter-chord from the span line
        iii. Camber is determined as the offset of the airfoil from the chord line
        iv. The local pitching angle is determined as the angle between the chord line and $\mathbf{x_a}$ in the airfoil plane ($\mathbf{x_a}$, $\mathbf{z_a}$)

d. Stroke plane deviation is the angle between the span line and the stroke plane

e. The flapping angle is the angle between the span line and $\mathbf{y_b}$ in the stroke plane ($\mathbf{x_b}$, $\mathbf{y_b}$).
(TIF)

S1 Video. Straight and level flight of Pratt's roundleaf bat (Re = 400): Flapping motion.
(MP4)

S2 Video. Straight and level flight of Pratt's roundleaf bat (Re = 400): Flapping motion with stroke plane deviation.
(MP4)

S3 Video. Straight and level flight of Pratt's roundleaf bat (Re = 400): Flapping and pitching with stroke plane deviation.
(MP4)

S4 Video. Straight and level flight of Pratt's roundleaf bat (Re = 400): Flapping and pitching with stroke plane deviation and cambering.
(MP4)

S5 Video. Straight and level flight of Pratt's roundleaf bat (Re = 400): Flapping and pitching with stroke plane deviation, cambering and flexion (native kinematics).
(MP4)

S6 Video. Straight and level flight of Pratt's roundleaf bat (Re = 1200): Flapping and pitching with stroke plane deviation, cambering and flexion (native kinematics).
(MP4)

S7 Video. Straight and level flight of Pratt's roundleaf bat (Re = 12000): Flapping and pitching with stroke plane deviation, cambering and flexion (native kinematics).
(MP4)

S8 Video. Animations of perspective view of background mesh (plotting every 5th grid line) for fluid simulation enclosing the bat and overlaid with isosurfaces of coherent vorticity (), with orthographic projections of top, front and side views (Re = 400).
(MP4)

Acknowledgments

The financial support of the NSF CBET Grant No. 1510797 and support from VT ICTAS/BIST Center is gratefully acknowledged. The authors would also like to acknowledge the computational resources provided by Advanced Research Computing (ARC) at Virginia Tech.

Author Contributions

Conceptualization: Susheel Sekhar, Xiaozhou Fan, Danesh K. Tafti.

Data curation: Susheel Sekhar, Peter Windes, Xiaozhou Fan.

Formal analysis: Susheel Sekhar, Peter Windes, Xiaozhou Fan.

Funding acquisition: Danesh K. Tafti.

Investigation: Susheel Sekhar, Peter Windes, Xiaozhou Fan.

Methodology: Peter Windes, Xiaozhou Fan, Danesh K. Tafti.

Project administration: Danesh K. Tafti.

Resources: Danesh K. Tafti.

Software: Peter Windes, Xiaozhou Fan, Danesh K. Tafti.

Supervision: Danesh K. Tafti.

Validation: Susheel Sekhar.

Visualization: Susheel Sekhar, Peter Windes.

Writing – original draft: Xiaozhou Fan.

Writing – review & editing: Susheel Sekhar, Peter Windes, Danesh K. Tafti.

References

1. Riskin DK, Willis DJ, Iriarte-Díaz J, Hedrick TL, Kostandov M, Chen J, et al. Quantifying the complexity of bat wing kinematics. J Theor Biol. 2008; 254: 604–615. https://doi.org/10.1016/j.jtbi.2008.06.011 PMID: 18621062
2. Young J, Walker SM, Bomphrey RJ, Taylor GK, Thomas ALR. Details of insect wing design and deformation enhance aerodynamic function and flight efficiency. Science (80-). 2009; 325: 1549–1552. https://doi.org/10.1126/science.1175928
3. Walker SM, Thomas ALR, Taylor GK. Deformable wing kinematics in the desert locust: How and why do camber, twist and topography vary through the stroke? J R Soc Interface. 2009; 6: 735–747. https://doi.org/10.1098/rsif.2008.0435 PMID: 19091683
4. Nakata T, Liu H. Aerodynamic performance of a hovering hawkmoth with flexible wings: a computational approach. Proc Biol Sci. 2012; 279: 722–731. https://doi.org/10.1098/rspb.2011.1023 PMID: 21831896
5. Zheng L, Hedrick TL, Mittal R. Time-Varying Wing-Twist Improves Aerodynamic Efficiency of Forward Flight in Butterflies. PLoS One. 2013; 8: 1–10. https://doi.org/10.1371/journal.pone.0053060
6. Maeda M, Nakata T, Kitamura I, Tanaka H, Liu H. Quantifying the dynamic wing morphing of hovering hummingbird. R Soc Open Sci. 2017; 4: 170307. https://doi.org/10.1098/rsos.170307 PMID: 28989736
7. Maxworthy T. The Fluid Dynamics of Insect Flight. Annu Rev Fluid Mech. 2003; 13: 329–350. https://doi.org/10.1146/annurev.fl.13.010181.001553
8. Ellington CP, van den Berg C, Willmott AP, Thomas ALR. Leading-edge vortices in insect flight. Nature. 1996; 384: 626. https://doi.org/10.1038/384626a0
9. Birch JM, Dickinson MH. Spanwise flow and the attachment of the leading-edge vortex on insect wings. Nature. 2001; 412: 729. https://doi.org/10.1038/35089071 PMID: 11507639
10. Shyy W, Trizila P, Kang C-K, Aono H. Can Tip Vortices Enhance Lift of a Flapping Wing? AIAA J. 2009; 47: 289–293. https://doi.org/10.2514/1.41732
11. Kang C-K, Aono H, Cesnik CES, Shyy W. Effects of flexibility on the aerodynamic performance of flapping wings. J Fluid Mech. 2011; 689: 32–74. https://doi.org/10.1017/jfm.2011.428
12. Shyy W, Liu H. Flapping Wings and Aerodynamic Lift: The Role of Leading-Edge Vortices. AIAA J. 2007; 45: 2817–2819. https://doi.org/10.2514/1.33205
13. Lentink D, Dickinson MH. Biofluiddynamic scaling of flapping, spinning and translating fins and wings. J Exp Biol. 2009; 212: 2691–2704. https://doi.org/10.1242/jeb.022251 PMID: 19648414
14. Lentink D, Dickinson MH. Rotational accelerations stabilize leading edge vortices on revolving fly wings. J Exp Biol. 2009; 212: 2705–2719. https://doi.org/10.1242/jeb.022269 PMID: 19648415
15. Sane SP. The aerodynamics of insect flight. J Exp Biol. 2003; 206: 4191–4208. https://doi.org/10.1242/jeb.00663 PMID: 14581590
16. Dickinson MH, Lehmann F-O, Sane SP. Wing Rotation and the Aerodynamic Basis of Insect Flight. Science (80-). 1999; 284: 1954–1960. https://doi.org/10.1126/science.284.5422.1954
17. Fung YC. An introduction to the theory of aeroelasticity. Dover Publications; 2008.
18. Weis-Fogh T. Quick Estimates of Flight Fitness in Hovering Animals, Including Novel Mechanisms for Lift Production. J Exp Biol. 1973; 59: 169–230.
19. Aono H, Chimakurthi SK, Wu P, Sallstrom E, Stanford BK, Cesnik CES, et al. A Computational and Experimental Study of Flexible Flapping Wing Aerodynamics. AIAA Aerosp Sci Meet Incl New Horizons Forum Aerosp Expo. 2010; 1–22. https://doi.org/10.2514/6.2010–554
20. Wu P, Ifju P, Stanford B. Flapping Wing Structural Deformation and Thrust Correlation Study with Flexible Membrane Wings. AIAA J. 2010; 48: 2111–2122. https://doi.org/10.2514/1.J050310

21. Curet OM, Swartz SM, Breuer KS. An aeroelastic instability provides a possible basis for the transition from gliding to flapping flight. J R Soc Interface. 2013; 10: 20120940. https://doi.org/10.1098/rsif.2012.0940 PMID: 23303221

22. Gopalakrishnan P, Tafti DK. Effect of Wing Flexibility on Lift and Thrust Production in Flapping Flight. AIAA J. 2010; 48: 865–877. https://doi.org/10.2514/1.39957

23. Sridhar M, Kang C. Aerodynamic performance of two-dimensional, chordwise flexible flapping wings at fruit fly scale in hover flight. Bioinspiration and Biomimetics. 2015; 10. https://doi.org/10.1088/1748-3190/10/3/036007

24. Mountcastle AM, Combes SA. Wing flexibility enhances load-lifting capacity in bumblebees. Proc Biol Sci. 2013; 280: 20130531. https://doi.org/10.1098/rspb.2013.0531 PMID: 23536604

25. Nakata T, Liu H. A fluid-structure interaction model of insect flight with flexible wings. J Comput Phys. 2012; 231: 1822–1847. https://doi.org/10.1016/j.jcp.2011.11.005

26. Le TQ, Truong T Van, Park SH, Truong TQ, Ko JH, Park HC, et al. Improvement of the aerodynamic performance by wing flexibility and elytra-hind wing interaction of a beetle during forward flight. J R Soc Interface. 2013; 10. https://doi.org/10.1098/rsif.2013.0312

27. Lucas KN, Johnson N, Beaulieu WT, Cathcart E, Tirrell G, Colin SP, et al. Bending rules for animal propulsion. Nat Commun. 2014; 5: 3293. https://doi.org/10.1038/ncomms4293 PMID: 24548870

28. Cheney JA, Konow N, Middleton KM, Breuer KS, Roberts TJ, Giblin EL, et al. Membrane muscle function in the compliant wings of bats. Bioinspiration and Biomimetics. 2014; 9: 25007. https://doi.org/10.1088/1748-3182/9/2/025007

29. Hedenström A, Johansson LC, Spedding GR. Bird or bat: Comparing airframe design and flight performance. Bioinspiration and Biomimetics. 2009; 4. https://doi.org/10.1088/1748-3182/4/1/015001

30. Hedenström A, Johansson LC. Bat flight: aerodynamics, kinematics and flight morphology. J Exp Biol. 2015; 218: 653–663. https://doi.org/10.1242/jeb.031203 PMID: 25740899

31. Gerdes JW, Gupta SK, Wilkerson SA. A Review of Bird-Inspired Flapping Wing Miniature Air Vehicle Designs. J Mech Robot. 2012; 4: 21003–21011. https://doi.org/10.1115/1.4005525

32. Ma KY, Chirarattananon P, Fuller SB, Wood RJ. Controlled Flight of a Biologically Inspired, Insect-Scale Robot. Science (80-). 2013; 340: 603–607. https://doi.org/10.1126/science.1231806

33. Lentink D, Jongerius SR, Bradshaw NL. The Scalable Design of Flapping Micro-Air Vehicles Inspired by Insect Flight. Flying Insects and Robots. Springer Berlin Heidelberg; 2010. pp. 185–205. https://doi.org/10.1007/978-3-540-89393-6_14

34. Nakata T, Liu H, Tanaka Y, Nishihashi N, Wang X, Sato A. Aerodynamics of a bio-inspired flexible flapping-wing micro air vehicle. Bioinspiration and Biomimetics. 2011; 6: 45002. https://doi.org/10.1088/1748-3182/6/4/045002

35. Chung S-J, Dorothy M. Neurobiologically Inspired Control of Engineered Flapping Flight. J Guid Control Dyn. 2010; 33: 440–453. https://doi.org/10.2514/1.45311

36. Ramezani A, Chung S-J, Hutchinson S. A biomimetic robotic platform to study flight specializations of bats. Sci Robot. 2017; 2. https://doi.org/10.1126/scirobotics.aal4916

37. Bender MJ, McClelland M, Bledt G, Kurdila A, Furukawa T, Müller R. Trajectory Estimation of Bat Flight Using a Multi-View Camera System. AIAA Modeling and Simulation Technologies Conference. 2015. https://doi.org/10.2514/6.2015-1806

38. Lin Y, Xu Y, Chen H, Bender MJ, Abbott AL, Müller R. Optimal Threshold and LoG Based Feature Identification and Tracking of Bat Flapping Flight. 2017 IEEE Winter Conference on Applications of Computer Vision (WACV). 2017. pp. 418–426. https://doi.org/10.1109/WACV.2017.53

39. Tian X, Iriarte-Diaz J, Middleton K, Galvao R, Israeli E, Roemer A, et al. Direct measurements of the kinematics and dynamics of bat flight. Bioinspiration and Biomimetics. 2006; 1. https://doi.org/10.1088/1748-3182/1/4/S02

40. Muijres FT, Johansson LC, Barfield R, Wolf M, Spedding GR, Hedenström A. Leading-Edge Vortex Improves Lift in Slow-Flying Bats. Science (80-). American Association for the Advancement of Science; 2008; 319: 1250–1253. https://doi.org/10.1126/science.1153019

41. Hubel TA, Riskin DK, Swartz SM, Breuer KS. Wake structure and wing kinematics: the flight of the lesser dog-faced fruit bat, Cynopterus brachyotis. J Exp Biol. 2010; 213: 3427–3440. https://doi.org/10.1242/jeb.043257 PMID: 20889823

42. Hubel TY, Hristov NI, Swartz SM, Breuer KS. Wake structure and kinematics in two insectivorous bats. Philos Trans R Soc B Biol Sci. The Royal Society; 2016; 371: 20150385. https://doi.org/10.1098/rstb.2015.0385

43. Bender M, Tian L, Fan X, Kurdila A, Müller R. Spatially recursive estimation and Gaussian process dynamic models of bat flapping flight. Nonlinear Dyn. Springer Netherlands; 2019; 95: 217–237. https://doi.org/10.1007/s11071-018-4560-z

44. Fan X, Windes P, Tafti D, Sekhar S, Bender M, Kurdila A, et al. Proper orthogonal decomposition of straight and level flight kinematics in an insectivorous bat. 2018 AIAA Modeling and Simulation Technologies Conference. 2018. https://doi.org/10.2514/6.2018-2155

45. Pivkin I V, Hueso E, Weinstein R, Laidlaw DH, Swartz S, Karniadakis GE. Simulation and Visualization of Air Flow Around Bat Wings During Flight. Computational Science—ICCS 2005—Lecture Notes in Computer Science. Springer Berlin Heidelberg; 2005. pp. 689–694. https://doi.org/10.1007/11428848_89

46. Viswanath K, Nagendra K, Tafti D. Climbing Flight of a Fruit Bat Deconstructed. 52nd Aerospace Sciences Meeting. 2014. https://doi.org/10.2514/6.2014-0220

47. Viswanath K, Nagendra K, Cotter J, Frauenthal M, Tafti DK. Straight-line climbing flight aerodynamics of a fruit bat. Phys Fluids. 2014; 26. https://doi.org/10.1063/1.4864297

48. Wang S, Zhang X, He G, Liu T. Numerical simulation of unsteady flows over a slow-flying bat. Theor Appl Mech Lett. 2015; 5: 5–8. https://doi.org/10.1016/j.taml.2015.01.006

49. Wang S, Zhang X, He G, Liu T. Lift enhancement by bats' dynamically changing wingspan. J R Soc Interface. 2015;

50. Wolf M, Johansson LC, von Busse R, Winter Y, Hedenstrom A. Kinematics of flight and the relationship to the vortex wake of a Pallas' long tongued bat (Glossophaga soricina). J Exp Biol. 2010; 213: 2142–2153. https://doi.org/10.1242/jeb.029777 PMID: 20511529

51. Norberg UM, Rayner JM V. Ecological Morphology and Flight in Bats (Mammalia; Chiroptera): Wing Adaptations, Flight Performance, Foraging Strategy and Echolocation. Philos Trans R Soc B Biol Sci. 1987; 316: 335–427. https://doi.org/10.1098/rstb.1987.0030

52. Windes P, Fan X, Bender M, Tafti DKK, Müller R. A computational investigation of lift generation and power expenditure of Pratt's roundleaf bat (Hipposideros pratti) in forward flight. PLoS One. 2018; 13: e0207613. https://doi.org/10.1371/journal.pone.0207613 PMID: 30485321

53. Svoboda T, Martinec D, Pajdla T. A Convenient Multicamera Self-Calibration for Virtual Environments. Presence Teleoperators Virtual Environ. MIT Press; 2005; 14: 407–422. https://doi.org/10.1162/105474605774785325

54. Cheng X, Sun M. Wing-kinematics measurement and aerodynamics in a small insect in hovering flight. Sci Rep. 2016; 6. https://doi.org/10.1038/srep25706

55. Viswanath K, Tafti DK. Effect of Stroke Deviation on Forward Flapping Flight. AIAA J. 2012; 51: 145–160. https://doi.org/10.2514/1.J051675

56. Tafti DK. Genidlest: A Scalable Parallel Computational Tool for Simulating Complex Turbulent Flows. Proc ASME Fluids Eng Div. ASME; 2001; 256: 347–356.

57. Tafti DK. Time-accurate techniques for turbulent heat transfer analysis in complex geometries. In: Amano R, Sunden B, editors. Computational Fluid Dynamics and Heat Transfer. Southampton, UK: WIT Press; 2011. pp. 217–264. https://doi.org/10.2495/978-1-84564-144-3/06

58. Nagendra K, Tafti DK, Viswanath K. A new approach for conjugate heat transfer problems using immersed boundary method for curvilinear grid based solvers. J Comput Phys. 2014; 267: 225–246. https://doi.org/10.1016/j.jcp.2014.02.045

59. He L, Tafti DK. Heat transfer in an assembly of ellipsoidal particles at low to moderate Reynolds numbers. Int J Heat Mass Transf. 2017; 114: 324–336. https://doi.org/10.1016/j.ijheatmasstransfer.2017.06.068

60. He L, Tafti D. Variation of drag, lift and torque in a suspension of ellipsoidal particles. Powder Technol. 2018; 335: 409–426. https://doi.org/10.1016/j.powtec.2018.05.031

61. Chong MS, Perry AE, Cantwell BJ. A general classification of three-dimensional flow fields. Phys Fluids A Fluid Dyn. 1990; 2: 765–777. https://doi.org/10.1063/1.857730

62. Gopalakrishnan P. Unsteady Aerodynamic and Aeroelastic Analysis of Flapping Flight. Mech Eng Virginia Tech. 2008;PhD Thesis.